Journal of
Mechanics of
Materials and Structures

■ mathematical sciences publishers

IN MEMORIAM: LIVIU LIBRESCU

SILVIO LEVY

In this issue we publish posthumously an article coauthored by Liviu Librescu (1930–2007). This unassuming man stood out not only as a research pioneer in many fields, but as an accomplished, warm, and generous teacher and human being. Since 1986 he had been a Professor of Engineering Science and Mechanics at the Virginia Polytechnic Institute and State University in Blacksburg, VA, where he lost his life on April 16 while saving those of his students. He left behind his wife Marlena (photo) and his sons Aryeh and Joe.

Born in Ploieşti, Romania, a mere seven years after the Jewish residents of that country achieved equality of rights, he soon saw those rights taken away as the Nazi-aligned Legionnaire regime took over. His father spent years in labor camps and the family survived great hardship. After the War, Librescu continued his studies and graduated in 1953 from the Faculty of Aeronautical Engineering of the Bucharest Polytechnic Institute.

He then started his fecund research career at the Institute of Applied Mechanics of the Romanian Academy of Science in Bucharest, at first working on elastic shells but soon branching out into fluid mechanics and aeroelasticity. In 1969 he obtained a Ph.D. from the Institute of Fluid Mechanics of the same Academy. In the 1970s he was again the target of government persecution, for refusing to pledge allegiance to the communist regime and for trying to move to Israel. He was finally allowed to emigrate in 1978, after the intervention of Israel's Prime Minister, and joined the faculty of Tel-Aviv University.

In 1985–86 he spent a sabbatical at Virginia Tech and was offered a professorship, so he moved to the United States and there continued his research in aeroelasticity, thermal stresses and composite materials. With 250 refereed journal articles in French, German, English and Russian, an equal number of contributed book chapters and proceedings articles, and a handful of research monographs, Librescu is surely one of the most published authors in the field.

Librescu's heroism during the Virginia Tech murders has been amply chronicled. He was buried in Israel with honors, and was equally recognized in Romania, whose president conferred on him on April 18 the highest civil order of that country, the Star of Romania (Grand Cross rank), for his scientific accomplishments and his selflessness.

We asked his coauthor Karam Y. Maalawi, as well as his colleagues from Virginia Tech, to write a few words in his memory, and we reproduce them on the next page.

IN MEMORY OF A VERY DEAR FRIEND

With great sorrow and deeply saddened heart, we mourn the passing away of our teacher, mentor and friend Professor Liviu Librescu.

Professor Librescu, a pioneer in the field of aerospace engineering, helped me a great deal during my stay in Virginia. His scientific guidance was invaluable to our research work.

Librescu's generosity extended to several of my colleagues at Virginia Tech in addition to myself.

Such was his kindness and love.

His memory will remain with me the rest of my life, and I promise to continue the work we planned to complete.

God rest his soul.

– Karam Y. Maalawi

FROM HIS COLLEAGUES AT VIRGINIA TECH

Liviu Librescu died as he lived, devoted to his students and his profession. He loved his position as professor, and gave himself to research and teaching, solely for the love of it. His son, Joe, says it best: "He was a scientist who did not work for money, but for the pleasure he got from his occupation." Always available to students, a caring teacher and inspiring graduate advisor, his last act was to sacrifice himself to save the students in his solid mechanics class. On that gruesome morning, he blocked the door of 204 Norris Hall with his body and ordered his students out the window. He saved all but one, and fell at last, pierced by several bullets.

We are thankful for all the years we had with him at Virginia Tech. It was fortunate for us that he chose to spend his 1985 sabbatical in our Engineering Science and Mechanics Department, and accepted the department's invitation to join us permanently. He was a helpful colleague, always ready to talk about research with anyone. His attitude towards the profession was based on a deep devotion to knowledge.

We miss him greatly. We will fulfill our mission with increased resolve in order to honor his memory. He will not be forgotten.

NONLINEAR SHELL THEORY: A DUALITY APPROACH

GIOVANNI ROMANO, CARMEN SELLITTO AND RAFFAELE BARRETTA

The nonlinear kinematics of thin shells is developed in full generality according to a duality approach in which kinematics plays the basic role in the definition of the model. The Kirchhoff–Love shell model is the central issue and is discussed in detail but shear deformable and polar models are also considered and critically reviewed. The analysis is developed with a coordinate-free approach which provides a direct geometrical picture of the shell model. The finite and tangent Green strains of the foliated continuum are explicitly expressed in terms of middle surface kinematics. The new expressions contributed here do not require the splitting of the velocity into parallel and normal components to the middle surface, and provide a computationally convenient context. Finite strain measures for the shell and their tangent and secant rates are analyzed and consistency and nonredundancy properties are discussed. The relations between the finite Green strain, its tangent and secant rates and the corresponding shell strains, are provided. The differential and boundary equilibrium equations of the shell are given in variational terms, both in unsplit and split form. A new expression of the boundary equilibrium equations is contributed and its mechanical soundness with respect to the classical one is emphasized. Equilibrium in a reference placement for the shell model is briefly discussed.

1. Introduction

The theory of shells is intimately connected with the geometry of Riemannian manifolds and elements of the relevant theory are summarized in the paper. The middle surface of a shell model is a two-dimensional submanifold of the three-dimensional euclidean space (the classical physical space). The treatment of large configuration changes of the Kirchhoff–Love shell is conveniently carried out by considering the shell as a foliation of the middle surface induced by a distance function. The description of the shell kinematics in terms of that of the middle surface is carried out by considering the nonlinear projection of the points of the foliation onto the middle surface and its derivative which is a symmetric linear operator expressible in terms of the linear projector onto the tangent plane and of the middle surface shape operator. Remarkably, this result is also useful in elastoplasticity for conveniently estimating the algorithmic tangent stiffness [Romano et al. 2005a; Romano et al. 2006]. The properties of consistency and nonredundancy to be fulfilled by a well defined strain measure are briefly illustrated to provide a basis for the analysis of shell models. The nonlinear analysis of shell deformation is developed in detail with a coordinate-free exposition. The treatment is founded on a variational approach in which kinematics plays a primary role while statics is introduced by duality. Stress fields are envisaged as Lagrange multipliers of the implicit representation of the rigidity constraint provided by a strain measure. In the classical three-dimensional continuum mechanics the Green strain measure is the most natural one. Accordingly,

---

a shell theory requires one to provide the expression of this strain measure and its rates in terms of the shell kinematical parameters. For the Kirchhoff–Love shell an expression is also provided in terms of the membrane and curvature strains of the middle surface and the relevant properties of consistency and nonredundancy are proven. The tangent deformation of the shell is then investigated to provide explicit expressions of the membrane and curvature tangent strains in terms of the velocity field of the shell middle surface, and their relation to the tangent Green strain is provided. The presentation is nontraditional since it makes no reference to coordinate systems and does not require one to split the velocity field into tangent and normal components to the middle surface. The equilibrium of membrane and flexural shells is analyzed in variational terms by relying on the virtual work theorem and on the divergence theorem on a surface, and the relevant differential and boundary conditions are provided. New results concerning both finite transformations and rate kinematics of the shell are contributed and a new expression of the equilibrium boundary condition is shown to have a sound mechanical interpretation. In fact, for nonflat shells, the classical expression of the boundary conditions does not properly take into account the rotation rate of the transversal fibers. The models of shear deformable shells and of polar shells, often adopted in computational mechanics, are illustrated and critically discussed.

2. Distance function and shape operator

A differentiable manifold $\mathbb{M}$ is a set locally diffeomorphic by C^k-charts to an open set of a model Banach space E. The tangent space $\mathbb{T}_{\mathbb{M}}(\mathbf{x})$ at a point $\mathbf{x} \in \mathbb{M}$ is the linear space of tangent vectors $\{\mathbf{x}, \mathbf{v}\} : \mathrm{C}^k(U_{\mathbf{x}}; \mathscr{R}) \mapsto \mathrm{C}^{k-1}(U_{\mathbf{x}}; \mathscr{R})$ where $\mathrm{C}^k(U_{\mathbf{x}}; \mathscr{R})$ is the germ of scalar functions which are k-times continuously differentiable in a neighborhood $U_{\mathbf{x}}$ of $\mathbf{x} \in \mathbb{M}$. Tangent vectors at a point are uniquely defined by requiring that they fulfill the formal properties of a point-derivation:

$$\begin{cases} (\mathbf{v}_1 + \mathbf{v}_2)(f) = \mathbf{v}_1(f) + \mathbf{v}_2(f), & \text{additivity,} \\ \mathbf{v}(af) = a\mathbf{v}(f), \quad a \in \mathscr{R}, & \text{homogeneity,} \\ \mathbf{v}(fg) = \mathbf{v}(f)g + f(\mathbf{v}(g)), & \end{cases} \left.\begin{array}{l} \\ \\ \\ \end{array}\right\} \quad \begin{array}{l} \mathscr{R}\text{-linearity,} \\ \\ \text{Leibniz rule,} \end{array}$$

where $f \in \mathrm{C}^k(U_{\mathbf{x}}; \mathscr{R})$. The *tangent bundle* $\mathbb{T}_{\mathbb{M}}$ of $\mathbb{M}$ is the disjoint union of the pairs $\{\mathbf{x}, \mathbb{T}_{\mathbb{M}}(\mathbf{x})\}$ with $\mathbf{x} \in \mathbb{M}$. An element $\{\mathbf{x}, \mathbf{v}\} \in \{\mathbf{x}, \mathbb{T}_{\mathbb{M}}(\mathbf{x})\}$ is said to be a tangent vector applied at the base point $\mathbf{x} \in \mathbb{M}$. We denote by $\mathbb{T}_{\mathbb{M}}(\mathscr{P}) \subseteq \mathbb{T}_{\mathbb{M}}$ the disjoint union of the pairs $\{\mathbf{x}, \mathbb{T}_{\mathbb{M}}(\mathbf{x})\}$ with $\mathbf{x} \in \mathscr{P} \subseteq \mathbb{M}$. With a look at the theory of shells, we recall some basic ingredients of surface theory. More generally, we may consider a $(n-1)$-dimensional hypersurface $\mathbb{M}$ embedded in an n-dimensional Riemannian manifold $\{\mathbb{S}, \mathbf{g}\}$. Since in shell theory the manifold $\{\mathbb{S}, \mathbf{g}\}$ is the euclidean space, the relevant connection will be denoted by the symbol ∂ of ordinary derivation. A distance function from $\mathbb{M} \subset \mathbb{S}$ is a twice continuously differentiable scalar valued map $r \in \mathrm{C}^2(\mathbb{S}; \mathscr{R})$ such that its gradient is a vector field with unitary norm: $\|\partial r(\mathbf{x})\| = 1$. To build a distance function we consider an open strip $U_{\mathbb{M}} \subset \mathbb{S}$ including $\mathbb{M}$ whose thickness is so small that every point $\mathbf{x} \in U_{\mathbb{M}}$ can be $\mathbf{g}$-orthogonally projected in an unique fashion onto a point $\mathbf{P}(\mathbf{x}) \in \mathbb{M}$. Denoting by $\mathbf{n}(\mathbf{P}(\mathbf{x}))$ the normal versor to $\mathbb{M}$ at $\mathbf{P}(\mathbf{x}) \in \mathbb{M}$, and by $\mathbf{n}(\mathbf{x})$ the normal versor at $\mathbf{x} \in U_{\mathbb{M}}$ to the parallel hypersurface $\mathbb{M}^r$ to $\mathbb{M}$ passing through the point $\mathbf{x} \in U_{\mathbb{M}}$, we have $\mathbf{n}(\mathbf{x}) = \mathbf{n}(\mathbf{P}(\mathbf{x}))$ and hence

$$\mathbf{x} = \mathbf{P}(\mathbf{x}) + r(\mathbf{x})\mathbf{n}(\mathbf{x}) = \mathbf{P}(\mathbf{x}) + r(\mathbf{x})\mathbf{n}(\mathbf{P}(\mathbf{x})).$$

Given $\mathbf{n}(\mathbf{x}) = \partial r(\mathbf{x})$ for all $\mathbf{x} \in U_{\mathbb{M}}$, the hessian $\partial^2 r(\mathbf{x})$ provides the variation of the normal to the hypersurface $\mathbb{M}^r$ through $\mathbf{x} \in U_{\mathbb{M}}$ and is named the shape operator of $\mathbb{M}^r$. Two basic properties are proven in the next Lemmas.

Lemma 2.1. The shape operator $\mathbf{S}(\mathbf{x}) := \partial\mathbf{n}(\mathbf{x}) = \partial^2 r(\mathbf{x})$ is symmetric.

Proof. The symmetry of $\mathbf{S}(\mathbf{x}) = \partial^2 r(\mathbf{x})$ is a direct consequence of the symmetry of the Riemannian connection of $\{\mathbb{S}, \mathbf{g}\}$. $\qquad\square$

Lemma 2.2. At any point $\mathbf{x} \in \mathbb{M}^r$ the normal versor $\mathbf{n}(\mathbf{x}) \in \mathbb{T}_{\mathbb{S}}(\mathbf{x})$ belongs to the kernel of the shape operator $\mathbf{S}(\mathbf{x}) \in BL(\mathbb{T}_{\mathbb{S}}(\mathbf{x}); \mathbb{T}_{\mathbb{S}}(\mathbf{x}))$:

$$\mathbf{S}(\mathbf{x})\mathbf{n}(\mathbf{x}) = \partial^2 r(\mathbf{x})\mathbf{n}(\mathbf{x}) = 0,$$

hence $\mathrm{Im}\,\mathbf{S}(\mathbf{x}) = (\mathrm{Ker}\,\mathbf{S}(\mathbf{x}))^{\perp} \subseteq \mathbb{T}_{\mathbb{M}^r}(\mathbf{x})$.

Proof. By the symmetry of $\mathbf{S}(\mathbf{x}) \in BL(\mathbb{T}_{\mathbb{S}}(\mathbf{x}); \mathbb{T}_{\mathbb{S}}(\mathbf{x}))$ we have

$$\mathbf{g}(\mathbf{Sn}, \mathbf{h}) = \mathbf{g}(\mathbf{Sh}, \mathbf{n}) = \mathbf{g}(\partial_{\mathbf{h}}\mathbf{n}, \mathbf{n}) = \frac{1}{2}\partial_{\mathbf{h}}\mathbf{g}(\mathbf{n}, \mathbf{n}) = 0,$$

for any $\mathbf{h} \in \mathbb{T}_{\mathbb{S}}(\mathbf{x})$. The last statement holds since the kernel and the image of a symmetric operator are mutual orthogonal complements.

From Lemma 2.2 it follows that the shape operator $\mathbf{S} \in BL(\mathbb{T}_{\mathbb{S}}; \mathbb{T}_{\mathbb{S}})$ may be also considered as an operator $\mathbf{S} \in BL(\mathbb{T}_{\mathbb{M}}; \mathbb{T}_{\mathbb{S}})$ or as an operator $\mathbf{S}_{\mathbb{M}} \in BL(\mathbb{T}_{\mathbb{M}}; \mathbb{T}_{\mathbb{M}})$, named the Weingarten operator. $\qquad\square$

3. Nonlinear projector

Let us provide here, for subsequent use, a formula concerning the derivative of the nonlinear projector $\mathbf{P} \in C^1(U_{\mathbb{M}}; \mathbb{M})$ on the hypersurface $\mathbb{M}$.

Lemma 3.1. Let $\mathbf{P} \in C^1(U_{\mathbb{M}}; \mathbb{M})$ be the nonlinear projector of the points of the foliation $U_{\mathbb{M}} \subset \mathbb{S}$ on the hypersurface $\mathbb{M}$. Its derivative at $\mathbf{x} \in \mathbb{M}^r \subset U_{\mathbb{M}}$ is a symmetric linear operator

$$\partial\mathbf{P}(\mathbf{x}) \in BL(\mathbb{T}_{\mathbb{S}}(\mathbf{x}); \mathbb{T}_{\mathbb{M}^r}(\mathbf{P}(\mathbf{x}))),$$

related to the linear projector $\mathbf{\Pi}(\mathbf{x}) \in BL(\mathbb{T}_{\mathbb{S}}(\mathbf{x}); \mathbb{T}_{\mathbb{M}^r}(\mathbf{x}))$ of the vectors $\mathbf{h} \in \mathbb{T}_{\mathbb{S}}(\mathbf{x})$ on the tangent plane at $\mathbf{x} \in \mathbb{M}^r$ to the r-level folium $\mathbb{M}^r$, by the formulas

$$\mathbf{\Pi}(\mathbf{x}) = \partial\mathbf{P}(\mathbf{x}) + r(\mathbf{x})\mathbf{S}^r(\mathbf{x}) = (\mathbf{I} + r(\mathbf{x})\mathbf{S}(\mathbf{P}(\mathbf{x})))\partial\mathbf{P}(\mathbf{x}) = \mathbf{\Pi}(\mathbf{P}(\mathbf{x})),$$

where $\mathbf{S}(\mathbf{P}(\mathbf{x}))$ is the shape operator of $\mathbb{M}$ at the point $\mathbf{P}(\mathbf{x}) \in \mathbb{M}$ and $\mathbf{S}^r(\mathbf{x})$ is the shape operator of $\mathbb{M}^r$ at the point $\mathbf{x} \in \mathbb{M}^r$. Moreover

$$\mathrm{Ker}\,\partial\mathbf{P}(\mathbf{x}) = \mathrm{Ker}\,\mathbf{\Pi}(\mathbf{x}) = \mathrm{Span}\,\mathbf{n}(\mathbf{x}) \qquad \text{and} \qquad \partial\mathbf{P}(\mathbf{x}) = (\mathbf{I} + r(\mathbf{x})\mathbf{S}(\mathbf{P}(\mathbf{x})))^{-1}\mathbf{\Pi}(\mathbf{x}).$$

Proof. Taking the directional derivative along any $\mathbf{h} \in \mathbb{T}_{\mathbb{S}}(\mathbf{x})$ in the formula

$$\mathbf{x} = \mathbf{P}(\mathbf{x}) + r(\mathbf{x})\mathbf{n}(\mathbf{x}) = \mathbf{P}(\mathbf{x}) + r(\mathbf{x})\mathbf{n}(\mathbf{P}(\mathbf{x}))$$

and observing that

$$\partial\mathbf{n}(\mathbf{x}) = \mathbf{S}^r(\mathbf{x}), \quad \partial(\mathbf{n} \circ \mathbf{P})(\mathbf{x}) = \partial\mathbf{n}(\mathbf{P}(\mathbf{x}))\partial\mathbf{P}(\mathbf{x}) = \mathbf{S}(\mathbf{P}(\mathbf{x}))\partial\mathbf{P}(\mathbf{x}),$$

we get $\mathbf{h} = \partial_{\mathbf{h}}\mathbf{P}(\mathbf{x}) + r(\mathbf{x})\mathbf{S}^r(\mathbf{x})\mathbf{h} = \partial_{\mathbf{h}}\mathbf{P}(\mathbf{x}) + r(\mathbf{x})\mathbf{S}(\mathbf{P}(\mathbf{x}))\partial_{\mathbf{h}}\mathbf{P}(\mathbf{x})$. The symmetry of $\partial\mathbf{P}(\mathbf{x})$ follows from that of $\mathbf{S}^r(\mathbf{x})$. Since

$$\partial_{\mathbf{n}}\mathbf{P}(\mathbf{x}) = 0, \qquad \mathbf{S}^r(\mathbf{x})\mathbf{n} = 0, \qquad \mathbf{S}(\mathbf{P}(\mathbf{x}))\mathbf{n} = 0,$$

we infer that $\mathbf{n}$ is in the kernel of the symmetric linear operator

$$\partial\mathbf{P}(\mathbf{x}) + r(\mathbf{x})\mathbf{S}^r(\mathbf{x}) = (\mathbf{I} + r(\mathbf{x})\mathbf{S}(\mathbf{P}(\mathbf{x})))\partial\mathbf{P}(\mathbf{x}).$$

By projecting on $\mathbb{T}_{\mathbb{M}^r}(\mathbf{x})$, we get the first result. To get the last formula we remark that the linear projector $\mathbf{\Pi}(\mathbf{x}) \in BL(\mathbb{T}_{\mathbb{S}}(\mathbf{x}); \mathbb{T}_{\mathbb{S}}(\mathbf{x}))$ is symmetric since $\mathbf{g}(\mathbf{\Pi a}, \mathbf{b}) = \mathbf{g}(\mathbf{\Pi a}, \mathbf{\Pi b})$, for all $\mathbf{a}, \mathbf{b} \in \mathbb{T}_{\mathbb{S}}(\mathbf{x})$ [Yosida 1974]. Moreover, the operator $\mathbf{I} + r(\mathbf{x})\mathbf{S}^r(\mathbf{x})$ is symmetric and positive definite, and hence invertible, due to the suitably small value of the thickness of the shell ensuring that the nonlinear projector $\mathbf{P} \in C^1(U_{\mathbb{M}}; \mathbb{M})$ is well defined. $\qquad\square$

Remark 3.1. The ranges of the operators $\mathbf{\Pi}(\mathbf{x}) \in BL(\mathbb{T}_{\mathbb{S}}(\mathbf{x}); \mathbb{T}_{\mathbb{S}}(\mathbf{x}))$ and $\partial\mathbf{P}(\mathbf{x}) \in BL(\mathbb{T}_{\mathbb{S}}(\mathbf{x}); \mathbb{T}_{\mathbb{S}}(\mathbf{P}(\mathbf{x})))$ at $\mathbf{x} \in \mathbb{M}^r$ are $\mathbb{T}_{\mathbb{M}^r}(\mathbf{x})$ and $\mathbb{T}_{\mathbb{M}}(\mathbf{P}(\mathbf{x}))$. In a euclidean space the linear subspaces $\mathbb{T}_{\mathbb{S}}(\mathbf{x})$ and $\mathbb{T}_{\mathbb{S}}(\mathbf{P}(\mathbf{x}))$ are identified by means of a translation. Accordingly, the subspaces $\mathbb{T}_{\mathbb{M}^r}(\mathbf{x})$ and $\mathbb{T}_{\mathbb{M}}(\mathbf{P}(\mathbf{x}))$ are also identified and considered as subspaces of the linear space $\mathbb{T}_{\mathbb{S}}(\mathbf{x})$.

4. First and second fundamental forms

The first fundamental form is the twice covariant tensor field $\mathbf{g}_{\mathbb{M}} \in BL(\mathbb{T}_{\mathbb{M}}^2; \mathcal{R})$ defined on $\mathbb{M}$ as the restriction of the metric $\mathbf{g} \in BL(\mathbb{T}_{\mathbb{S}}^2; \mathcal{R})$ of $\{\mathbb{S}, \mathbf{g}\}$ to the vectors of the tangent spaces $\mathbb{T}_{\mathbb{M}}(\mathbf{x})$. The pair $\{\mathbb{M}, \mathbf{g}_{\mathbb{M}}\}$ is a Riemannian manifold. The second fundamental form on $\mathbb{M}$ is the twice covariant tensor field $\mathbf{s}_{\mathbb{M}} \in BL(\mathbb{T}_{\mathbb{M}}^2; \mathcal{R})$ defined by

$$\mathbf{s}_{\mathbb{M}}(\mathbf{a}, \mathbf{b}) = \mathbf{g}_{\mathbb{M}}(\mathbf{S}_{\mathbb{M}}\mathbf{a}, \mathbf{b}), \qquad \text{for all } \mathbf{a}, \mathbf{b} \in \mathbb{T}_{\mathbb{M}}.$$

Lemma 4.1. The Weingarten operator $\mathbf{S}_{\mathbb{M}} \in BL(\mathbb{T}_{\mathbb{M}}; \mathbb{T}_{\mathbb{M}})$ meets the identity

$$\mathbf{g}_{\mathbb{M}}(\mathbf{S}_{\mathbb{M}}\mathbf{a}, \mathbf{b}) = -\mathbf{g}(\mathbf{n}, \partial_{\mathbf{a}}\mathbf{b}), \qquad \text{for all } \mathbf{a}, \mathbf{b} \in \mathbb{T}_{\mathbb{M}}.$$

Proof. For any vector field $\mathbf{b} \in C^1(\mathbb{M}; \mathbb{T}_{\mathbb{M}})$ the inner product $\mathbf{g}(\mathbf{n}, \mathbf{b})$ vanishes identically on $\mathbb{M}$, so that $0 = \partial_{\mathbf{a}}\mathbf{g}(\mathbf{n}, \mathbf{b}) = \mathbf{g}_{\mathbb{M}}(\mathbf{S}_{\mathbb{M}}\mathbf{a}, \mathbf{b}) + \mathbf{g}(\mathbf{n}, \partial_{\mathbf{a}}\mathbf{b})$, for all $\mathbf{a} \in \mathbb{T}_{\mathbb{M}}$. $\qquad\square$

Remark 4.1. The identity in Lemma 4.1 is often taken as the definition of the Weingarten operator. It is important to highlight the tensoriality property of the bilinear form $\mathbf{g}(\mathbf{n}, \partial_{\mathbf{a}}\mathbf{b})$ in spite of the apparent dependence of the derivative $\partial_{\mathbf{a}}\mathbf{b}$ on the local behavior of the field $\mathbf{b} \in C^1(\mathbb{M}; \mathbb{T}_{\mathbb{M}})$.

5. Strain measures and constrained continua

As a premise to the discussion of shell models, we present here some general considerations that will be referred to in Section 13. A detailed account may be found in [Romano et al. 2002]. Motions of a continuous body are mathematically described by flows of a submanifold $\mathbb{B}$ in a finite dimensional ambient manifold $\mathbb{S}$, whose points are the kinematical parameters. Vector fields $\mathbf{v} \in C^1(\mathbb{B}; \mathbb{T}_{\mathbb{S}})$, defined on the body-submanifold and tangent to the ambient manifold, are called virtual displacements. The basic issue in formulating a structural model is the statement of what is understood for a rigid transformation of the body in the ambient manifold, when passing from any placement to another one. Rigidity is an

essential issue in defining the elastic response of materials and in formulating the equilibrium conditions. Rigid transformations form a group under map composition. Once the group of rigid transformations has been defined, one may choose among several alternative ways to provide an implicit description of the rigidity group as a submanifold of the manifold of all configuration-changes. This description is accomplished by choosing a strain measure, that is a suitable differential operator which associates, to any configuration-change of the body from any given placement, a set of tensor-valued fields, defined on that placement, which vanish if and only if the configuration-change is a rigid transformation. Although there are many possible choices in defining a strain measure, definite rules must be fulfilled. A first rule is expressed by a nonredundancy requirement, a condition which in optimization theory is dubbed *constraint qualification*. It is expressed by the property that no set of lower dimensional tensor-valued fields can do the job in providing an implicit description of the rigidity group. A further *consistency* requirement states that a strain measure must meet a pseudo-additivity property as a function of the configuration-changes. To state this property let us consider a flow $\boldsymbol{\psi}_{\tau,t} \in C^1(\mathbb{B}; \mathbb{S})$ with $\boldsymbol{\psi}_{\tau,s} = \boldsymbol{\psi}_{\tau,t} \circ \boldsymbol{\psi}_{t,s}$ and $\boldsymbol{\psi}_{s,s}$ the identity map. Denoting by $\mathbf{G}(\boldsymbol{\psi}_{\tau,s})$ the strain measure corresponding to the configuration-change $\boldsymbol{\psi}_{\tau,s}$, the pseudo-additivity property is

$$\mathbf{G}(\boldsymbol{\psi}_{\tau,s}) = \mathbf{G}(\boldsymbol{\psi}_{t,s}) + \mathbf{A}(\boldsymbol{\psi}_{t,s}, \mathbf{G}(\boldsymbol{\psi}_{\tau,t})), \qquad \text{with } \mathbf{A}(\boldsymbol{\psi}_{t,s}, 0) = 0,$$

so that the strain measure value is unaffected by a post composition of the configuration-change by a rigid transformation. The operator $\mathbf{A}$ is assumed differentiable with respect to the second argument, with an invertible derivative so that a stress field conjugate to the strain measure can be defined. Indeed a stress field is the Lagrange multiplier associated with an implicit representation of the rigidity constraint. It follows that the equilibrium of the body at any placement can be expressed in terms of the virtual work of the stress field by the time derivative of the strain measure from that placement to the actual one [Romano et al. 2002]. The three-dimensional Cauchy continuum is the standard model for experimental tests on materials and elastic stress and strain computations on a body. To define lower-dimensional structural models providing suitable approximations, the first step is to choose a simplified kinematics by specifying which configuration changes are admissible. If the Green strain measure of the continuum from a reference natural placement can be expressed as a differentiable function of the strain measure of the approximate model (by means of a strain-relating map) the elastic potential of the model is defined as the composition between the elastic potential of the continuum and the strain-relating map. Once the elastic solution of the model is found, the corresponding Green strain measure of the continuum is available and hence the approximate Cauchy stress field is recovered by means of the constitutive relations via the one-to one correspondence with the referential stress field. Often engineers, in assigning the constitutive properties of approximate models, are guided by the results to be expected for the standard three-dimensional continuum. Accordingly, in shell theories, when the transversal shell fibers are considered elastically inextensible, the elastic relations of the linear isotropic material in a plane stress state are assumed and the Poisson effect in the transversal direction is taken into account only after the elastic solution in terms of stress is found. The following basic result of three-dimensional kinematics in the euclidean space ensures that, for any diffeomorphic transformation $\boldsymbol{\psi} \in C^2(\mathbb{B}; \mathbb{S})$ of a three-dimensional continuum, the difference between the pull-back of the metric tensor and the metric tensor itself is a well defined strain measure. This measure is known as the Green strain and is defined

by

$$2\mathbf{g}(\mathbf{G}_{\boldsymbol{\psi}}\mathbf{h}_1, \mathbf{h}_2) := \mathbf{g}((\partial_{\mathbf{h}_1}\boldsymbol{\psi}_{\varphi}), (\partial_{\mathbf{h}_2}\boldsymbol{\psi}_{\varphi})) - \mathbf{g}(\mathbf{h}_1, \mathbf{h}_2), \qquad \text{for all } \mathbf{h}_1, \mathbf{h}_2 \in \mathbb{T}_{\mathbb{S}}.$$

A direct computation shows that the Green strain is consistent.

Theorem 5.1 (Homogeneous finite strains). Let $\mathbb{B} \subset \mathbb{S}$ be a connected open set and $\boldsymbol{\psi} \in C^2(\mathbb{B}; \mathbb{S})$ be a diffeomorphism such that the associated Green strain tensor field is constant on $\mathbb{B}$. Then the differential $\partial\boldsymbol{\psi} \in C^1(\mathbb{B}; BL(\mathbb{T}_{\mathbb{S}}(\mathbb{B}); \mathbb{T}_{\mathbb{S}}(\boldsymbol{\psi}(\mathbb{B}))))$ is a constant field. If the Green strain field vanishes on $\mathbb{B}$, the differential $\partial\boldsymbol{\psi}$ is a constant isometry on $\mathbb{B}$.

Proof. Let $\mathbf{h}_1, \mathbf{h}_2, \mathbf{h} \in \mathbb{T}_{\mathbb{S}}$ be arbitrary constant fields. By assumption:

$$\partial_{\mathbf{h}}\mathbf{g}(\partial_{\mathbf{h}_1}\boldsymbol{\psi}(\mathbf{x}), \partial_{\mathbf{h}_2}\boldsymbol{\psi}(\mathbf{x})) = \mathbf{g}(\partial^2_{\mathbf{h}\mathbf{h}_1}\boldsymbol{\psi}(\mathbf{x}), \partial_{\mathbf{h}_2}\boldsymbol{\psi}(\mathbf{x})) + \mathbf{g}(\partial^2_{\mathbf{h}\mathbf{h}_2}\boldsymbol{\psi}(\mathbf{x}), \partial_{\mathbf{h}_1}\boldsymbol{\psi}(\mathbf{x})) = 0.$$

By exchanging $\mathbf{h}_1$ with $\mathbf{h}$ and $\mathbf{h}_2$ with $\mathbf{h}$ we get the relations:

$$\mathbf{g}(\partial^2_{\mathbf{h}\mathbf{h}_1}\boldsymbol{\psi}(\mathbf{x}), \partial_{\mathbf{h}_2}\boldsymbol{\psi}(\mathbf{x})) + \mathbf{g}(\partial_{\mathbf{h}_1}\boldsymbol{\psi}(\mathbf{x}), \partial^2_{\mathbf{h}\mathbf{h}_2}\boldsymbol{\psi}(\mathbf{x})) = 0,$$
$$\mathbf{g}(\partial^2_{\mathbf{h}_1\mathbf{h}}\boldsymbol{\psi}(\mathbf{x}), \partial_{\mathbf{h}_2}\boldsymbol{\psi}(\mathbf{x})) + \mathbf{g}(\partial_{\mathbf{h}}\boldsymbol{\psi}(\mathbf{x}), \partial^2_{\mathbf{h}_1\mathbf{h}_2}\boldsymbol{\psi}(\mathbf{x})) = 0,$$
$$\mathbf{g}(\partial^2_{\mathbf{h}_2\mathbf{h}_1}\boldsymbol{\psi}(\mathbf{x}), \partial_{\mathbf{h}}\boldsymbol{\psi}(\mathbf{x})) + \mathbf{g}(\partial_{\mathbf{h}_1}\boldsymbol{\psi}(\mathbf{x}), \partial^2_{\mathbf{h}_2\mathbf{h}}\boldsymbol{\psi}(\mathbf{x})) = 0.$$

From these equalities, by the symmetry of the second derivative, we infer that $\mathbf{g}(\partial^2_{\mathbf{h}_1\mathbf{h}_2}\boldsymbol{\psi}(\mathbf{x}), \partial_{\mathbf{h}}\boldsymbol{\psi}(\mathbf{x})) = 0$. Then, by the nonsingularity of $\partial\boldsymbol{\psi}(\mathbf{x})$, we have $\partial^2_{\mathbf{h}_1\mathbf{h}_2}\boldsymbol{\psi}(\mathbf{x}) = 0$ for all $\mathbf{x} \in \mathbb{B}$ and by the connectedness of $\mathbb{B}$, we get that $\partial\boldsymbol{\psi}$ is a constant field. $\qquad\square$

Let $\mathbf{Fl}^{\mathbf{v}}_{t,s} \in C^1(\mathbb{S}; \mathbb{S})$ be a flow in the space $\mathbb{S}$, with velocity field $\mathbf{v} \in C^k(\mathbb{S}; \mathbb{T}_{\mathbb{S}})$, that is, $\mathbf{v} = \partial_{t=s}\mathbf{Fl}^{\mathbf{v}}_{t,s}$. The tangent Green strain at s is the time-derivative at $t = s$ of the Green strain evaluated at the configuration change from $\mathbb{B}$ to $\boldsymbol{\psi}_{t,s}(\mathbb{B})$:

$$\mathbf{g}(\dot{\mathbf{G}}(\mathbf{v})\mathbf{h}_1, \mathbf{h}_2) := \frac{1}{2}\partial_{t=s}\mathbf{g}(\partial_{\mathbf{h}_1}\mathbf{Fl}^{\mathbf{v}}_{t,s}, \partial_{\mathbf{h}_2}\mathbf{Fl}^{\mathbf{v}}_{t,s}) = \mathbf{g}((\text{sym }\partial\mathbf{v})\mathbf{h}_1, \mathbf{h}_2),$$

Then the following rate counterpart of Theorem 5.1 holds.

Theorem 5.2 (Homogeneous tangent strains). Let $\mathbb{B} \subset \mathbb{S}$ be a connected open set and $\mathbf{v} \in C^2(\mathbb{B}; \mathbb{T}_{\mathbb{S}})$ be a tangent displacement such that the associated tangent Green strain tensor field is constant on $\mathbb{B}$. Then the gradient field $\partial\mathbf{v} \in BL(\mathbb{T}_{\mathbb{S}}(\mathbb{B}); \mathbb{T}_{\mathbb{S}}(\mathbb{B}))$ is constant on $\mathbb{B}$. In particular, if the tangent Green strain field vanishes in $\mathbb{B}$ then the tangent displacement is rigid:

$$\mathbf{v}(\mathbf{x}) - \mathbf{v}(\mathbf{y}) = \mathbf{W}(\mathbf{x} - \mathbf{y}), \qquad \text{for all } \mathbf{x}, \mathbf{y} \in \mathbb{B},$$

where $\mathbf{W} \in BL(\mathbb{T}_{\mathbb{S}}(\mathbf{x}); \mathbb{T}_{\mathbb{S}}(\mathbf{x}))$ is a skew-symmetric tensor.

Proof. Let $\mathbf{h}_1, \mathbf{h}_2, \mathbf{h} \in \mathbb{T}_{\mathbb{S}}$ be arbitrary constant fields. By assumption:

$$\partial_{\mathbf{h}}(\mathbf{g}(\partial_{\mathbf{h}_1}\mathbf{v}(\mathbf{x}), \mathbf{h}_2) + \mathbf{g}(\partial_{\mathbf{h}_2}\mathbf{v}(\mathbf{x}), \mathbf{h}_1)) = \mathbf{g}(\partial^2_{\mathbf{h}\mathbf{h}_1}\mathbf{v}(\mathbf{x}), \mathbf{h}_2) + \mathbf{g}(\partial^2_{\mathbf{h}\mathbf{h}_2}\mathbf{v}(\mathbf{x}), \mathbf{h}_1) = 0.$$

By exchanging $\mathbf{h}_1$ with $\mathbf{h}$ and $\mathbf{h}_2$ with $\mathbf{h}$, we get two more relations, so that

$$\mathbf{g}(\partial^2_{\mathbf{h}\mathbf{h}_1}\mathbf{v}(\mathbf{x}), \mathbf{h}_2) + \mathbf{g}(\partial^2_{\mathbf{h}\mathbf{h}_2}\mathbf{v}(\mathbf{x}), \mathbf{h}_1) = 0,$$

$$\mathbf{g}(\partial^2_{\mathbf{h}_1\mathbf{h}}\mathbf{v}(\mathbf{x}), \mathbf{h}_2) + \mathbf{g}(\partial^2_{\mathbf{h}_1\mathbf{h}_2}\mathbf{v}(\mathbf{x}), \mathbf{h}) = 0,$$

$$\mathbf{g}(\partial^2_{\mathbf{h}_2\mathbf{h}_1}\mathbf{v}(\mathbf{x}), \mathbf{h}) + \mathbf{g}(\partial^2_{\mathbf{h}_2\mathbf{h}}\mathbf{v}(\mathbf{x}), \mathbf{h}_1) = 0.$$

From these equalities, by the symmetry of the second derivative, we infer that $\mathbf{g}(\partial^2_{\mathbf{h}_1\mathbf{h}_2}\mathbf{v}(\mathbf{x}), \mathbf{h}) = 0$ and hence that $\partial^2_{\mathbf{h}_1\mathbf{h}_2}\mathbf{v}(\mathbf{x}) = 0 \iff \partial^2\mathbf{v}(\mathbf{x}) = 0$, for all $\mathbf{x} \in \mathbb{B}$. By the connectedness of $\mathbb{B}$ we infer that $\partial\mathbf{v}$ is a constant field. If its symmetric part vanishes, we get $\partial\mathbf{v} = \mathbf{W}$, a skew-symmetric tensor. $\square$

6. Shell models

We will primarily be interested in presenting a general, coordinate free exposition of the classical shell model without shear deformation, known in the literature as the Kirchhoff–Love shell model. This basic model provides also the guidelines for the investigation of some more sophisticated shell models proposed in the discouragingly vast literature on the topic. We will not even try to be exhaustive in this respect and will limit our attention to the most popular shell models for computational purposes. These models will be briefly illustrated, with critical remarks, in Section 13.2. Also, neither constitutive relations nor computational issues will be treated in detail, since attention is focused on the basic kinematical aspects of the models.

6.1. *Kirchhoff–Love shell model.* In the classical Kirchhoff–Love model, a shell is described as the foliation $U_{\mathbb{M}} \subset \mathbb{S}$ of a regular surface $\mathbb{M}$ in the three-dimensional euclidean physical space $\{\mathbb{S}, \mathbf{g}\}$. To this end we consider a distance function from it and define the folii of the shell as level sets for the distance function by assuming that the thickness of the shell is small enough to ensure that a distance function of any of its points from the middle surface $\mathbb{M}$ is well defined. Let $\boldsymbol{\varphi} \in C^1(\mathbb{M}; \mathbb{S})$ be a one-to-one transformation of the middle surface $\mathbb{M}$ of the shell in the physical space $\mathbb{S}$ which is a diffeomorphism from the placement $\mathbb{M} \subset \mathbb{S}$ to the placement $\boldsymbol{\varphi}(\mathbb{M}) \subset \mathbb{S}$. The differential $\partial\boldsymbol{\varphi}(\mathbf{x}) \in BL(\mathbb{T}_{\mathbb{M}}(\mathbf{x}); \mathbb{T}_{\boldsymbol{\varphi}(\mathbb{M})}(\boldsymbol{\varphi}(\mathbf{x})))$ is a linear isomorphism:

$$\operatorname{Im} \partial\boldsymbol{\varphi}(\mathbf{x}) = \mathbb{T}_{\boldsymbol{\varphi}(\mathbb{M})}(\boldsymbol{\varphi}(\mathbf{x})),$$

$$\operatorname{Ker} \partial\boldsymbol{\varphi}(\mathbf{x}) = \{0\} \in \mathbb{T}_{\mathbb{M}}(\mathbf{x}).$$

The $\mathbf{g}$-transposed operator $\partial\boldsymbol{\varphi}^T(\boldsymbol{\varphi}(\mathbf{x})) \in BL(\mathbb{T}_{\boldsymbol{\varphi}(\mathbb{M})}(\boldsymbol{\varphi}(\mathbf{x})); \mathbb{T}_{\mathbb{M}}(\mathbf{x}))$ is a linear isomorphism too, with

$$\operatorname{Im} \partial\boldsymbol{\varphi}^T(\boldsymbol{\varphi}(\mathbf{x})) = (\operatorname{Ker} \partial\boldsymbol{\varphi}(\mathbf{x}))^{\perp} = \mathbb{T}_{\mathbb{M}}(\mathbf{x}),$$

$$\operatorname{Ker} \partial\boldsymbol{\varphi}^T(\mathbf{x}) = (\operatorname{Im} \partial\boldsymbol{\varphi}(\mathbf{x}))^{\perp} = \{0\} \in \mathbb{T}_{\boldsymbol{\varphi}(\mathbb{M})}(\boldsymbol{\varphi}(\mathbf{x})).$$

Performing the decomposition $\mathbf{x} = \mathbf{P}(\mathbf{x}) + r(\mathbf{x})\mathbf{n}(\mathbf{P}(\mathbf{x}))$, with $\mathbf{x} \in U_{\mathbb{M}}$, the induced transformation

$$\boldsymbol{\psi}_{\boldsymbol{\varphi}} \in C^1(U_{\mathbb{M}}; \mathbb{S})$$

of the shell is defined by

$$\boldsymbol{\psi}_{\boldsymbol{\varphi}}(\mathbf{x}) := \boldsymbol{\varphi}(\mathbf{P}(\mathbf{x})) + r(\mathbf{x})\mathbf{n}_{\boldsymbol{\varphi}}(\boldsymbol{\varphi}(\mathbf{P}(\mathbf{x}))), \qquad \text{for all } \mathbf{x} \in U_{\mathbb{M}},$$

where $\mathbf{n}_{\boldsymbol{\varphi}}(\boldsymbol{\varphi}(\mathbf{P}(\mathbf{x})))$ is the normal versor to $\boldsymbol{\varphi}(\mathbb{M})$ at $\boldsymbol{\varphi}(\mathbf{P}(\mathbf{x}))$. This is the basic kinematical assumption in the Kirchhoff–Love shell model: material fibers normal to the middle surface remain normal to it and do not change their length when transformations of the shell in the physical space take place. Given $\partial_{\mathbf{h}}r = \mathbf{g}(\mathbf{h}, \mathbf{n})$, the differential $\partial\boldsymbol{\psi}_{\boldsymbol{\varphi}}$ is given by:

$$\partial_{\mathbf{h}}\boldsymbol{\psi}_{\boldsymbol{\varphi}} = (\mathbf{I} + r\mathbf{S}_{\boldsymbol{\varphi}})\partial\boldsymbol{\varphi}\partial_{\mathbf{h}}\mathbf{P} + \mathbf{g}(\mathbf{h}, \mathbf{n})\mathbf{n}_{\boldsymbol{\varphi}} \circ \boldsymbol{\varphi} \circ \mathbf{P}, \qquad \text{for all } \mathbf{h} \in \mathbb{T}_{\mathbb{S}},$$

where $\mathbf{S}_{\boldsymbol{\varphi}} := \partial\mathbf{n}_{\boldsymbol{\varphi}} \in BL(\mathbb{T}_{\boldsymbol{\varphi}(\mathbb{M})}; \mathbb{T}_{\boldsymbol{\varphi}(\mathbb{M})})$ is the shape operator of the deformed middle surface $\boldsymbol{\varphi}(\mathbb{M})$. The last two terms are mutually orthogonal. If $r = 0$ and $\mathbf{h} \in \mathbb{T}_{\mathbb{M}}$ by Lemma 3.1 it is $\partial_{\mathbf{h}}\boldsymbol{\psi}_{\boldsymbol{\varphi}} = \partial_{\mathbf{h}}\boldsymbol{\varphi}$.

Proposition 6.1. The Green's strain

$$\mathbf{G}_{\boldsymbol{\varphi}} := \frac{1}{2}(\boldsymbol{\psi}_{\boldsymbol{\varphi}}^T\boldsymbol{\psi}_{\boldsymbol{\varphi}} - \mathbf{I}),$$

is expressed, in terms of the transformation $\boldsymbol{\varphi} \in \mathrm{C}^1(\mathbb{M}; \mathbb{S})$ of the shell middle surface $\mathbb{M}$, by:

$$2\mathbf{g}(\mathbf{G}_{\boldsymbol{\varphi}}\mathbf{h}_1, \mathbf{h}_2) := \mathbf{g}((\partial_{\mathbf{h}_1}\boldsymbol{\psi}_{\boldsymbol{\varphi}}), (\partial_{\mathbf{h}_2}\boldsymbol{\psi}_{\boldsymbol{\varphi}})) - \mathbf{g}(\mathbf{h}_1, \mathbf{h}_2) = \mathbf{g}((\mathbf{I} + r\mathbf{S}_{\boldsymbol{\varphi}})^2\partial\boldsymbol{\varphi}\partial_{\mathbf{h}_1}\mathbf{P}, \partial\boldsymbol{\varphi}\partial_{\mathbf{h}_2}\mathbf{P}) - \mathbf{g}(\mathbf{\Pi}\mathbf{h}_1, \mathbf{\Pi}\mathbf{h}_2),$$

for all $\mathbf{h}_1, \mathbf{h}_2 \in \mathbb{T}_{\mathbb{S}}(\mathbf{x})$, $\mathbf{x} \in U_{\mathbb{M}}$ or, in operator form:

$$\begin{aligned}2\mathbf{G}_{\boldsymbol{\varphi}} &= \mathbf{\Pi}^T((\mathbf{I} + r\mathbf{S}_{\mathbb{M}})^{-1}\partial\boldsymbol{\varphi}^T(\mathbf{I} + r\mathbf{S}_{\boldsymbol{\varphi}})^2\partial\boldsymbol{\varphi}(\mathbf{I} + r\mathbf{S}_{\mathbb{M}})^{-1} - \mathbf{I})\mathbf{\Pi}\\ &= \partial\mathbf{P}^T(\partial\boldsymbol{\varphi}^T\partial\boldsymbol{\varphi} + 2r\partial\boldsymbol{\varphi}^T\mathbf{S}_{\boldsymbol{\varphi}}\partial\boldsymbol{\varphi} + r^2\partial\boldsymbol{\varphi}^T\mathbf{S}_{\boldsymbol{\varphi}}^2\partial\boldsymbol{\varphi})\partial\mathbf{P} - \mathbf{\Pi}^T\mathbf{\Pi},\end{aligned}$$

with $\partial\mathbf{P} = (\mathbf{I} + r\mathbf{S}_{\mathbb{M}})^{-1}\mathbf{\Pi} = \mathbf{\Pi} - r\mathbf{S}^r = \partial\mathbf{P}^T$ and $\mathbf{\Pi}^T = \mathbf{\Pi}$ and $\mathbf{\Pi}^2 = \mathbf{\Pi}$.

Proof. From the expression of $\partial\boldsymbol{\psi}_{\boldsymbol{\varphi}} \in \mathrm{C}^1(U_{\mathbb{M}}; BL(\mathbb{T}_{\mathbb{S}}; \mathbb{T}_{\mathbb{S}}))$ we have

$$\mathbf{g}(\partial_{\mathbf{h}_1}\boldsymbol{\psi}_{\boldsymbol{\varphi}}, \partial_{\mathbf{h}_2}\boldsymbol{\psi}_{\boldsymbol{\varphi}}) = \mathbf{g}((\mathbf{I} + r\mathbf{S}_{\boldsymbol{\varphi}})\partial\boldsymbol{\varphi}\partial_{\mathbf{h}_1}\mathbf{P}, (\mathbf{I} + r\mathbf{S}_{\boldsymbol{\varphi}})\partial\boldsymbol{\varphi}\partial_{\mathbf{h}_2}\mathbf{P}) + \mathbf{g}(\mathbf{h}_1^{\perp}, \mathbf{h}_2^{\perp}).$$

Subtracting $\mathbf{g}(\mathbf{h}_1, \mathbf{h}_2) = \mathbf{g}(\mathbf{h}_1^{||}, \mathbf{h}_2^{||}) + \mathbf{g}(\mathbf{h}_1^{\perp}, \mathbf{h}_2^{\perp})$, we get the result. $\square$

Proposition 6.2. The Green strain field in the shell vanishes if and only if the following two conditions are fulfilled:

$$\partial\boldsymbol{\varphi}^T\partial\boldsymbol{\varphi} = \mathbf{I}_{\mathbb{M}}, \qquad \partial\boldsymbol{\varphi}^T\mathbf{S}_{\boldsymbol{\varphi}}\partial\boldsymbol{\varphi} = \mathbf{S}_{\mathbb{M}},$$

where $\mathbf{I}_{\mathbb{M}}$ is the identity in $\mathbb{T}_{\mathbb{M}}$.

Proof. To prove the *if* part of the statement we observe that from the two assumptions it follows that

$$\partial\boldsymbol{\varphi}^T\mathbf{S}_{\boldsymbol{\varphi}}\partial\boldsymbol{\varphi} = \mathbf{S}_{\mathbb{M}} = \partial\boldsymbol{\varphi}^T\partial\boldsymbol{\varphi}\mathbf{S}_{\mathbb{M}} \quad \Longleftrightarrow \quad \partial\boldsymbol{\varphi}^T(\mathbf{S}_{\boldsymbol{\varphi}}\partial\boldsymbol{\varphi} - \partial\boldsymbol{\varphi}\mathbf{S}_{\mathbb{M}}) = 0.$$

Since $\mathrm{Ker}\,\partial\boldsymbol{\varphi}^T(\mathbf{x}) = \{0\}$, we get $\mathbf{S}_{\boldsymbol{\varphi}}\partial\boldsymbol{\varphi} = \partial\boldsymbol{\varphi}\mathbf{S}_{\mathbb{M}}$. Then

$$\partial\boldsymbol{\varphi}^T\mathbf{S}_{\boldsymbol{\varphi}}^2\partial\boldsymbol{\varphi} = \partial\boldsymbol{\varphi}^T\mathbf{S}_{\boldsymbol{\varphi}}\partial\boldsymbol{\varphi}\mathbf{S}_{\mathbb{M}} = \mathbf{S}_{\mathbb{M}}^2,$$

and, substituting in the expression for the Green strain field, we get

$$2\mathbf{G}_{\boldsymbol{\varphi}} = \mathbf{\Pi}^T((\mathbf{I} + r\mathbf{S})^{-1}(\mathbf{I} + r\mathbf{S})^2(\mathbf{I} + r\mathbf{S})^{-1})\mathbf{\Pi} - \mathbf{\Pi}^T\mathbf{\Pi} = 0.$$

The proof of the *only if* part of the statement is conveniently carried out by making recourse to Theorem 5.1 which ensures that, if $\mathbf{G}_{\boldsymbol{\varphi}} = 0$, the differential $\partial\boldsymbol{\psi}_{\boldsymbol{\varphi}} \in \mathrm{C}^1(U_{\mathbb{M}}; BL(\mathbb{T}_{\mathbb{S}}; \mathbb{T}_{\mathbb{S}}))$ of the transformation

$\boldsymbol{\psi}_{\boldsymbol{\varphi}} \in C^2(U_{\mathbb{M}}; \mathbb{S})$ is a constant proper isometry in $\mathbb{S}$. Then $\partial\boldsymbol{\varphi}^T \partial\boldsymbol{\varphi} = \mathbf{I}_{\mathbb{M}}$ and $\mathbf{n}_{\boldsymbol{\varphi}} = \partial\boldsymbol{\psi}_{\boldsymbol{\varphi}} \cdot \mathbf{n}$. Taking the derivative along any vector in $\mathbb{T}_{\mathbb{M}}$, and observing that $\partial\boldsymbol{\psi}_{\boldsymbol{\varphi}}$ is constant, we get the equality

$$\mathbf{S}_{\boldsymbol{\varphi}}\partial\boldsymbol{\varphi} = \partial\mathbf{n}_{\boldsymbol{\varphi}} = \partial\boldsymbol{\psi}_{\boldsymbol{\varphi}} \cdot \partial\mathbf{n} = \partial\boldsymbol{\varphi}\partial\mathbf{n} = \partial\boldsymbol{\varphi}\mathbf{S}.$$

Then $\partial\boldsymbol{\varphi}^T \mathbf{S}_{\boldsymbol{\varphi}} \partial\boldsymbol{\varphi} = \partial\boldsymbol{\varphi}^T \partial\boldsymbol{\varphi}\mathbf{S} = \mathbf{S}$.

To provide an explicit expression of the tangent Green's strain in terms of the shell kinematics, we consider the middle surface $\mathbb{M}$ flying in the euclidean space $\mathbb{S}$ dragged by a flow $\mathbf{Fl}_{t,s}^{\mathbf{v}} \in C^1(\mathbb{S}; \mathbb{S})$ associated with the velocity field $\mathbf{v} \in C^1(\mathbb{S}; \mathbb{T}_{\mathbb{S}})$, defined by the differential equation: $\mathbf{v} = \partial_{t=s}\mathbf{Fl}_{t,s}^{\mathbf{v}}$. The time derivative of the normal versor to the middle surface $\mathbf{Fl}_{t,s}^{\mathbf{v}}(\mathbb{M})$ is defined by

$$\dot{\mathbf{n}} := \partial_{t=s}\mathbf{n}_{\mathbf{Fl}_{t,s}^{\mathbf{v}}}.$$

Since $\mathbf{g}(\mathbf{n}_{\mathbf{Fl}_{t,s}^{\mathbf{v}}}, \mathbf{n}_{\mathbf{Fl}_{t,s}^{\mathbf{v}}}) = 1$ at any time t we have

$$\partial_{t=s}\mathbf{g}(\mathbf{n}_{\mathbf{Fl}_{t,s}^{\mathbf{v}}}, \mathbf{n}_{\mathbf{Fl}_{t,s}^{\mathbf{v}}}) = 2\mathbf{g}(\dot{\mathbf{n}}, \mathbf{n}) = 0.$$

We denote by $\partial\mathbf{v}_{\mathbb{M}}\mathbf{\Pi}$ the derivative of a vector field $\mathbf{v}_{\mathbb{M}} \in C^1(\mathbb{M}; \mathbb{T}_{\mathbb{S}}(\mathbb{M}))$ along vectors in $\mathbb{T}_{\mathbb{M}}$ and by $\nabla\mathbf{v}_{\mathbb{M}} = \mathbf{\Pi}\partial\mathbf{v}_{\mathbb{M}}\mathbf{\Pi}$ the covariant derivative in $\mathbb{M}$. □

Lemma 6.1. The material time derivative of the normal versor to a surface $\mathbb{M}$ dragged by the flow $\mathbf{Fl}_{t,s}^{\mathbf{v}} \in C^1(\mathbb{S}; \mathbb{S})$ is given by

$$\dot{\mathbf{n}} = -(\partial\mathbf{v}_{\mathbb{M}}\mathbf{\Pi})^T\mathbf{n} = \mathbf{S}_{\mathbb{M}}\mathbf{v}_{\mathbb{M}} - \nabla v_{\mathbf{n}},$$

where $\mathbf{v}_{\mathbb{M}} \in C^1(\mathbb{M}; \mathbb{T}_{\mathbb{S}}(\mathbb{M}))$ is the velocity of the middle surface $\mathbb{M}$ dragged by the flow $\mathbf{Fl}_{t,s}^{\mathbf{v}} \in C^1(\mathbb{S}; \mathbb{S})$ and $\nabla v_{\mathbf{n}} \in \mathbb{T}_{\mathbb{M}}$ is the gradient of $v_{\mathbf{n}} = \mathbf{g}(\mathbf{v}_{\mathbb{M}}, \mathbf{n}) \in C^1(\mathbb{M}; \mathcal{R})$.

Proof. The first equality holds since, for all $\mathbf{a} \in \mathbb{T}_{\mathbb{M}}(\mathbf{x})$:

$$\begin{aligned}
0 = \partial_{t=s}\mathbf{g}(\mathbf{n}_{\mathbf{Fl}_{t,s}^{\mathbf{v}}}, \partial_{\mathbf{a}}\mathbf{Fl}_{t,s}^{\mathbf{v}}) &= \mathbf{g}(\dot{\mathbf{n}}, \mathbf{a}) + \mathbf{g}(\mathbf{n}, \partial_{t=s}\partial_{\mathbf{a}}\mathbf{Fl}_{t,s}^{\mathbf{v}}) \\
&= \mathbf{g}(\dot{\mathbf{n}}, \mathbf{a}) + \mathbf{g}(\mathbf{n}, \partial_{\mathbf{a}}\partial_{t=s}\mathbf{Fl}_{t,s}^{\mathbf{v}}) \\
&= \mathbf{g}(\dot{\mathbf{n}}, \mathbf{a}) + \mathbf{g}(\mathbf{n}, \partial_{\mathbf{a}}\mathbf{v}_{\mathbb{M}}) \\
&= \mathbf{g}_{\mathbb{M}}(\dot{\mathbf{n}}, \mathbf{a}) + \mathbf{g}_{\mathbb{M}}((\partial\mathbf{v}_{\mathbb{M}}\mathbf{\Pi})^T\mathbf{n}, \mathbf{a}).
\end{aligned}$$

The second equality follows from Leibniz rule:

$$\mathbf{g}(\mathbf{n}, \partial_{\mathbf{a}}\mathbf{v}_{\mathbb{M}}) = \partial_{\mathbf{a}}(\mathbf{g}(\mathbf{v}_{\mathbb{M}}, \mathbf{n})) - \mathbf{g}_{\mathbb{M}}(\mathbf{v}_{\mathbb{M}}, \mathbf{S}_{\mathbb{M}}\mathbf{a}) = \mathbf{g}_{\mathbb{M}}(\nabla v_{\mathbf{n}}, \mathbf{a}) - \mathbf{g}_{\mathbb{M}}(\mathbf{S}_{\mathbb{M}}\mathbf{v}_{\mathbb{M}}, \mathbf{a}).$$

□

Theorem 6.1. If the middle surface $\mathbb{M}$ is dragged by a flow $\mathbf{Fl}_{t,s}^{\mathbf{v}} \in C^1(\mathbb{S}; \mathbb{S})$, the tangent Green strain in the shell $\dot{\mathbf{G}}(\mathbf{v}) := \partial_{t=s}\mathbf{G}_{\mathbf{Fl}_{t,s}^{\mathbf{v}}} = \text{sym}\,\partial\mathbf{v}$ in terms of the middle surface velocity $\mathbf{v}_{\mathbb{M}} \in C^1(\mathbb{M}; \mathbb{T}_{\mathbb{S}}(\mathbb{M}))$ is given by:

$$\mathbf{g}(\dot{\mathbf{G}}(\mathbf{v})\mathbf{h}_1, \mathbf{h}_2) = \mathbf{g}_{\mathbb{M}}((\text{sym}\,\nabla\mathbf{v}_{\mathbb{M}})\mathbf{a}, \mathbf{b}) + r\mathbf{g}_{\mathbb{M}}(\nabla_{\mathbf{a}}\dot{\mathbf{n}}, \mathbf{b}) + r\mathbf{g}_{\mathbb{M}}(\mathbf{S}_{\mathbb{M}}\mathbf{a}, \nabla_{\mathbf{b}}\mathbf{v}_{\mathbb{M}}) + r^2\mathbf{g}_{\mathbb{M}}(\text{sym}(\mathbf{S}_{\mathbb{M}}\nabla\dot{\mathbf{n}})\mathbf{a}, \mathbf{b}),$$

where $\mathbf{a} := \partial_{\mathbf{h}_1}\mathbf{P}$, $\mathbf{b} := \partial_{\mathbf{h}_2}\mathbf{P}$ and $\dot{\mathbf{n}} = -(\partial\mathbf{v}_{\mathbb{M}}\mathbf{\Pi})^T\mathbf{n}$ by Lemma 6.1. In operator form:

$$\dot{\mathbf{G}}(\mathbf{v}) = \partial\mathbf{P}^T(\text{sym}\,\nabla\mathbf{v}_{\mathbb{M}} + r(\nabla\dot{\mathbf{n}} + (\mathbf{S}_{\mathbb{M}}\nabla\mathbf{v}_{\mathbb{M}})^T) + r^2\,\text{sym}(\mathbf{S}_{\mathbb{M}}\nabla\dot{\mathbf{n}}))\partial\mathbf{P}.$$

Proof. A direct computation shows that

$$\partial_{t=s}\mathbf{g}(\partial_{\mathbf{a}}\mathbf{Fl}_{t,s}^{\mathbf{v}}, \partial_{\mathbf{b}}\mathbf{Fl}_{t,s}^{\mathbf{v}}) = \mathbf{g}_{\mathbb{M}}(\nabla_{\mathbf{a}}\mathbf{v}_{\mathbb{M}}, \mathbf{b}) + \mathbf{g}_{\mathbb{M}}(\mathbf{a}, \nabla_{\mathbf{b}}\mathbf{v}_{\mathbb{M}}),$$

$$\partial_{t=s}\mathbf{g}(\partial_{\mathbf{a}}\mathbf{n}_{\mathbf{Fl}_{t,s}^{\mathbf{v}}}, \partial_{\mathbf{b}}\mathbf{Fl}_{t,s}^{\mathbf{v}}) = \mathbf{g}_{\mathbb{M}}(\nabla_{\mathbf{a}}\dot{\mathbf{n}}, \mathbf{b}) + \mathbf{g}_{\mathbb{M}}(\mathbf{S}_{\mathbb{M}}\mathbf{a}, \nabla_{\mathbf{b}}\mathbf{v}_{\mathbb{M}}),$$

$$\partial_{t=s}\mathbf{g}(\partial_{\mathbf{a}}\mathbf{n}_{\mathbf{Fl}_{t,s}^{\mathbf{v}}}, \partial_{\mathbf{b}}\mathbf{n}_{\mathbf{Fl}_{t,s}^{\mathbf{v}}}) = \mathbf{g}_{\mathbb{M}}(\nabla_{\mathbf{a}}\dot{\mathbf{n}}, \mathbf{S}_{\mathbb{M}}\mathbf{b}) + \mathbf{g}_{\mathbb{M}}(\mathbf{S}_{\mathbb{M}}\mathbf{a}, \nabla_{\mathbf{b}}\dot{\mathbf{n}}),$$

and the result follows from the formula in Proposition 6.1.   □

Let us explicitly observe that the operator $\nabla\dot{\mathbf{n}} + (\mathbf{S}_{\mathbb{M}}\nabla\mathbf{v}_{\mathbb{M}})^T$ is symmetric despite of the single terms $\nabla\dot{\mathbf{n}}$ and $\mathbf{S}_{\mathbb{M}}\nabla\mathbf{v}_{\mathbb{M}}$ being not symmetric, in general.

Remark 6.1. Let a spherical shell of mean radius R be subject to a homothetical transformation

$$\boldsymbol{\psi}_{\varphi}(\mathbf{x}) = \alpha\mathbf{x},$$

with $\mathbf{x}$ originating from the center. Then $\mathbf{S} = R^{-1}\mathbf{I}_{\mathbb{M}}$, $\partial\varphi^T\partial\varphi = \alpha^2\mathbf{I}_{\mathbb{M}}$, and $\mathbf{n}_{\varphi} = \mathbf{n}$, so that:

$$\partial_{\mathbf{a}}\mathbf{n}_{\varphi} = \partial_{\mathbf{a}}\mathbf{n},$$

$$\mathbf{g}(\mathbf{S}_{\varphi}\partial_{\mathbf{a}}\varphi, \partial_{\mathbf{b}}\varphi) = \alpha\mathbf{g}(\mathbf{S}\mathbf{a}, \mathbf{b}),$$

$$\mathbf{g}(\mathbf{S}_{\varphi}\partial_{\mathbf{a}}\varphi, \mathbf{S}_{\varphi}\partial_{\mathbf{b}}\varphi) = \mathbf{g}(\mathbf{S}\mathbf{a}, \mathbf{S}\mathbf{b}).$$

Given $(1 + rR^{-1})\partial\mathbf{P} = \mathbf{\Pi}$, the Green strain is given by the formula

$$2(1 + rR^{-1})^2\mathbf{G}_{\varphi} = (\alpha^2 - 1 + \alpha(2rR^{-1} + r^2R^{-2})\mathbf{\Pi}.$$

If $rR^{-1} \ll 1$ we may set $\mathbf{G}_{\varphi} \approx \frac{1}{2}(\alpha^2 - 1)\mathbf{\Pi}$.

7. Shell strains

The result of Proposition 6.2 shows that a strain measure of the shell, associated with a configuration change $\varphi \in C^1(\mathbb{M}; \mathbb{S})$ of the middle surface, is provided by the pair of symmetric operators

$$\mathbf{E}_{\varphi}(\mathbf{x}) \in BL(\mathbb{T}_{\mathbb{M}}(\mathbf{x}); \mathbb{T}_{\mathbb{M}}(\mathbf{x})), \qquad \mathbf{K}_{\varphi}(\mathbf{x}) \in BL(\mathbb{T}_{\mathbb{M}}(\mathbf{x}); \mathbb{T}_{\mathbb{M}}(\mathbf{x})),$$

defined by

$$2\mathbf{E}_{\varphi} := \partial\varphi^T\partial\varphi - \mathbf{I}_{\mathbb{M}}, \qquad \mathbf{K}_{\varphi} := \partial\varphi^T\mathbf{S}_{\varphi}\partial\varphi - \mathbf{S}_{\mathbb{M}},$$

where $\partial\varphi(\mathbf{x}) \in BL(\mathbb{T}_{\mathbb{M}}(\mathbf{x}); \mathbb{T}_{\varphi(\mathbb{M})}(\mathbf{x}))$ and $\partial\varphi^T(\mathbf{x}) \in BL(\mathbb{T}_{\varphi(\mathbb{M})}(\mathbf{x}); \mathbb{T}_{\mathbb{M}}(\mathbf{x}))$. The related pair $\boldsymbol{\varepsilon}_{\varphi} = \mathbf{g}\mathbf{E}_{\varphi}$ and $\boldsymbol{\chi}_{\varphi} = \mathbf{g}\mathbf{K}_{\varphi}$ of symmetric tensor fields $\boldsymbol{\varepsilon}_{\varphi}(\mathbf{x}) \in BL(\mathbb{T}_{\mathbb{M}}^2(\mathbf{x}); \mathcal{R})$, $\boldsymbol{\chi}_{\varphi}(\mathbf{x}) \in BL(\mathbb{T}_{\mathbb{M}}^2(\mathbf{x}); \mathcal{R})$ are given by:

$$2\boldsymbol{\varepsilon}_{\varphi}(\mathbf{a}, \mathbf{b}) := \mathbf{g}(\partial_{\mathbf{a}}\varphi, \partial_{\mathbf{b}}\varphi) - \mathbf{g}(\mathbf{a}, \mathbf{b}),$$

$$\boldsymbol{\chi}_{\varphi}(\mathbf{a}, \mathbf{b}) := \mathbf{g}(\partial_{\mathbf{a}}(\mathbf{n}_{\varphi} \circ \varphi), \partial_{\mathbf{b}}\varphi) - \mathbf{g}(\partial_{\mathbf{a}}\mathbf{n}, \mathbf{b}) = \mathbf{g}(\mathbf{S}_{\varphi}\partial_{\mathbf{a}}\varphi, \partial_{\mathbf{b}}\varphi) - \mathbf{g}(\mathbf{S}\mathbf{a}, \mathbf{b}),$$

where $\mathbf{a}, \mathbf{b} \in \mathbb{T}_{\mathbb{M}}$. The symmetric tensor fields $\boldsymbol{\varepsilon}_{\varphi}$ and $\boldsymbol{\chi}_{\varphi}$ are called the membrane and the curvature strains and can be expressed in terms of pull-backs of the first and of the second fundamental forms of the middle surface: $2\boldsymbol{\varepsilon}_{\varphi} := \varphi\!\downarrow\!\mathbf{g}_{\varphi(\mathbb{M})} - \mathbf{g}_{\mathbb{M}}$ and $\boldsymbol{\chi}_{\varphi} := \varphi\!\downarrow\!\mathbf{s}_{\varphi(\mathbb{M})} - \mathbf{s}_{\mathbb{M}}$.

By Proposition 6.2, the shell strain fields vanish on $\mathbb{M}$ if and only if the configuration change $\boldsymbol{\psi}_\varphi \in C^1(U_\mathbb{M}; \mathbb{S})$ is a rigid transformation of the shell. Consistency of the shell strain measure follows from the relations:

$$\boldsymbol{\varepsilon}_{\boldsymbol{\psi}\circ\varphi}(\mathbf{a}, \mathbf{b}) = \boldsymbol{\varepsilon}_{\boldsymbol{\psi}}(\partial_\mathbf{a}\varphi, \partial_\mathbf{b}\varphi) + \boldsymbol{\varepsilon}_\varphi(\mathbf{a}, \mathbf{b}),$$

$$\boldsymbol{\chi}_{\boldsymbol{\psi}\circ\varphi}(\mathbf{a}, \mathbf{b}) = \boldsymbol{\chi}_{\boldsymbol{\psi}}(\partial_\mathbf{a}\varphi, \partial_\mathbf{b}\varphi) + \boldsymbol{\chi}_\varphi(\mathbf{a}, \mathbf{b}).$$

Theorem 7.1. The Green finite strain measure in the shell is expressed in terms of the membrane and the curvature strains of the middle surface and of the shape operators by:

$$\mathbf{g}(\mathbf{G}_\varphi\mathbf{h}_1, \mathbf{h}_2) = \boldsymbol{\varepsilon}_\varphi(\mathbf{a}, \mathbf{b}) + r\boldsymbol{\chi}_\varphi(\mathbf{a}, \mathbf{b}) + \frac{1}{2}r^2\boldsymbol{\chi}_\varphi(\mathbf{a}, \mathbf{Sb}) + \frac{1}{2}r^2\mathbf{g}(\mathbf{S}_\varphi\partial_\mathbf{a}\varphi, (\mathbf{S}_\varphi\partial\varphi - \partial\varphi\mathbf{S})\mathbf{b}),$$

with $\mathbf{a} := \partial_{\mathbf{h}_1}\mathbf{P}$, $\mathbf{b} := \partial_{\mathbf{h}_2}\mathbf{P}$. In operator form, we have

$$\mathbf{G}_\varphi = \partial\mathbf{P}^T(\mathbf{E}_\varphi + r\mathbf{K}_\varphi + \tfrac{1}{2}r^2(\mathbf{K}_\varphi + \mathbf{S})(\mathbf{I}_\mathbb{M} + 2\mathbf{E}_\varphi)^{-1}(\mathbf{K}_\varphi + \mathbf{S}) - \tfrac{1}{2}r^2\mathbf{S}^2)\partial\mathbf{P}.$$

Note that $\mathbf{G}_\varphi$ and $\partial\mathbf{P}$ are evaluated at $\mathbf{x} \in \mathbb{M}^r$ while all other tensors are evaluated at $\mathbf{P}(\mathbf{x}) \in \mathbb{M}$.

Proof. By Proposition 6.1 we have $2\mathbf{g}(\mathbf{G}_\varphi\mathbf{h}_1, \mathbf{h}_2) = \mathscr{A} + 2r\mathscr{B} + r^2\mathscr{C}$ with

$$\mathscr{A} = \mathbf{g}(\partial_\mathbf{a}\varphi, \partial_\mathbf{b}\varphi) - \mathbf{g}(\boldsymbol{\Pi}\mathbf{h}_1, \boldsymbol{\Pi}\mathbf{h}_2),$$

$$\mathscr{B} = \mathbf{g}(\mathbf{S}_\varphi\partial_\mathbf{a}\varphi, \partial_\mathbf{b}\varphi),$$

$$\mathscr{C} = \mathbf{g}(\mathbf{S}_\varphi\partial_\mathbf{a}\varphi, \mathbf{S}_\varphi\partial_\mathbf{b}\varphi).$$

A little algebra shows that

$$\mathscr{A} = 2\boldsymbol{\varepsilon}_\varphi(\mathbf{a}, \mathbf{b}) + \mathbf{g}(\mathbf{a}, \mathbf{b}) - \mathbf{g}(\boldsymbol{\Pi}\mathbf{h}_1, \boldsymbol{\Pi}\mathbf{h}_2),$$

$$\mathscr{B} = \boldsymbol{\chi}_\varphi(\mathbf{a}, \mathbf{b}) + \mathbf{g}(\mathbf{Sa}, \mathbf{b}),$$

$$\mathscr{C} = \boldsymbol{\chi}_\varphi(\mathbf{a}, \mathbf{Sb}) + \mathbf{g}(\mathbf{Sa}, \mathbf{Sb}) + \mathbf{g}(\mathbf{S}_\varphi\partial_\mathbf{a}\varphi, (\mathbf{S}_\varphi\partial\varphi - \partial\varphi\mathbf{S})\mathbf{b}).$$

The result then follows by observing that

$$\mathbf{g}(\mathbf{a}, \mathbf{b}) + r\mathbf{g}(\mathbf{Sa}, \mathbf{b}) = \mathbf{g}((\mathbf{I} + r\mathbf{S})\mathbf{a}, \mathbf{b}) = \mathbf{g}(\boldsymbol{\Pi}\mathbf{h}_1, \mathbf{b}),$$

$$r\mathbf{g}(\mathbf{Sa}, \mathbf{b}) + r^2\mathbf{g}(\mathbf{Sa}, \mathbf{Sb}) = r\mathbf{g}((\mathbf{I} + r\mathbf{S})\mathbf{a}, \mathbf{Sb}) = r\mathbf{g}(\boldsymbol{\Pi}\mathbf{h}_1, \mathbf{Sb}),$$

$$\mathbf{g}(\boldsymbol{\Pi}\mathbf{h}_1, \mathbf{b}) + r\mathbf{g}(\boldsymbol{\Pi}\mathbf{h}_1, \mathbf{Sb}) = \mathbf{g}(\boldsymbol{\Pi}\mathbf{h}_1, \boldsymbol{\Pi}\mathbf{h}_2).$$

To get the operator expression we write

$$\boldsymbol{\chi}_\varphi(\mathbf{a}, \mathbf{Sb}) = \mathbf{g}(\mathbf{K}_\varphi\mathbf{a}, \mathbf{Sb}) = \mathbf{g}(\mathbf{SK}_\varphi\mathbf{a}, \mathbf{b}),$$

$$\mathbf{g}(\mathbf{S}_\varphi\partial_\mathbf{a}\varphi, (\mathbf{S}_\varphi\partial\varphi - \partial\varphi\mathbf{S})\mathbf{b}) = \mathbf{g}(\mathbf{a}, \partial\varphi^T\mathbf{S}_\varphi(\mathbf{S}_\varphi\partial\varphi - \partial\varphi\mathbf{S})\mathbf{b}).$$

Then, given $\mathbf{S}_\varphi = \partial\varphi^{-T}(\mathbf{K}_\varphi + \mathbf{S})\partial\varphi^{-1}$, we have

$$\partial\varphi^T\mathbf{S}_\varphi(\mathbf{S}_\varphi\partial\varphi - \partial\varphi\mathbf{S}) = (\mathbf{K}_\varphi + \mathbf{S})\partial\varphi^{-1}\partial\varphi^{-T}(\mathbf{K}_\varphi + \mathbf{S}) - (\mathbf{K}_\varphi + \mathbf{S})\mathbf{S}.$$

Recalling that $\partial\varphi^T\partial\varphi = 2\mathbf{E}_\varphi + \mathbf{I}_\mathbb{M}$ and taking the transpose, we get

$$(\partial\varphi^T\mathbf{S}_\varphi(\mathbf{S}_\varphi\partial\varphi - \partial\varphi\mathbf{S}))^T = (\mathbf{K}_\varphi + \mathbf{S})(2\mathbf{E}_\varphi + \mathbf{I}_\mathbb{M})^{-1}(\mathbf{K}_\varphi + \mathbf{S}) - \mathbf{S}(\mathbf{K}_\varphi + \mathbf{S}).$$

Adding the two expressions, the terms in $\mathbf{SK}_\varphi$ cancel and we get the result. $\qquad\square$

Remark 7.1. For an initially flat shell (a plate) the expression of the Green strain becomes

$$\mathbf{G}_\varphi = \mathbf{\Pi}^T \left(\mathbf{E}_\varphi + r\mathbf{K}_\varphi + \frac{1}{2}r^2\mathbf{K}_\varphi(\mathbf{I}_\mathbb{M} + 2\mathbf{E}_\varphi)^{-1}\mathbf{K}_\varphi \right) \mathbf{\Pi}.$$

If the extensional strain $\mathbf{E}_\varphi$ vanishes, then $\mathbf{G}_\varphi = \mathbf{\Pi}^T((\mathbf{I}_\mathbb{M} + r\mathbf{K}_\varphi)^2 - \mathbf{I}_\mathbb{M})\mathbf{\Pi}$ and the ratio between final and initial lengths of the principal fibers has a linear variation along the thickness.

8. Tangent shell strains

The tangent membrane strain $\dot{\mathbf{E}}_\mathbb{M}(\mathbf{v}_\mathbb{M}) \in BL(\mathbb{T}_\mathbb{M}; \mathbb{T}_\mathbb{M})$, associated with a flow $\mathbf{Fl}_{t,s}^\mathbf{v} \in \mathrm{C}^1(\mathbb{S}; \mathbb{S})$, is defined by

$$\dot{\mathbf{E}}_\mathbb{M}(\mathbf{v}_\mathbb{M}) := \partial_{t=s}\mathbf{E}_{\mathbf{Fl}_{t,s}^\mathbf{v}} = \frac{1}{2}\partial_{t=s}(\partial\mathbf{Fl}_{t,s}^\mathbf{v})^T\partial\mathbf{Fl}_{t,s}^\mathbf{v},$$

and the tangent curvature strain $\dot{\mathbf{K}}_\mathbb{M}(\mathbf{v}_\mathbb{M}) \in BL(\mathbb{T}_\mathbb{M}; \mathbb{T}_\mathbb{M})$ is given by

$$\dot{\mathbf{K}}_\mathbb{M}(\mathbf{v}_\mathbb{M}) := \partial_{t=s}\mathbf{K}_{\mathbf{Fl}_{t,s}^\mathbf{v}} = \partial_{t=s}(\partial\mathbf{Fl}_{t,s}^\mathbf{v})^T\mathbf{S}_{\mathbf{Fl}_{t,s}^\mathbf{v}}\partial\mathbf{Fl}_{t,s}^\mathbf{v}.$$

We have the following results.

Theorem 8.1 (Tangent membrane strain). The tangent membrane strain $\dot{\mathbf{E}}_\mathbb{M}(\mathbf{v}_\mathbb{M}) \in \mathrm{C}^{k-1}(\mathbb{M}; BL(\mathbb{T}_\mathbb{S}; \mathbb{T}_\mathbb{S}))$ is expressed in terms of the velocity field $\mathbf{v}_\mathbb{M} \in \mathrm{C}^k(\mathbb{M}; \mathbb{T}_\mathbb{S}(\mathbb{M}))$ of the middle surface dragged by the flow by the formula:

$$\dot{\mathbf{E}}_\mathbb{M}(\mathbf{v}_\mathbb{M}) = \mathrm{sym}(\mathbf{\Pi}\partial\mathbf{v}_\mathbb{M}\mathbf{\Pi}) = \mathrm{sym}(\nabla\mathbf{v}_\mathbb{M}).$$

Proof. The result follows from the equality:

$$\mathbf{g}(\partial_\mathbf{a}\mathbf{Fl}_{t,s}^\mathbf{v}, \partial_\mathbf{b}\mathbf{Fl}_{t,s}^\mathbf{v}) = \mathbf{g}(\partial_\mathbf{a}\mathbf{v}_\mathbb{M}, \mathbf{b}) + \mathbf{g}(\mathbf{a}, \partial_\mathbf{b}\mathbf{v}_\mathbb{M}), \qquad \text{for all } \mathbf{a}, \mathbf{b} \in \mathbb{T}_\mathbb{M}.$$

It is often expedient to decompose a vector field $\mathbf{v}_\mathbb{M} \in \mathbb{T}_\mathbb{S}(\mathbb{M})$ into its parallel and orthogonal components to the tangent plane to $\mathbb{M}$: $\mathbf{v}_\mathbb{M} = \mathbf{v}_\mathbb{M}^{\|} + v_\mathbf{n}\mathbf{n}$, with $v_\mathbf{n} = \mathbf{g}(\mathbf{v}_\mathbb{M}, \mathbf{n})$ and $\mathbf{v}_\mathbb{M}^{\|} = \mathbf{\Pi}\mathbf{v}_\mathbb{M} := \mathbf{v}_\mathbb{M} - v_\mathbf{n}\mathbf{n}$, so that $\mathbf{g}(\mathbf{v}_\mathbb{M}^{\|}, \mathbf{n}) = 0$. $\qquad\square$

Theorem 8.2 (Tangent membrane strain — second formula). Setting $\mathbf{v}_\mathbb{M} = \mathbf{v}_\mathbb{M}^{\|} + v_\mathbf{n}\mathbf{n}$ with $\mathbf{v}_\mathbb{M}^{\|} \in \mathbb{T}_\mathbb{M}$, the tangent membrane strain is given by

$$\dot{\mathbf{E}}_\mathbb{M}(\mathbf{v}_\mathbb{M}) = \mathrm{sym}(\nabla\mathbf{v}_\mathbb{M}^{\|}) + v_\mathbf{n}\mathbf{S}_\mathbb{M}.$$

Proof. The formula follows from the equality:

$$\begin{aligned}
\mathbf{g}(\partial_\mathbf{a}\mathbf{v}_\mathbb{M}, \mathbf{b}) &= \mathbf{g}(\partial_\mathbf{a}(\mathbf{v}_\mathbb{M}^{\|} + v_\mathbf{n}\mathbf{n}), \mathbf{b}) \\
&= \mathbf{g}(\partial_\mathbf{a}\mathbf{v}_\mathbb{M}^{\|}, \mathbf{b}) + v_\mathbf{n}\mathbf{g}(\mathbf{Sa}, \mathbf{b}) + (\partial_\mathbf{a}v_\mathbf{n})\mathbf{g}(\mathbf{n}, \mathbf{b}) \\
&= \mathbf{g}(\nabla_\mathbf{a}\mathbf{v}_\mathbb{M}^{\|}, \mathbf{b}) + v_\mathbf{n}\mathbf{g}(\mathbf{Sa}, \mathbf{b}),
\end{aligned}$$

for all $\mathbf{a}, \mathbf{b} \in \mathbb{T}_\mathbb{M}$. $\qquad\square$

Theorem 8.3 (Tangent curvature strain). The tangent curvature strain field $\dot{\mathbf{K}}_{\mathbb{M}}(\mathbf{v}_{\mathbb{M}}) \in BL(\mathbb{T}_{\mathbb{M}}; \mathbb{T}_{\mathbb{M}})$ is given by the formula

$$\dot{\mathbf{K}}_{\mathbb{M}}(\mathbf{v}_{\mathbb{M}}) = \nabla \dot{\mathbf{n}} + (\mathbf{S}_{\mathbb{M}} \nabla \mathbf{v}_{\mathbb{M}})^T = -\nabla((\partial \mathbf{v}_{\mathbb{M}} \mathbf{\Pi})^T \mathbf{n}) + (\mathbf{S}_{\mathbb{M}} \nabla \mathbf{v}_{\mathbb{M}})^T.$$

Proof. The result follows from Theorem 6.1. ∎

Theorem 8.4 (Tangent curvature strain — second formula). The tangent curvature strain is expressed in terms of the normal and parallel components of the velocity field by the formula:

$$\dot{\mathbf{K}}_{\mathbb{M}}(\mathbf{v}_{\mathbb{M}}) = \nabla(\mathbf{S}_{\mathbb{M}} \mathbf{v}_{\mathbb{M}}^{||}) - \nabla^2 v_{\mathbf{n}} + (\mathbf{S}_{\mathbb{M}} \nabla \mathbf{v}_{\mathbb{M}}^{||})^T + v_{\mathbf{n}} \mathbf{S}_{\mathbb{M}}^2.$$

Proof. Given $\dot{\mathbf{n}} = \mathbf{S}_{\mathbb{M}} \mathbf{v}_{\mathbb{M}} - \nabla v_{\mathbf{n}}$, we infer that $\nabla \dot{\mathbf{n}} = \nabla(\mathbf{S}_{\mathbb{M}} \mathbf{v}_{\mathbb{M}}^{||}) - \nabla^2 v_{\mathbf{n}}$. Moreover, since $\mathbf{Sn} = 0$, we have

$$\mathbf{S} \nabla \mathbf{v}_{\mathbb{M}} = \mathbf{S}_{\mathbb{M}} \nabla \mathbf{v}_{\mathbb{M}}^{||} + \mathbf{S} \nabla(v_{\mathbf{n}} \mathbf{n}) = \mathbf{S}_{\mathbb{M}} \nabla \mathbf{v}_{\mathbb{M}}^{||} + \mathbf{S}(\mathbf{n} \otimes \nabla v_{\mathbf{n}} + v_{\mathbf{n}} \nabla \mathbf{n}) = \mathbf{S}_{\mathbb{M}} \nabla \mathbf{v}_{\mathbb{M}}^{||} + v_{\mathbf{n}} \mathbf{S}_{\mathbb{M}}^2,$$

Substituting in the formula of Theorem 8.3 we get the result. ∎

Remark 8.1. At a planar point of the shell the shape operator $\mathbf{S}$ vanishes and we get the formula $\dot{\mathbf{K}}_{\mathbb{M}}(\mathbf{v}_{\mathbb{M}}) = \nabla(\mathbf{S}_{\mathbb{M}} \mathbf{v}_{\mathbb{M}}^{||}) - \nabla^2 v_{\mathbf{n}}$. In a planar shell (a plate) the normal versor $\mathbf{n} \in C^2(\mathbb{M}; \mathbb{T}_{\mathbb{S}}(\mathbb{M}))$ is a constant field and the shape operator $\mathbf{S}$ vanishes identically so that the general formula specializes into $\dot{\mathbf{K}}_{\mathbb{M}}(\mathbf{v}_{\mathbb{M}}) = -\nabla^2 v_{\mathbf{n}}$ and the expression of the linearized curvature strain tensor field of a plate, in terms of the transversal displacement field, is recovered.

Theorem 8.5 (Tangent Green strain). The tangent Green strain in the shell $\dot{\mathbf{G}}(\mathbf{v}) := \partial_{t=s} \mathbf{G}_{\mathbf{Fl}_{t,s}^{\mathbf{v}}} = \operatorname{sym} \partial \mathbf{v}$, in terms of the tangent membrane and curvature strains, is expressed by:

$$\mathbf{g}(\dot{\mathbf{G}}(\mathbf{v})\mathbf{h}_1, \mathbf{h}_2) = \mathbf{g}(\dot{\mathbf{E}}_{\mathbb{M}}(\mathbf{v}_{\mathbb{M}})\mathbf{a}, \mathbf{b}) + r\mathbf{g}(\dot{\mathbf{K}}_{\mathbb{M}}(\mathbf{v}_{\mathbb{M}})\mathbf{a}, \mathbf{b}) + r^2(\mathbf{g}(\operatorname{sym}(\mathbf{S}\dot{\mathbf{K}}_{\mathbb{M}}(\mathbf{v}_{\mathbb{M}}))\mathbf{a}, \mathbf{b}) - \mathbf{g}(\mathbf{S}\dot{\mathbf{E}}_{\mathbb{M}}(\mathbf{v}_{\mathbb{M}})\mathbf{Sa}, \mathbf{b}))$$

where $\mathbf{a} := \partial_{\mathbf{h}_1} \mathbf{P}$, $\mathbf{b} := \partial_{\mathbf{h}_2} \mathbf{P}$. In operator form we may write

$$\dot{\mathbf{G}}(\mathbf{v}) = \partial \mathbf{P}^T (\dot{\mathbf{E}}_{\mathbb{M}}(\mathbf{v}_{\mathbb{M}}) + r\dot{\mathbf{K}}_{\mathbb{M}}(\mathbf{v}_{\mathbb{M}}) + r^2 \operatorname{sym}(\mathbf{S}\dot{\mathbf{K}}_{\mathbb{M}}(\mathbf{v}_{\mathbb{M}}) - \mathbf{S}\dot{\mathbf{E}}_{\mathbb{M}}(\mathbf{v}_{\mathbb{M}})\mathbf{S}) \partial \mathbf{P}.$$

Proof. The result follows by computing the derivative $\partial_{t=s} \mathbf{G}_{\mathbf{Fl}_{t,s}^{\mathbf{v}}}$ by the formula in Theorem 7.1 and observing that by the formula for the derivative of the inverse, it is

$$\partial_{t=s}(2\mathbf{E}_{\mathbf{Fl}_{t,s}^{\mathbf{v}}} + \mathbf{I}_{\mathbb{M}})^{-1} = -2\dot{\mathbf{E}}_{\mathbb{M}}(\mathbf{v}_{\mathbb{M}}).$$

A direct proof in components notation is provided in [Ciarlet 2000, Theorem 2.6-2]. ∎

Remark 8.2. If a spherical balloon of mean radius R is inflated we see that $v_{\mathbf{n}}$ is a constant field and $\mathbf{v}^{||} = 0$ identically. Hence $\dot{\mathbf{E}}_{\mathbb{M}}(\mathbf{v}) = v_{\mathbf{n}} \mathbf{S}$ and $\dot{\mathbf{K}}_{\mathbb{M}}(\mathbf{v}) = v_{\mathbf{n}} \mathbf{S}^2$. The tangent Green strain is then given by the formula $(1 + rR^{-1})^2 \dot{\mathbf{G}}_{\boldsymbol{\varphi}}(\mathbf{v}) = v_{\mathbf{n}}(\mathbf{S} + r\mathbf{S}^2)$. Since $\mathbf{S} = R^{-1}\mathbf{\Pi}$, all material fibers tangent to a shell folium have the same elongation rate $v_{\mathbf{n}} R^{-1}(1 + rR^{-1})^{-1}$. If $r \ll R$ we may assume the elongation rate to be $\approx v_{\mathbf{n}} R^{-1}$.

Theorem 8.6. The tangent Green strain of the shell vanishes if and only if the tangent membrane and curvature strains of the middle surface vanish.

Proof. That $\dot{\mathbf{E}}_{\mathbb{M}}(\mathbf{v}_{\mathbb{M}}) = 0$, $\dot{\mathbf{K}}_{\mathbb{M}}(\mathbf{v}_{\mathbb{M}}) = 0$ implies $\dot{\mathbf{G}}(\mathbf{v}) = 0$ follows directly from Theorem 8.5. To get the converse implication we set $r = 0$ to infer that $\dot{\mathbf{E}}_{\mathbb{M}}(\mathbf{v}_{\mathbb{M}}) = 0$ and hence, by a continuity argument for $r \to 0$, conclude that $\dot{\mathbf{K}}_{\mathbb{M}}(\mathbf{v}_{\mathbb{M}}) = 0$. That $\dot{\mathbf{G}}(\mathbf{v}) = 0$ implies $\dot{\mathbf{E}}_{\mathbb{M}}(\mathbf{v}_{\mathbb{M}}) = 0$, $\dot{\mathbf{K}}_{\mathbb{M}}(\mathbf{v}_{\mathbb{M}}) = 0$ may be also deduced from Theorem 5.2. Indeed, if $\dot{\mathbf{G}}(\mathbf{v}) = 0$, we infer that

$$\mathbf{v}_{\mathbb{M}}(\mathbf{x}) = \mathbf{v}_0 + \mathbf{W}\mathbf{x} \quad \text{and} \quad \partial \mathbf{v}_{\mathbb{M}}(\mathbf{x}) = \mathbf{W}.$$

Then

$$\dot{\mathbf{E}}_{\mathbb{M}}(\mathbf{v}_{\mathbb{M}}) = \mathrm{sym}(\nabla \mathbf{v}_{\mathbb{M}}) = \mathrm{sym}(\mathbf{\Pi}^T \mathbf{W} \mathbf{\Pi}) = 0,$$

and also

$$\dot{\mathbf{K}}_{\mathbb{M}}(\mathbf{v}_{\mathbb{M}}) = -\nabla((\partial \mathbf{v}_{\mathbb{M}} \mathbf{\Pi})^T \mathbf{n}) + (\mathbf{S}\nabla \mathbf{v}_{\mathbb{M}})^T = -\nabla((\mathbf{W}\mathbf{\Pi})^T \mathbf{n}) + (\mathbf{S}\mathbf{W}\mathbf{\Pi}^T)^T = \mathbf{\Pi}\mathbf{W}\nabla \mathbf{n} - \mathbf{\Pi}\mathbf{W}\nabla \mathbf{n} = 0.$$

$\square$

Remark 8.3. Let $\{\mathbf{e}_\alpha \in \mathbb{T}_{\mathbb{M}}, \alpha = 1, 2\}$ be base vectors of a coordinate system on $\mathbb{M}$. Recalling that the Christoffel symbols associated with the covariant derivative on $\mathbb{M}$ are defined by the relation

$$\nabla_{\mathbf{e}_\alpha} \mathbf{e}_\beta := \mathbf{\Pi} \partial_{\mathbf{e}_\alpha} \mathbf{e}_\beta = \Gamma^\gamma_{\alpha\beta} \mathbf{e}_\gamma,$$

and that the components of the second fundamental form are given by

$$S_{\alpha\beta} := \mathbf{g}(\partial_{\mathbf{e}_\alpha} \mathbf{n}, \mathbf{e}_\beta) = \mathbf{g}(\mathbf{S}\mathbf{e}_\alpha, \mathbf{e}_\beta) = -\mathbf{g}(\partial_{\mathbf{e}_\alpha} \mathbf{e}_\beta, \mathbf{n}),$$

we get the Gauss formula

$$\partial_{\mathbf{e}_\alpha} \mathbf{e}_\beta = \mathbf{g}(\partial_{\mathbf{e}_\alpha} \mathbf{e}_\beta, \mathbf{e}^\gamma)\mathbf{e}_\gamma + \mathbf{g}(\partial_{\mathbf{e}_\alpha} \mathbf{e}_\beta, \mathbf{n})\mathbf{n} = \Gamma^\gamma_{\alpha\beta}\mathbf{e}_\gamma - S_{\alpha\beta}\mathbf{n} = \nabla_{\mathbf{e}_\alpha} \mathbf{e}_\beta - S_{\alpha\beta}\mathbf{n}.$$

By these formulas we may put all the relations above in component form.

9. Divergence theorem on a manifold

We recall here some basic definitions and results for subsequent reference [Marsden and Hughes 1983; Romano et al. 2005b]. The exterior derivative of a $(n-1)$-form is uniquely defined by Stokes formula:

$$\int_{\mathbb{M}} d\boldsymbol{\omega} = \oint_{\partial\mathbb{M}} \boldsymbol{\omega}.$$

It states the equality of the integral of a differential $(n-1)$-form $\boldsymbol{\omega}$ on the boundary $\partial\mathbb{M}$, a $(n-1)$D manifold, to the integral of the exterior derivative $d\boldsymbol{\omega}$, which is a differential n-form, on the nD manifold $\mathbb{M}$. The divergence of a vector field $\mathbf{w} \in C^k(\mathbb{M}; \mathbb{T}_{\mathbb{M}})$ on a nD manifold $\mathbb{M}$ is defined, in terms of the exterior derivative, by the formula: $d(\boldsymbol{\mu}_{\mathbb{M}}\mathbf{w}) = (\mathrm{div}\mathbf{w})\boldsymbol{\mu}_{\mathbb{M}}$, where $\boldsymbol{\mu}_{\mathbb{M}}\mathbf{w}$ is the $(n-1)$-form obtained by evaluating the n-form $\boldsymbol{\mu}_{\mathbb{M}}$ with $\mathbf{w}$ as the first argument. Substituting in Stokes formula, we get the divergence theorem

$$\int_{\mathbb{M}} (\mathrm{div}\,\mathbf{w})\boldsymbol{\mu}_{\mathbb{M}} = \oint_{\partial\mathbb{M}} \boldsymbol{\mu}_{\mathbb{M}}\mathbf{w}.$$

Let us now recall the definition of the divergence of tensor fields on a submanifold $\mathbb{M}$ of a Riemannian manifold $\{\mathbb{S}, \mathbf{g}\}$. We are interested in the definition of the divergence for two kinds of tensor fields.

(i) The divergence div maps a tensor field $\mathbf{L} \in C^k(\mathbb{M}; BL(\mathbb{T}_\mathbb{M}; \mathbb{T}_\mathbb{M}))$ into the vector field $\mathrm{div}\mathbf{L} \in C^{k-1}(\mathbb{M}; \mathbb{T}_\mathbb{M})$ defined by the relation

$$\mathbf{g}(\mathrm{div}\mathbf{L}, \mathbf{a}) := \mathrm{div}(\mathbf{L}^T\mathbf{a}) - \mathbf{L} : \nabla\mathbf{a}, \qquad \text{for all } \mathbf{a} \in C^1(\mathbb{M}; \mathbb{T}_\mathbb{M}),$$

with $\mathbf{L}^T\mathbf{a} \in C^k(\mathbb{M}; \mathbb{T}_\mathbb{M})$ and $\mathrm{div}(\mathbf{L}^T\mathbf{a}) := \mathrm{tr}(\nabla(\mathbf{L}^T\mathbf{a}))$ and $\mathbf{L} : (\nabla\mathbf{a}) := \mathrm{tr}(\mathbf{L}^T\nabla\mathbf{a})$. At any $\mathbf{x} \in \mathbb{M}$, the l.h.s in the definition of $\mathrm{div}\mathbf{L}$ is an inner product which depends only on the point value $\mathbf{a}(\mathbf{x}) \in \mathbb{T}_\mathbb{M}(\mathbf{x})$ of the vector field $\mathbf{a} \in C^1(\mathbb{M}; \mathbb{T}_\mathbb{M})$. However, the evaluation of $(\mathrm{div}\mathbf{L})(\mathbf{x})$ requires to compute the r.h.s and this requires that a field of frames be assigned on $\mathbb{M}$.

(ii) The divergence Div maps a tensor field $\mathbf{A} \in C^k(\mathbb{M}; BL(\mathbb{T}_\mathbb{M}; \mathbb{T}_\mathbb{S}(\mathbb{M})))$ into the vector field $\mathrm{Div}\mathbf{A} \in C^{k-1}(\mathbb{M}; \mathbb{T}_\mathbb{S}(\mathbb{M}))$ defined by the relation

$$\mathbf{g}(\mathrm{Div}\mathbf{A}, \mathbf{v}) := \mathrm{div}(\mathbf{A}^T\mathbf{v}) - \mathbf{A} : \partial\mathbf{v}\mathbf{\Pi}, \qquad \text{for all } \mathbf{v} \in C^1(\mathbb{M}; \mathbb{T}_\mathbb{S}(\mathbb{M})),$$

with $\mathbf{A}^T \in C^k(\mathbb{M}; BL(\mathbb{T}_\mathbb{S}(\mathbb{M}); \mathbb{T}_\mathbb{M}))$ so that $\mathbf{A}^T\mathbf{v} \in C^k(\mathbb{M}; \mathbb{T}_\mathbb{M})$ and

$$\mathrm{div}(\mathbf{A}^T\mathbf{v}) := \mathrm{tr}(\nabla(\mathbf{A}^T\mathbf{v})), \quad \mathbf{A} : \partial_\mathbb{M}\mathbf{v} := \mathrm{tr}(\mathbf{A}^T\partial\mathbf{v}\mathbf{\Pi})).$$

At any $\mathbf{x} \in \mathbb{T}_\mathbb{M}(\mathbb{M})$, the l.h.s in the definition of $\mathrm{Div}\mathbf{A}$ is an inner product which depends only on the point value $\mathbf{v}(\mathbf{x}) \in \mathbb{T}_\mathbb{M}(\mathbf{x})$.

If the tensor field $\mathbf{A} \in C^k(\mathbb{M}; BL(\mathbb{T}_\mathbb{M}; \mathbb{T}_\mathbb{S}(\mathbb{M})))$ is such that $Im\mathbf{A} \subset \mathbb{T}_\mathbb{M} \subset \mathbb{T}_\mathbb{S}(\mathbb{M})$, then the divergence formulas yield the identity

$$\mathbf{g}(\mathrm{Div}\mathbf{A}, \mathbf{v}) := \mathrm{div}(\mathbf{A}^T\mathbf{v}) - \mathbf{A} : \nabla\mathbf{v} = \mathbf{g}(\mathrm{div}\mathbf{A}_\mathbb{M}, \mathbf{v}), \qquad \text{for all } \mathbf{v} \in C^1(\mathbb{M}; \mathbb{T}_\mathbb{M}),$$

where $\mathbf{A} = \mathbf{A}_\mathbb{M} \in C^k(\mathbb{M}; BL(\mathbb{T}_\mathbb{M}; \mathbb{T}_\mathbb{M}))$.

10. Equilibrium of a membrane shell

A membrane is a shell model whose kinematics admits any change of curvature strain in a rigid transformation. Accordingly, the strain measure reduces to the variation of the first fundamental form of the middle surface due to the transformation and the dual field is the membrane stress. The tangent membrane strain

$$\dot{\mathbf{E}}_\mathbb{M}(\mathbf{v}_\mathbb{M}) \in C^{k-1}(\mathbb{M}; BL(\mathbb{T}_\mathbb{M}; \mathbb{T}_\mathbb{M}))$$

associated with a velocity field $\mathbf{v}_\mathbb{M} \in C^k(\mathbb{M}; \mathbb{T}_\mathbb{S}(\mathbb{M}))$ is $\dot{\mathbf{E}}_\mathbb{M}(\mathbf{v}_\mathbb{M}) = \mathrm{sym}(\nabla\mathbf{v}_\mathbb{M})$ and hence the membrane stress is a symmetric tensor field $\mathbf{N}_\mathbb{M} \in \mathscr{L}^2(\mathbb{M}; BL(\mathbb{T}_\mathbb{M}; \mathbb{T}_\mathbb{M}))$ or equivalently a tensor field $\mathbf{N} \in \mathscr{L}^2(\mathbb{M}; BL(\mathbb{T}_\mathbb{M}; \mathbb{T}_\mathbb{S}(\mathbb{M})))$ with $Im\mathbf{N} \subset \mathbb{T}_\mathbb{M} \subset \mathbb{T}_\mathbb{S}(\mathbb{M})$. Assuming that the vector field

$$\mathrm{Div}\mathbf{N} \in \mathscr{L}^2(\mathbb{M}; \mathbb{T}_\mathbb{S}(\mathbb{M}))$$

is square integrable on $\mathbb{M}$, the divergence theorem yields the Green's formula:

$$\int_\mathbb{M} \mathbf{N} : (\partial\mathbf{v}_\mathbb{M}\mathbf{\Pi})\boldsymbol{\mu}_\mathbb{M} = \int_\mathbb{M} -\mathbf{g}(\mathrm{Div}\mathbf{N}, \mathbf{v}_\mathbb{M})\boldsymbol{\mu}_\mathbb{M} + \oint_{\partial\mathbb{M}} \mathbf{g}(\mathbf{N}\mathbf{n}_{\partial\mathbb{M}}, \mathbf{v}_\mathbb{M})\boldsymbol{\mu}_{\partial\mathbb{M}},$$

and hence the differential and boundary Cauchy's laws of equilibrium:

$$\begin{cases} -\mathrm{Div}\mathbf{N} = \mathbf{p} \in \mathscr{L}^2(\mathbb{M}; \mathbb{T}_\mathbb{S}(\mathbb{M})), & \text{body force on } \mathbb{M}, \\ \mathbf{N}\mathbf{n}_{\partial\mathbb{M}} = \mathbf{t} \in \mathscr{L}^2(\partial\mathbb{M}; \mathbb{T}_\mathbb{M}(\partial\mathbb{M})), & \text{boundary traction on } \partial\mathbb{M}. \end{cases}$$

Splitting the body force on the shell middle surface into the parallel and the normal component,

$$\mathbf{p} = \mathbf{p}^{\|} + p_\mathbf{n}\mathbf{n},$$

with $\mathbf{p}^{\|} \in \mathbb{T}_\mathbb{M}$, being $\mathbf{N}^T\mathbf{n} = 0$ identically, from the divergence formula we get

$$p_\mathbf{n} = \mathbf{g}(\mathbf{p}, \mathbf{n}) = -\mathbf{g}(\mathrm{Div}\mathbf{N}, \mathbf{n}) = -\mathrm{div}(\mathbf{N}^T\mathbf{n}) + \mathbf{N} : \partial_\mathbb{M}\mathbf{n} = \mathbf{N}_\mathbb{M} : \mathbf{S}_\mathbb{M}.$$

Given that

$$\mathbf{g}(\mathrm{Div}\mathbf{N}, \mathbf{v}_\mathbb{M}^{\|}) = \mathbf{g}_\mathbb{M}(\mathrm{div}\mathbf{N}_\mathbb{M}, \mathbf{v}_\mathbb{M}^{\|}),$$

we have $\mathbf{p}^{\|} = -\mathrm{div}\mathbf{N}_\mathbb{M}$.

Equilibrium then requires that normal loads must vanish at planar points of the membrane shell and that boundary tractions must be tangent to the middle surface of the membrane shell.

11. Equilibrium of a membrane-flexural shell

The tangent strain for the Kirchhoff–Love shell model is provided by the rates of variation of the first and second fundamental forms of the middle surface along a virtual transformation. The dual stress fields are represented by tensor fields of membrane stresses and bending-torsional moments. The basic step in the analysis of the equilibrium of the shell consists again in providing the relevant Green's formula. The virtual work principle for the shell subject to a force system $\mathbf{f}$ has the expression:

$$\int_\mathbb{M} \mathbf{N}_\mathbb{M} : \dot{\mathbf{E}}_\mathbb{M}(\mathbf{v}_\mathbb{M})\boldsymbol{\mu}_\mathbb{M} + \int_\mathbb{M} \mathbf{M}_\mathbb{M} : \dot{\mathbf{K}}_\mathbb{M}(\mathbf{v}_\mathbb{M})\boldsymbol{\mu}_\mathbb{M} = \langle \mathbf{f}, \mathbf{v}_\mathbb{M} \rangle,$$

where $\mathbf{v}_\mathbb{M} \in C^1(\mathbb{M}; \mathbb{T}_\mathbb{S}(\mathbb{M}))$ is a virtual displacement field of the actual placement of the shell. Recalling that the tangent membrane and curvature strains are given by

$$\dot{\mathbf{E}}_\mathbb{M}(\mathbf{v}_\mathbb{M}) = \mathrm{sym}(\nabla\mathbf{v}_\mathbb{M}) \quad \text{and} \quad \dot{\mathbf{K}}_\mathbb{M}(\mathbf{v}_\mathbb{M}) = \nabla\dot{\mathbf{n}} + (\mathbf{S}_\mathbb{M}\nabla\mathbf{v}_\mathbb{M})^T,$$

the appropriate divergence formulae yield

$$\mathbf{N}_\mathbb{M} : \dot{\mathbf{E}}_\mathbb{M}(\mathbf{v}_\mathbb{M}) = \mathbf{N} : \nabla\mathbf{v}_\mathbb{M} = \mathrm{div}(\mathbf{N}^T\mathbf{v}_\mathbb{M}) - \mathbf{g}(\mathrm{Div}\mathbf{N}, \mathbf{v}_\mathbb{M}),$$

$$\mathbf{M}_\mathbb{M} : \dot{\mathbf{K}}_\mathbb{M}(\mathbf{v}_\mathbb{M}) = \mathbf{M}_\mathbb{M} : \nabla\dot{\mathbf{n}} + \mathbf{M}_\mathbb{M} : \mathbf{S}\nabla\mathbf{v}_\mathbb{M} = \mathbf{M}_\mathbb{M} : \nabla\dot{\mathbf{n}} + \mathbf{S}_\mathbb{M}\mathbf{M}_\mathbb{M} : \nabla\mathbf{v}_\mathbb{M} = \mathrm{div}(\mathbf{M}_\mathbb{M}\dot{\mathbf{n}}) - \mathbf{g}_\mathbb{M}(\mathrm{div}\mathbf{M}_\mathbb{M}, \dot{\mathbf{n}})$$
$$+ \mathrm{div}((\mathbf{S}_\mathbb{M}\mathbf{M}_\mathbb{M})^T\mathbf{v}_\mathbb{M}) - \mathbf{g}(\mathrm{Div}(\mathbf{S}\mathbf{M}_\mathbb{M}), \mathbf{v}_\mathbb{M}).$$

It is convenient to define the shear vector field $\mathbf{T}_{\mathbb{M}} \in C^{k-1}(\mathbb{M}; \mathbb{T}_{\mathbb{M}})$ to be $\mathbf{T}_{\mathbb{M}} := \mathrm{div}\mathbf{M}_{\mathbb{M}}$ and its normal component at the boundary $T := \mathbf{g}_{\mathbb{M}}(\mathbf{T}_{\mathbb{M}}, \mathbf{n}_{\partial\mathbb{M}})$. Then, being $\dot{\mathbf{n}} = -(\partial\mathbf{v}_{\mathbb{M}}\boldsymbol{\Pi})^T \mathbf{n}$, we may write:

$$-\mathbf{g}_{\mathbb{M}}(\mathrm{div}\mathbf{M}_{\mathbb{M}}, \dot{\mathbf{n}}) = \mathbf{g}_{\mathbb{M}}(\mathbf{T}_{\mathbb{M}}, (\partial\mathbf{v}_{\mathbb{M}}\boldsymbol{\Pi})^T \mathbf{n}) = \mathbf{g}_{\mathbb{M}}((\partial\mathbf{v}_{\mathbb{M}}\boldsymbol{\Pi})\mathbf{T}_{\mathbb{M}}, \mathbf{n})$$
$$= \mathbf{n} \otimes \mathbf{T}_{\mathbb{M}} : \partial\mathbf{v}_{\mathbb{M}}\boldsymbol{\Pi}$$
$$= \mathrm{div}((\mathbf{T}_{\mathbb{M}} \otimes \mathbf{n})\mathbf{v}_{\mathbb{M}}) - \mathbf{g}(\mathrm{Div}(\mathbf{n} \otimes \mathbf{T}_{\mathbb{M}}), \mathbf{v}_{\mathbb{M}})$$
$$= \mathrm{div}(v_{\mathbf{n}}\mathbf{T}_{\mathbb{M}}) - \mathbf{g}(\mathrm{Div}(\mathbf{n} \otimes \mathbf{T}_{\mathbb{M}}), \mathbf{v}_{\mathbb{M}}).$$

An application of the divergence theorem provides the variational form of the equilibrium condition:

$$\langle \mathbf{f}, \mathbf{v}_{\mathbb{M}} \rangle = \int_{\mathbb{M}} -\mathbf{g}((\mathrm{Div}(\mathbf{N} + \mathbf{S}\mathbf{M}_{\mathbb{M}} + \mathbf{n} \otimes \mathbf{T}_{\mathbb{M}}), \mathbf{v}_{\mathbb{M}})\boldsymbol{\mu}_{\mathbb{M}}$$
$$+ \oint_{\partial\mathbb{M}} \mathbf{g}((\mathbf{N} + \mathbf{S}\mathbf{M}_{\mathbb{M}})\mathbf{n}_{\partial\mathbb{M}}, \mathbf{v}_{\mathbb{M}}) + \mathbf{g}_{\mathbb{M}}(\mathbf{M}_{\mathbb{M}}\mathbf{n}_{\partial\mathbb{M}}, \dot{\mathbf{n}}) + T v_{\mathbf{n}}\boldsymbol{\mu}_{\partial\mathbb{M}},$$

for any virtual displacement $\mathbf{v}_{\mathbb{M}} \in C^1(\mathbb{M}; \mathbb{T}_{\mathbb{S}}(\mathbb{M}))$.

11.1. *Differential equilibrium equation.* By localizing the variational form of the equilibrium condition we get the differential equilibrium equation:

$$-\mathrm{Div}(\mathbf{N} + \mathbf{S}\mathbf{M}_{\mathbb{M}} + \mathbf{n} \otimes \mathbf{T}_{\mathbb{M}}) = \mathbf{p},$$

To split this equation into tangent and normal components to the middle surface, we observe that:

$$-\mathbf{g}(\mathrm{Div}(\mathbf{N} + \mathbf{S}\mathbf{M}_{\mathbb{M}}), \mathbf{v}_{\mathbb{M}}^{\|}) = -\mathrm{div}((\mathbf{N} + \mathbf{S}\mathbf{M}_{\mathbb{M}})\mathbf{v}_{\mathbb{M}}^{\|}),$$
$$-\mathbf{g}(\mathrm{Div}(\mathbf{N} + \mathbf{S}\mathbf{M}_{\mathbb{M}}), \mathbf{n}) = -\mathrm{div}((\mathbf{N} + \mathbf{S}\mathbf{M}_{\mathbb{M}})^T \mathbf{n}) + (\mathbf{N}_{\mathbb{M}} + \mathbf{S}_{\mathbb{M}}\mathbf{M}_{\mathbb{M}}) : \mathbf{S}_{\mathbb{M}}$$
$$= (\mathbf{N}_{\mathbb{M}} + \mathbf{S}_{\mathbb{M}}\mathbf{M}_{\mathbb{M}}) : \mathbf{S}_{\mathbb{M}},$$

since $(\mathbf{N} + \mathbf{S}\mathbf{M}_{\mathbb{M}})^T \mathbf{n} = 0$. Moreover, substituting $(\mathbf{n} \otimes \mathbf{T}) : \nabla\mathbf{n} = \mathrm{tr}(\nabla\mathbf{n}(\mathbf{n} \otimes \mathbf{T})) = 0$, we have

$$\mathbf{g}(\mathrm{Div}(\mathbf{n} \otimes \mathbf{T}), \mathbf{n}) = \mathrm{div}((\mathbf{T} \otimes \mathbf{n})\mathbf{n}) - (\mathbf{n} \otimes \mathbf{T}) : \nabla\mathbf{n} = \mathrm{div}\mathbf{T},$$
$$\mathbf{g}(\mathrm{Div}(\mathbf{n} \otimes \mathbf{T}), \mathbf{v}_{\mathbb{M}}^{\|}) = \mathbf{g}((\nabla\mathbf{n})\mathbf{T}, \mathbf{v}_{\mathbb{M}}^{\|}) + (\mathrm{div}\mathbf{T})\mathbf{g}(\mathbf{n}, \mathbf{v}_{\mathbb{M}}^{\|}) = \mathbf{g}(\mathbf{S}\mathbf{T}, \mathbf{v}_{\mathbb{M}}^{\|}).$$

Hence the differential equilibrium equation may be split into

$$-\mathrm{div}(\mathbf{N}_{\mathbb{M}} + \mathbf{S}_{\mathbb{M}}\mathbf{M}_{\mathbb{M}}) - \mathbf{S}_{\mathbb{M}}\mathbf{T}_{\mathbb{M}} = \mathbf{p}^{\|},$$
$$-\mathrm{div}\,\mathrm{div}\mathbf{M}_{\mathbb{M}} + (\mathbf{N}_{\mathbb{M}} + \mathbf{S}_{\mathbb{M}}\mathbf{M}_{\mathbb{M}}) : \mathbf{S}_{\mathbb{M}} = p_{\mathbf{n}}.$$

11.2. *Interpretation of the boundary terms.* To get a clearer mechanical interpretation of the boundary virtual work, we split the boundary spin $\dot{\mathbf{n}}$ into the bending and the torsional components: $\dot{\mathbf{n}} = \dot{n}_b\mathbf{n}_{\partial\mathbb{M}} + \dot{n}_t\mathbf{t}_{\partial\mathbb{M}}$ with $\dot{n}_b = -\mathbf{g}_{\mathbb{M}}(\partial_{\mathbf{n}_{\partial\mathbb{M}}}\mathbf{v}_{\mathbb{M}}, \mathbf{n})$ and $\dot{n}_t = -\mathbf{g}_{\mathbb{M}}(\partial_{\mathbf{t}_{\partial\mathbb{M}}}\mathbf{v}_{\mathbb{M}}, \mathbf{n})$. Setting $\mathbf{M}_{\mathbb{M}}\mathbf{n}_{\partial\mathbb{M}} = M_b\mathbf{n}_{\partial\mathbb{M}} + M_t\mathbf{t}_{\partial\mathbb{M}}$ we have

$$\oint_{\partial\mathbb{M}} \mathbf{g}_{\mathbb{M}}(\mathbf{M}_{\mathbb{M}}\mathbf{n}_{\partial\mathbb{M}}, \dot{\mathbf{n}})\boldsymbol{\mu}_{\partial\mathbb{M}} = \oint_{\partial\mathbb{M}} (M_b\dot{n}_b + M_t\dot{n}_t)\boldsymbol{\mu}_{\partial\mathbb{M}}.$$

Then, given

$$\oint_{\partial\mathbb{M}} M_t \dot{n}_t \boldsymbol{\mu}_{\partial\mathbb{M}} = -\oint_{\partial\mathbb{M}} \mathbf{g}(\partial_{\mathbf{t}_{\partial\mathbb{M}}} \mathbf{v}_\mathbb{M}, M_t \mathbf{n}) \boldsymbol{\mu}_{\partial\mathbb{M}}$$

$$= -\oint_{\partial\mathbb{M}} \partial_{\mathbf{t}_{\partial\mathbb{M}}}(M_t v_\mathbf{n}) \boldsymbol{\mu}_{\partial\mathbb{M}} + \oint_{\partial\mathbb{M}} \mathbf{g}(\partial_{\mathbf{t}_{\partial\mathbb{M}}}(M_t \mathbf{n}), \mathbf{v}_\mathbb{M}) \boldsymbol{\mu}_{\partial\mathbb{M}}$$

$$= \oint_{\partial\mathbb{M}} (\partial_{\mathbf{t}_{\partial\mathbb{M}}} M_t) v_\mathbf{n} \boldsymbol{\mu}_{\partial\mathbb{M}} + \oint_{\partial\mathbb{M}} M_t \mathbf{g}(\mathbf{St}_{\partial\mathbb{M}}, \mathbf{v}_\mathbb{M}) \boldsymbol{\mu}_{\partial\mathbb{M}},$$

the boundary virtual work may be written as

$$\oint_{\partial\mathbb{M}} \mathbf{g}((\mathbf{N}+\mathbf{SM}_\mathbb{M})\mathbf{n}_{\partial\mathbb{M}} + M_t\mathbf{St}_{\partial\mathbb{M}}, \mathbf{v}_\mathbb{M}^{\|}) \boldsymbol{\mu}_{\partial\mathbb{M}} + \oint_{\partial\mathbb{M}} (T + \partial_{\mathbf{t}_{\partial\mathbb{M}}} M_t) v_\mathbf{n} \boldsymbol{\mu}_{\partial\mathbb{M}} + \oint_{\partial\mathbb{M}} M_b \dot{n}_b \boldsymbol{\mu}_{\partial\mathbb{M}}.$$

Hence the boundary equilibrium conditions are given by

$$(\mathbf{N}+\mathbf{SM}_\mathbb{M})\mathbf{n}_{\partial\mathbb{M}} + M_t\mathbf{St}_{\partial\mathbb{M}} = \mathbf{t}^{\|}, \quad \text{dual of} \quad \mathbf{v}_\mathbb{M}^{\|},$$

$$T + \partial_{\mathbf{t}_{\partial\mathbb{M}}} M_t = t_\mathbf{n}, \qquad\qquad \text{dual of} \quad v_\mathbf{n},$$

$$M_b = m, \qquad\qquad\qquad \text{dual of} \quad \dot{n}_b.$$

These boundary conditions differ from the ones reported in the literature which will be referred to as the standard boundary conditions. Indeed, the bending couple M_b, per-unit-length along the boundary, is here considered as the force system dual of the bending spin

$$\dot{n}_b = \mathbf{g}_\mathbb{M}(\dot{\mathbf{n}}, \mathbf{n}_{\partial\mathbb{M}}) = -\mathbf{g}_\mathbb{M}(\partial_{\mathbf{n}_{\partial\mathbb{M}}} \mathbf{v}_\mathbb{M}, \mathbf{n}).$$

In the literature, the bending couple per-unit-length along the boundary has typically been assumed to be the force system dual of the derivative $\partial_{\mathbf{n}_{\partial\mathbb{M}}} v_\mathbf{n}$ of the virtual velocity $v_\mathbf{n}$, normal to the middle surface, along the outward normal to the boundary. This choice has been apparently suggested by the analogous formula for flat plates. However, when the shell is not flat, the two choices are not equivalent since

$$\dot{n}_b = -\partial_{\mathbf{n}_{\partial\mathbb{M}}} v_\mathbf{n} + \mathbf{g}_\mathbb{M}(\mathbf{Sn}_{\partial\mathbb{M}}, \mathbf{v}_\mathbb{M}^{\|}).$$

In fact, the derivative $\partial_{\mathbf{n}_{\partial\mathbb{M}}} v_\mathbf{n}$ has not a clear kinematical meaning, while apparently $\dot{n}_b = \mathbf{g}_\mathbb{M}(\dot{\mathbf{n}}, \mathbf{n}_{\partial\mathbb{M}})$ is the appropriate expression for the bending rate of the normal fibers of the shell at a boundary. To highlight the connection between the new and the standard boundary equilibrium conditions we observe that

$$M_b \dot{n}_b = M_b \mathbf{g}_\mathbb{M}(\dot{\mathbf{n}}, \mathbf{n}_{\partial\mathbb{M}}) = M_b \mathbf{g}_\mathbb{M}(\mathbf{Sv}_\mathbb{M} - \nabla v_\mathbf{n}, \mathbf{n}_{\partial\mathbb{M}})$$

$$= \mathbf{g}_\mathbb{M}(\mathbf{Sv}_\mathbb{M}, \mathbf{M}_\mathbb{M}\mathbf{n}_{\partial\mathbb{M}}) - \mathbf{g}_\mathbb{M}(\mathbf{Sv}_\mathbb{M}, M_t\mathbf{t}_{\partial\mathbb{M}}) - M_b \partial_{\mathbf{n}_{\partial\mathbb{M}}} v_\mathbf{n}$$

$$= \mathbf{g}_\mathbb{M}(\mathbf{SM}_\mathbb{M}\mathbf{n}_{\partial\mathbb{M}} - M_t\mathbf{St}_{\partial\mathbb{M}}, \mathbf{v}_\mathbb{M}) - M_b \partial_{\mathbf{n}_{\partial\mathbb{M}}} v_\mathbf{n}.$$

Substituting this expression into the boundary virtual work we recover the standard boundary conditions:

$$(\mathbf{N}+2\mathbf{SM}_\mathbb{M})\mathbf{n}_{\partial\mathbb{M}} = \mathbf{t}^{\|}, \quad \text{dual of} \quad \mathbf{v}_\mathbb{M}^{\|},$$

$$T + \partial_{\mathbf{t}_{\partial\mathbb{M}}} M_t = t_\mathbf{n}, \qquad \text{dual of} \quad v_\mathbf{n},$$

$$M_b = m^*, \qquad\qquad \text{dual of} \quad -\partial_{\mathbf{n}_{\partial\mathbb{M}}} v_\mathbf{n}.$$

Remark 11.1. The split form of the differential condition of equilibrium is reported in coordinate expression in [Ciarlet 2000; 2005]. The coordinate form of the standard boundary conditions can be found in [Ciarlet 2005, Theorem 4.4-4]. The unsplit differential condition and the new form of the boundary conditions are contributed here for the first time in the context of a duality approach to shell theory. The treatment of shell equilibrium, according to the so-called direct approach in the restricted theory, is reviewed in the comprehensive article by [Naghdi 1972, section 15] and in the book by [Libai and Simmonds 1998]. In this context, a differential equilibrium equation formally similar to our was provided in [Steele 1971].

12. Equilibrium in a reference placement

In the nonlinear analysis of elastic shells the equilibrium condition must be written in terms of fields defined in a reference placement since constitutive laws are expressed in terms of strain measures from a natural reference placement. Moreover, in computational mechanics the suitable form of the equilibrium condition is the variational one in terms of virtual work. Once the referential stress fields are evaluated, it is needed to recover the physically significant stress fields in the actual placement. To this end we remark that, by the consistency of the shell strain measure, proven in Section 6.1, the rigid virtual displacements can be characterized as vector fields in the kernel of the rates of the strain measure from a fixed reference placement $\mathbb{M}$ to the moving actual one $\boldsymbol{\varphi}(\mathbb{M})$. The strain measure associated with the configuration map $\boldsymbol{\varphi} \in \mathrm{C}^1(\mathbb{M}; \mathbb{S})$ is given by the pair of strain fields:

$$2\mathbf{E}_{\boldsymbol{\varphi}} := \partial\boldsymbol{\varphi}^T \partial\boldsymbol{\varphi} - \mathbf{I}_{\mathbb{M}}, \qquad \mathbf{K}_{\boldsymbol{\varphi}} := \partial\boldsymbol{\varphi}^T \mathbf{S}_{\boldsymbol{\varphi}} \partial\boldsymbol{\varphi} - \mathbf{S}_{\mathbb{M}}.$$

Let $\mathbf{Fl}_{t,s}^{\mathbf{v}} \in \mathrm{C}^1(\mathbb{S}; \mathbb{S})$ be a flow with velocity $\mathbf{v} = \partial_{t=s}\mathbf{Fl}_{t,s}^{\mathbf{v}} \in \mathrm{C}^1(\mathbb{S}; \mathbb{T}_{\mathbb{S}})$. The tangent membrane and curvature strain rates at $\boldsymbol{\varphi}(\mathbb{M})$, are the time derivative $\partial_{t=s}$ of the shell strains in the transformation from $\boldsymbol{\varphi}(\mathbb{M})$ to $(\mathbf{Fl}_{t,s}^{\mathbf{v}} \circ \boldsymbol{\varphi})(\mathbb{M})$ evaluated at $\boldsymbol{\varphi}(\mathbb{M})$, and are given by

$$\dot{\mathbf{E}}_{\boldsymbol{\varphi}(\mathbb{M})}(\mathbf{v}) = \mathrm{sym}\,\nabla\mathbf{v}, \quad \dot{\mathbf{K}}_{\boldsymbol{\varphi}(\mathbb{M})}(\mathbf{v}) = \nabla\dot{\mathbf{n}}_{\boldsymbol{\varphi}} + (\mathbf{S}_{\boldsymbol{\varphi}}\nabla\mathbf{v})^T.$$

The secant membrane and curvature strain rates at $\boldsymbol{\varphi}(\mathbb{M})$, are the time derivative $\partial_{t=s}$ of the shell strains in the transformation from $\mathbb{M}$ to $(\mathbf{Fl}_{t,s}^{\mathbf{v}} \circ \boldsymbol{\varphi})(\mathbb{M})$ evaluated at $\boldsymbol{\varphi}(\mathbb{M})$, and are given by

$$\dot{\mathbf{E}}_{\{\mathbb{M},\boldsymbol{\varphi}(\mathbb{M})\}}(\mathbf{v}) := \partial_{t=s}\mathbf{E}_{\mathbf{Fl}_{t,s}^{\mathbf{v}} \circ \boldsymbol{\varphi}} = \mathrm{sym}(\partial\boldsymbol{\varphi}^T \partial\mathbf{v}\partial\boldsymbol{\varphi}) = \partial\boldsymbol{\varphi}^T \dot{\mathbf{E}}_{\boldsymbol{\varphi}(\mathbb{M})}(\mathbf{v})\partial\boldsymbol{\varphi},$$

$$\dot{\mathbf{K}}_{\{\mathbb{M},\boldsymbol{\varphi}(\mathbb{M})\}}(\mathbf{v}) := \partial_{t=s}\mathbf{K}_{\mathbf{Fl}_{t,s}^{\mathbf{v}} \circ \boldsymbol{\varphi}} = \partial\boldsymbol{\varphi}^T(\nabla\dot{\mathbf{n}}_{\boldsymbol{\varphi}} + (\mathbf{S}_{\boldsymbol{\varphi}}\nabla\mathbf{v})^T)\partial\boldsymbol{\varphi} = \partial\boldsymbol{\varphi}^T \dot{\mathbf{K}}_{\boldsymbol{\varphi}(\mathbb{M})}(\mathbf{v})\partial\boldsymbol{\varphi}.$$

The shell stress tensors in the reference placement are defined, in tems of the shell stress tensors in the actual placement, by the invertible relations

$$\mathbf{N}_{\boldsymbol{\varphi}(\mathbb{M})} = J_{\boldsymbol{\varphi}}\partial\boldsymbol{\varphi}\mathbf{N}_{\{\mathbb{M},\boldsymbol{\varphi}(\mathbb{M})\}}\partial\boldsymbol{\varphi}^T, \qquad \mathbf{M}_{\boldsymbol{\varphi}(\mathbb{M})} = J_{\boldsymbol{\varphi}}\partial\boldsymbol{\varphi}\mathbf{M}_{\{\mathbb{M},\boldsymbol{\varphi}(\mathbb{M})\}}\partial\boldsymbol{\varphi}^T,$$

where $J_{\boldsymbol{\varphi}}$ is the jacobian determinant associated with the map $\boldsymbol{\varphi} \in \mathrm{C}^1(\mathbb{M}; \mathbb{S})$. Then we have the equality:

$$\int_{\boldsymbol{\varphi}(\mathbb{M})} \mathbf{N}_{\boldsymbol{\varphi}(\mathbb{M})} : \dot{\mathbf{E}}_{\boldsymbol{\varphi}(\mathbb{M})}(\mathbf{v})\boldsymbol{\mu} + \int_{\boldsymbol{\varphi}(\mathbb{M})} \mathbf{M}_{\boldsymbol{\varphi}(\mathbb{M})} : \dot{\mathbf{K}}_{\boldsymbol{\varphi}(\mathbb{M})}(\mathbf{v})\boldsymbol{\mu}$$

$$= \int_{\mathbb{M}} \mathbf{N}_{\{\mathbb{M}, \boldsymbol{\varphi}(\mathbb{M})\}} : \dot{\mathbf{E}}_{\{\mathbb{M}, \boldsymbol{\varphi}(\mathbb{M})\}}(\mathbf{v}) J_{\boldsymbol{\varphi}}\boldsymbol{\mu} + \int_{\mathbb{M}} \mathbf{M}_{\{\mathbb{M}, \boldsymbol{\varphi}(\mathbb{M})\}} : \dot{\mathbf{K}}_{\{\mathbb{M}, \boldsymbol{\varphi}(\mathbb{M})\}}(\mathbf{v}) J_{\boldsymbol{\varphi}}\boldsymbol{\mu},$$

for any virtual displacement $\mathbf{v} \in \mathrm{C}^1(\boldsymbol{\varphi}(\mathbb{M}); \mathbb{T}_{\mathbb{S}})$ of the actual placement of the shell.

13. Shear deformable and polar shell models

In what follows we outline the main ingredients of two shell models proposed in the literature and widely adopted for computational purposes. In the former model the shear defomability of the shell is approximately taken into account since the transversal fibers are allowed to rotate with respect to the middle surface. In the latter model, a polar structure is introduced with the aim to match the shell kinematic parameters with that of a shear deformable beam. We will not develop these models here in full detail but will illustrate some critical remarks that provide guidelines for their modification or rejection.

13.1. *Shells with transversal shear deformation.* In this shell model transversal shear deformation is simulated by means of rigid oriented *needles* hinged at the points of the middle surface. The middle surface has then the geometrical structure of a fiber manifold and is commonly called a Cosserat surface [Naghdi 1972]. However, such a nickname may lead to the misleading conclusion that the need for a polar structure of the ambient space is implied. The needles are described by a field of directors $\mathbf{d} \in \mathrm{C}^1(\mathbb{M}; S^2(1))$ defined on $\mathbb{M}$ and with values on the unit sphere $S^2(1)$, which is a 2D submanifold of the euclidean space $\mathbb{S}$. Directors play a role similar to that of normal versors in the Kirchhoff–Love shell model and hence the shell kinematics describes a 2D model which is a constrained three-dimensional Cauchy continuum model. In a model with inextensible needles, the shell thickness is assumed to be small enough to ensure that for all $\mathbf{x} \in U_{\mathbb{M}}$ there exists an unique decomposition such that:

$$\mathbf{x} = \mathbf{P_d}(\mathbf{x}) + r(\mathbf{x})\mathbf{d}(\mathbf{P_d}(\mathbf{x})) = \mathbf{P_d}(\mathbf{x}) + r(\mathbf{x})\mathbf{d}(\mathbf{x}),$$

with $\mathbf{P_d} \in \mathrm{C}^1(U_{\mathbb{M}}; \mathbb{M})$ and $\partial \mathbf{P_d}(\mathbf{x}) \in BL(\mathbb{T}_{\mathbb{S}}(\mathbf{x}); \mathbb{T}_{\mathbb{M}}(\mathbf{P_d}(\mathbf{x})))$. The surfaces which are level sets of the function $r \in \mathrm{C}^2(U_{\mathbb{M}}; \mathfrak{R})$ do not form a foliation of the shell middle surface. Indeed $\mathbf{g}(\partial r, \mathbf{d}) = 1$ and $\mathbf{g}(\mathbf{d}, \mathbf{n})\partial r = \mathbf{n}$. Hence r is not a distance function unless $\mathbf{d} = \mathbf{n}$. The derivative $\partial \mathbf{d} \in BL(\mathbb{T}_{\mathbb{M}}; \mathbb{T}_{\mathbb{S}})$ is not necessarily symmetric, so that $\mathbf{d} \in \mathrm{Ker}\, \partial \mathbf{d}^T$ and $\mathrm{Im}\, \partial \mathbf{d} \subseteq (\mathrm{Span}\partial \mathbf{d})^{\perp}$. Taking the derivative we get: $\mathbf{h} = \partial_{\mathbf{h}}\mathbf{P_d} + r\partial \mathbf{d}\partial_{\mathbf{h}}\mathbf{P_d} + (\partial_{\mathbf{h}}r)\mathbf{d}$.

The transformation $\boldsymbol{\psi}_{\boldsymbol{\varphi}, \mathbf{d}} \in \mathrm{C}^1(U_{\mathbb{M}}; \mathbb{S})$ of the shell, induced by a diffeomorphic transformation $\boldsymbol{\varphi} \in \mathrm{C}^1(\mathbb{M}; \mathbb{S})$ of the middle surface $\mathbb{M}$ and by a field of directors $\mathbf{d}_{\boldsymbol{\varphi}} \in \mathrm{C}^1(\boldsymbol{\varphi}(\mathbb{M}); \mathbb{T}_{\mathbb{S}})$, is given by

$$\boldsymbol{\psi}_{\boldsymbol{\varphi}, \mathbf{d}}(\mathbf{x}) := \boldsymbol{\varphi}(\mathbf{P_d}(\mathbf{x})) + r(\mathbf{x})\mathbf{d}_{\boldsymbol{\varphi}}(\boldsymbol{\varphi}(\mathbf{P_d}(\mathbf{x}))), \qquad \text{for all } \mathbf{x} \in U_{\mathbb{M}}.$$

with $\mathbf{d}_{\boldsymbol{\varphi}} \in \mathrm{C}^1(\boldsymbol{\varphi}(\mathbb{M}); S^2(1))$ director field on $\boldsymbol{\varphi}(\mathbb{M})$.

Then

$$\partial_{\mathbf{h}}\boldsymbol{\psi}_{\boldsymbol{\varphi}, \mathbf{d}_{\boldsymbol{\varphi}}} = (\mathbf{I} + r\partial \mathbf{d}_{\boldsymbol{\varphi}})\partial \boldsymbol{\varphi}\partial_{\mathbf{h}}\mathbf{P_d} + (\partial_{\mathbf{h}}r)\mathbf{d}_{\boldsymbol{\varphi}} \circ \boldsymbol{\varphi},$$

and Green strain is:

$$\mathbf{G}_{\boldsymbol{\varphi},\mathbf{d}_{\boldsymbol{\varphi}}} = \partial \mathbf{P}_{\mathbf{d}}^T (\partial \boldsymbol{\varphi}^T \partial \boldsymbol{\varphi} + r \operatorname{sym}(\partial \boldsymbol{\varphi}^T \partial_{\mathbb{M}}(\mathbf{d}_{\boldsymbol{\varphi}} \circ \boldsymbol{\varphi}))$$

$$+ \frac{1}{2} r^2 \partial_{\mathbb{M}}(\mathbf{d}_{\boldsymbol{\varphi}} \circ \boldsymbol{\varphi})^T \partial_{\mathbb{M}}(\mathbf{d}_{\boldsymbol{\varphi}} \circ \boldsymbol{\varphi})) \partial \mathbf{P}_{\mathbf{d}} + \operatorname{sym}(\partial \mathbf{P}_{\mathbf{d}}^T \partial \boldsymbol{\varphi}^T (\mathbf{d}_{\boldsymbol{\varphi}} \circ \boldsymbol{\varphi} \otimes \partial r)) - \mathbf{I}.$$

In the relevant literature, [Simo and Fox 1989; VuQuoc et al. 2000], membranal, curvature and shear strains for the shell have been defined as:

$$2\boldsymbol{\varepsilon}_{\boldsymbol{\varphi}}(\mathbf{a}, \mathbf{b}) := \mathbf{g}(\partial_{\mathbf{a}} \boldsymbol{\varphi}, \partial_{\mathbf{b}} \boldsymbol{\varphi}) - \mathbf{g}(\mathbf{a}, \mathbf{b}),$$

$$\boldsymbol{\chi}_{\boldsymbol{\varphi},\mathbf{d}_{\boldsymbol{\varphi}}}(\mathbf{a}, \mathbf{b}) := \mathbf{g}(\partial_{\mathbf{a}}(\mathbf{d}_{\boldsymbol{\varphi}} \circ \boldsymbol{\varphi}), \partial_{\mathbf{b}} \boldsymbol{\varphi}) - \mathbf{g}(\partial_{\mathbf{a}} \mathbf{d}, \mathbf{b}),$$

$$\boldsymbol{\delta}_{\boldsymbol{\varphi},\mathbf{d}_{\boldsymbol{\varphi}}}(\mathbf{a}) := \mathbf{g}(\mathbf{d}_{\boldsymbol{\varphi}} \circ \boldsymbol{\varphi}, \partial_{\mathbf{a}} \boldsymbol{\varphi}) - \mathbf{g}(\mathbf{d}, \mathbf{a}),$$

where $\mathbf{a}, \mathbf{b} \in \mathbb{T}_{\mathbb{M}}$. The membranal strain is a 2×2 symmetric tensor, while the curvature strain is a 2×2 unsymmetric tensor and the shear strain is a 2D vector. We have then $3 + 4 + 2 = 9$ scalar strain parameters. Despite of its wide usage, this strain measure is redundant. A more economical set of strain fields can be envisaged by substituting the unsymmetrical curvature strain $\boldsymbol{\chi}_{\boldsymbol{\varphi},\mathbf{d}}$ with its symmetric part or by retaining the same membranal and curvature strains of the Kirchhoff–Love shell model, adding to these the shear strain measure. We have then $3 + 3 + 2 = 8$ scalar strain parameters. In the literature no attention seems to have been payed to the issue of redundancy but the topic has been only indirectly treated by assuming that the shell stress tensor dual of the curvature strain be symmetric [Naghdi 1972; Simo and Fox 1989]. Moreover, an explicit expression of the Green strain in terms of shell strains is still lacking. A computational analysis of the shell model with transversal shear strain can be carried out by a direct recourse to the expression of the Green strain provided above thus avoiding the introduction of shell strain fields.

13.2. Polar Shells. In the polar model of a shell, a rigid triad is hinged at each point of the middle surface and arbitrary rotations are allowed for. This is called the shell model with drilling rotations [Fox and Simo 1992; Ibrahimbegovic 1994]. A placement of the polar shell is described by a placement of the middle surface $\mathbb{M}$ and by a field of rotations which simulate a rigid body kinematics along the thickness of the shell. The ambient space is then the Cosserat manifold $\mathbb{S} \times SO(3)$ which is a trivial fiber bundle whose base manifold is the euclidean space $\mathbb{S}$. The nonlinear fiber manifold $SO(3)$ is the three-dimensional compact group of rotations, the special orthogonal group. A configuration change is a map $\mathbf{u}_{t,s} : \mathbb{M} \mapsto \mathbb{S} \times SO(3)$ described by a configuration change $\boldsymbol{\varphi}_{t,s} \in C^1(\mathbb{M}; \mathbb{S})$ of the base manifold $\mathbb{M}$ and by a field of rotations $\mathbf{Q}_{t,s} \in C^1(\mathbb{M}; SO(3))$, with respect to a reference triad. Then, at each point $\mathbf{x} \in \mathbb{M}$, we have $\mathbf{u}_{t,s}(\mathbf{x}) = \{\boldsymbol{\varphi}_{t,s}(\mathbf{x}), \mathbf{Q}_{t,s}(\mathbf{x})\} \in \mathbb{S} \times SO(3)$. In the literature [Fox and Simo 1992; Ibrahimbegovic 1994], the strain measure is defined to be the pair

$$\begin{cases} \mathbf{Q}_{t,s}^T \partial_{\mathbb{M}} \boldsymbol{\varphi}_{t,s} - \mathbf{I}_{\mathbb{M}}, & \text{membrane-shear strain,} \\ \mathbf{Q}_{t,s}^T \partial_{\mathbb{M}} \mathbf{Q}_{t,s}, & \text{wryness strain,} \end{cases}$$

where $\partial_{\mathbb{M}}$ denoted the derivative along tangent vectors in $\mathbb{T}_{\mathbb{M}}$ and $\mathbf{I}_{\mathbb{M}}$ is the identity in $\mathbb{T}_{\mathbb{M}}$. Since the tangent spaces $\mathbb{T}_{\mathbb{M}}(\mathbf{x})$ are 2D and $\mathbf{Q}$ belongs to the three-dimensional manifold $SO(3)$, the vanishing of the wryness is expressed by 6 scalar differential conditions. The vanishing of the membrane-shear strain

is also expressed by 6 scalar differential conditions. By decomposing the membrane-shear strain into its normal and tangent components, the membrane and shear components of the strain measure are given by [Ibrahimbegovic 1994]:

$$\boldsymbol{\varepsilon}_{\varphi,\mathbf{Q}}(\mathbf{a}, \mathbf{b}) := \mathbf{g}(\partial\varphi \cdot \mathbf{a}_1, \mathbf{Q}\mathbf{a}_2) - \mathbf{g}(\mathbf{a}_1, \mathbf{a}_2), \qquad \mathbf{a}, \mathbf{b} \in \mathbb{T}_\mathbb{M},$$

$$\boldsymbol{\delta}_{\varphi,\mathbf{Q}}(\mathbf{a}) := \mathbf{g}(\partial\varphi \cdot \mathbf{a}, \mathbf{Q}\mathbf{n}) - \mathbf{g}(\mathbf{a}, \mathbf{n}), \qquad \mathbf{a} \in \mathbb{T}_\mathbb{M}.$$

The wryness may be also expressed in terms of the axial vector $\boldsymbol{\Omega}\mathbf{b} := \operatorname{axial}((\partial_\mathbf{b}\mathbf{Q})\mathbf{Q}^T)$. An expression of the wryness as a 2×2 bilinear form was provided in [Ibrahimbegovic 1994] by setting $\boldsymbol{\chi}_\mathbf{Q}(\mathbf{a}, \mathbf{b}) := \mathbf{g}(\mathbf{Q}\mathbf{a}, \boldsymbol{\Omega}\mathbf{b})$ but this is a misstatement since only 4 scalar components are involved, instead of the 6 needed. The polar shell model is redundant. To see this, let us assume that the membrane-shear strain vanishes, that is, $\partial\varphi(\mathbf{x}) \cdot \mathbf{a} = \mathbf{Q}(\mathbf{x})\mathbf{a}$, for all $\mathbf{a} \in \mathbb{T}_\mathbb{M}(\mathbf{x})$. Hence $\mathbf{n}_\varphi(\mathbf{x}) = \mathbf{Q}(\mathbf{x})\mathbf{n}(\mathbf{x})$. Then the membrane strain $\boldsymbol{\varepsilon}_\varphi$ vanishes and moreover it is sufficient to impose the vanishing of the curvature strain $\boldsymbol{\chi}_\varphi$ to ensure that the shell transformation is rigid, so that $\partial_\mathbb{M}\mathbf{Q} = 0$. We then need only $6 + 3 = 9$ scalar differential expressions to get a strain measure instead of the $6 + 6 = 12$ included in the strain measure of the polar shell model. This basic criticism, which stems from integrability requirements, also applies to the Cosserat polar model of a three-dimensional continuum and to the more sophisticated polar models of micromorphic and microstretch continua proposed in the literature [Eringen 1998]. A discussion on this topic is presented in [Romano 2002]. Since the polar shell model is a constrained three-dimensional Cosserat continuum, the constitutive relations of a Cauchy continuum are not applicable and this should compel the supporters of this model to envisage new nonconventional ones.

14. Concluding remarks

The initial motivation for this investigation on shell models stemmed from the unpleasant sensation that any aesthetically minded scholar feels in reading most treatises or articles on shells, and from the headaches provoked by the hoard of indexes that have to be dealt with. Also, it is hard to keep track of the geometrical significance of the quantities involved when the notation is too disturbing. In the attempt to overcome these shortcomings, several useful facts have been discovered and the ones most deserving of attention are recalled below. Basic results of surface geometry needed in a shell theory have been presented without recourse to coordinate systems or fields of frames. As a premise, the rules to be followed in the formulation of a structural model as a constrained three-dimensional Cauchy continuum are illustrated, to ensure that the model itself is well posed and that the experimental evidences, provided in the three-dimensional context, be available for the model. The *rigidity theorem* providing the uniqueness, up to isometries, of a surface with given first and second fundamental forms, is proven as a special case of a more general result of kinematics in an euclidean space. The result is given both in finite and in rate form (Theorems 5.1 and 5.2). Explicit expressions of the finite and tangent Green strains for a Kirchhoff–Love shell, in terms of the shell kinematical parameters and of the membranal and curvature strains of the shell, are provided. These basic tools are needed to properly state the variational equilibrium condition and the constitutive laws for the shell. A new expression of the tangent curvature strain is provided and allows for a direct application of the divergence theorem to get Green's formula for the shell model. The basic differential and boundary equilibrium conditions are derived in a straight way without performing the usual split into tangent and normal components. A new set of boundary

conditions is provided, since it is shown that the classical definition of the bending couple does not take properly into account the bending rotation rate of the transversal fibers. Equilibrium conditions in a reference placement are also dealt with. Two shell models, presently most popular in the computational mechanics community, are also discussed (Section 13). The former is the shell with transversal shear deformation while the latter, the polar shell with drilling rotations, has been proposed in the literature to provide rotational kinematical parameters which allow for the assembly between shell elements and beam elements, with the aim to give a tool to engineers for the analysis of shells with beam-like reinforcements. The polar shell model is then a constrained Cosserat three-dimensional continuum model. A closer look at the strain measure adopted for these shell models reveals, on the basis of the discussion in Section 5, that the set of strain parameters is redundant in both cases. This unpleasant feature forces one, by duality, to introduce more stress parameters than necessary and renders the models mechanically unsound. A suitable remedy for the former model is proposed. Unfortunately, the redundancy of the polar model, also shared by the Cosserat three-dimensional continuum model, appears to be of a troublesome resolution and should eventually force researchers to open new ways for the proposal of well posed mechanical models with a polar structure or to find better alternatives.

References

[Ciarlet 2000] P. G. Ciarlet, *Theory of Shells*, vol. 3, North-Holland, Amsterdam, 2000.

[Ciarlet 2005] P. G. Ciarlet, "An Introduction to Differential Geometry with Applications to Elasticity", Technical report, City University of Hong Kong, 2005.

[Eringen 1998] A. C. Eringen, *Microcontinuum field theories*, Springer, Berlin, 1998.

[Fox and Simo 1992] D. D. Fox and J. C. Simo, "A drill rotation formulation for geometrically exact shells", *Comput. Methods Appl. Mech. Engrg.* **98** (1992), 329–342.

[Ibrahimbegovic 1994] A. Ibrahimbegovic, "Stress resultant geometrically nonlinear shell theory with drilling rotations - Part I: A consistent formulation", *Comp. Meth. Appl. Mech. Engng.* **118** (1994), 265–284.

[Libai and Simmonds 1998] A. Libai and J. G. Simmonds, *The Nonlinear Theory of Elastic Shells*, Cambridge Univ. Press, 1998.

[Marsden and Hughes 1983] J. E. Marsden and T. J. R. Hughes, *Mathematical foundations of elasticity*, Prentice-Hall, Redwood City, CA, 1983.

[Naghdi 1972] P. M. Naghdi, *Handbuch der Physik*, vol. VIa/2, Chapter The Theory of Shells and Plates, pp. 425–640, Springer, Berlin, 1972.

[Romano 2002] G. Romano, *Scienza delle Costruzioni*, Hevelius Edizioni, 2002.

[Romano et al. 2002] G. Romano, M. Diaco, and C. Sellitto, *Trends and Applications of Mathematics to Mechanics*, Chapter Tangent Stiffness of Elastic Continua on Manifolds, pp. 155–184, Springer Verlag, 2002.

[Romano et al. 2005a] G. Romano, R. Barretta, and C. Sellitto, "On the evaluation of the elastoplastic tangent stiffness", pp. 1118–1121 in *VIII International Conference on Computational Plasticity* (Barcelona), 2005.

[Romano et al. 2005b] G. Romano, M. Diaco, and R. Barretta, "Continuum mechanics: A Differential Geometric Approach", Research report, Dept. of Structural Engineering, Univ. of Naples Federico II, 2005.

[Romano et al. 2006] G. Romano, M. Diaco, and R. Barretta, "A geometric approach to the algorithmic tangent stiffness", pp. 121–129 in *III European Conference on Computational Mechanics* (Lisbon), 2006.

[Simo and Fox 1989] J. C. Simo and D. D. Fox, "On a stress resultant geometrically exact shell model—Part I: Formulation and optimal parametrization", *Comput. Methods Appl. Mech. Engrg.* **72** (1989), 267–304.

[Steele 1971] C. R. Steele, "A geometric optics solution for the thin shell equation", *Int. J. of Engng. Sci.* **9** (1971), 681–704.

[VuQuoc et al. 2000] L. VuQuoc, H. Deng, and X. G. Tan, "Geometrically-exact sandwich shells: The static case", *Comput. Methods Appl. Mech. Engrg.* **189** (2000), 167–203.

[Yosida 1974] K. Yosida, *Functional Analysis*, 4th ed., Springer, New York, 1974.

GIOVANNI ROMANO: romano@unina.it
University of Naples Federico II, Department of Structural Engineering, via Claudio 21, 80125 Naples, Italy

CARMEN SELLITTO: c.sellitto@cira.it
Centro Italiano Ricerche Aerospaziali (CIRA), LAMC (Computational Mechanics Laboratory), via Maiorise, 81043 Capua (CE), Italy

RAFFAELE BARRETTA: rabarret@unina.it
University of Naples Federico II, Department of Structural Engineering, via Claudio 21, 80125 Naples, Italy

A COHESIVE ZONE FINITE ELEMENT APPROACH TO MODEL TENSILE CRACKS IN THIN FILM COATINGS

Srikant Nekkanty, Mark E. Walter and Rajiv Shivpuri

A two-dimensional finite element model using cohesive zone elements was developed to predict cracking in thin film coating-interlayer-substrate systems that are subjected to tensile loading. The constitutive models were chosen to represent a metal carbide/diamond-like carbon composite coating with a titanium interlayer and a steel substrate. Material properties of the coating and interlayer along with the cohesive finite element parameters were varied to study effects on stress distributions and coating cracking. Stress distributions were highly nonuniform through the coating thickness. Thus the initiation and arrest of tensile cracks differed from what is predicted by simple shear-lay theory. Intercrack spacing distributions resulting from the variation of different parameters were quantified and compared with those from experiments.

1. Introduction

Coating systems provide enabling technologies that have enhanced productivity for a wide variety of applications. Hard coatings are a class of coating that has been developed as a surface engineering enhancement solution for cutting tools, dies, drills, and other tribological applications. All of these applications rely on the fact that the coatings are extremely hard, abrasion-resistant, and/or provide low-friction surfaces. Most hard coatings are ceramic compounds such as carbides, nitrides, ceramic alloys, cermets, and metastable materials such as diamond and cubic boron nitride. Their properties and environmental resistance depend on composition, stoichiometry, impurities, microstructure, and texture. To effectively design coating systems for specific applications, it is necessary to know the chemical, mechanical, and tribological properties of the coatings.

To a large extent, adhesion at the coating-substrate interface and toughness of the coating itself determines the durability of hard coating systems. Loss of adhesion at the coating-substrate interface leads to premature failure of otherwise wear resistant and tough coatings. There have been many investigations of failure properties of coatings using indentation [Begley and Hutchinson 1998; Rabiei et al. 1999]. Investigations have measured the adhesion of brittle films on a ductile substrate [Li and Bhushan 1998] and have observed preferred pathways for local cracking and separation in thermal spray coatings [Nekkanty and Walter 2004]. Li and Bhushan [1998] have used indentation techniques to measure the fracture toughness of thin, amorphous carbon films. Previous work by the authors presented the results of Vickers indentation experiments carried out on four different boron carbide/diamond-like carbon (DLC) composition coatings that were sputter deposited onto 52100 steel disks [Nekkanty and Walter 2004]. Although the indentation depths for these experiments ranged from less than 10% of the coating thickness to many times more than the coating thickness, qualitative comparisons of coating toughness were made.

Keywords: thin film coatings, cohesive zone finite element modeling, tensile cracking, intercrack spacing.

There have been numerous investigations to explore indentation coating failure using numerical methods. Begley et al. [2000] analyzed a wedge impression test for measuring interface toughness between films and substrates using numerical methods. Chen et al. [2005] recently developed numerical methods to explore the mechanics of indentation-induced lateral cracking. Based on finite element analysis (FEA) of spherical indentation of a thin hard film deposited on a soft substrate, Sriram et al. [2003] have carried out studies to understand the mechanics of film fracture. Theoretical issues surrounding the extraction of elastic and plastic properties from indentation load versus displacement data have also advanced; however, there are still a number of ambiguities surrounding actual physical processes involving indentation of such small volumes (for example, [Brotzen 1994; VanLandingham 2003]). Equipment calibration also becomes critical at such small displacements and loads.

Scratch testing is a widely used technique for evaluating the adhesion of thin, hard coatings. Scratch testing is useful to compare the adherence of similar coating-substrate systems; however, it fails to *quantify* parameters such as interfacial strength between the coating and the substrate and cohesive strength of the coating. A novel method for evaluating adhesion strength was proposed by Agrawal and Raj [1989]. This tensile cracking approach evaluates both the cohesive strength of the coating and the interfacial adhesion strength between the coating and the substrate. The approach is based on subjecting a brittle coating on a ductile substrate to tension and thereby propagating coating cracks that are oriented transverse to the tensile direction. A micrograph showing transverse cracks in a tungsten carbide/DLC (WC-DLC) coating on a stainless steel tensile specimen is shown in Figure 1. The crack density increases with substrate tension until the crack spacing reaches a saturation value when it is no longer influenced by the increase in substrate tension. The model relates $\hat{\tau}$, the interfacial shear strength between the coating and the substrate to $\hat{\sigma}$, the tensile fracture strength of the film, $\hat{\lambda}$, the characteristic saturation crack spacing, and δ, the coating thickness [Agrawal and Raj 1989] as

$$\hat{\tau} = \frac{\pi \delta \hat{\sigma}}{\hat{\lambda}}. \tag{1}$$

For a highly elastic coating, the tensile strength of the coating, $\hat{\sigma}$ can be written as

$$\hat{\sigma} = E \varepsilon_f, \tag{2}$$

where E is the modulus of elasticity of the coating and ε_f is the strain corresponding to the onset of cracking in the coating.

Agrawal and Raj [1989] proposed the full sine wave function shown in Figure 2a for approximating the interfacial shear stress. This approximation results in zero interfacial shear stress values at the mid point and at both ends of the intercrack spacing in the coating. Other research groups have asserted that, as shown in Figure 2b, the interfacial shear stress should have its maximum value located at each end of the intercrack spacing and be zero at the midpoint of the intercrack spacing in the coating [Wojciechowski and Mendolia 1989; Yanaka et al. 1998; Chen et al. 1999; 2000]. The recent analytical work of Yanaka et al. [1998] and Wojciechowski and Mendolia [1989], and the experiments and FEA of Chen et al. [1999; 2000], indicate that the interfacial shear stress distribution is best approximated by a distribution like the one shown in Figure 2b. The applicability of these two different shear stress distributions may be related to how the crack spacing compares to the coating thickness.
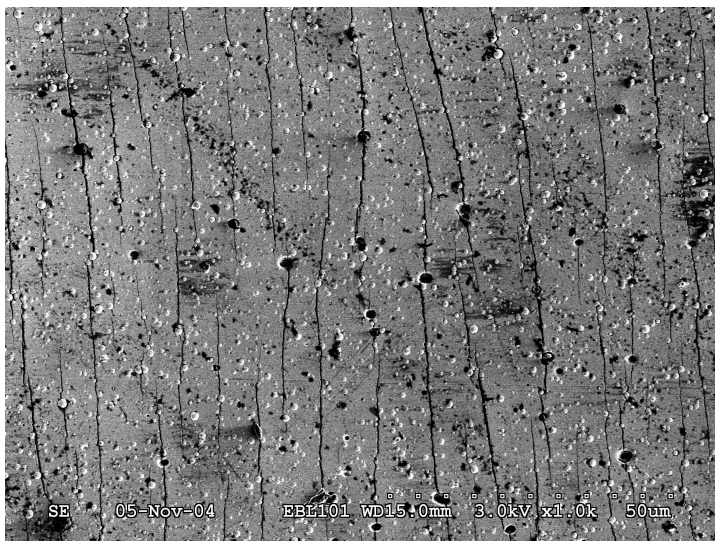
Figure 1. WC-DLC coating pulled to 4% strain resulting in longitudinal cracks. Tensile direction is perpendicular (horizontal in the figure) to the longitudinal cracks.
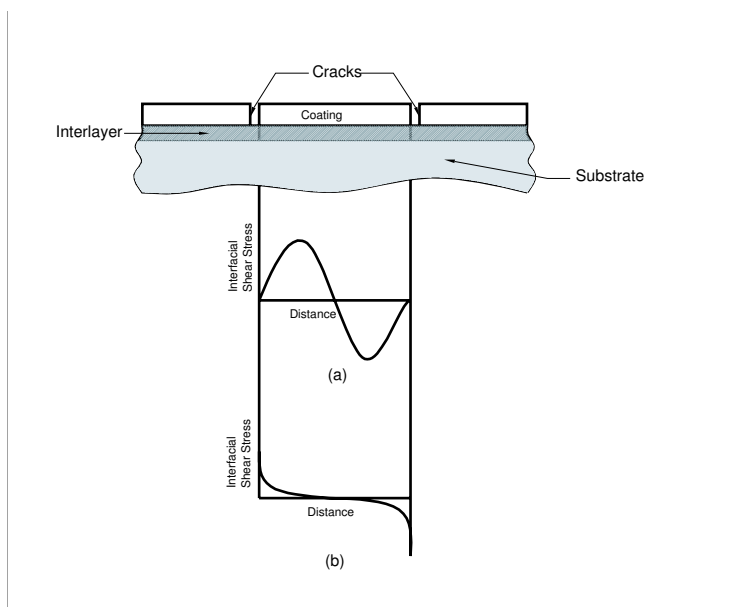
Figure 2. Two different theories predicting the distribution of interfacial shear stresses along the coating-interlayer interface between two cracks when the coating-interlayer-substrate system is subject to tensile loads: (a) sinusoidal distribution with zero stress at the endpoints [Agrawal and Raj 1989], and (b) maximum stress at the endpoints [Chen et al. 2000; Yanaka et al. 1998; Wojciechowski and Mendolia 1989].

The previous work with finite element analysis of tensile cracking assumes preexisting cracks by introducing fine notches in the model [Wojciechowski and Mendolia 1989; Yanaka et al. 1998; Chen et al. 1999; 2000; Krishnamurthy and Reimanis 2005]. Few researchers have developed finite element models which can simulate the formation and propagation of tensile cracks and thus predict coating performance. The present work uses cohesive zone elements to model crack development in the coating. After calibration with simple tensile cracking experiments, the finite element model could be used to predict the behavior of the coating-substrate system for the more complex loadings associated with actual applications. The next section of this paper describes the finite element model and the various physical and numerical parameters. The model is based on tensile cracking experiments that were carried out with WC-DLC coatings on 310 stainless steel substrates. The third section presents results for varying model parameters, and the final section then discusses the resulting simulated tensile cracking behavior.

2. Finite element model description

An idealization of the coating system that was modeled is shown in Figure 3a. Figure 3b shows the magnified view of the coating showing where cohesive elements were placed. The ABAQUS 6.5.1 commercial FEA package was used for all the modeling. As indicated above, the model was loosely based on tensile cracking experiments with WC-DLC coatings. The coating was $1.3\,\mu$m thick and was assumed to be homogeneous, isotropic, and perfectly elastic. The 310 stainless steel substrate followed an elastic-plastic material model with linear strain hardening.

The substrate thickness was 230 times the coating thickness. A $1.3\,\mu$m thick elastic-plastic titanium interlayer was present between the coating and substrate. Base values for the substrate properties were obtained from in-house experiments. Base values for the coating modulus and interlayer properties, henceforth referred to as the reference case, were obtained from [Voevodin et al. 1999] and www.matweb.com, respectively. The coating is assumed to be homogeneous along the thickness. The material properties for the substrate, coating, and interlayer are provided in Table 1. Four-node (QUAD4) plane strain elements were used for the analysis. As shown in Figure 3, symmetry boundary conditions were applied along the bottom of the model, and displacements were applied at the right and left edges. Displacements were specified at the edge nodes of the substrate and interlayer but not on the coating. The maximum displacement values were such that the strain in the direction of the loading was 4%. The final 4% strain value was chosen to be consistent with experiments.

Cohesive zone finite elements were placed through the thickness of the coating. These bilinear elements are available in the standard ABAQUS element library. The cohesive behavior assumes a linear elastic traction separation law prior to damage and a linear damage evolution based on energy dissipated due to failure, G_C. The input parameters for the cohesive elements are further described below. The layout of these elements is shown in Figure 3b. In the middle of the coating the distance between each row of cohesive zone elements is $1\,\mu$m. Away from the middle of the model, the spacing was increased to $10\,\mu$m. In this way, computational expense was reduced while focusing on a region that is far away from any edge effects. The interface is assumed to be perfectly bonded, and therefore there are no cohesive elements along the interface. This assumption is based on industry experience with state of the art PVD thin film coatings. In addition, Wang et al. [1998] have predicted that the interface toughness is greater than $150\,\mathrm{J/m^2}$, while the film toughness is approximately $30\,\mathrm{J/m^2}$ for DLC films on steel substrates.
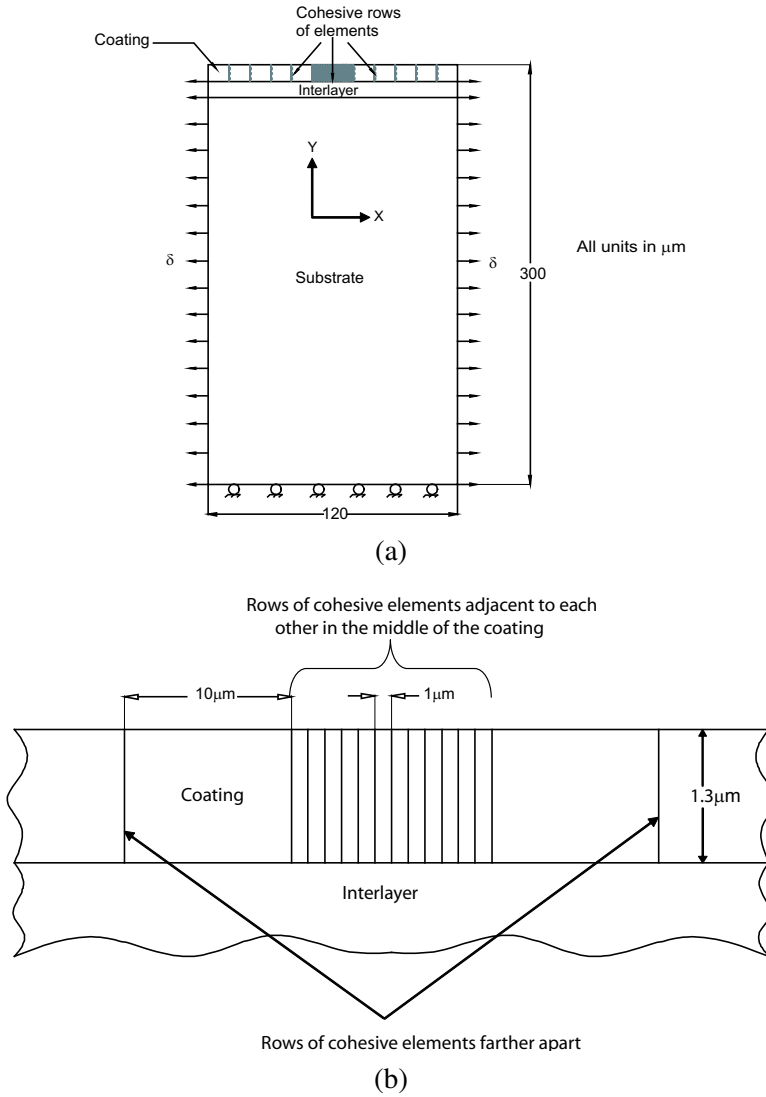
Figure 3. (a) Schematic of the FE model (not to scale); (b) illustration of cohesive zones in the coating (magnified view of (a)).

As shown in Figure 4, the response of the cohesive zone element is determined by specifying K, the loading slope or cohesive stiffness, σ_C, the critical normal stress, and G_C, the area under the traction versus displacement curve. The area under the traction versus displacement curve is called G_C because it is a measure of the critical energy release rate. Values for the cohesive zone element parameters are provided in Table 1. The critical normal stress values were estimated based on experiments with acoustic emission [Nekkanty and Walter 2006]. From experiments, the strain corresponding to the onset of cracking was estimated to be 1.2%. The critical normal stress, σ_C, can then be obtained from Equation (2). Similar strain values were also observed by Wang et al. [1998]. The baseline G_C values used in
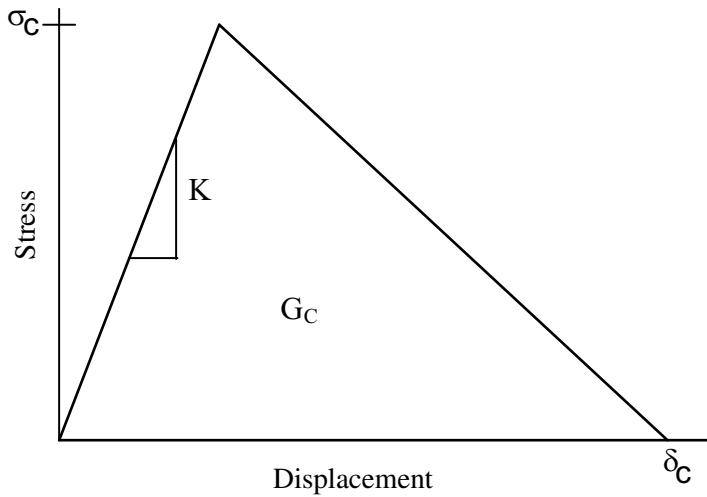
Figure 4. Bilinear law followed by the cohesive elements used in the study. Cohesive elements have a stiffness K and fail when the critical stresses in the elements reach beyond the critical stress σ_C.

this study were consistent with those predicted by Wang et al. [1998]. The cohesive stiffness was held constant for all cohesive zone elements.

Although at a given location in the coating the cohesive parameters were kept the same for all the coating through-thickness lines of cohesive zone elements, the σ_C and G_C parameters were allowed to vary along the x-direction. The different σ_C values were obtained by using MATLAB's random number generator to generate uniformly distributed values in a prescribed range. The range of variation for σ_C was ±75 MPa. The critical separation (δ_C, in Figure 4) was held constant, and therefore the range of variation for G_C was 32-37 J/m². The random assignment of different parameter values to different cohesive zone elements served the following two purposes: (a) it simulated the natural, statistical variation of the coating's cohesive strength, and (b) the different values of critical stresses in different cohesive zones ensured that not all the cohesive zone elements failed together when the critical tensile load was reached.

The modeling of progressive damage involves softening of the material response, which leads to convergence difficulties in an implicit solution procedure. To overcome such convergence problems, ABAQUS/Standard implements a viscous regularization parameter. This parameter regularizes the traction separation laws by permitting stresses to be just outside the limits set by the traction separation law. Using a small value for the viscosity regularization parameter improves the rate of convergence of the model in the softening regime and does not alter the sequence of cracking. Detailed discussion of this parameter can be found in [ABAQUS 2005; Alfano and Crisfield 2001]. The parameter was kept the same for all the cohesive zone elements. By trial and error, the smallest value that still produced converged solutions was used. The solution was carried out using implicit analysis and converged in approximately 550 total iterations. Up to the point where cohesive elements would start failing, the stresses in the coating were found to be the same in the models without and with cohesive elements.

This indicates that the inclusion of the cohesive elements was not altering the stress state before damage initiation.

The model was also checked for mesh convergence. The original mesh scheme described above (5 elements between two neighboring cohesive elements in the middle of the coating, and 9 elements along the thickness of the coating) was compared with two other mesh schemes: a coarser mesh containing 3 elements between two neighboring cohesive elements in the middle of the coating and 5 elements along the thickness of the coating, and a refined mesh containing 8 elements between two neighboring cohesive elements in the middle of the coating and 13 elements along the thickness of the coating. Figure 5 shows the horizontal-direction normal stress along the surface of the coating, and plotted for a region with higher cohesive element density. The three different mesh schemes are shown at 2% strain. From Figure 5, since there is little difference between the original and refined meshes, it is assumed that mesh convergence was achieved with the original mesh.

3. Results

In order to explore the effect of various parameters on the model response, one set of parameters was designated as the reference case (see Table 1). The subsequent studies were variations on the reference case. The next two subsections discuss the stress distributions in the reference case and the effect of variation of different parameters with respect to the reference case.

		Reference case	Mod. #1	Mod. #2	Mod. #3	Mod. #4
Coating	Modulus (GPa)	200	300	200	200	200
	Poisson ratio	0.3	0.3	0.3	0.3	0.3
Substrate properties	Modulus (GPa)	200	200	200	200	200
	Poisson ratio	0.2	0.2	0.2	0.2	0.2
	Yield strength (MPa)	200	200	200	200	200
	Tangent modulus of plastic region	2000	2000	2000	2000	2000
Interlayer properties	Modulus (GPa)	110	110	110	110	110
	Poisson Ratio	0.3	0.3	0.3	0.3	0.3
	Yield strength (MPa)	140	140	140	140	140
	Strain hardening slope (MPa)	720	720	1440	360	720
Cohesive properties	Critical stress (σ_C)	2500–2650	2500–2650	2500–2650	2500–2650	1500-1650
	G_C (J/m^2)	32–37	32–37	32–37	32–37	32–37

Table 1. Coating, interlayer, and substrate properties used for the different simulations.
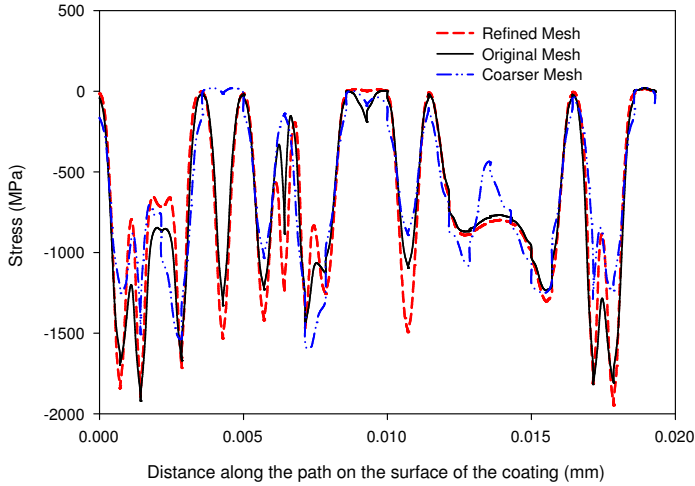
Figure 5. Horizontal-direction normal stress profiles at 2% strain along the surface of the coating for 3 different mesh schemes.

3.1. *Stress distributions.* For the reference case, when the normal stress in the tensile direction (σ_{xx}) in the coating exceeds the smallest random σ_C value, the first crack(s) appear. The tractions on the newly formed crack faces go to zero, and therefore the coating stresses are redistributed. An example of two σ_{xx} surface stress contours between two cracks which are 20 μm apart is shown in Figure 6. Since the σ_{xx} surface stress is zero at the cracks, both edges of the plot show zero stress. For the ith load increment,
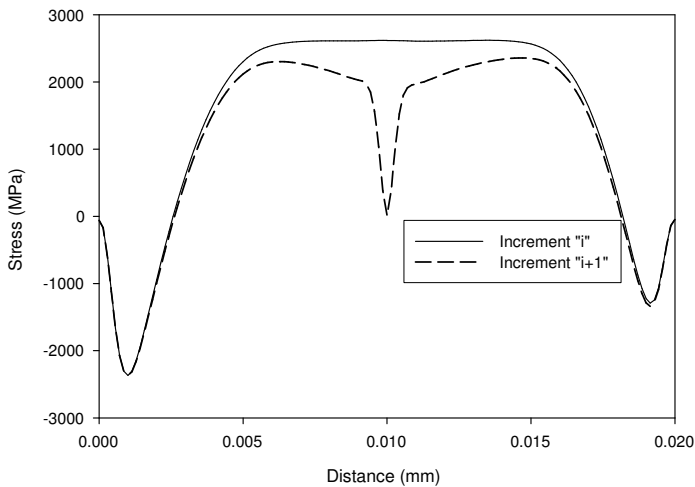
Figure 6. Evolution of tensile stresses between two cracks 20 microns apart with the increase in load.
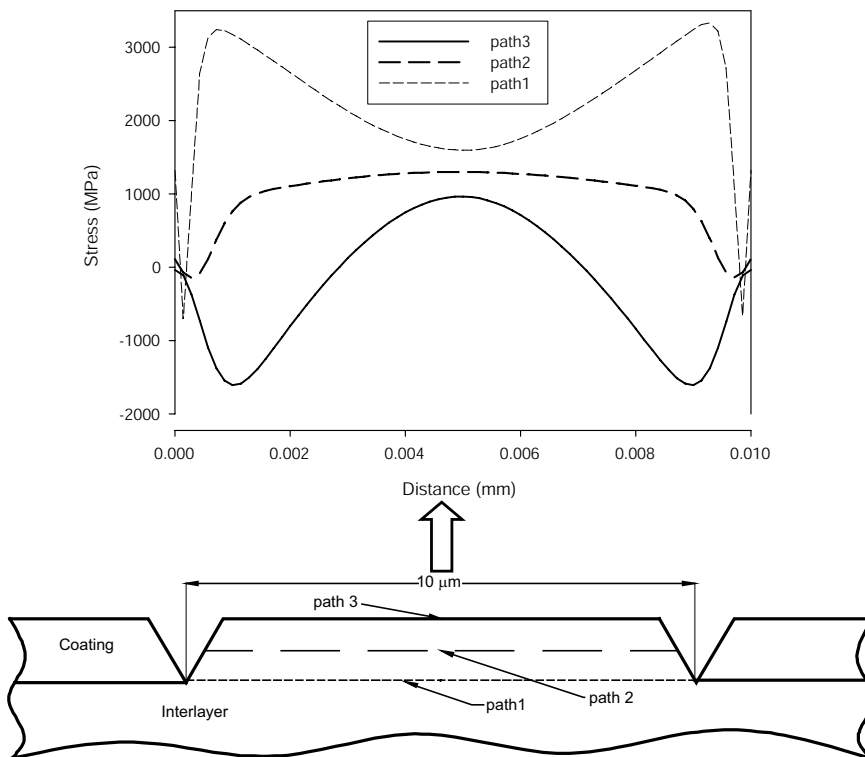
Figure 7. Normal stress distribution along paths in the coating between two cracks 10 microns apart.

the stress is still uniform in the middle region between the two cracks. In the $i + 1'$ increment the stress in the middle of the region of interest has exceeded the critical value for one of the cohesive zone elements, a new crack is generated, and the σ_{xx} surface stresses go towards zero. This crack progression is consistent with the shear lag models for tensile cracking [Agrawal and Raj 1989; Wojciechowski and Mendolia 1989; Yanaka et al. 1998; Chen et al. 1999; 2000].

From shear lag assumptions and from the above description of the contours in Figure 6, one would expect the cracks always to form at the midpoint between two adjacent cracks. However, this expectation is based on the assumption that the stress profile in Figure 6 is unchanged through the thickness of the coating. Uniform stresses along the thickness of the coating are also an underlying assumption in the analytical models referred to above [Agrawal and Raj 1989; Wojciechowski and Mendolia 1989; Yanaka et al. 1998; Chen et al. 1999; 2000]. It was found that the stresses are not uniform through the coating thickness. Since one side of the coating is free and the other side is bound to the interlayer, stresses should vary through the thickness of the coating. The crack formed at the midpoint in Figure 6 because of the particular combination of geometric and materials parameters.

In Figure 7, for the region between two cracks that are $10 \, \mu$m apart (there are no cohesive elements between these cracks) the σ_{xx} stress profiles are plotted for paths at different coating depths. The stress
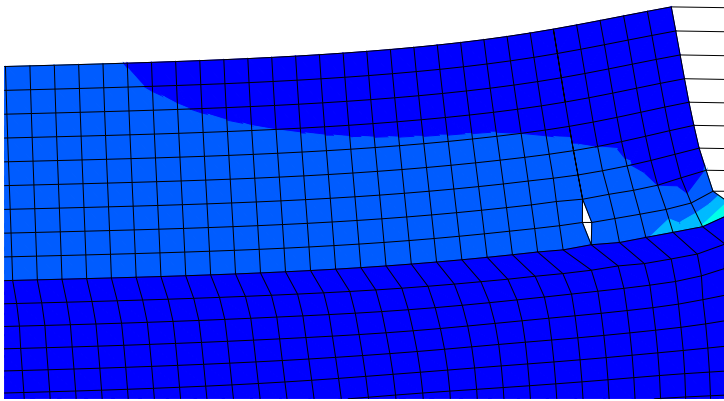
Figure 8. Crack in the coating originating from the interface.
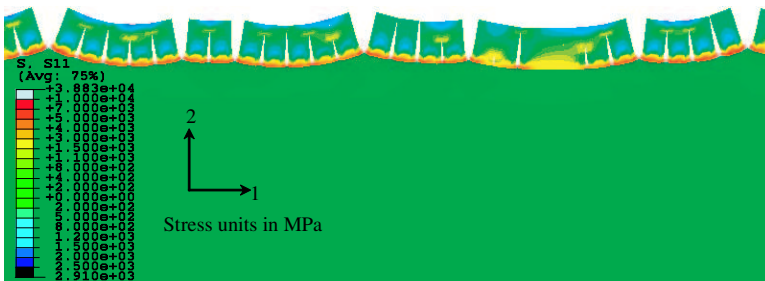
(a)
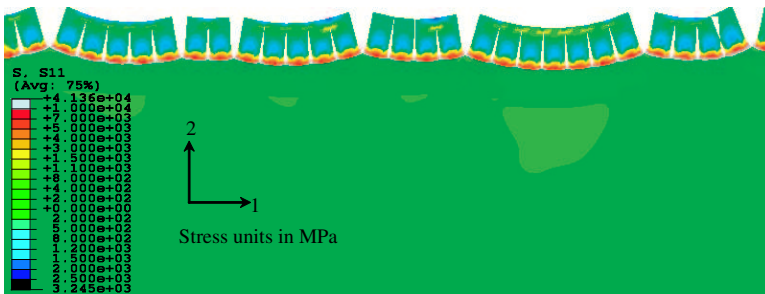
(b)

Figure 9. Cracks in the coating for reference model: (a) 2.5% strain, and (b) 4% strain. Notice the crack arrest.

profiles are not at all self-similar, and the location of the maximum σ_{xx} is not always at the midpoint between two adjacent cracks. In particular, the highest σ_{xx} stresses are found close to the interface and close to the existing cracks. Figure 7 also serves to highlight that near-crack stresses along the surface of the coating are compressive, and near-crack stresses near the interface are tensile. All stresses become tensile as one approaches the midpoint of the region. A similar stress distribution was observed by Krishnamurthy and Reimanis [2005].

As shown in Figure 8, the internal stresses and boundary conditions on an unbroken coating segment are such that the coating undergoes significant bending. The bending of the coating results in compressive near-crack stresses close to the surface of the coating. This stress distribution has important implications for crack propagation, with the high tensile near-crack stresses close to the interface suggesting that the cracks will originate from the interface. Indeed, the tensile cracking experiments performed by Krishnamurthy and Reimanis [2005] indicated that cracks may be originating from the interface.

The near-crack compressive stresses that exist closer to the surface of the coating will cause cracks originating from the interface to be arrested. Figure 9 shows a longer portion of the cracked coating for 2.5% and 4% overall strain, respectively. Figure 9 shows that, although multiple cracks originating from the interface were present at 2.5% strain, there was little or no continued crack propagation towards the surface even after 4% strain. If the coating is examined from the top and in the direction of the loading, the number of cracks reaching the surface becomes constant at higher strain levels. In other words the inter-crack spacing has saturated.

3.2. *Parameter study.* As shown in Table 1, the first modification of the reference case was increasing the modulus of the coating. All other material and cohesive parameters were kept the same. The higher coating modulus resulted in higher stresses at lower overall strains and, as expected, the fracture strain (the strain at which the first crack appears) decreased. Furthermore, as a result of the higher stresses in the coating, it can be seen from Figure 10a that more cracks have progressed from the interface to the surface of the coating.

The second modification to the reference case model was made by increasing the slope of the tangent modulus for the plastic region of the interlayer. This essentially increased the strain hardening of the interlayer. It can be seen in Figure 10b that compared to the reference case, more cracks have progressed from the interface to the surface of the coating. This results from the higher stresses in the interlayer for the same amount of strain as compared to the reference case. With a less deformable interlayer, the unbroken coating segment does not bend as much and therefore the near-crack compressive stresses close to the surface of the coating are diminished. As a result, cracks can more readily propagate to the surface.

A third modification to the reference model was made by decreasing the slope of the tangent modulus for the plastic region of the interlayer. This change has the overall effect of making the interlayer more deformable. The contour plot in Figure 10c shows that there is more curvature of the segments and the cracks have larger openings. The curvature of the coating increases due to the increase in the softening of the interlayer. The increase in the curvature results in an increase of the compressive stresses near the surface of the coating. Consequently, there are fewer cracks progressing to the surface. Also, there is an increase in the curvature of the interface as well. This leads to the higher tensile stresses near the interface, and as a result, more cracks originate from the interface compared to the reference case. This can be seen in Figure 11 where σ_{xx} stress profiles between two cracks are plotted at the surface of the coating and near the interface (paths 3 and 1 of Figure 7) for the two different interlayer cases.

For the last modification of the reference case, the σ_C values of all the cohesive zone elements were decreased by 1000 MPa compared to the reference case while keeping G_C the same. Decreasing σ_C while keeping G_C constant essentially decreases the softening slope of the cohesive zone element and, hence, the critical separation (δ_C, in Figure 4) increases. These changes result in a decrease in the fracture strain compared to the reference case. When compared with the reference case, at 2% strain, Figures 12a
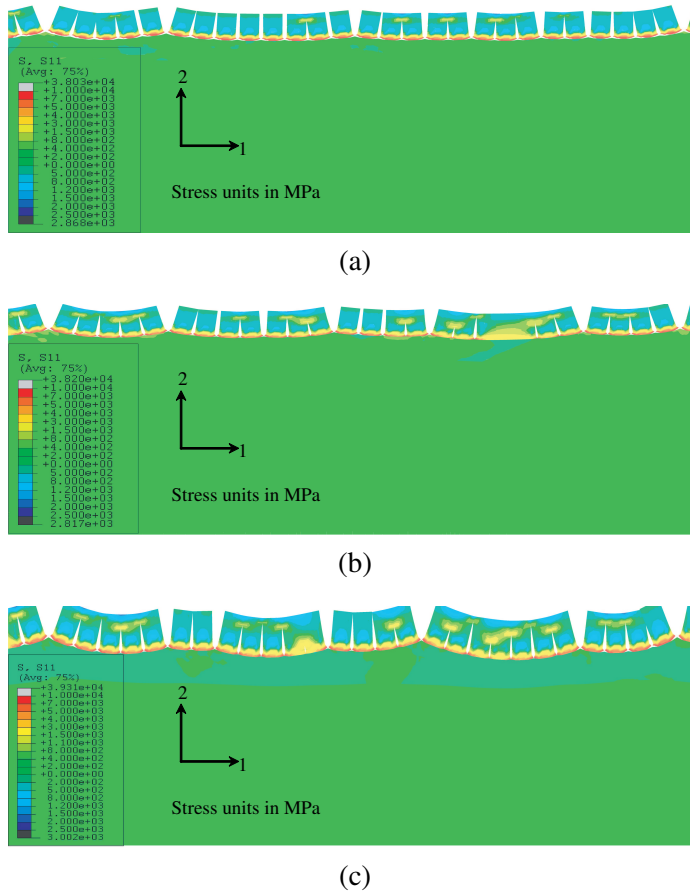
(a)

(b)

(c)

Figure 10. Change in cracks from reference model due to: (a) increase in coating modulus; (b) increase in tangent modulus slope in interlayer; and (c) decrease in tangent modulus slope in interlayer. All images correspond to 2.5% strain.

and 12b show that the decreased σ_C results in more cracks being generated. It could be argued that if the reference case coating-substrate system were pulled to higher strains, then more cracks would propagate to the surface. However, as will be discussed in the next section, there are assumptions with the two-dimensional model that need to be taken into account before making such an argument.

4. Discussion

The above parameter study indicates that cracking in the coating is sensitive to the material properties of the coating and interlayer and also to the cohesive zone element parameters. The model also demonstrates surface level crack saturation which means that no new cracks will appear on the surface with increasing tensile strain. Shear lag analysis of tensile cracking that includes the assumption of uniform through-thickness stresses predicts that the crack spacing will saturate [Agrawal and Raj 1989; Wojciechowski and Mendolia 1989; Yanaka et al. 1998; Chen et al. 1999; 2000]. The current simulations indicate that

(a)

(b)
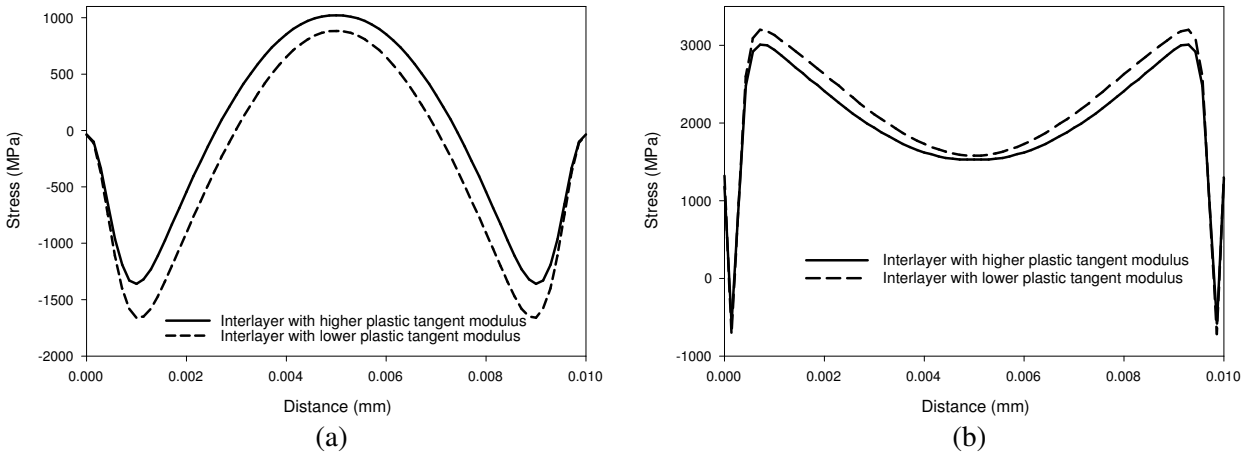
Figure 11. Comparison of σ_{xx} stresses between two cracks $10\,\mu$m apart for two interlayer cases: (a) stresses at the surface of the coating, and (b) stresses near the coating-interlayer interface.

(a)

(b)
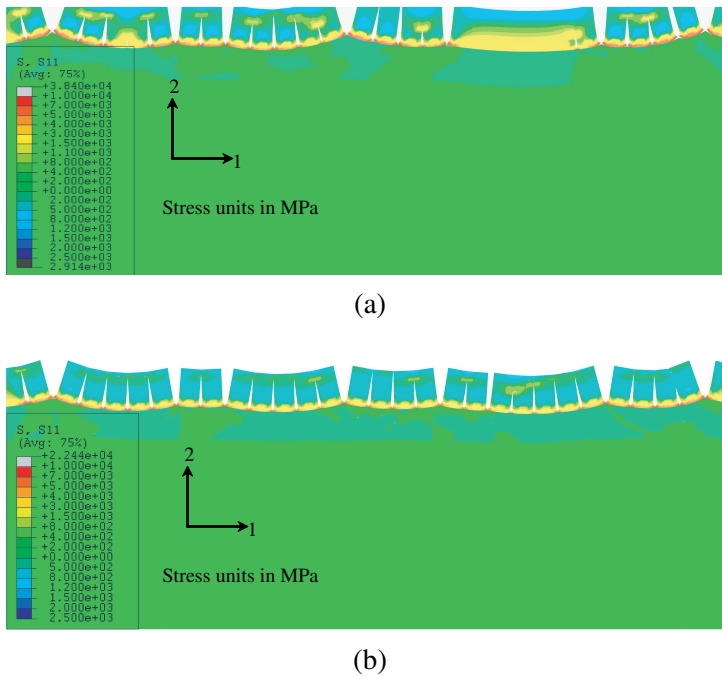
Figure 12. Differences in the formation of cracks for 2% strain: (a) reference case, and (b) decreased σ_C.
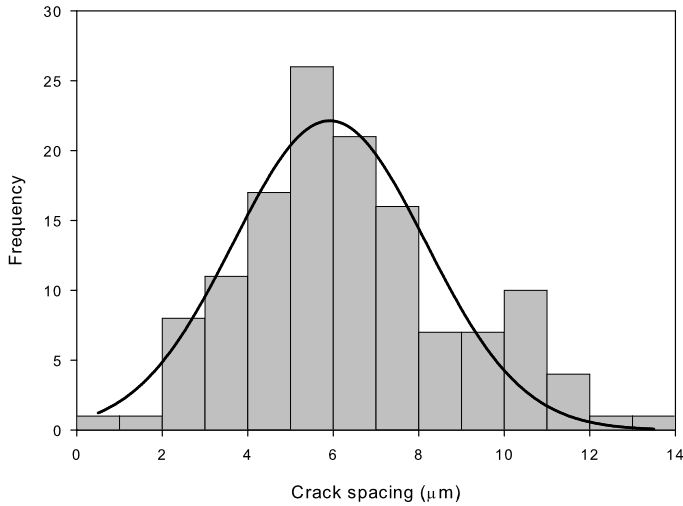
Figure 13. Distribution of intercrack spacing for WC/DLC coating pulled to 4% strain.

although the crack saturation can exist at the coating surface level, there may be subsurface cracks that have not propagated all the way to the surface.

In the current model, further straining of the coating substrate system would eventually cause all cracks to propagate to the surface. However, this situation is the result of having a two-dimensional model. In reality, the stress state is no longer uniaxial at very high strains. The triaxial nature of the stress state in the plastic region causes slant cracks at approximately 45° to the existing transverse cracks appear in the coating [Chen et al. 1999]. The existence of these slant cracks is a fair indication that strains are beyond the surface saturation strains and that the stress state is no longer uniaxial. Without a three-dimensional model, slant cracks cannot be modeled. Experimental results for the WC-DLC system indicated that slant crack began at approximately 4.5% strain. For this reason, the current simulations were run to 4% strain.

The distribution of the crack spacing for the cracks in Figure 1 is given in Figure 13. The mean value of the crack spacing is $6.0\,\mu$m with a standard deviation of 2.4. A normal distribution with the given mean and standard deviation values is provided in the same plot. The distributions of crack spacing from the numerical simulations described in Section 3.2 are shown in Figures 14a–d. Only cracks which have propagated all the way to the surface of the coating are included in the distribution plots. As seen from Figure 14a, the mean crack spacing for the reference case is less than that from the experiments. Also, as seen in Figures 14b and 14d, with the increase in coating modulus and the decrease in σ_C, respectively, the distribution of crack spacing is unrealistically small since almost every cohesive element has failed. As expected, Figure 14c shows that the mean crack spacing for the case of increase in tangent modulus slope of the interlayer is less than that of the reference case. It must be pointed that the distributions in Figure 14 are based on a coating span of only $40\,\mu$m as compared to the coating span of $130\,\mu$m used for the experimental results shown in Figure 13.
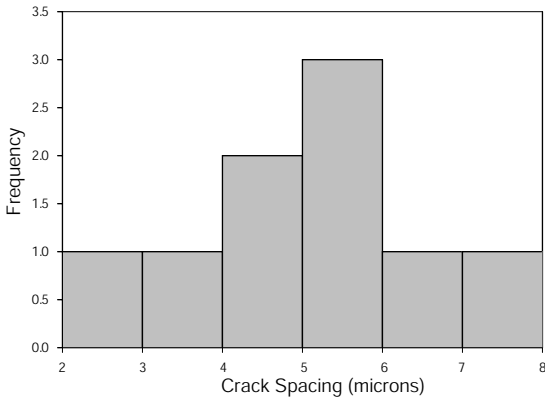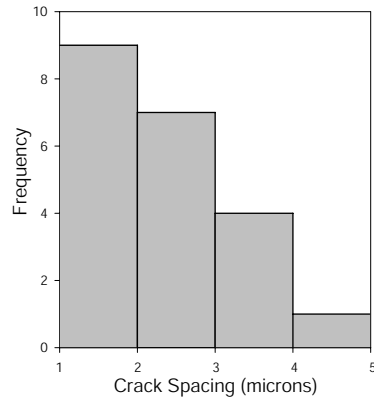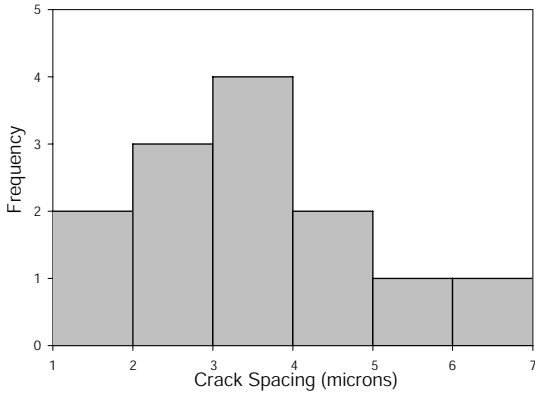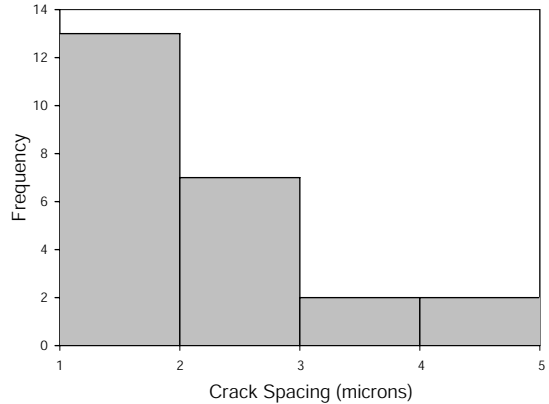
Figure 14. Distribution of intercrack spacing observed in numerical simulation: (a) reference case; (b) increase in coating modulus; (c) increase in tangent modulus slope in interlayer; and (d) decrease in σ_C of cohesive elements.

In the numerical simulations discussed above, the coatings were assumed to be isotropic, homogeneous, and free of defects. However, as seen in Figure 1, pits of various sizes are present on the surface of the coating. Although many of the cracks go through pits, there are also pits without any cracks. More detailed investigation is required to confirm whether or not pits are assisting crack propagation. Microstructural observations would need to be performed in order to determine if there are any additional microstructural inhomogeneities that affect crack spacing.

Investigation of residual stresses was undertaken with compressive residual stresses of 1 GPa as uniform prestresses in the coating. It was observed that inclusion of compressive residual stresses caused the fracture strain (the strain at which the first crack appears) to increase from 1.2% to 1.7%. At lower

strain values, for example, 2%, there are fewer cracks compared to same strain value in the reference case. However at large strain values ($> 4\%$), results look very similar to the reference case results.

5. Summary

A two-dimensional finite element model was created to simulate the response of a coating-interlayer-substrate system to in-plane uniaxial tension. Coating cracking was simulated with cohesive zone elements that followed a bilinear cohesive law. Some degree of randomness was introduced into the model through the assignment of random critical cohesive stresses. Due to the unsymmetrical boundary conditions at the top surface and coating-interlayer interface, bending occurred and introduced nonuniform stresses through the coating thickness. Thus coating cracks propagated from the interface and were often arrested near the surface of the coating by the presence of high compressive stresses. The effects of different coating modulus, tangent modulus for the interlayer hardening, and critical stress values (σ_C) of the cohesive zone elements were studied. The distribution of crack spacing for different parameter changes were quantified and compared to an experimental crack spacing distribution.

Due to the limitations of using a two-dimensional model, crack formation and propagation at high plastic strain values was not predicted accurately. Incorporating measured residual stresses into the model is necessary for more realistic simulations. The model has been shown to be sensitive to material and cohesive parameters and could thus be used to optimize coatings. The described tensile cracking experiment could be used to calibrate cohesive parameters for subsequent modeling of more complicating loading schemes.

References

[ABAQUS 2005] *ABAQUS 6.5 user manual*, Version 6.5, Hibbitt Karlsson Sorensen Inc., Pawtucket, RI, 2005.

[Agrawal and Raj 1989] D. C. Agrawal and R. Raj, "Measurement of the ultimate shear-strength of a metal ceramic interface", *Acta Metall.* **37**:4 (1989), 1265–1270.

[Alfano and Crisfield 2001] G. Alfano and M. A. Crisfield, "Finite element interface models for the delamination analysis of laminated composites: mechanical and computational issues", *Int. J. Numer. Methods Eng.* **50**:7 (2001), 1701–1736.

[Begley and Hutchinson 1998] M. R. Begley and J. W. Hutchinson, "The mechanics of size-dependent indentation", *J. Mech. Phys. Solids* **46**:10 (1998), 2049–2068.

[Begley et al. 2000] M. R. Begley, D. R. Mumm, A. G. Evans, and J. W. Hutchinson, "Analysis of a wedge impression test for measuring the interface toughness between films/coatings and ductile substrates", *Acta Mater.* **48**:12 (2000), 3211–3220.

[Brotzen 1994] F. R. Brotzen, "Mechanical testing of thin-films", *Int. Mater. Rev.* **39**:1 (1994), 24–45.

[Chen et al. 1999] B. F. Chen, J. Hwang, G. P. Yu, and J. H. Huang, "In situ observation of the cracking behavior of TiN coating on 304 stainless steel subjected to tensile strain", *Thin Solid Films* **352**:1-2 (1999), 173–178.

[Chen et al. 2000] B. F. Chen, J. Hwang, I. F. Chen, G. P. Yu, and J. H. Huang, "A tensile-film-cracking model for evaluating interfacial shear strength of elastic film on ductile substrate", *Surf. Coat. Technol.* **126**:2-3 (2000), 91–95.

[Chen et al. 2005] X. Chen, J. W. Hutchinson, and A. G. Evans, "The mechanics of indentation induced lateral cracking", *J. Am. Ceram. Soc.* **88**:5 (2005), 1233–1238.

[Krishnamurthy and Reimanis 2005] S. Krishnamurthy and I. Reimanis, "Multiple cracking in CrN and Cr2N films on brass", *Surf. Coat. Technol.* **192**:2-3 (2005), 291–298.

[Li and Bhushan 1998] X. D. Li and B. Bhushan, "Measurement of fracture toughness of ultra-thin amorphous carbon films", *Thin Solid Films* **315**:1-2 (1998), 214–221.

[Nekkanty and Walter 2004] S. Nekkanty and M. E. Walter, "Indentation damage to boron carbide-DLC coatings with different compositions", *Surf. Coat. Technol.* **183**:1 (2004), 1–9.

[Nekkanty and Walter 2006] S. Nekkanty and M. E. Walter, "Tensile cracking experiments with in situ acoustic emission", 2006.

[Rabiei et al. 1999] A. Rabiei, D. R. Mumm, J. W. Hutchinson, R. Schweinfest, M. Ruhle, and A. G. Evans, "Microstructure, deformation and cracking characteristics of thermal spray ferrous coatings", *Mater. Sci. Eng. A* **269**:1-2 (1999), 152–165.

[Sriram et al. 2003] K. Sriram, R. Narasimhan, and S. K. Biswas, "A numerical fracture analysis of indentation into thin hard films on soft substrates", *Eng. Fract. Mech.* **70**:10 (2003), 1323–1338.

[VanLandingham 2003] M. R. VanLandingham, "Review of instrumented indentation", *J. Res. Natl. Inst. Stand. Technol.* **108**:4 (2003), 249–265.

[Voevodin et al. 1999] A. A. Voevodin, J. P. O'Neill, and J. S. Zabinski, "Tribological performance and tribochemistry of nanocrystalline WC/amorphous diamond-like carbon composites", *Thin Solid Films* **342**:1-2 (1999), 194–200.

[Wang et al. 1998] J. S. Wang, Y. Sugimura, A. G. Evans, and W. K. Tredway, "The mechanical performance of DLC films on steel substrates", *Thin Solid Films* **325**:1-2 (1998), 163–174.

[Wojciechowski and Mendolia 1989] P. H. Wojciechowski and M. S. Mendolia, "On the multiple fracture of low-elongation thin-films deposited on high-elongation substrates", *J. Vac. Sci. Technol. A* **7**:3 (1989), 1282–1288.

[Yanaka et al. 1998] M. Yanaka, Y. Tsukahara, N. Nakaso, and N. Takeda, "Cracking phenomena of brittle films in nanostructure composites analysed by a modified shear lag model with residual strain", *J. Mater. Sci.* **33**:8 (1998), 2111–2119.

SRIKANT NEKKANTY: nekkanty.1@osu.edu
Department of Industrial, Welding and Systems Engineering, Ohio State University, Columbus, OH 43210, United States

MARK E. WALTER: walter.80@osu.edu
Department of Mechanical Engineering, E331 Scott Laboratory, Ohio State University, 201 W. 19th Avenue, Columbus, OH 43210, United States

RAJIV SHIVPURI: shivpuri.1@osu.edu
Department of Industrial, Welding and Systems Engineering, Ohio State University, Columbus, OH 43210, United States

OPTIMIZATION OF STIFFENED PANELS CONSIDERING GEOMETRIC NONLINEARITY

PEYMAN KHOSRAVI, RAMIN SEDAGHATI AND RAJAMOHAN GANESAN

In this study, an optimality criterion is presented for thickness optimization of plate structures with geometric nonlinearity. The optimization problem considers the thickness of each element of the finite element mesh as a design variable and aims to maximize the load-carrying capacity of the structure subject to constant total volume. The result of the thickness optimization of a nonstiffened panel is then used for locating the potential places to add the stiffeners. It is shown that the load-carrying capacity of the original panel may be improved significantly while having the same volume of material. Application of the method is illustrated by numerical examples.

1. Introduction

Structural optimization can be used to improve a design by changing the geometrical properties of the structure, considering a set of design constraints. In structural optimization, the thickness, shape, or topology of the structure is iteratively changed until an optimal design is achieved [Bendsøe 1989; Bendsøe and Mota Soares 1993; Rozvany 1997; Maute et al. 1998; Bendsøe and Sigmund 1999; 2003; Lógó and Ghaemi 2002]. Developing design optimization techniques that efficiently combine the iterative optimization process and iterative analysis of nonlinear structures is a challenging and complex task which has not yet received sufficient attention. Optimization based on nonlinear mathematical programming techniques involves many evaluations of the objective function and constraints at each optimization iteration before a new search direction and step size can be established. This makes the design optimization of nonlinear structures computationally very expensive, as nonlinear analysis by itself is a highly iterative process.

Optimality criterion methods may significantly reduce the time and cost of the optimization process in nonlinear structures. Optimality criteria could be in the form of intuitive criteria, such as fully stressed design (FS), simultaneous failure mode design (SFM), uniform strain energy density design (USED), constant internal force distribution design (CIFD), or mathematically defined equations, such as classical optimality criteria method (COC), dual optimality criteria method (DOC), and general optimality criteria method (GOC) [Lógó 2005].

Gallagher [1973] pointed out that the fully stressed design (FS) criterion is inadequate for minimum weight design of structures. Prager and Taylor [1968] showed that the optimum structure with uniform material properties and linear relation between the stiffness and volume has a uniform energy density distribution. A similar criterion was proposed by Venkayya et al. [1968; 1969] for discretized structures, stating that the average strain energy density is the same for all elements of the optimum structure. Later, Venkayya [1971] developed a more general form for the optimality criteria stating that the ratio of strain energy to strain energy capacity is constant for every member in the optimum structure.

Keywords: thickness optimization, optimality criterion, stiffened plates, geometric nonlinearity.

Berke [1971] proposed an algorithm to satisfy the optimality criteria, considering that if a criterion works for statically determinate structures, then it would converge in a few iterations for most indeterminate structures (in the same manner as the FSD criterion). Berke's work was extended to multiple constraints by Gellatly and Berke [1971; 1973] who proposed the envelope method for multiple displacement constraint structures. Nagtegaal [1973] directly used the displacement constraint equations to formulate an iteration scheme using the Lagrange multiplier. Berke and Khot [1974] proposed an intuitive iteration scheme for Lagrange multipliers. Khot et al. [1979] applied classical optimality criteria method for both stress and displacement constraints. For a more detailed literature survey on optimality criteria methods, the reader is referred to a recent paper by Lógó [2005].

The main focus of the present study is to find the optimum location of the ribs in stiffened panels. Layout optimization problems for rib reinforcement were considered almost two decades ago by Bendsøe and Kikuchi [1988]. An overview of the research in layout and topology optimization is given in the paper by Rozvany et al. [1995]. Stok and Mihelic [1996] presented a method to identify the rib location by performing thickness distribution. Chung and Lee [1997] employed a topology optimization technique to identify the size of the ribs for a predetermined rib layout. Lee et al. [2000] have used modal design sensitivity analysis for topology optimization of an automobile hood. Lam and Santhikumar [2003] developed a method to find the optimum locations of the ribs subject to design constraints using thickness optimization with the uniform strain energy density criterion. All of the above mentioned studies on the stiffened panels are based on linear analysis, whereas many plate and shell structures may display nonlinear behavior under applied loads.

In this study, first an optimality criterion, called uniform average of strain energy variation (UASEV), is developed for thickness optimization in the general case of the combination of membrane and bending deformations. It will be shown that the USED criterion (with strain energy density defined as the strain energy stored in unit volume) cannot be used for thickness optimization, unless the structure is in pure membrane or in pure bending mode. Subsequently, the result of the thickness optimization with the proposed criterion is used for locating the ribs on the original panel. It is shown that the load-carrying capacity of the original panel subject to design constraints may significantly be improved with the same volume of the material. Illustrated applications are also presented.

2. Optimality criterion for thickness optimization

In this section, an optimality criterion is developed for thickness optimization of plates and shells modeled by finite elements. In our study, the thickness of each element in the finite element mesh is considered as a design variable, and an optimization criterion is found subject to constant total volume (Figure 1).

We assume that a plate or shell structure with uniform material properties is modeled by N facet elements. This structure is analyzed under the conservative and proportional nodal force vector λR in which R is a constant reference nodal force vector, and λ is a load level factor which can be gradually increased until a design constraint (displacement, stress, or stability constraint) is violated. At this instant, λR is called the *load capacity* of this structure with respect to design constraints. The optimization problem is to find the optimum thickness t_i ($i = 1, \ldots, N$) for each element in order to maximize λ subject to constant total volume of the material (that is, $V = V_0$, where V is the total volume of the material.)
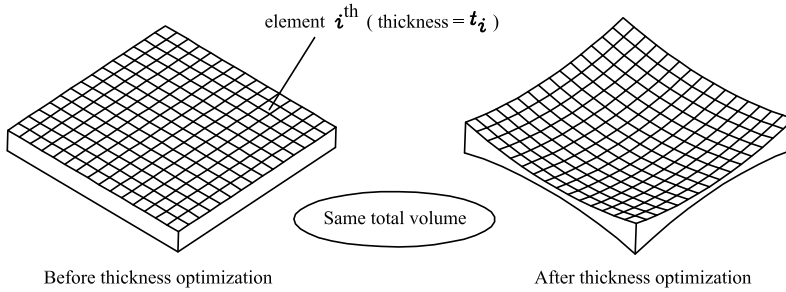
Figure 1. Concept of thickness optimization subject to constant volume.

The Lagrangian for this optimization problem is

$$L = -\lambda + \mu(V - V_0), \tag{1}$$

where μ is the Lagrange multiplier. The Karush–Kuhn–Tucker (KKT) conditions [Arora 1989] for minimization of L with respect to each design variable t_i results in

$$\frac{\partial L}{\partial t_i} = 0; \quad (i = 1, \ldots, N). \tag{2}$$

Thus

$$-\frac{\partial \lambda}{\partial t_i} + \mu \frac{\partial V}{\partial t_i} = 0; \quad (i = 1, \ldots, N) \tag{3}$$

or

$$-\frac{\partial \lambda}{\partial t_i} + \mu A_i = 0; \quad (i = 1, \ldots, N), \tag{4}$$

where A_i is the area of the ith element. Now we write the total potential energy of the structure, assuming that the load is conservative and proportional as

$$\Pi = \sum_{i=1}^{N} e_i - \lambda u^T R, \tag{5}$$

where u and λR are the nodal displacement vector in the global coordinate system and the vector of the applied loads, respectively, and e_i is the strain energy of the ith element. Considering Π_{opt} as the total potential energy associated with the optimum design, the equation $\Pi = \Pi_{opt}$ should also be satisfied for the optimum design. Taking the derivative from both sides of this equation with respect to each design variable t_i (noticing that u and λ are also functions of the design variable t_i) we have

$$\frac{\partial e_i}{\partial t_i} + \sum_{j=1}^{m} \frac{\partial \Pi}{\partial u_j} \frac{\partial u_j}{\partial t_i} + \frac{\partial \Pi}{\partial \lambda} \frac{\partial \lambda}{\partial t_i} = 0; \quad (i = 1, \ldots, N), \tag{6}$$

where m is the number of the nodal displacement components. From the principle of stationary total potential energy we have $\frac{\partial \Pi}{\partial u} = 0$, thus Equation (6) changes to

$$\frac{\partial e_i}{\partial t_i} + 0 - u^T R \frac{\partial \lambda}{\partial t_i} = 0, \tag{7}$$

in which $\frac{\partial \Pi}{\partial \lambda}$ has been substituted by $-u^T R$. Substituting for $\frac{\partial \lambda}{\partial t_i}$ from Equation (7) into Equation (4) results in

$$\frac{-1}{u^T R} \frac{\partial e_i}{\partial t_i} + \mu A_i = 0 \tag{8}$$

or

$$\frac{1}{A_i} \frac{\partial e_i}{\partial t_i} = \mu u^T R. \tag{9}$$

This equation (hereinafter called the uniform average of strain energy variation (UASEV) criterion), states that a design in which the value of $\tilde{e}_i = \frac{1}{A_i} \frac{\partial e_i}{\partial t_i}$ is the same for all elements is a candidate for optimality. It should be noted that since the second variation of the Lagrangian is not examined in this study, this optimality criterion is only an empirical local-optimality condition. Also, since this criterion is satisfied only at the final load (load capacity), it assumes monotonic structural behavior and excludes path dependency.

In the case that the structure is made of an isotropic material with the Poisson's ratio ν and the Young's modulus $E_\circ$, the strain energy of the ith element is computed as

$$e_i = \frac{1}{2} \int_{A_i} \left(\{\varepsilon_m^\circ\}^T D_i^{(1)} \{\varepsilon_m^\circ\} + \{\varepsilon_b^\circ\}^T D_i^{(2)} \{\varepsilon_b^\circ\} \right) dA_i, \tag{10}$$

where $D_i^{(1)}$ and $D_i^{(2)}$ are the membrane and flexural stiffness matrices at the location of the ith element with thickness t_i

$$D_i^{(1)} = \frac{E_\circ t_i}{1 - \nu^2} \begin{bmatrix} 1 & \nu & 0 \\ \nu & 1 & 0 \\ 0 & 0 & \frac{1-\nu}{2} \end{bmatrix}, \qquad D_i^{(2)} = \frac{E_\circ t_i^3}{12(1 - \nu^2)} \begin{bmatrix} 1 & \nu & 0 \\ \nu & 1 & 0 \\ 0 & 0 & \frac{1-\nu}{2} \end{bmatrix}, \tag{11}$$

and $\{\varepsilon_m^\circ\} = \{\varepsilon_x^\circ \varepsilon_y^\circ \gamma_{xy}^\circ\}^T$ and $\{\varepsilon_b^\circ\} = \{\kappa_x^\circ \kappa_y^\circ \kappa_{xy}^\circ\}^T$ are the membrane and flexural strains in the mid-surface of the ith element, respectively.

Now the average strain energy variation can be described as

$$\tilde{e}_i = \frac{1}{A_i} \frac{\partial e_i}{\partial t_i} = \frac{1}{2A_i} \int_{A_i} \left(\{\varepsilon_m^\circ\}^T \frac{D_i^{(1)}}{t_i} \{\varepsilon_m^\circ\} + \{\varepsilon_b^\circ\}^T \frac{3D_i^{(2)}}{t_i} \{\varepsilon_b^\circ\} \right) dA_i. \tag{12}$$

One can easily see that $\tilde{e}_i$ computed by Equation (12) in the general case of combination of membrane and bending deformations is different from the strain energy density, which is usually defined as $e_i / (t_i A_i)$:

$$\bar{e}_i = \frac{e_i}{t_i A_i} = \frac{1}{2A_i} \int_{A_i} \left(\{\varepsilon_m^\circ\}^T \frac{D_i^{(1)}}{t_i} \{\varepsilon_m^\circ\} + \{\varepsilon_b^\circ\}^T \frac{D_i^{(2)}}{t_i} \{\varepsilon_b^\circ\} \right) dA_i \tag{13}$$

As a result, thickness optimization of plates and shells using a uniform strain energy density criterion with the values computed by Equation (13) in the general case of the combination of membrane and

bending deformations is unjustified. However in case of pure membrane strain energy (that is, $\{\varepsilon_b^\circ\} = 0$), using USED criteria instead of UASEV leads to the same result (because in this case Equations (12) and (13) are equivalent). Also, in the case of the pure bending strain energy (that is, $\{\varepsilon_m^\circ\} = 0$) results are again the same, since based on Equations (12) and (13), uniform distribution of $\bar{e}_i$ and uniform distribution of $\tilde{e}_i$ in the case of $\{\varepsilon_m^\circ\} = 0$ are equivalent by a scale factor of 3.

Considering element thicknesses as the design variables is not the only possible approach in thickness optimization. One may instead consider nodal thicknesses as the design variables, which has the advantage of leading to a smooth thickness profile. However in that case, the related equations are more complicated, since each design variable is connected to more than one element. For example, $\partial V / \partial t_i$ is no longer equal to A_i when passing from Equation (3) to Equation (4), or $\partial e_i / \partial t_i$ in Equation (6) changes to the summation of the same term for all elements sharing the nodal thickness t_i. In Section 4 it is explained how using the proposed method with linear interpolation can lead to a smooth thickness profile as well.

3. Recurrence relation

In order to satisfy the UASEV criterion, a resizing algorithm has to be employed in the optimization process. First, we rewrite Equation (9) assuming that at the optimum design $\mu u^T R = 1/\Lambda$,

$$\tilde{e}_i = \frac{1}{A_i} \frac{\partial e_i}{\partial t_i} = \frac{1}{\Lambda}. \tag{14}$$

Thus

$$1 = \Lambda \tilde{e}_i. \tag{15}$$

A recurrence relation for resizing the thickness of each element may be written by multiplying both sides of Equation (15) by t_i and taking the rth root as

$$(t_i)_{\upsilon+1} = (t_i)_\upsilon (\Lambda \tilde{e}_i)_\upsilon^{1/r}, \tag{16}$$

where $\upsilon + 1$ and υ are the iteration numbers, and r is the step size parameter which can be changed by assigning appropriate value [Stok and Mihelic 1996; Lam and Santhikumar 2003]. The value of Λ at the optimal design may be found from Equation (15) by minimizing the sum of the squares of the residuals at iteration υ as

$$\text{Res}_\upsilon = \sum_{i=1}^N (1 - \Lambda \tilde{e}_i)^2. \tag{17}$$

Thus

$$\frac{d\,\text{Res}_\upsilon}{d\Lambda} = 0 \Rightarrow \Lambda = \left(\sum_{i=1}^N \tilde{e}_i \right) / \left(\sum_{i=1}^N \tilde{e}_i^2 \right). \tag{18}$$

Substituting Equation (18) into Equation (16) we finally obtain the recurrence relation

$$(t_i)_{\upsilon+1} = (t_i)_\upsilon \left(\left(\sum_{i=1}^N \tilde{e}_i \right) / \left(\sum_{i=1}^N \tilde{e}_i^2 \right) \tilde{e}_i \right)_\upsilon^{1/r}, \tag{19}$$

which is used to optimize the thickness of each element iteratively. In order to keep the total volume equal to constant V_0, after each iteration, all t_i are scaled by a scale factor β:

$$\beta = \frac{V_0}{V} = \frac{V_0}{\sum_{i=1}^{N} t_i A_i}. \tag{20}$$

The iterative process of thickness optimization may be stopped when the following condition is satisfied:

$$\Delta(\lambda R)_\upsilon \leq (\text{tol})\Delta(\lambda R)_1, \tag{21}$$

where $\Delta(\lambda R)_1$ and $\Delta(\lambda R)_\upsilon$ are the changes in the load capacity of the structure in the first and υth iterations respectively, and tol is usually chosen in the range of tol $\leq 10^{-2}$, depending on the accuracy required.

4. Methodology

After performing the thickness optimization, the optimal shape is still rough and should be smoothed by passing to nodal thicknesses. The thickness of the plate at each node is found by taking the average of the thicknesses of all elements connected to that node. Then, a smooth thickness profile may be created by linear interpolation using nodal thicknesses. Finally the regions where elements have higher thickness values are identified as potential rib locations.

In the next step, stiffeners with variable height according to the results found in the first step are added to the plate with constant thickness. The height of the ribs varies proportionally to the obtained thickness distribution, but not more than a maximum value considered in the design constraint. Finally, thicknesses of the plate and stiffeners are found such that the constant volume constraint is satisfied. The whole process may be repeated to find additional stiffeners.

As an example, Figure 2 shows how the potential locations for adding the stiffeners are found for a simple plate. Variation of the thickness after performing the thickness optimization is shown by thickness contours. Considering the cross sections of the plate at different locations, one can identify the locations of the local maximum thickness at each section. The lines which connect these points of local maximum thickness are called the lines of maximum thickness, and are selected as the potential locations for stiffeners. Any design constraint or limitation is also considered in locating the stiffeners. The locations and the directions of the sections are arbitrary, and usually they are selected by the designer in a way to perform the design with the least number of sections. Obviously, the final design may not be completely unique, and will somehow depend on the designer's point of view.

This method is similar to the one used by Stok and Mihelic [1996] and Lam and Santhikumar [2003], except that in their studies, the USED criterion was used instead of UASEV. As mentioned before, it is important to note that in the general case of the combination of membrane and bending deformations, using the USED criterion instead of UASEV is unjustified, and only in the case of pure membrane or pure bending behavior are the results the same.

In topology optimization a checkerboard pattern, which is an unnatural result with artificially high stiffness, may frequently occur [Díaz and Sigmund 1995; Jog and Haber 1996]. Several techniques have been proposed to avoid such a checkerboard pattern as an optimal solution [Poulsen 2002; Sigmund and Petersson 1998; Zhou et al. 2001]. In this study we use a simple procedure similar to the one used
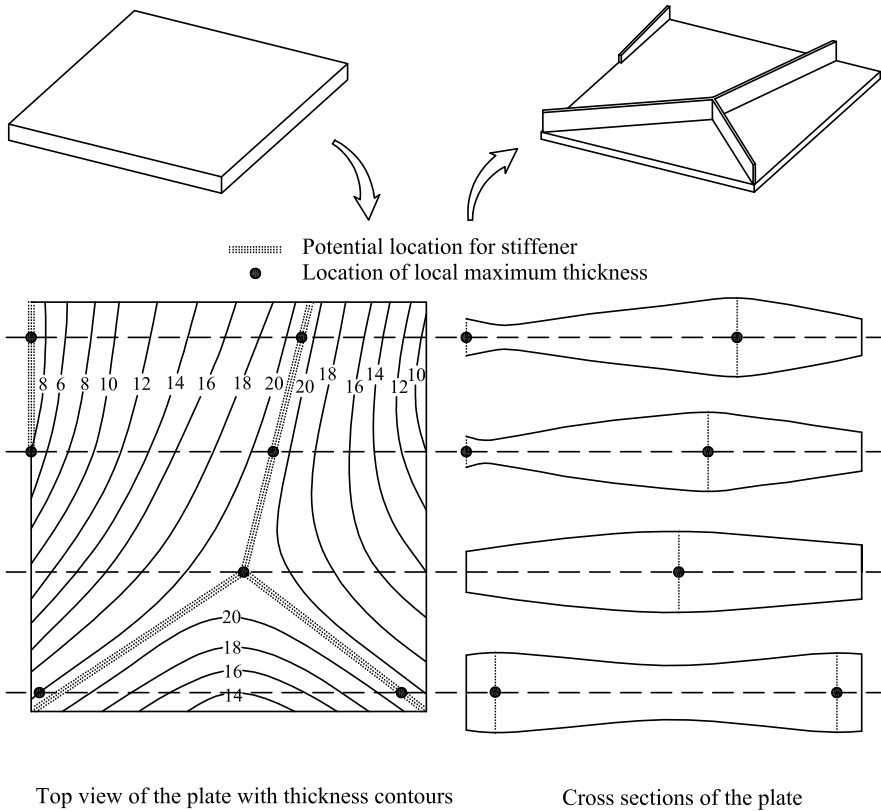
Figure 2. Identifying potential locations for stiffeners using thickness optimization.

by Gáspár et al. [2001], in which a primary meshing is subdivided into further finite elements called secondary elements. In this study, first a primary mesh is considered with square elements, and then each square in the primary mesh is divided into two triangular elements. The new thickness of each square in the primary mesh (after each iteration) is found by taking the average of the new thicknesses of its two triangular elements.

Strain energy for most of the elements available in literature is not accurate when used in coarse meshes [Felippa 2003]. This makes the problem of thickness optimization very expensive, since a large number of elements is needed in nonlinear analysis to get a desirable accuracy. On the other hand, when modeling the ribs in stiffened plates (after performing the thickness optimization and selecting the potential places to add the ribs), it frequently happens that some elements have very high or very low geometrical aspect ratios in the stiffener parts. Response of these elements can affect the response of the whole structure, leading to erroneous results about the behavior of the stiffened plate [Felippa 2003]. Thus, it is preferable to model the structure with an element which has the least aspect ratio sensitivity and highest accuracy for strain energy.

The element in this study is a facet triangular shell element with 3 nodes and 6 degrees of freedom per node (3 translations and 3 rotations) [Khosravi et al. 2007]. This element is a combination of the discrete Kirchhoff triangular plate bending element (DKT) [Batoz et al. 1980], and the optimal triangular

membrane element (OPT) [Felippa 2003]. The OPT membrane element has been formulated based on the ANDES (assumed natural deviatoric strain) template, and for any arbitrary aspect ratio its strain energy is accurate. In a recent paper [Khosravi et al. 2007], it has been shown that using this element leads to acceptable results even in case of relatively coarse meshes. As a result, the cost of the optimization in a nonlinear regime may be extensively reduced using this element.

In this study, a corotational approach is used to analyze the structure with geometric nonlinearity. In this approach the contribution of the rigid body motion to the total deformation of the element is removed before performing the element computations. This enables one to upgrade the structural elements so as to treat problems with large rotations but small strains. For a detailed explanation of the shell element used in this study and the corotational nonlinear analysis using triangular facet elements, the reader is referred to [Khosravi et al. 2007]. In order to follow the nonlinear load deflection path, the arc length method [Crisfield 1981] is used.

It should be mentioned that recently some doubts have been raised about the mathematical convergence of facet elements [Chapelle and Bathe 2003]. In particular, when refining the mesh, finite element solutions are expected to converge to the exact solution of a well-defined mathematical model. However, some numerical experiments have shown that facet shell elements may not exactly converge when the mesh is refined, although their results lie within a few percent of the reference values [Chapelle and Bathe 2003]. It is believed that the best shell elements are formulated using 3D continuum mechanics incorporating shell theory assumptions. However facet elements are used in this study since the formulation of a corotational approach using curved elements is extremely difficult to perform and is not even well developed.

5. Numerical results

In this section, four examples are presented. In the first and second examples, the proposed UASEV criterion is used for thickness optimization of plate structures, and results are compared with those found by using the USED criterion, that is, Equation (13) instead of Equation (12). The third and fourth examples show the application of thickness optimization in stiffener location and load capacity maximization of plates subject to constant volume. In all examples, Equations (19)–(21) with tol $= 10^{-2}$ are used for thickness optimization.

Example 1. Figure 3 shows a cantilever plate subject to the shear load F and axial force $P = 20\,F$ at the tip. The dimensions of the plate are $40\,\text{cm} \times 4\,\text{cm}$ with overall thickness $t = 0.4\,\text{cm}$, and the plate is made of isotropic material (steel) with the following mechanical properties: $E = 200\,\text{GPa}$, $G = 77\,\text{GPa}$, $v = 0.3$.

The objective is to perform the thickness optimization in order to maximize the load capacity F subject to constant volume. It is assumed that the load capacity F is found based on the displacement $W = 1\,\text{cm}$, where W is the vertical deflection at the tip of the plate. The plate is modeled by 40 triangular elements, and due to symmetry, only half of the plate is analyzed.

Nonlinear analysis results in $F = 49.81\,\text{N}$ as the initial load capacity of the plate. Figure 4 shows the results of thickness optimization subject to constant volume, using UASEV and also USED criteria. In both cases, convergence is achieved in 5 iterations, with $r = 2$ as the step size parameter. Nonlinear behavior of the plate optimized by UASEV and USED criteria is also shown in Figure 5.
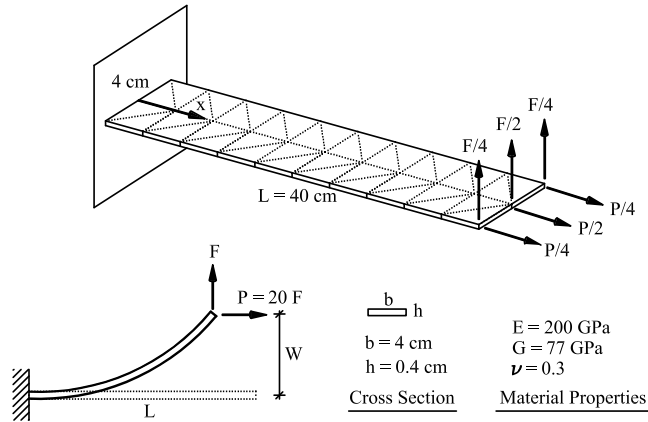
Figure 3. Cantilever plate subject to axial and shear forces at the tip.
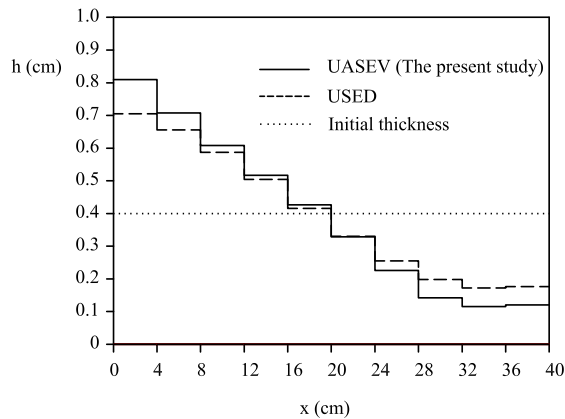

Figure 4. Variation of the thickness over the length of the cantilever plate after optimization.

It is observed that optimization using the UASEV criterion increases the load capacity of the plate to $F = 150.36\,N$, compared to $F = 131.16\,N$ obtained by using USED criterion. In Figure 5, it is interesting to note that in the range of $W \leq 0.75\,cm$, the load capacity of the plate optimized by UASEV criterion is slightly less than that of the one optimized by USED; however since the optimality criteria are applied at the limit point (that is, $W = 1\,cm$), UASEV finally overcomes USED and leads to a higher load capacity.

Example 2. Figure 6 shows a simply supported square plate under the biaxial compressive edge forces $N_x = N_y$. The dimensions of the plate are $80\,cm \times 80\,cm$ with overall thickness $t = 0.4\,cm$, and the plate is made of isotropic material (steel) with the following mechanical properties: $E = 200\,GPa$, $G = 77\,GPa$, $\nu = 0.3$.

In order to initiate the lateral deflection, an imperfection in the form of a half sine wave with the maximum value 1 mm at the center of the plate is considered. The objective is to optimize the thickness of the plate, while having the same total volume, in order to maximize the load capacity for $W = 0.4\,cm$, where W is the vertical deflection at the center of the plate. The plate is modeled by 800 triangular

elements, and due to symmetry only a quarter of the plate is analyzed. Performing the nonlinear analysis results in $N_x = N_y = 369.5$ N/cm as the initial load capacity of this plate.

Figures 7a and 7b show the results of thickness optimization subject to constant volume for a quarter of the plate using Equations (19)–(21) in 8 iterations, and UASEV and USED criteria, respectively. In both cases $r = 4$ has been considered as the step size parameter. It is observed that optimization based on USED criteria tends to reduce the thickness in the middle of the plate, and to increase it on the corners and mid-sides. Instead, UASEV criterion tends to reduce the thickness on the mid-sides and to increase it on the corners and somewhat in the middle. Figure 8 shows the change of load-carrying capacity of the plate during the thickness optimization. Nonlinear analysis of an optimal plate under the applied loads shows that the load capacity of this plate has been increased to $N_x = N_y = 584.3$ N/cm, and $N_x = N_y = 509.2$ N/cm for UASEV and USED criteria, respectively, while having the same total
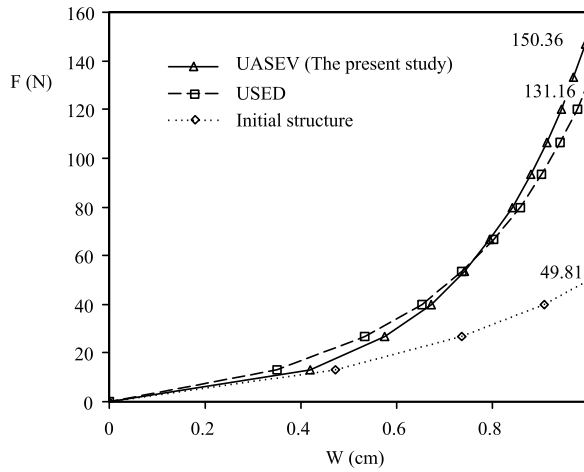
Figure 5. Nonlinear behavior of the cantilever plate before and after optimization.
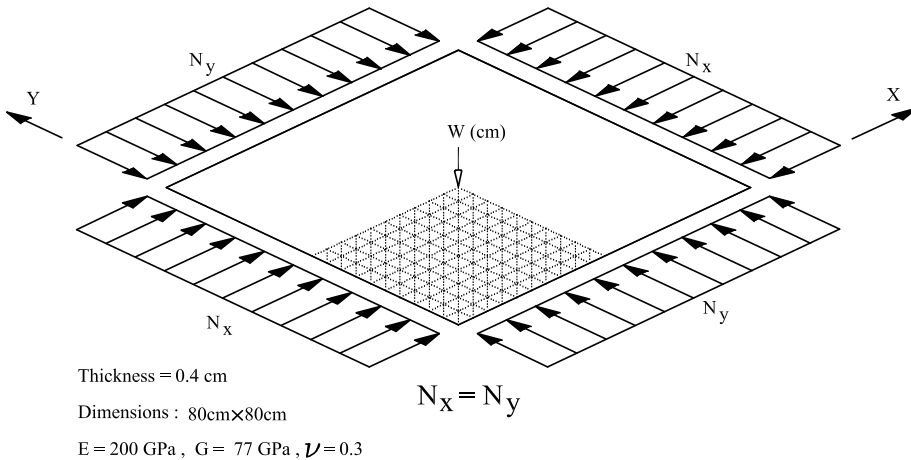
Figure 6. Square plate with simple supports subjected to biaxial compressive forces.
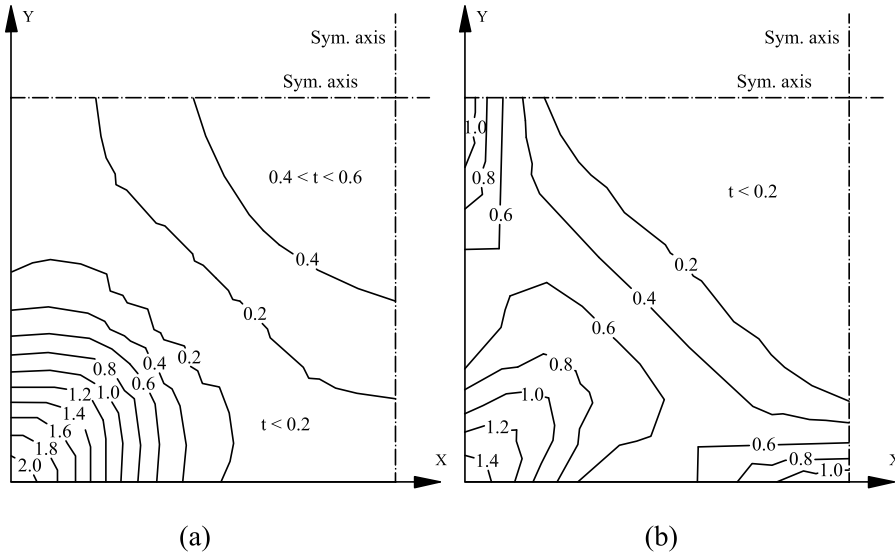
Figure 7. Results of thickness optimization (cm) for a quarter of the plate shown in Figure 6: (a) UASEV criterion; (b) USED criterion.

volume. Although using any one of these two criteria increases the strength (or load capacity) of the plate, it is obvious that the UASEV criterion is more efficient than that of USED.

Example 3. In this example the application of the UASEV criterion is shown for thickness optimization, and subsequently stiffener location in a stiffened plate. Figure 9 shows an 80×80 cm simply-supported square plate with overall thickness $t = 0.4$ cm and a 24 cm $\times$ 24 cm square hole in the center. Loading and material properties are similar to those in the previous example. Also, an imperfection in the form of a half sine wave with the value of 1 mm around the central hole is considered to initiate the lateral deflection. The objective is to optimize the thickness and find the potential stiffener locations subject to constant volume, in order to maximize the load capacity for $W = 0.4$ cm, where W is the deflection at
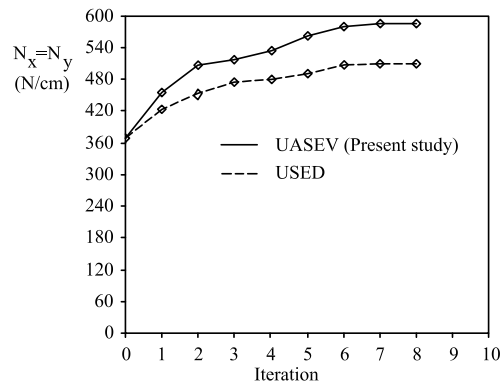
Figure 8. Change of load-carrying capacity of the plate shown in Figure 6 during the thickness optimization using USED and UASEV criteria.
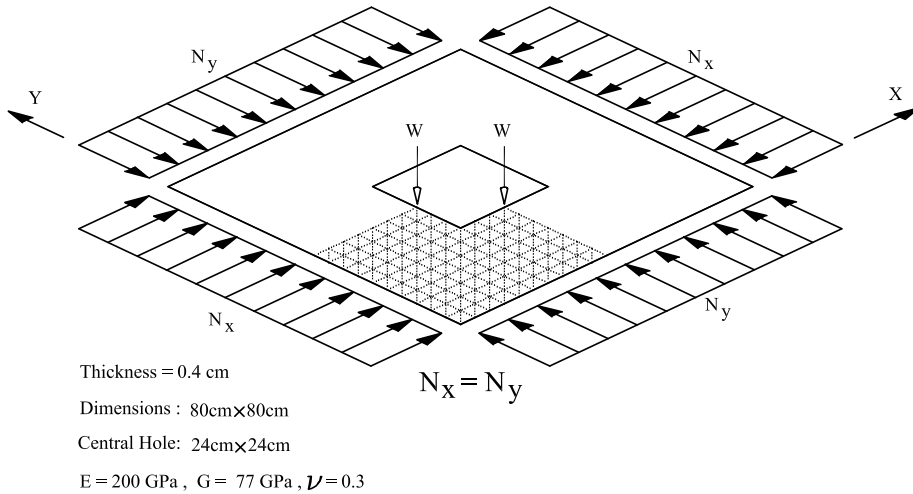
Figure 9. Square plate with a square hole in the center and simple supports, subjected to biaxial compressive forces.

the midpoint of the hole edges. In this example, the following design constraints should also be satisfied for the final design:

- The maximum height of the stiffeners is 5 cm.

- The stiffeners and the plate have the same thickness in the final design.

Similar to the previous example, a quarter of the plate is modeled by 182 triangular elements. Performing the nonlinear analysis results in $N_x = N_y = 290.8$ N/cm as the load capacity of this plate for $W = 0.4$ cm. Thickness optimization is performed using the UASEV criterion with $r = 4$ as the step size parameter. The iterative process converged after 9 iterations. Variation of the thickness for a quarter of the plate, based on the results of thickness optimization subject to constant total volume is shown in Figure 10. Load carrying capacity of this plate after performing the thickness optimization, has increased to $N_x = N_y = 654.3$ N/cm.

Based on this shape, and predefined design constraints mentioned above, stiffeners are located on the lines of maximum thicknesses (as shown in Figure 11) on a plate with constant thickness. Height of the stiffeners are proportional to the thickness of the elements, with the maximum value of 5 cm according to the first design constraint. Keeping the total volume equal to the initial volume 2329.6 cm³, and considering the same thickness for stiffeners and plate (per the second design constraint) a new overall thickness of $t = 0.36$ cm is found for the plate and the stiffeners. A nonlinear analysis of this stiffened plate shows that the load capacity has increased to $N_x = N_y = 560.4$ N/cm compared to $N_x = N_y = 290.8$ N/cm for the initial plate, however it has been reduced compared to $N_x = N_y = 654.3$ N/cm for the plate with optimized thickness.

Example 4. A plate similar to the one in Example 3 is considered under the downward surface load q. Boundary conditions are similar to those in Example 3 except that in-plane deflections are not allowed for all four edges. As a result, membrane forces arise during the deflections due to bending. The objective is
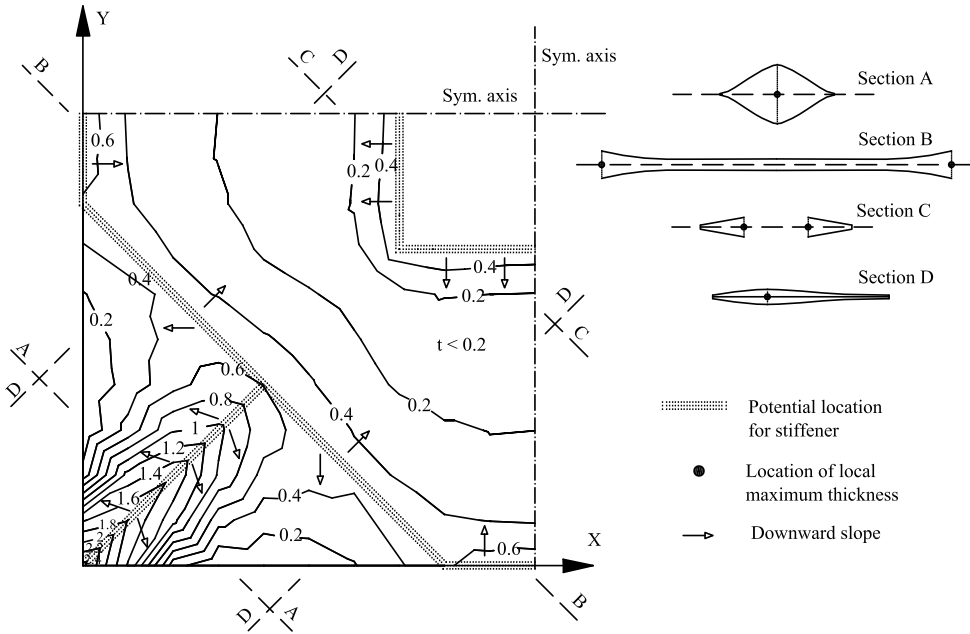
Figure 10. Result of thickness optimization (cm) for a quarter of the plate shown in Figure 9. Thicknesses of the sections have been exaggerated for better view.

to maximize the load capacity for $W = 0.3$ cm using UASEV criterion, subject to constant total volume. The following design constraints should also be satisfied in this problem:

- The maximum height of the stiffeners is 10 cm.
- The thickness of the stiffeners is 0.4 cm.

A quarter of the plate is modeled by 182 triangular elements. Also, we can see that a nonlinear analysis results in $q = 0.318$ N/cm^2 as the load capacity of this plate. In the next step, UASEV criterion with $r = 4$ is employed for thickness optimization. The new thickness distribution and potential locations for stiffeners are shown in Figure 12, and are found after 9 iterations. The load-carrying capacity of this plate after performing the thickness optimization has increased to $q = 0.865$ N/cm^2.
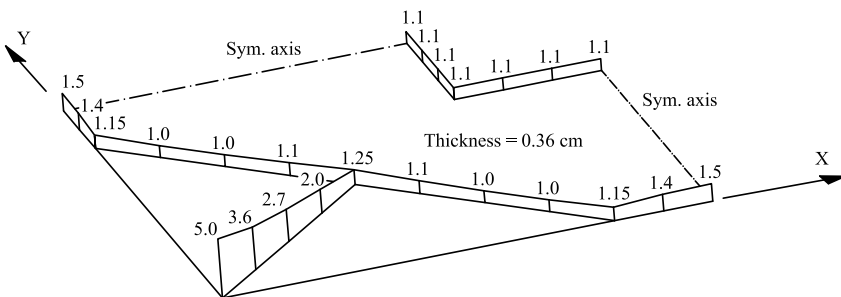
Figure 11. A quarter of the plate shown in Figure 9 (Example 3) with stiffeners at potential locations. Numbers show the height of the stiffeners (cm).
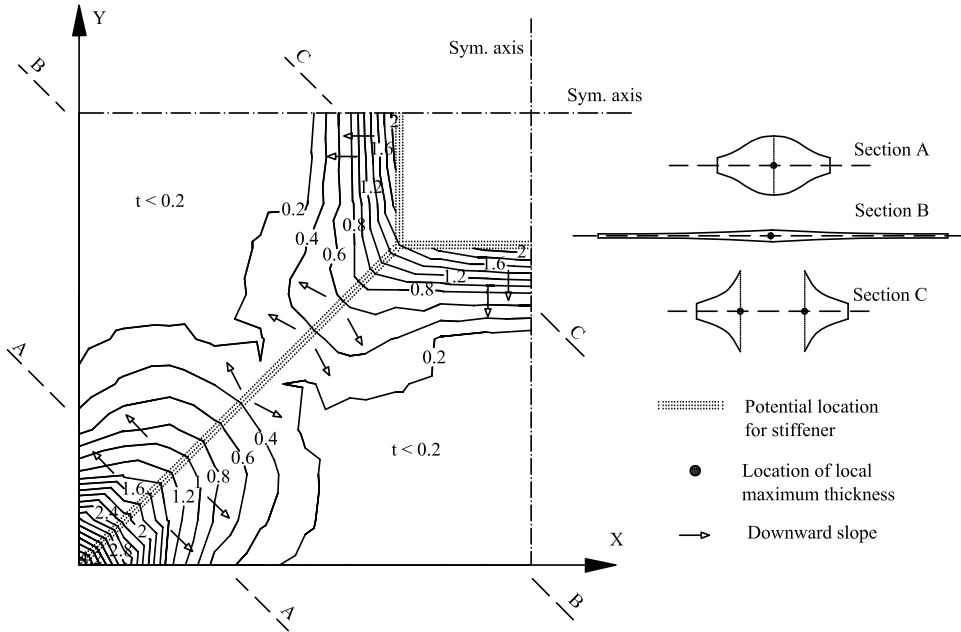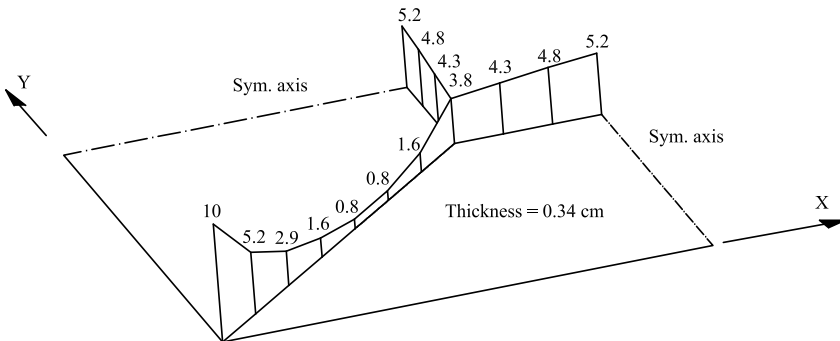
Figure 12. Result of thickness optimization (cm) for a quarter of the plate shown in Figure 9 with hinged supports ($u = v = w = 0$ at the edges) under the downward surface pressure load. Thicknesses of the sections have been exaggerated for a better view.

Figure 13 shows the stiffeners located on the lines of maximum thickness, with their height proportional to the new thickness of the elements, but not more than 10 cm, and their thickness equal to 0.4 cm according to the design constraint. Keeping the total volume equal to the initial volume, a new thickness $t = 0.339 \approx 0.34$ cm is found for the plate. Nonlinear analysis shows that the load capacity for $W = 0.3$ cm has increased to $q = 1.26$ N/cm^2 compared to $q = 0.318$ N/cm^2 for the initial plate, and compared to $q = 0.865$ N/cm^2 for the plate with optimized thickness.

Figure 13. A quarter of the plate in Example 4 with stiffeners at potential locations. Numbers show the height of the stiffeners (cm).

Figure 14. A quarter of the plate in Example 4 with stiffeners at potential locations after two rounds of optimization. Numbers show the height of the stiffeners (cm).

It should be mentioned that once the ribs are placed on a plate, structural behavior of the plate changes considerably. Thus, as mentioned before, it seems appropriate to repeat the optimization process for the stiffened plate, to obtain any further possible stiffener locations, and also modify the heights of the previously located stiffeners. Figure 14 shows the result of the optimized plate in Example 4 after the second round of optimization. It may be seen that a new series of stiffeners are found and the heights of the previous stiffeners have also been modified. Performing nonlinear analysis, the load capacity of the stiffened plate after the second round of optimization is found to be $q = 1.57\,\text{N/cm}^2$ compared to $q = 1.26\,\text{N/cm}^2$ after the first round.

6. Conclusion

In this study a methodology for rib location and design optimization of stiffened plates based on an optimality criterion for thickness optimization is presented. The optimality criterion for thickness optimization (called UASEV in this study) states that in an optimum design, the derivative of the strain energy with respect to the thickness, over the area of element, is the same for all elements. It was shown that in the general case of the combination of membrane and bending deformations, using the USED criterion instead of UASEV is unjustified. Only in case of pure membrane or pure bending behavior are their results the same. Applying the proposed criterion through an iterative process, it is possible to find the potential locations to add stiffeners and increase the strength of the plate while consuming the same amount of material.

References

[Arora 1989] J. S. Arora, *Introduction to optimum design*, McGraw-Hill, New York, 1989.

[Batoz et al. 1980] J. L. Batoz, K. J. Bathe, and L. W. Ho, "A study of three-node triangular plate bending elements", *Int. J. Numer. Methods Eng.* **15**:12 (1980), 1771–1812.

[Bendsøe 1989] M. P. Bendsøe, "Optimal shape design as a material distribution problem", *Struct. Multidiscip. O.* **1**:4 (1989), 193–202.

[Bendsøe and Kikuchi 1988] M. P. Bendsøe and N. Kikuchi, "Generating optimal topologies in structural design using a homogenization method", *Comput. Methods Appl. Mech. Eng.* **71**:2 (1988), 197–224.

[Bendsøe and Mota Soares 1993] M. P. Bendsøe and C. A. Mota Soares, "Topology design of structures", pp. xvi+569 in *Proceedings of the NATO Advanced Research Workshop held in Sesimbra, June 20–26, 1992* (Sesimbra, Portugal), edited by

M. P. Bendsøe and C. A. M. Soares, NATO Advanced Science Institutes Series E: Applied Sciences **227**, Kluwer, Dordrecht, 1993.

[Bendsøe and Sigmund 1999] M. P. Bendsøe and O. Sigmund, "Material interpolation schemes in topology optimization", *Arch. Appl. Mech.* **69**:9-10 (1999), 635–654.

[Bendsøe and Sigmund 2003] M. P. Bendsøe and O. Sigmund, *Topology optimization: theory, methods and applications*, Springer, Berlin, 2003.

[Berke 1971] L. Berke, "An efficient approach to the minimum weight design of deflection limited design", technical report AFFDL-TR-70-4-FDTR, Air Force Flight Dynamics Laboratory, 1971.

[Berke and Khot 1974] L. Berke and N. S. Khot, "Use of optimality criteria methods for large scale systems", *AGARD Lect. Ser.* **70** (1974), 1–29.

[Chapelle and Bathe 2003] D. Chapelle and K. J. Bathe, *The finite element analysis of shells—fundamentals*, Computational fluid and solid mechanics, Springer, Berlin, 2003.

[Chung and Lee 1997] J. Chung and K. Lee, "Optimal design of rib structures using the topology optimization technique", *Proc. Inst. Mech. Eng. C J. Mech. Eng. Sci.* **211**:6 (1997), 425–437.

[Crisfield 1981] M. A. Crisfield, "A fast incremental-iterative solution procedure that handles 'snap-through'", *Comput. Struct.* **13**:1-3 (1981), 55–62.

[Díaz and Sigmund 1995] A. R. Díaz and O. Sigmund, "Checkerboard patterns in layout optimization", *Struct. Multidiscip. O.* **10**:1 (1995), 40–45.

[Felippa 2003] C. A. Felippa, "A study of optimal membrane triangles with drilling freedoms", *Comput. Methods Appl. Mech. Eng.* **192**:16-18 (2003), 2125–2168.

[Gallagher 1973] R. H. Gallagher, "Fully stressed design", pp. 19–32 in *Optimum structural design: theory and applications*, edited by R. H. Gallagher and O. C. Zienkiewicz, Wiley, London, 1973.

[Gáspár et al. 2001] Z. S. Gáspár, J. Lógó, and G. I. N. Rozvany, "On design-dependent constraints and singular topologies", *Struct. Multidiscip. O.* **21**:2 (2001), 164–172. Addenda in **24**:2 (2002), 338–342.

[Gellatly and Berke 1971] R. A. Gellatly and L. Berke, "Optimal structural design", technical report, Air Force Flight Dynamics Laboratory, 1971. AFFDL-TR-70-165.

[Gellatly and Berke 1973] R. A. Gellatly and L. Berke, "Optimality criterion based algorithms", pp. 33–49 in *Optimum structural design: theory and applications*, edited by R. H. Gallagher and O. C. Zienkiewicz, Wiley, London, 1973.

[Jog and Haber 1996] C. S. Jog and R. B. Haber, "Stability of finite element models for distributed-parameter optimization and topology design", *Comput. Methods Appl. Mech. Eng.* **130**:3-4 (1996), 203–226.

[Khosravi et al. 2007] P. Khosravi, R. Ganesan, and R. Sedaghati, "Corotational nonlinear analysis of thin plates and shells using a new shell element", *Int. J. Numer. Methods Eng.* **69**:4 (2007), 859–885.

[Khot et al. 1979] N. S. Khot, L. Berke, and V. B. Venkayya, "Comparison of optimality criteria algorithms for minimum weight design of structures", *AIAA J.* **17**:2 (1979), 182–190.

[Lam and Santhikumar 2003] Y. C. Lam and S. Santhikumar, "Automated rib location and optimization for plate structures", *Struct. Multidiscip. O.* **25**:1 (2003), 35–45.

[Lee et al. 2000] T. H. Lee, S. Y. Han, and J. K. Lim, "Topology optimization of the inner reinforcement for an automobile hood using modal design sensitivity analysis", *Key Eng. Mater.* **183–187** (2000), 439–444.

[Lógó 2005] J. Lógó, "New type of optimal topologies by iterative method", *Mech. Based Des. Struct. Mach.* **33**:2 (2005), 149–171.

[Lógó and Ghaemi 2002] J. Lógó and M. Ghaemi, "Topology optimization by SIMP method", in *Proceedings of the 9th International Conference on Numerical Methods and Computational Mechanics* (Miskolc, Hungary), edited by A. Galántay and G. Szeidl, 2002.

[Maute et al. 1998] K. Maute, S. Schwarz, and E. Ramm, "Adaptive topology optimization of elastoplastic structures", *Struct. Multidiscip. O.* **15**:2 (1998), 81–91.

[Nagtegaal 1973] J. C. Nagtegaal, "A new approach to optimal design of elastic structures", *Comput. Methods Appl. Mech. Eng.* **2**:3 (1973), 255–264.

[Poulsen 2002] T. A. Poulsen, "A simple scheme to prevent checkerboard patterns and one node connected hinges in topology optimization", *Struct. Multidiscip. O.* **24**:5 (2002), 396–399.

[Prager and Taylor 1968] W. Prager and J. E. Taylor, "Problems of optimal structural design", *J. Appl. Mech.* (*Trans. ASME*) **35** (1968), 102–106.

[Rozvany 1997] G. I. N. Rozvany, "Aims, scope, basic concepts and methods of topology optimization", pp. 1–55 in *Topology optimization in structural mechanics*, CISM Courses and Lectures **374**, Springer, Vienna, 1997.

[Rozvany et al. 1995] G. I. N. Rozvany, M. P. Bendsøe, and U. Kirsch, "Layout optimization of structures", *Appl. Mech. Rev.* **48** (1995), 41–111.

[Sigmund and Petersson 1998] O. Sigmund and J. Petersson, "Numerical instabilities in topology optimization—a survey on procedures dealing with checkerboards, mesh-dependencies and local minima", *Struct. Multidiscip. O.* **16**:1 (1998), 68–75.

[Stok and Mihelic 1996] B. Stok and A. Mihelic, "Two-stage design optimization of shell structures", *Struct. Eng. Rev.* **8**:2-3 (1996), 91–97.

[Venkayya 1971] V. B. Venkayya, "Design of optimum structures", *Comput. Struct.* **1**:1-2 (1971), 265–309.

[Venkayya et al. 1968] V. B. Venkayya, N. S. Khot, and V. S. Reddy, "Optimization of structures based on the study of energy distribution", technical report AFFDL-TR-68-150, Air Force Flight Dynamics Laboratory, 1968, Available at http://handle.dtic.mil/100.2/ADA447802.

[Venkayya et al. 1969] V. B. Venkayya, N. S. Khot, and V. S. Reddy, "Energy distribution in an optimum structural design", technical report AFFDL-TR-68-156, Air Force Flight Dynamics Laboratory, 1969.

[Zhou et al. 2001] M. Zhou, Y. K. Shyy, and H. L. Thomas, "Checkerboard and minimum member size control in topology optimization", *Struct. Multidiscip. O.* **21**:2 (2001), 152–158.

PEYMAN KHOSRAVI: peyma_kh@encs.concordia.ca
Department of Mechanical and Industrial Engineering, Concordia University, Montreal, Quebec H3G 1M8, Canada

RAMIN SEDAGHATI: sedagha@encs.concordia.ca
Department of Mechanical and Industrial Engineering, Concordia University, Montreal, Quebec H3G 1M8, Canada

RAJAMOHAN GANESAN: ganesan@vax2.concordia.ca
Department of Mechanical and Industrial Engineering, Concordia University, Montreal, Quebec H3G 1M8, Canada

UNIFIED EFFICIENT LAYERWISE THEORY FOR SMART BEAMS WITH SEGMENTED EXTENSION/SHEAR MODE, PIEZOELECTRIC ACTUATORS AND SENSORS

SANTOSH KAPURIA AND PETER HAGEDORN

A unified coupled efficient layerwise theory is presented for the dynamics of smart laminated beams with surface-mounted and embedded piezoelectric actuators and sensors with arbitrary poling directions, acting in extension or shear mode. The theory considers a global third-order variation across the thickness combined with a layerwise linear variation for the axial displacement, expressed in terms of only three primary variables, and accounts for the transverse normal strain due to the electric field in the approximation for the transverse displacement. The electric potential is approximated as piecewise quadratic across sublayers. A finite element is developed which has two physical nodes with mechanical and some electric potential degrees of freedom (DOF), and an *electric node* for the electric potentials of the electroded surfaces of the piezoelectric patches. The *electric nodes* eliminate the need for imposition of equality constraints of the electric DOF on the equipotential electroded surfaces of the segmented piezoelectric elements and result in significant reduction in the number of electric DOF. The electric DOF associated with the physical nodes allow for the inplane electric field that is induced via a direct piezoelectric effect. The accuracy of the formulation is established by comparing the results with those available in literature and the 2D piezoelasticity solutions for extension and shear mode actuators, sensors and adaptive beams. The effect of segmentation of the electroded surface on the deflection, sensory potential and natural frequencies is illustrated for both extension and shear mode cases. The influence of the location of extension and shear mode actuators and sensors on the response is investigated for a hybrid mode composite beam. The effect of actuator thickness on the actuation authority is studied.

1. Introduction

Adaptive laminated structures, incorporating some surface-mounted and embedded piezoelectric patches for sensing and actuation, are now widely used in noise, vibration, acoustic, shape and position control applications. Even though the orthorhombic piezoelectric materials of symmetry class mm2 [Auld 1973] have five piezoelectric constants, namely, d_{31}, d_{32} d_{33}, d_{15}, d_{24}, most research and development efforts in this technology have generally been focused on the piezoelectric elements that are poled parallel to the applied electric field (in the thickness direction) and use only the d_{31}, d_{32} constants to use membrane strains. This is known as the extension actuation mechanism (EAM). Consequently, most of the existing refined models incorporating advanced kinematics and two-way electromechanical coupling also consider the extension mode piezoelectric elements; see, for example, the review articles of Saravanos and Heyliger [1999], Gopinathan et al. [2000] and Benjeddou [2000]. Coupled discrete layer theories (DLT)

with layerwise linear description of inplane displacements and electric potential have been presented for hybrid beams [Lee and Saravanos 1996] and plates [Saravanos et al. 1997; Lage et al. 2004]. Plagianakos and Saravanos [2005] presented a higher-order DLT for hybrid beams using layerwise quadratic and cubic variations for the inplane displacements and electric potential, respectively. These theories yield excellent accuracy, but the computational effort increases in proportion to the number of layers, which restricts their application for practical dynamics and control problems. Mixed coupled equivalent single layer (ESL) theories such as the first-order shear deformation theory (FSDT) [Saravanos 1999; Wang 2004] and refined third-order theory (TOT) [Correia et al. 2000], considering a global variation for the displacements across the entire thickness and a layerwise distribution for the electric potential, have been employed for the dynamic analysis of hybrid plates. It is now well known that since these theories do not account for the layerwise (zigzag) nature of distributions of the inplane displacements, they yield inaccurate results for moderately thick laminates and even thin laminates with strong inhomogeneity across the thickness. Vasques and Rodrigues [2005] presented a finite element formulation based on a coupled partial layerwise theory for three layer piezoelectric beams. Kapuria [2001] and Kapuria and Alam [2006] presented a coupled zigzag theory for hybrid beams, which considers a layerwise approximation for the inplane displacement, like the DLT, but the number of primary displacement variables is reduced to only three as in the ESL theories, FSDT and TOT, by enforcing the conditions on the transverse shear stresses at the top and bottom surfaces and the layer interfaces. Comparison with the two-dimensional (2D) piezoelasticity solutions have established the excellent accuracy of this theory for active and sensory dynamic response of moderately thick hybrid beams for various inhomogeneous lay-ups and boundary conditions.

The piezoelectric materials, when constrained and poled perpendicularly to the applied electric field, undergo transverse shear deformation through the d_{15}, d_{24} constants, which is known as the shear actuation mechanism (SAM). The use of shear mode actuators for adaptive structures was first investigated by Sun and Zhang [1995] who carried out a 2D finite element analysis of a plane strain adaptive beam consisting of an axially poled piezoelectric core embedded between two elastic face sheets. The results showed that the shear actuators are subjected to much lower stresses compared to the extension actuators under the same electric field. Zhang and Sun [1996] presented a *three layer sandwich* beam theory for the shear actuated laminate by modeling the face layers as classical Euler–Bernoulli beams and the central core as a Timoshenko beam, without considering the two-way electromechanical coupling. Benjeddou et al. [1997] presented a finite element (FE) formulation based on this uncoupled three-layer beam model for analysis of adaptive sandwich beams with elastic/EAM piezoelectric faces and SAM piezoelectric/elastic core. An improved FE model [Benjeddou et al. 1999] eliminating the shear locking problem was used for comparing SAM and EAM actuators for static and free vibration response [Benjeddou et al. 2000]. Raja et al. [2002; 2004] generalized the sandwich model by considering laminates (instead of single layers) for the faces and the core and by incorporating the electric DOF. The electric potential was assumed to be linear across a sublaminate (core/face). Trindade and Benjeddou [2005] extended their previous model by modeling the core with the TOT and considering the variation of the electric potential to be cubic across the core thickness and linear across the faces. It was shown that this led to a significantly stiffer response, but the results did not match with the 2D FE results. It is important to note that all the publications reported above use a three layer beam model, which is rather restrictive for modeling general laminates with EAM and SAM actuators to be placed at any arbitrary location

across the thickness. It has been observed from 2D piezoelasticity solutions that the electric potential follows a nearly quadratic variation across the thickness in extension mode piezoelectric elements [Dube et al. 1996] and a nearly cubic variation in shear mode elements [Parashar et al. 2005]. It is also well established that the assumption of a linear electric potential along the thickness can cause a significant error in the computed response [Bisegna and Caruso 2001; Sze et al. 2004; Parashar et al. 2005]. Khdeir and Aldraihem [2001; 2003] presented a closed form solution for deflection analysis of beams with shear and extension actuators employing the uncoupled FSDT and an uncoupled higher-order theory. Parashar et al. [2004] presented a coupled FSDT for the nonlinear vibration of shear actuators considering material nonlinearities.

Conventionally, the finite element models based on coupled theories consider electric DOF at the nodes. However, the piezoelectric sensing and actuating patches are always electroded with metallic coating, which makes their surfaces equipotential. To model this condition, particularly for sensing, it would be necessary to impose the constraint of equality on the electric DOF of the nodes on the same electroded surface. To avoid this tedious task, the concept of electric nodes has been used by Sze and Yao [2000], wherein the electric DOF are separated from the kinetic (physical) nodes with which only mechanical DOF are associated. It results in significant reduction in the number of electric DOF. But in this approach, as all the electric DOF are associated with electric nodes, the inplane electric fields which may be induced due to direct piezoelectric effect cannot be accounted for.

In this work, a new unified coupled efficient layerwise formulation is presented for hybrid laminated beams with surface-bonded or embedded piezoelectric actuators and sensors with arbitrary poling directions, which act in extension or shear mode. The constitutive equations of piezoelectric plane stress beams and plane strain panels with arbitrary poling direction are derived using transformation rules. The axial displacement is approximated as a third-order zigzag variation across the thickness, which is expressed in terms of only three primary displacement variables. The transverse displacement is approximated to account for the transverse normal strain due to the electric field, and the electric potential is assumed to follow a quadratic variation across sublayers, which can effectively model the observed quadratic and cubic variations in, respectively, the extension and shear mode piezoelectric elements. A novel finite element is developed consisting of two physical nodes with kinetic and some electric DOF, and an *electric node* with the electric DOF for the equipotential surfaces of the electroded piezoelectric patches. The electric nodes conveniently model the equipotential condition of electroded surfaces with significantly reduced number of electric DOF. The quadratic component of electric DOF associated with the physical nodes enable modeling the inplane electric field induced due to the direct piezoelectric effect.

2. Constitutive equations for piezoelectric beams/panels with arbitrary poling direction

The 3D linear constitutive equations of a piezoelectric orthorhombic material of class mm2 symmetry (commonly used materials PZT and PVDF belong to this class or its subset), with principal material axes x_1, x_2, x_3 and polarized along axis x_3, are given by [Auld 1973]

$$\varepsilon' = S\,\sigma' + d^{\mathrm{T}}E', \qquad D' = d\,\sigma' + \epsilon\,E'; \qquad \sigma' = C\varepsilon' - e^{\mathrm{T}}E', \qquad D' = e\,\varepsilon' + \eta\,E'. \qquad (1)$$
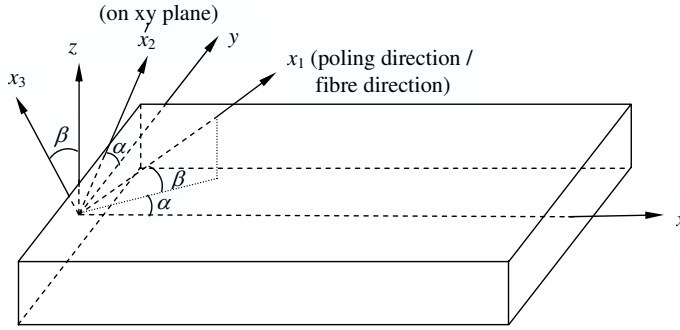
Figure 1. Reference axes (x, y, z) and material principal axes (x_1, x_2, x_3) of piezoelectric material with arbitrary poling direction.

The superscript $(\ )^T$ denotes matrix transpose. The components of stress σ', engineering strain ε', electric field E' and electric displacement D' are given with respect to the principal material axes by

$$\sigma'=\begin{bmatrix} \sigma_1 & \sigma_2 & \sigma_3 & \tau_{23} & \tau_{31} & \tau_{12} \end{bmatrix}^T, \ \varepsilon'=\begin{bmatrix} \varepsilon_1 & \varepsilon_2 & \varepsilon_3 & \gamma_{23} & \gamma_{31} & \gamma_{12} \end{bmatrix}^T, \ E'=\begin{bmatrix} E_1 & E_2 & E_3 \end{bmatrix}^T, \ D'=\begin{bmatrix} D_1 & D_2 & D_3 \end{bmatrix}^T.$$

S, d, η are the matrices of elastic compliance, piezoelectric strain constants and electric permittivities, with $C = S^{-1}$, $e = dS^{-1}$, $\epsilon = \eta + ed^T$, where

$$S = \begin{bmatrix} s_{11} & s_{12} & s_{13} & 0 & 0 & 0 \\ s_{12} & s_{22} & s_{23} & 0 & 0 & 0 \\ s_{13} & s_{23} & s_{33} & 0 & 0 & 0 \\ 0 & 0 & 0 & s_{44} & 0 & 0 \\ 0 & 0 & 0 & 0 & s_{55} & 0 \\ 0 & 0 & 0 & 0 & 0 & s_{66} \end{bmatrix}, \qquad d^T = \begin{bmatrix} 0 & 0 & d_{31} \\ 0 & 0 & d_{32} \\ 0 & 0 & d_{33} \\ 0 & d_{24} & 0 \\ d_{15} & 0 & 0 \\ 0 & 0 & 0 \end{bmatrix}, \qquad \eta = \begin{bmatrix} \eta_{11} & 0 & 0 \\ 0 & \eta_{22} & 0 \\ 0 & 0 & \eta_{33} \end{bmatrix}.$$

Consider that the material axis x_1 is spatially oriented at angles α with the reference axis x and β with the xy-plane (Figure 1). The axis x_2 is assumed to lie on the xy-plane. Thus the poling direction x_3 is at angle β with the reference axis z which is along the thickness direction. Using transformation rules, σ, ε, E and D in the reference coordinate system (x, y, z) can be related to those in the material coordinate system (x_1, x_2, x_3) by

$$\sigma' = T\sigma, \qquad \varepsilon' = RTR^{-1}\varepsilon, \qquad D' = aD, \qquad E' = aE, \tag{2}$$

where

$$\sigma=\begin{bmatrix} \sigma_x & \sigma_y & \sigma_z & \tau_{yz} & \tau_{zx} & \tau_{xy} \end{bmatrix}^T, \ \varepsilon=\begin{bmatrix} \varepsilon_x & \varepsilon_y & \varepsilon_z & \gamma_{yz} & \gamma_{zx} & \gamma_{xy} \end{bmatrix}^T, \ E=\begin{bmatrix} E_x & E_y & E_z \end{bmatrix}^T, \ D=\begin{bmatrix} D_x & D_y & D_z \end{bmatrix}^T,$$

and the transformation matrices a, T and R are defined in the Appendix in terms of direction parameters $c = \cos\alpha$, $s = \sin\alpha$, $p = \cos\beta$, and $q = \sin\beta$. Using the transformation rules in Equation (1), the constitutive equations of a piezoelectric medium with arbitrary poling direction, with respect to reference

axes x, y, z, are obtained as

$$\varepsilon = \bar{S}\sigma + \bar{d}^{\mathrm{T}}E, \qquad D = \bar{d}\sigma + \bar{\epsilon}E; \qquad \sigma = \bar{C}\varepsilon - \bar{e}^{\mathrm{T}}E, \qquad D = \bar{e}\varepsilon + \bar{\eta}E, \tag{3}$$

where

$$\bar{S} = T^{\mathrm{T}}S\,T, \quad \bar{d} = a^{\mathrm{T}}d\,T, \quad \bar{\epsilon} = a^{\mathrm{T}}\epsilon\,a, \quad \bar{C} = T^{-1}C\,(T^{-1})^{\mathrm{T}}, \quad \bar{e} = a^{\mathrm{T}}e\,(T^{-1})^{\mathrm{T}}, \quad \bar{\eta} = a^{\mathrm{T}}\eta\,a.$$

For structural applications as sensors and actuators, the electric field is generally applied in the thickness direction z. Thus, for extension mode sensing/actuation mechanism, the poling direction x_3 will be along the z-axis, that is, $\beta = 0 \Rightarrow p = 1, q = 0$. For the shear mode case, the poling direction will be perpendicular to the z-axis so that $\beta = \pm 90° \Rightarrow p = 0, q = \pm 1$. Thus for extension and shear mode actuation/sensing, $pq = 0$. For this case, Equation (3) assumes the following form

$$\begin{bmatrix} \varepsilon_x \\ \varepsilon_y \\ \varepsilon_z \\ \gamma_{yz} \\ \gamma_{zx} \\ \gamma_{xy} \end{bmatrix} = \begin{bmatrix} \bar{s}_{11} & \bar{s}_{12} & \bar{s}_{13} & 0 & 0 & \bar{s}_{16} \\ \bar{s}_{12} & \bar{s}_{22} & \bar{s}_{23} & 0 & 0 & \bar{s}_{26} \\ \bar{s}_{13} & \bar{s}_{23} & \bar{s}_{33} & 0 & 0 & \bar{s}_{36} \\ 0 & 0 & 0 & \bar{s}_{44} & \bar{s}_{45} & 0 \\ 0 & 0 & 0 & \bar{s}_{45} & \bar{s}_{55} & 0 \\ \bar{s}_{16} & \bar{s}_{26} & \bar{s}_{36} & 0 & 0 & \bar{s}_{66} \end{bmatrix} \begin{bmatrix} \sigma_x \\ \sigma_y \\ \sigma_z \\ \tau_{yz} \\ \tau_{zx} \\ \tau_{xy} \end{bmatrix} + \begin{bmatrix} \bar{d}_{11} & \bar{d}_{21} & \bar{d}_{31} \\ \bar{d}_{12} & \bar{d}_{22} & \bar{d}_{32} \\ \bar{d}_{13} & \bar{d}_{23} & \bar{d}_{33} \\ \bar{d}_{14} & \bar{d}_{24} & \bar{d}_{34} \\ \bar{d}_{15} & \bar{d}_{25} & \bar{d}_{35} \\ \bar{d}_{16} & \bar{d}_{26} & \bar{d}_{36} \end{bmatrix} \begin{bmatrix} E_x \\ E_y \\ E_z \end{bmatrix},$$

$$\begin{bmatrix} D_x \\ D_y \\ D_z \end{bmatrix} = \begin{bmatrix} \bar{d}_{11} & \bar{d}_{12} & \bar{d}_{13} & \bar{d}_{14} & \bar{d}_{15} & \bar{d}_{16} \\ \bar{d}_{21} & \bar{d}_{22} & \bar{d}_{23} & \bar{d}_{24} & \bar{d}_{25} & \bar{d}_{26} \\ \bar{d}_{31} & \bar{d}_{32} & \bar{d}_{33} & \bar{d}_{34} & \bar{d}_{35} & \bar{d}_{36} \end{bmatrix} \begin{bmatrix} \sigma_x \\ \sigma_y \\ \sigma_z \\ \tau_{yz} \\ \tau_{zx} \\ \tau_{xy} \end{bmatrix} + \begin{bmatrix} \bar{\epsilon}_{11} & \bar{\epsilon}_{12} & 0 \\ \bar{\epsilon}_{12} & \bar{\epsilon}_{22} & 0 \\ 0 & 0 & \bar{\epsilon}_{33} \end{bmatrix} \begin{bmatrix} E_x \\ E_y \\ E_z \end{bmatrix}. \tag{4}$$

For a beam of small width along the direction y, a state of plane stress ($\sigma_y = \tau_{yz} = \tau_{xy} = 0$) is assumed as in [Robbins and Reddy 1991; Lee and Saravanos 1996; Plagianakos and Saravanos 2005]. We neglect transverse normal stress σ_z, that is, $\sigma_z \simeq 0$. The axial and transverse displacements u, w and electric potential ϕ are assumed to be independent of y. With these assumptions, Equation (4) reduces to

$$\begin{bmatrix} \varepsilon_x \\ \gamma_{zx} \\ D_x \\ D_z \end{bmatrix} = \begin{bmatrix} \bar{s}_{11} & 0 & \bar{d}_{11} & \bar{d}_{31} \\ 0 & \bar{s}_{55} & \bar{d}_{15} & \bar{d}_{35} \\ \bar{d}_{11} & \bar{d}_{15} & \bar{\epsilon}_{11} & 0 \\ \bar{d}_{31} & \bar{d}_{35} & 0 & \bar{\epsilon}_{33} \end{bmatrix} \begin{bmatrix} \sigma_x \\ \tau_{zx} \\ E_x \\ E_z \end{bmatrix}. \tag{5}$$

The explicit expressions of $\bar{s}_{ij}$, $\bar{d}_{ij}$ and $\bar{\epsilon}_{ij}$ in terms their values in the material coordinate system are given in the Appendix. Inversely, Equation (5) can be written as

$$\begin{bmatrix} \sigma_x \\ \tau_{zx} \\ D_x \\ D_z \end{bmatrix} = \begin{bmatrix} \hat{Q}_{11} & 0 & \bar{e}_{11} & \hat{e}_{31} \\ 0 & \hat{Q}_{55} & \hat{e}_{15} & \hat{e}_{35} \\ \hat{e}_{11} & \hat{e}_{15} & -\hat{\eta}_{11} & -\hat{\eta}_{13} \\ \hat{e}_{31} & \hat{e}_{35} & -\hat{\eta}_{13} & -\hat{\eta}_{33} \end{bmatrix} \begin{bmatrix} \varepsilon_x \\ \gamma_{zx} \\ -E_x \\ -E_z \end{bmatrix} \tag{6}$$

with

$$\hat{\eta}_{11} = \bar{\epsilon}_{11} - \hat{e}_{11}\bar{d}_{11} - \hat{e}_{15}\bar{d}_{15}, \quad \hat{\eta}_{33} = \bar{\epsilon}_{33} - \hat{e}_{31}\bar{d}_{31} - \hat{e}_{35}\bar{d}_{35}, \quad \hat{\eta}_{13} = -(\hat{e}_{31}\bar{d}_{11} + \hat{e}_{35}\bar{d}_{15}),$$

$$\hat{Q}_{11} = 1/\bar{s}_{11}, \quad \hat{Q}_{55} = 1/\bar{s}_{55}, \quad \hat{e}_{11} = \bar{d}_{11}/\bar{s}_{11}, \quad \hat{e}_{31} = \bar{d}_{31}/\bar{s}_{11}, \quad \hat{e}_{15} = \bar{d}_{15}/\bar{s}_{55}, \quad \hat{e}_{35} = \bar{d}_{35}/\bar{s}_{55}. \tag{7}$$

For infinite panels (infinite dimension along y direction), a state of plane strain exist, that is, $\varepsilon_y = \gamma_{yz} = \gamma_{xy} = 0$. For this case, with the assumption of $\sigma_z \simeq 0$, the other components of Equation (3) can be reduced to the same form as Equation (6) with the associated material constants defined as

$$\hat{\eta}_{11} = \bar{\eta}_{11} + \bar{e}_{13}^2/\bar{c}_{33}, \quad \hat{\eta}_{33} = \bar{\eta}_{33} + \bar{e}_{33}^2/\bar{c}_{33}, \quad \hat{\eta}_{13} = \bar{e}_{13}\bar{e}_{33}/\bar{c}_{33}, \quad \hat{Q}_{11} = \bar{c}_{11} - \bar{c}_{13}^2/\bar{c}_{33},$$

$$\hat{Q}_{55} = \bar{c}_{55}, \quad \hat{e}_{11} = \bar{e}_{11} - \bar{c}_{13}\bar{e}_{13}/\bar{c}_{33}, \quad \hat{e}_{31} = \bar{e}_{31} - \bar{c}_{13}\bar{e}_{33}/\bar{c}_{33}, \quad \hat{e}_{15} = \bar{e}_{15}, \quad \hat{e}_{35} = \bar{e}_{35}. \tag{8}$$

The expressions of $\bar{c}_{ij}$, $\bar{e}_{ij}$ and $\bar{\eta}_{ij}$ are given in the Appendix. Thus, Equation (6) and the subsequent development are valid for both plane stress (thin width) and plane strain (infinite panel) beams, with the material constants to be calculated using Equations (7) and (8), respectively.

3. Potential and displacement field approximations

Consider a hybrid beam having any lay-up, whose thickness h and the number of layers L may vary segment-wise due to the presence of piezoelectric patches, which can be either surface-bonded or embedded; see Figure 2. The piezoelectric patches can have the poling direction parallel or normal to the z-axis, depending on their use in extension or shear mode. The longitudinal and thickness axes are along the x and z directions. The xy-plane is chosen to be the plane which is the midplane for most of the length of the beam. Let the planes $z = z_0$ and $z = z_L$ be the bottom and top surfaces of the beam, which
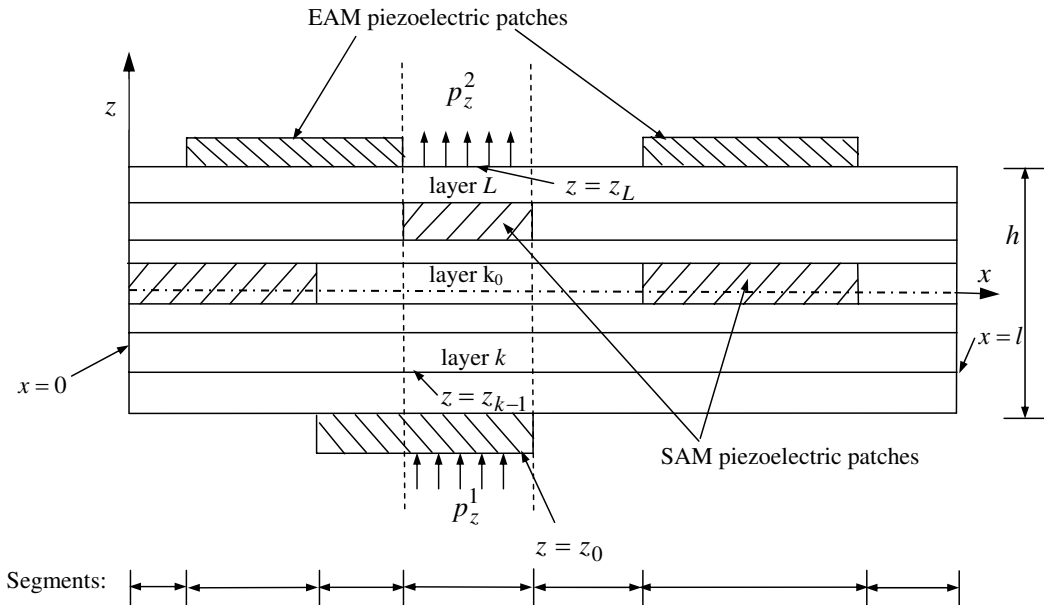
Figure 2. Geometry of hybrid beam with EAM and SAM piezoelectric patches.

may vary segment-wise. The z-coordinate of the bottom surface of the kth layer numbered from the bottom is denoted as z_{k-1} and its material axis x_1 has orientation angles α_k and β_k. The reference plane $z = 0$ either passes through or is the bottom surface of the k_0th layer. All the elastic and piezoelectric layers are perfectly bonded. The beam is loaded transversely on the bottom and top with no variation along the width b.

Two-dimensional coupled piezoelasticity solutions for piezoelectric beams/panels have revealed (see Section 6) that the electric potential ϕ follows a nearly quadratic distribution across the thickness for the extension mode [Dube et al. 1996] and a nearly cubic distribution with zero quadratic contribution for the shear mode [Parashar et al. 2005]. To model according to these observations, the potential field at time t is assumed as piecewise quadratic between n_ϕ points at $z = z_\phi^j$ across the thickness (Figure 3):

$$\phi(x, z, t) = \Psi_\phi^j(z)\phi^j(x, t) + \Psi_c^l(z)\phi_c^l(x, t), \tag{9}$$

where $\phi^j(x, t)$ is the electric potential at $z = z_\phi^j$, $\phi_c^l(x, t)$ denotes the quadratic component of electric potential at $z = (z_\phi^l + z_\phi^{l+1})/2$, and the summation convention is used with the indices j and l taking values $j = 1, 2, \ldots, n_\phi$ and $l = 1, 2, \ldots, n_\phi - 1$. $\Psi_\phi^j(z)$ and $\Psi_c^l(z)$ are the piecewise linear and quadratic functions, respectively, given by

$$\Psi_\phi^j(z) = \begin{cases} 0, & \text{if } z \leq z_\phi^{j-1} \quad \text{or} \quad z \geq z_\phi^{j+1}, \\ (z - z_\phi^{j-1})/(z_\phi^j - z_\phi^{j-1}), & \text{if } z_\phi^{j-1} < z < z_\phi^j, \\ (z_\phi^{j+1} - z)/(z_\phi^{j+1} - z_\phi^j), & \text{if } z_\phi^j < z < z_\phi^{j+1}, \end{cases}$$

$$\Psi_c^l(z) = \begin{cases} 4(z_\phi^{l+1} - z)(z - z_\phi^l)/(z_\phi^{l+1} - z_\phi^l)^2, & \text{if } z_\phi^l \leq z \leq z_\phi^{l+1}, \\ 0, & \text{otherwise.} \end{cases}$$

The surfaces of the piezoelectric sensor and actuator patches are always electroded with metallic coating, which makes the surfaces equipotential. Thus, ϕ^j should be taken as independent of x in a finite element
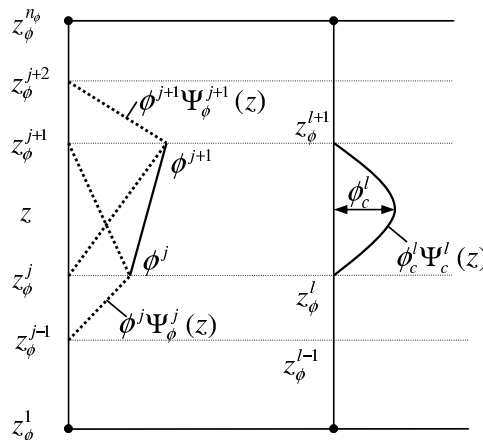
Figure 3. Approximation of ϕ along z-direction.

covering the electroded patch. With this description, ϕ in the piezoelectric layer can be modeled by a single layer discretization ($n_\phi = 2$) for the extension mode case and by a two-sublayer discretization ($n_\phi = 3$) for the shear mode case. In the latter case, since the quadratic contribution in the variation of ϕ is zero [Parashar et al. 2005], the mid-surface between the equipotential top and bottom surfaces will also be equipotential and, hence the above discretization holds well.

Exact 2D piezoelasticity solutions for hybrid beams and panels [Kapuria et al. 1997] have revealed that for moderately thick beams under electric field E_z the deflection w has significant variation across the thickness of the piezoelectric layers due to the significant contribution of E_z ($\bar{d}_{33}$ effect) to ε_z, which is much greater than the negligible contributions of the inplane electric field E_x and the stresses. Hence, w is approximated by integrating the constitutive Equation (4) for ε_z by neglecting the contributions of E_x and the stresses. It may be noted that the contribution of the inplane stresses to ε_z via Poisson's effect is neglected in most one-dimensional theories for elastic laminated beams, wherein w is approximated to be constant across the thickness. Thus, integrating $\varepsilon_z = w_{,z} = \bar{s}_{13}\sigma_x + \bar{s}_{23}\sigma_y + \bar{d}_{13}E_x + \bar{d}_{33}E_z \simeq -\bar{d}_{33}\phi_{,z}$ yields

$$w(x, z, t) = w_0(x, t) - \delta_1\{\bar{\Psi}_\phi^j(z)\phi^j(t) + \bar{\Psi}_c^l(z)\phi_c^l(t)\}, \tag{10}$$

where $\delta = 1$ or 0 depending upon whether or not the nonuniformity terms are considered, and

$$\bar{\Psi}_\phi^j(z) = \int_0^z \bar{d}_{33}\Psi_{\phi,z}^j(z)\,dz, \qquad \bar{\Psi}_c^l = \int_0^z \bar{d}_{33}\Psi_{c,z}^l(z)\,dz.$$

A subscript comma denotes differentiation. The axial displacement u is assumed to follow a global third-order variation with a layerwise linear variation across the thickness [Shu and Sun 1994; Kapuria et al. 2003]:

$$u(x, z, t) = u_k(x, t) - zw_{0,x}(x, t) + z\psi_k(x, t) + z^2\xi(x, t) + z^3\eta(x, t),$$

where u_k and ψ_k denote the translation and shear rotation variables of the kth layer, representing the layerwise linear variation, and ξ and η are the quadratic and cubic terms in z, representing the global cubic variation across the entire laminate thickness. The $2L + 3$ displacement variables u_k, ψ_k, ξ, η and w_0 are expressed in terms of only three variables by imposing the $2(L-1)$ conditions of continuity of transverse shear stress τ_{zx} and u at the layer interfaces, and the two conditions of zero transverse shear at the top and bottom surfaces. This gives

$$u(x, z, t) = u_0(x, t) - zw_{0,x}(x, t) + R^k(z)\psi_0(x, t), \tag{11}$$

where u_0 denotes the axial displacement of the reference ($z = 0$) plane and ψ_0 is related to the shear strain of the reference plane. $R^k(z)$ is a layer-wise function of z for the kth layer given by

$$R^k(z) = \hat{R}_1^k + z\hat{R}_2^k + z^2\hat{R}_3 + z^3\hat{R}_4, \tag{12}$$

where the coefficients $\hat{R}_1^k$, $\hat{R}_2^k$, $\hat{R}_3$ and $\hat{R}_4$ are dependent on the lay-up and the material properties of the layers and are defined in the Appendix. Equation (11) for u can expressed as

$$u = f_1(z)\bar{u}_1, \tag{13}$$

where

$$\bar{u}_1 = \begin{bmatrix} u_0 & -w_{0,x} & \psi_0 \end{bmatrix}^{\mathrm{T}}, \qquad f_1(z) = \begin{bmatrix} 1 & z & R^k(z) \end{bmatrix}.$$

Using Equations (9), (10) and (13), the strains and the electric fields can be expressed as

$$
\begin{aligned}
\varepsilon_x = u_{,x} = f_1(z)\bar{\varepsilon}_1, && E_x = -\phi_{,x} = -f_3(z)\bar{\varepsilon}_3, \\
\gamma_{zx} = u_{,z} + w_{,x} = f_2(z)\bar{\varepsilon}_2, && E_z = -\phi_{,z} = -f_4(z)\bar{\varepsilon}_4,
\end{aligned}
\tag{14}
$$

with

$$
\bar{\varepsilon}_1 = \bar{u}_{1,x} = \begin{bmatrix} u_{0,x} & -w_{0,xx} & \psi_{0,x} \end{bmatrix}^{\mathrm{T}}, \quad \bar{\varepsilon}_2 = \begin{bmatrix} \psi_0 & -\phi_{c,x}^l \end{bmatrix}^{\mathrm{T}}, \quad \bar{\varepsilon}_3 = \phi_{c,x}^l, \quad \bar{\varepsilon}_4 = \begin{bmatrix} \phi_c^l & \phi^j \end{bmatrix}^{\mathrm{T}},
\tag{15}
$$
$$
f_2(z) = \begin{bmatrix} R_{,z}^k(z) & \delta_1 \bar{\Psi}_c^l(z) \end{bmatrix}, \quad f_3(z) = \Psi_c^l(z), \quad f_4(z) = \begin{bmatrix} \Psi_{c,z}^l(z) & \Psi_{\phi,z}^j(z) \end{bmatrix}.
$$

4. Variational principle for the coupled one-dimensional theory

Let p_z^1, p_z^2 be the normal forces per unit area on the bottom and top surfaces of the beam in direction z. Let there be distributed viscous resistance force with the distributed viscous damping coefficient c_1 per unit area per unit transverse velocity of the top surface of the beam. Using the notation

$$
\langle \ldots \rangle = \sum_{k=1}^{L} \int_{z_{k-1}^+}^{z_k^-} (\ldots) b \, dz
$$

for integration across the thickness, the extended Hamilton's principle [Tiersten 1969] for the beam reduces to

$$
\begin{aligned}
\int_x & \Big[\langle \rho^k \ddot{u} \delta u + \rho^k \ddot{w} \delta w + \sigma_x \delta \varepsilon_x + \tau_{zx} \delta \gamma_{zx} - D_x \delta E_x - D_z \delta E_z \rangle - b p_z^1 \delta w(x, z_0, t) \\
& - b \{ p_z^2 - c_1 \dot{w}(x, z_L, t) \} \delta w(x, z_L, t) + b D_z(x, z_0, t) \delta \phi^1 - b D_z(x, z_L, t) \delta \phi^{n\phi} \Big] dx \\
& \hspace{5cm} - \langle \sigma_x \delta u + \tau_{zx} \delta w + D_x \delta \phi \rangle \big|_x = 0, \quad (16)
\end{aligned}
$$

for all δu_0, δw_0, $\delta \psi_0$, $\delta \phi_c^l$, $\delta \phi^j$, where ρ^k is the material mass density of the kth layer. It has been observed elsewhere [Kapuria and Alam 2006] that the explicit contribution of electric potential terms in w (see Equation (10)) to inertia and damping can be neglected to achieve computational efficiency without sacrificing virtually any accuracy. Considering this, substituting the expressions (9), (10) and (13) for ϕ, w and u and (14) for ε_x, γ_{zx}, E_x, E_z into Equation (16) yields

$$
\begin{aligned}
\int_x & \Big[\delta \bar{u}_1^{\mathrm{T}} I \ddot{\bar{u}}_1 + \delta w_0 \hat{I} \ddot{w}_0 + \delta \bar{\varepsilon}_1^{\mathrm{T}} F_1 + \delta \bar{\varepsilon}_2^{\mathrm{T}} F_2 + \delta \bar{\varepsilon}_3^{\mathrm{T}} F_3 + \delta \bar{\varepsilon}_4^{\mathrm{T}} F_4 - (P_2 + \hat{P}_2) \delta w_0 - P_\phi^j \delta \phi^j \Big] dx \\
& - \Big[\bar{N}_x \delta \bar{u}_0 + \bar{V}_x \delta \bar{w}_0 - \bar{M}_x \delta \bar{w}_{0,x} + \bar{P}_x \delta \bar{\psi}_0 + (\bar{H}^j - \delta_1 \bar{V}_\phi^j) \delta \bar{\phi}^j + (\bar{H}_c^l - \delta_1 \bar{V}_c^l) \delta \bar{\phi}_c^l \Big] \big|_x = 0, \quad (17)
\end{aligned}
$$

where an over-bar on the stress and electric resultants and on u_0, w_0, ψ_0, ϕ^j, ϕ_c^l means values at the ends. In this equation, I and $\hat{I}$ are the inertia terms defined by

$$
I = \langle \rho^k f_1^{\mathrm{T}}(z) f_1(z) \rangle = \begin{bmatrix} I_{11} & I_{12} & I_{13} \\ I_{12} & I_{22} & I_{23} \\ I_{13} & I_{23} & I_{33} \end{bmatrix}, \qquad \hat{I} = \langle \rho^k \rangle = I_{11}.
\tag{18}
$$

The stress resultants F_1 of σ_x, F_2, V_x, V_ϕ^j, V_c^l of τ_{zx}, and the electric displacement resultants F_3, H^j of D_x and F_4 of D_z are defined by

$$F_1 = \begin{bmatrix} N_x \\ M_x \\ P_x \end{bmatrix} = \langle f_1^{\mathrm{T}}(z)\sigma_x \rangle, \quad F_2 = \begin{bmatrix} Q_x \\ \bar{Q}_x^l \end{bmatrix} = \langle f_2^{\mathrm{T}}(z)\tau_{zx} \rangle, \quad F_3 = H_c^l = \langle f_3(z)D_x \rangle, \tag{19}$$

$$F_4 = \begin{bmatrix} G_c^l \\ G^j \end{bmatrix} = \langle f_4^{\mathrm{T}}(z)D_z \rangle, \quad H^j = \langle \Psi_\phi^j(z)D_x \rangle, \quad V_x = \langle \tau_{zx} \rangle, \quad V_\phi^j = \langle \bar{\Psi}_\phi^j(z)\tau_{zx} \rangle, \quad V_c^l = \langle \bar{\Psi}_c^l(z)\tau_{zx} \rangle. \tag{20}$$

The mechanical load P_2, electrical loads P_ϕ^j and damping load $\hat{P}_2$ are defined as

$$P_2 = b(p_z^1 + p_z^2), \qquad P_\phi^j = b\big[-p_z^1 \bar{\Psi}_\phi^j(z_0) - p_z^2 \bar{\Psi}_\phi^j(z_L) + D_{z_L}\delta_{jn_\phi} - D_{z_0}\delta_{j1} \big], \qquad \hat{P}_2 = -\hat{c}_1 \dot{w}_0,$$

where δ_{ij} is Kronecker's delta, $D_{z_0} = D_z(x, z_0, t)$, $D_{z_L} = D_z(x, z_L, t)$ and $\hat{c}_1 = bc_1$.

Define generalized strains $\bar{\varepsilon}$ and generalized stress resultants $\bar{F}$ as

$$\bar{\varepsilon} = \begin{bmatrix} \bar{\varepsilon}_1^{\mathrm{T}} & \bar{\varepsilon}_2^{\mathrm{T}} & \bar{\varepsilon}_3^{\mathrm{T}} & \bar{\varepsilon}_4^{\mathrm{T}} \end{bmatrix}^{\mathrm{T}}, \qquad \bar{F} = \begin{bmatrix} F_1^{\mathrm{T}} & F_2^{\mathrm{T}} & F_3^{\mathrm{T}} & F_4^{\mathrm{T}} \end{bmatrix}^{\mathrm{T}}. \tag{21}$$

Substituting the constitutive Equation (6) into Equation (19), the beam constitutive equation relating the generalized beam stress resultants $\bar{F}$ with the generalized strains $\bar{\varepsilon}$ can be obtained as

$$\bar{F} = \bar{D}\bar{\varepsilon}, \tag{22}$$

where

$$\bar{D} = \begin{bmatrix} A & 0 & e_1^{\mathrm{T}} & e_2^{\mathrm{T}} \\ 0 & \bar{A} & e_3^{\mathrm{T}} & e_4^{\mathrm{T}} \\ e_1 & e_3 & -\eta_1 & -\eta_2^{\mathrm{T}} \\ e_2 & e_4 & -\eta_2 & -\eta_3 \end{bmatrix}, \tag{23}$$

with

$$A = \langle \hat{Q}_{11} f_1^{\mathrm{T}}(z)f_1(z) \rangle = \begin{bmatrix} A_{11} & A_{12} & A_{13} \\ A_{12} & A_{22} & A_{23} \\ A_{13} & A_{32} & A_{33} \end{bmatrix}, \qquad \bar{A} = \langle \hat{Q}_{55} f_2^{\mathrm{T}}(z)f_2(z) \rangle = \begin{bmatrix} \bar{A}_{11} & \bar{A}_{12}^{l'} \\ \bar{A}_{12}^{l} & \bar{A}_{22}^{ll'} \end{bmatrix}_{n_\phi \times 3},$$

$$e_1 = \langle \hat{e}_{11} f_3^{\mathrm{T}}(z)f_1(z) \rangle = \begin{bmatrix} e_1^{1l} & e_2^{1l} & e_3^{1l} \end{bmatrix}_{(n_\phi-1)\times 3}, \qquad e_2 = \langle \hat{e}_{31} f_4^{\mathrm{T}}(z)f_1(z) \rangle = \begin{bmatrix} e_{11}^{2l} & e_{12}^{2l} & e_{13}^{2l} \\ e_{21}^{2j} & e_{22}^{2j} & e_{23}^{2j} \end{bmatrix}_{(2n_\phi-1)\times 3},$$

$$e_3 = \langle \hat{e}_{15} f_3^{\mathrm{T}}(z)f_2(z) \rangle = \begin{bmatrix} e_1^{3l} & \delta_1 e_2^{3ll'} \end{bmatrix}_{(n_\phi-1)\times n_\phi}, \qquad e_4 = \langle \hat{e}_{35} f_4^{\mathrm{T}}(z)f_2(z) \rangle = \begin{bmatrix} e_{11}^{4l} & \delta_1 e_{12}^{4ll'} \\ e_{21}^{4j} & \delta_1 e_{22}^{4jl'} \end{bmatrix}_{(2n_\phi-1)\times n\phi},$$

$$\eta_1 = \langle \hat{\eta}_{11} f_3^{\mathrm{T}}(z)f_3(z) \rangle = \begin{bmatrix} \eta_1^{ll'} \end{bmatrix}_{(n_\phi-1)\times(n_\phi-1)}, \qquad \eta_2 = \langle \hat{\eta}_{13} f_4^{\mathrm{T}}(z)f_3(z) \rangle = \begin{bmatrix} \eta_1^{2ll'} \\ \eta_2^{2jl'} \end{bmatrix}_{(2n_\phi-1)\times(n_\phi-1)},$$

$$\eta_3 = \langle \hat{\eta}_{33} f_4^{\mathrm{T}}(z)f_4(z) \rangle = \begin{bmatrix} \eta_{11}^{3ll'} & \eta_{12}^{3lj'} \\ \eta_{12}^{3jl'} & \eta_{22}^{3jj'} \end{bmatrix}_{(2n_\phi-1)\times(2n_\phi-1)}. \tag{24}$$

The indices l' and j' take values $l' = 1, 2, \ldots, n_\phi - 1$ and $j' = 1, 2, \ldots, n_\phi$ like l and j, respectively. Using Equations (21) and (22), the contribution T^e of an element of length a to the integral in Equation (17) can be expressed as

$$T^e = \int_0^a \left[\delta \bar{u}^\mathrm{T} \bar{I} \ddot{\bar{u}} + \delta \bar{\varepsilon}^\mathrm{T} \bar{D} \bar{\varepsilon} - \delta \bar{u}^\mathrm{T} f_{u\phi} + \delta \bar{u}^\mathrm{T} \bar{C} \dot{\bar{u}} \right] dx, \tag{25}$$

where

$$\bar{u} = \left[\bar{u}_1^\mathrm{T} \ w_0 \ \phi^j \right]^\mathrm{T} = \left[u_0 \ -w_{0,x} \ \psi_0 \ w_0 \ \phi^j \right]^\mathrm{T}, \tag{26}$$

$$\bar{I} = \begin{bmatrix} I & 0 & 0 \\ 0 & \hat{I} & 0 \\ 0 & 0 & 0 \end{bmatrix}, \qquad \bar{C} = \begin{bmatrix} 0 & 0 & 0 \\ 0 & \hat{c}_1 & 0 \\ 0 & 0 & 0 \end{bmatrix}, \qquad f_{u\phi} = \left[0 \ P_2 \ P_\phi^j \right]^\mathrm{T}. \tag{27}$$

5. Finite element model

The highest derivatives of u_0, ψ_0, w_0, ϕ_c^l and ϕ^j appearing in the variational Equation (17) are $u_{0,x}$, $w_{0,xx}$, $\psi_{0,x}$, $\phi_{c,x}^l$ and ϕ^j. Accordingly, to meet the convergence requirement, the interpolation functions for u_0, $w_{0,x}$, ψ_0 and ϕ_c^l must be continuous at the element boundaries. These variables are interpolated using two physical nodes as shown in Figure 4. The variable w_0 is interpolated using the C^1-continuous cubic Hermitian function in terms of the nodal values of w_0, $w_{0,x}$, and u_0, ψ_0, ϕ_c^l are interpolated using a C^0-continuous linear Lagrangian function. Since ψ_0 is a measure of shear strain at the reference plane and not the rotation of the normal, a linear interpolation for ψ_0 does not cause shear locking [Kapuria and Alam 2006]. Thus, at the element level, each physical node will have four degrees of freedom, u_0, w_0, $w_{0,x}$, ψ_0, for the displacements and $(n_\phi - 1)$ degrees of freedom of ϕ_c^l for the electric potential.

As stated in Section 3, ϕ^j is constant in an element. However, if a number of elements fall in the same electroded surface, it would be necessary to impose the constraint of equality on the electric DOF ϕ^j of the elements on the same electroded surface. To avoid this task, the set of ϕ^j of the equipotential surfaces of piezoelectric patches in a beam section are associated with a separate *electric node* p, see Figure 4, which can be connected to several elements. The electric node does not have any x-coordinate unlike the physical nodes, and has n_ϕ degrees of freedom. This concept not only eliminates the need of imposing equality constraints on the electric DOF for equipotential condition, but also results in
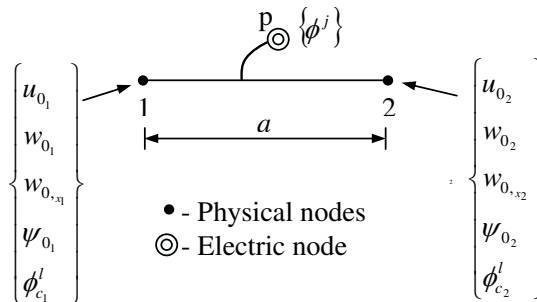
Figure 4. Degrees of freedom for the beam element.

significant reduction in the number electric DOF. Thus, denoting the values of an entity (.) at the physical node i by $(\,.\,)_i$, the variables $u_0, \psi_0, w_0, \phi_c^l$ are interpolated in an element of length a as

$$u_0 = Nu_0^e, \qquad w_0 = \bar{N}w_0^e, \qquad \psi_0 = N\psi_0^e, \qquad \phi_c^l = N\phi_c^{le}, \tag{28}$$

with

$$u_0^e = \begin{bmatrix} u_{0_1} & u_{0_2} \end{bmatrix}^{\mathrm{T}}, \quad w_0^e = \begin{bmatrix} w_{0_1} & w_{0,x_1} & w_{0_2} & w_{0,x_2} \end{bmatrix}^{\mathrm{T}}, \quad \psi_0^e = \begin{bmatrix} \psi_{0_1} & \psi_{0_2} \end{bmatrix}^{\mathrm{T}}, \quad \phi_c^{le} = \begin{bmatrix} \phi_{c_1}^l & \phi_{c_2}^l \end{bmatrix}^{\mathrm{T}},$$

$$N = \begin{bmatrix} N_1 & N_2 \end{bmatrix}, \qquad \bar{N} = \begin{bmatrix} \bar{N}_1 & \bar{N}_2 & \bar{N}_3 & \bar{N}_4 \end{bmatrix}, \qquad N_1 = 1 - (x/a), \qquad N_2 = \frac{x}{a},$$

$$\bar{N}_1 = 1 - \frac{3x^2}{a^2} + \frac{2x^3}{a^3}, \qquad \bar{N}_2 = x - \frac{2x^2}{a} + \frac{x^3}{a^2}, \qquad \bar{N}_3 = \frac{3x^2}{a^2} - \frac{2x^3}{a^3}, \qquad \bar{N}_4 = -\frac{x^2}{a} + \frac{x^3}{a^2}.$$

Defining the element generalized displacement vector U^e as $U^{e\mathrm{T}} = [u_0^{e\mathrm{T}} \ w_0^{e\mathrm{T}} \ \psi_0^{e\mathrm{T}} \ \phi_c^{le\mathrm{T}} \ \phi^j]$ and using Equation (28), the generalized displacements $\bar{u}$ and strains $\bar{\varepsilon}$ defined in Equations (15), (21) and (26) can be related to U^e as

$$\bar{u} = \hat{N}U^e, \qquad \bar{\varepsilon} = \hat{B}U^e, \tag{29}$$

where

$$\hat{N} = \begin{bmatrix} N & 0 & 0 & 0 & 0 \\ 0 & -\bar{N}_{,x} & 0 & 0 & 0 \\ 0 & 0 & N & 0 & 0 \\ 0 & \bar{N} & 0 & 0 & 0 \\ 0 & 0 & 0 & 0 & 1 \end{bmatrix}, \qquad \hat{B} = \begin{bmatrix} N_{,x} & 0 & 0 & 0 & 0 \\ 0 & -\bar{N}_{,xx} & 0 & 0 & 0 \\ 0 & 0 & N_{,x} & 0 & 0 \\ 0 & 0 & N & 0 & 0 \\ 0 & 0 & 0 & -N_{,x} & 0 \\ 0 & 0 & 0 & N_{,x} & 0 \\ 0 & 0 & 0 & N & 0 \\ 0 & 0 & 0 & 0 & 1 \end{bmatrix}. \tag{30}$$

Substituting the expressions for $\hat{u}$ and $\hat{\varepsilon}$ from Equation (29) into Equation (25), T^e can be expressed as

$$T^e = \int_0^a \delta U^{e\mathrm{T}} \big[\hat{N}^{\mathrm{T}} \bar{I} \hat{N} \ddot{U}^e + \hat{N}^{\mathrm{T}} \bar{C} \hat{N} \dot{U}^e + \hat{B}^{\mathrm{T}} \bar{D} \hat{B} U^e - \hat{N}^{\mathrm{T}} f_{u\phi} \big] \, dx$$

$$= \delta U^{e\mathrm{T}} \big[M^e \ddot{U}^e + C^e \dot{U}^e + K^e U^e - P^e \big],$$

where M^e, C^e and K^e are the generalized element inertia, damping and stiffness matrices, and P^e is the element load vector defined as

$$M^e = \int_0^a \hat{N}^{\mathrm{T}} \bar{I} \hat{N} \, dx = \begin{bmatrix} M_{uu}^e & 0 & 0 \\ 0 & 0 & 0 \\ 0 & 0 & 0 \end{bmatrix}, \qquad C^e = \int_0^a \hat{N}^{\mathrm{T}} \bar{C} \hat{N} \, dx = \begin{bmatrix} C_{uu}^e & 0 & 0 \\ 0 & 0 & 0 \\ 0 & 0 & 0 \end{bmatrix},$$

$$K^e = \int_0^a \hat{B}^{\mathrm{T}} \bar{D} \hat{B} \, dx = \begin{bmatrix} K_{uu}^e & K_{ul}^e & K_{uj}^e \\ K_{lu}^e & K_{ll}^e & K_{lj}^e \\ K_{ju}^e & K_{jl}^e & K_{jj}^e \end{bmatrix}, \qquad P^e = \int_0^a \hat{N}^{\mathrm{T}} f_{u\phi} \, dx = \begin{bmatrix} P_u^e \\ 0 \\ P_j^e \end{bmatrix}. \tag{31}$$

The subscripts u, l and j correspond to the mechanical displacement variables, ϕ_c^l and ϕ^j, respectively. The elements of the submatrices in Equation (31) are listed in the Appendix. The elements of the same

electroded surface are connected to one electric node having a global degree of freedom number for the potential ϕ^j of the equipotential surface at $z = z_\phi^j$. The node numbers of the two physical nodes and the electric node of each element are stored in the element connectivity matrix. The element matrices are then assembled using the standard assembly procedure, by storing the global DOF numbers of all element DOF in an index matrix, and placing the elements of the element matrix in the appropriate locations of the global matrix, according to the global DOF numbers [Chandrupatla and Belegundu 2002]. Summing up contributions of all elements to the integral in Equation (17), the system equation can be obtained as

$$M\ddot{U} + C\dot{U} + KU = P, \tag{32}$$

in which M, C, K are assembled from the element matrices M^e, C^e, K^e and U, P are the assembled counterparts of U^e, P^e.

At the actuated surfaces (closed circuit condition), electric potentials have known prescribed values. At the sensory surfaces under open circuit condition, the electric loads are known (zero electric charge, that is, $\int_0^{a_e} bD_z\,dx = 0$, a_e being the length of the electrode), but the electric potentials are unknown. The system vector U is partitioned into vectors of mechanical displacements $\bar{U}$, unknown output voltages Φ_s and known input actuation voltages Φ_a. Thus, Equation (32) can be partitioned and arranged as

$$
\begin{bmatrix} M^{uu} & 0 & 0 \\ 0 & 0 & 0 \\ 0 & 0 & 0 \end{bmatrix}
\begin{bmatrix} \ddot{\bar{U}} \\ \ddot{\Phi}_s \\ \ddot{\Phi}_a \end{bmatrix}
+
\begin{bmatrix} C^{uu} & 0 & 0 \\ 0 & 0 & 0 \\ 0 & 0 & 0 \end{bmatrix}
\begin{bmatrix} \dot{\bar{U}} \\ \dot{\Phi}_s \\ \dot{\Phi}_a \end{bmatrix}
+
\begin{bmatrix} K^{uu} & K^{us} & K^{ua} \\ K^{su} & K^{ss} & K^{sa} \\ K^{au} & K^{as} & K^{aa} \end{bmatrix}
\begin{bmatrix} \bar{U} \\ \Phi_s \\ \Phi_a \end{bmatrix}
=
\begin{bmatrix} \bar{P} \\ Q_s \\ Q_a \end{bmatrix}. \tag{33}
$$

Equation (33) yields the output potentials as

$$\Phi_s = -(K^{ss})^{-1}\big[K^{su}\bar{U} + K^{sa}\Phi_a - Q_s\big]. \tag{34}$$

Substitution of Equation (34) into Equation (33) yields

$$M^{uu}\ddot{\bar{U}} + C^{uu}\dot{\bar{U}} + \big[K^{uu} - K^{us}(K^{ss})^{-1}K^{su}\big]\bar{U} = \bar{P} - K^{us}(K^{ss})^{-1}Q_s - \big[K^{ua} - K^{us}(K^{ss})^{-1}K^{sa}\big]\Phi_a. \tag{35}$$

For undamped free vibration, the damping matrix C^{uu} and the right-hand side vector of the above equation are set to zero. The resulting generalized eigenvalue problem is solved using subspace iteration method [Petyt 1990] to obtain the undamped natural frequencies ω and the mode shapes. For transient response, Equation (35) can be solved using Newmark direct time integration method [Petyt 1990]. The advantage of first partitioning the electric potential vector Φ into Φ_s and Φ_a, and then carrying out the condensation as per Equations (34) and (35) is that it can model the response of the structure under any electric boundary conditions, namely, in the active mode (closed circuit), the sensory mode (open circuit) and the combined *active-sensory* mode (some electrodes in open circuit and some in closed circuit). In contrast, if the entire electric potential vector Φ is condensed out as in [Tzou and Tseng 1990], the resulting free vibration problem would give only the open circuit frequencies.

Equation (17) indicates that the mechanical boundary conditions for simply-supported, clamped and free ends are:

simply-supported	$N_x = 0,$	$w_0 = 0,$	$M_x = 0,$	$P_x = 0,$
clamped	$u_0 = 0,$	$w_0 = 0,$	$w_{0,x} = 0,$	$\psi_0 = 0,$
free	$N_x = 0,$	$V_x = 0,$	$M_x = 0,$	$P_x = 0.$

6. Results and discussion

6.1. *Validation.* In order to validate the new FE formulation and the computer program developed, cantilever plane strain beams (a) and (b) made of aluminum substrate with surface-bonded and embedded PZT-5H layers, respectively, are considered, which have been analyzed in [Zhang and Sun 1996; Benjeddou et al. 1999]. The configurations and the dimensions of the beams are shown in Figure 5 and the material properties are selected as in the references mentioned above:

(i) PZT-5H:

$$\{c_{11}, c_{22}, c_{33}, c_{12}, c_{23}, c_{31}, c_{44}, c_{55}, c_{66}\} = \{126, 126, 117, 79.5, 84.1, 84.1, 23, 23, 23.25\} \text{ GPa},$$

$$\{e_{31}, e_{32}, e_{33}, e_{15}, e_{24}\} = \{-6.5, -6.5, 23.3, 17.0, 17.0\} \text{ C/m}^2,$$

$$\{\eta_{11}, \eta_{22}, \eta_{33}\} = \{1.503, 1.503, 1.3\} \times 10^{-8} \text{ F/m}, \rho = 7500 \text{ kg/m}^3;$$

Adaptive SAM beam (a)

Bimorph EAM beam (c)

Adaptive EAM beam (b)

SAM piezoelecric beam (d)

Adaptive SAM-EAM composite beam (e)
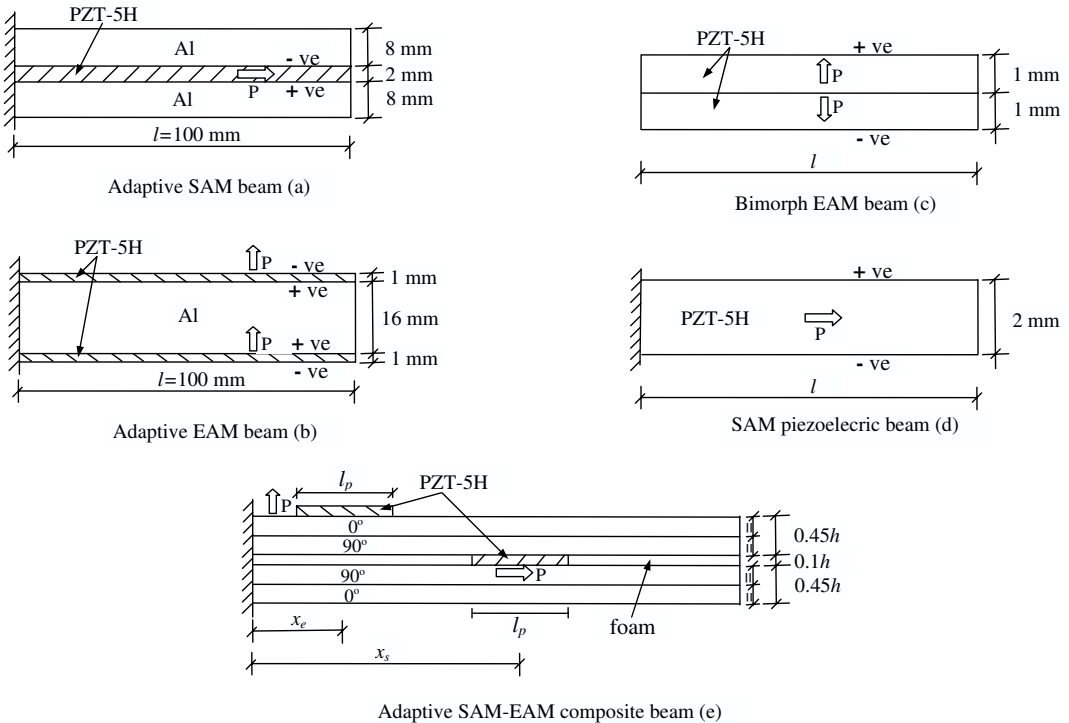
Figure 5. Configurations of SAM and EAM beams.

(ii) Al:

$$Y_1 = Y_2 = Y_3 = Y = 70.3\text{GPa}, \nu_{12} = \nu_{23} = \nu_{31} = \nu = 0.345, \rho = 2710\,\text{kg/m}^3,$$

where Y_i and ν_{ij} denote the Young's moduli and Poisson's ratios.

In beam (a) the piezoelectric layer embedded between the two aluminum layers is polarized along the axial direction x ($\alpha = 0$, $\beta = -90°$), and hence an applied electric potential across its thickness gives rise to shear mode actuation. For actuation, a voltage of 20 V is applied at the bottom surface of the actuator, while its top surface is grounded. In beam (b) the surface-mounted PZT layers at the top and bottom of the aluminum substrate are polarized along the thickness direction z, and hence an applied electric potential across its thickness causes extension mode actuation. In this case a potential of -10 V is applied at the top and bottom surfaces of the beam for actuation. Both the beams are modeled with 20 equal-size elements to obtain converged results. The shear mode piezoelectric layer in beam (a) is divided into two sublayers and those in beam (b) are modeled as one sublayer for the discretization of potential ϕ. The present results for the deflection profile of the centerline ($z = 0$) are compared in Figure 6 with the FE FSDT results of Benjeddou et al. [1999] for beam (a) and with the analytical FSDT solution of Zhang and Sun [1996] for beam (b). It is found that the present results are in excellent agreement with the reference results in both cases. The beams are also analyzed using the commercial FE software ABAQUS employing eight-node plane strain element, CPE8RE, with a mesh of 20 (thickness)$\times$50 (length). The 2D FE results are also plotted in Figure 6, which compare very well with the present results.

The present result for the tip deflection of the shear actuated beam (a) is compared in Table 1 with other available results. While the present result and those obtained using a sandwich model using FSDT for the core [Zhang and Sun 1996; Benjeddou et al. 1999] match closely with the 2D FE results of ABAQUS, while those reported by Trindade and Benjeddou [2005] considering an improved sandwich model with the core modeled with the TOT have considerable difference from the 2D results. This difference between the FSDT and the TOT modeling of the core predicted by Trindade and Benjeddou [2005] appears to be inconsistent, since the 2D FE solution does not involve any approximation on the through-the-thickness variations of field variables and hence are accurate. The electric field E_z in the
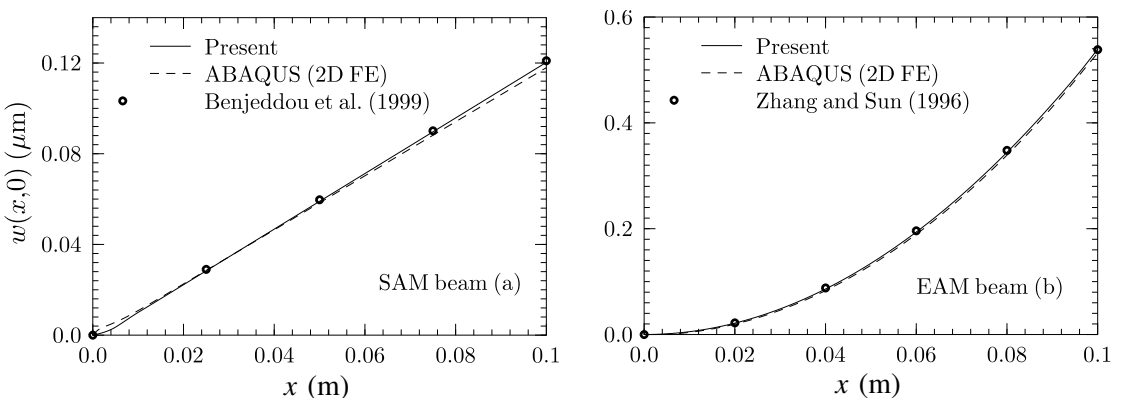
Figure 6. Central deflection of beams with shear and extension mode actuators under potential load.

Model	$w(l, 0)$ (μm)	E_z (V/mm)
Present	0.1203	10
FSDT analytic [Zhang and Sun 1996]	0.1196	10
FSDT FE [Benjeddou et al. 1999]	0.1196	10
TSDT FE, ϕ linear [Trindade and Benjeddou 2005]	0.0999	–
TSDT FE, ϕ cubic [Trindade and Benjeddou 2005]	0.0879	6.94–16.11
ABAQUS	0.1180	10

Table 1. Tip deflection of SAM beam (a) under actuation potential of 20 V.

piezoelectric layer obtained from different models are also compared in Table 1. It is seen from the 2D FE results that E_z is almost uniform across the thickness of the PZT layer and the same is predicted by the present model. Trindade and Benjeddou [2005] have, however, reported a quadratic variation of E_z across the thickness, which is attributed to the induced potential due to the direct piezoelectric effect. This also seems incorrect, since the 2D results show no such trend. It may also be noted that while Zhang and Sun [1996] and Benjeddou et al. [1999] have assumed a linear variation for the electric potential ϕ, the present model with 2 sublayers in the PZT layer can capture the cubic variation of ϕ, and has still predicted a practically linear variation of ϕ as in the 2D solution. The cubic component of ϕ induced to the direct piezoelectric effect is predicted as 0.010 V only, which is very small compared to the applied electric potential of 20 V.

Beams (a) and (b) are also analyzed for a uniform pressure load of $p_z^2 = 1000$ N/m^2 with the surfaces of the PZT layers kept at zero potential (closed circuit condition). The midsurface deflection obtained from the present one-dimensional model is compared with 2D FE result of ABAQUS in Figure 7. The two results are found to be in excellent agreement for both SAM and EAM beams.

No results for the free vibration response of the above beams have been reported in literature. To validate the present model for the free vibration response, the present results for natural frequencies of the first 7 modes (of which five are flexural modes and two are extension modes) are compared in Table 2
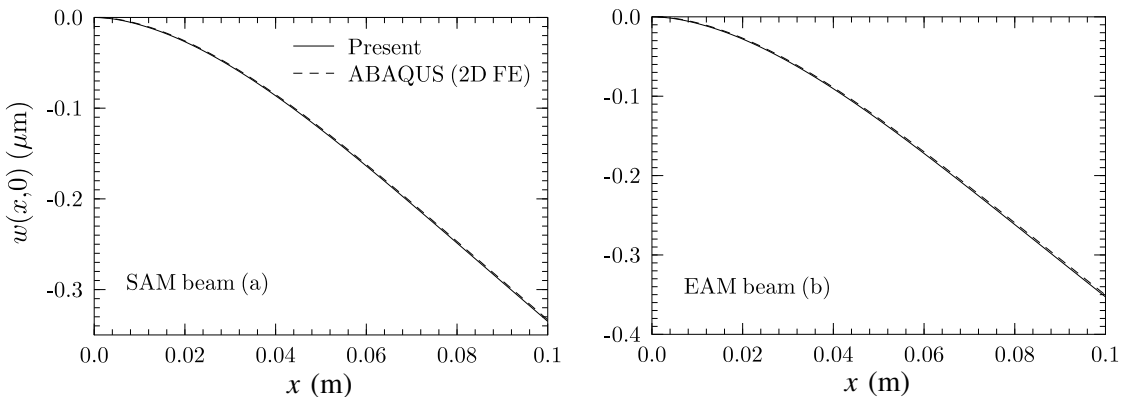
Figure 7. Central deflection of beams with shear and extension mode actuators under pressure load.

Beam	Mode, n	Type	Frequency, f_n (Hz)			
			ABAQUS (2D FE)	Present model (# of elts.)		
				10	20	30
	1	flexural	1414.6	1404.2	1403.6	1403.4
	2	flexural	7796.2	7728.6	7693.5	7684.0
	3	extension	12799	12251	12242	12240
(a)	4	flexural	18876	18757	18582	18537
	5	flexural	31767	31693	31234	31125
	6	extension	38057	37056	36801	36754
	7	flexural	45598	45764	44815	44622
	1	flexural	1370.8	1365.1	1364.5	1364.4
	2	flexural	7475.6	7471.5	7439.6	7430.9
	3	extension	12345	12292	12282	12280
(b)	4	flexural	17996	18053	17897	17855
	5	flexural	30172	30381	29969	29868
	6	extension	36752	37179	36922	36875
	7	flexural	43207	43715	42870	42691

Table 2. Closed circuit natural frequencies of SAM beam (a) and EAM beam (b).

with the 2D FE results obtained using ABAQUS. The present results are obtained with 10, 20 and 30 equal-size elements to study the convergence. It is observed that very good convergence is achieved with 20 elements, and the present results are in excellent agreement with the 2D FE results with a maximum error of 0.8% for the fundamental frequency and 2% for the higher mode frequencies up to the 7th mode (5th flexural mode).

6.2. *Bimorph EAM beam.* A simply-supported plane-stress (thin width) bimorph extension mode actuator beam (c) made of two layers of PZT-5H polarized along opposite transverse directions, see Figure 5, is analyzed for the following two load cases:

(1) Uniform potential $\phi^{n_\phi} = \phi_0$ applied on the top surface with the bottom being grounded ($\phi^1 = 0$).

(2) Uniform pressure $p_z^2 = -p_0$ applied on the top surface with $\phi^{n_\phi} = \phi^1 = 0$ (closed circuit condition).

These results and all subsequent ones for beams (c) and (d) for the potential and pressure load cases are nondimensionalized as:

1. $\bar{w} = 10w/S^2 d_0 \phi_0,$ $\bar{\sigma}_x = \sigma_x h/10 Y_0 d_0 \phi_0,$ $\bar{\phi} = \phi/\phi_0,$

2. $\bar{w} = w Y_0/l S^3 p_0,$ $\bar{\sigma}_x = \sigma_x/S^2 p_0,$ $\bar{\phi} = 100 \phi Y_0 d_0/h S^2 p_0,$

with $Y_0 = 60\,\text{GPa}$ and $d_0 = 274.8 \times 10^{-12}\,\text{CN}^{-1}$. S is the span-to-thickness ratio (l/h). Using symmetry the half length of the beam is discretized with 20 equal-size elements and only one electric node is used to model the closed circuit equipotential surfaces at the top and bottom. Each PZT layer is considered as
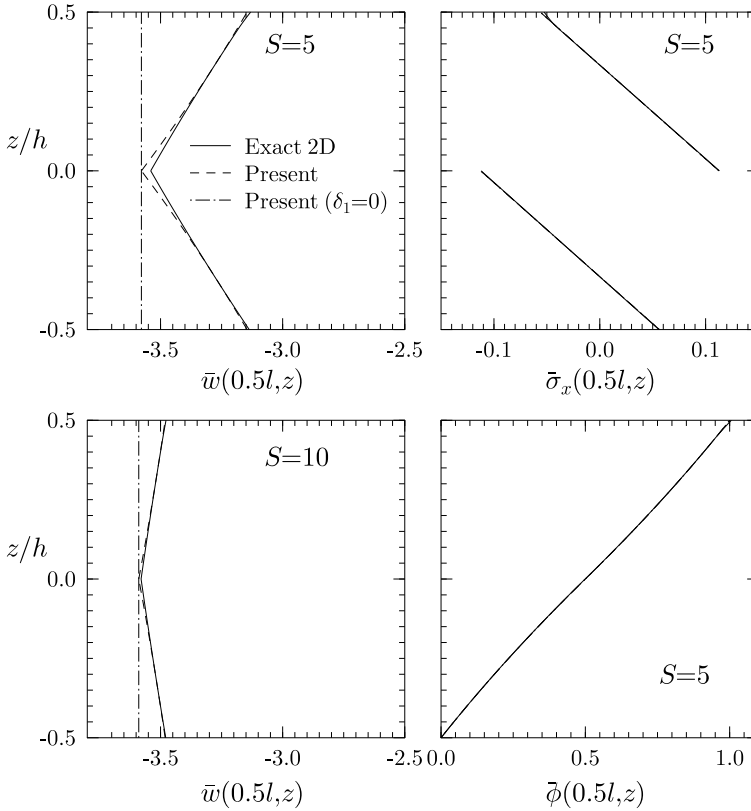
Figure 8. Through-the-thickness distributions of $\bar{w}, \bar{\sigma}_x, \bar{\phi}$ for bimorph EAM beam (c) under potential load 1.

one sublayer for ϕ-discretization. It is pertinent to note here that the number of electric potential DOF for the piezoelectric surfaces is only 3 in the present model using the electric node, which would have been 63 if the traditional concept of nodal electric variables were used. For a 2D plate or shell problem this reduction will be even more significant.

The present through-the-thickness distributions of deflection $\bar{w}$, axial stress $\bar{\sigma}_x$ and potential $\bar{\phi}$ are compared in Figure 8 with the exact 2D solution of Kapuria et al. [1997] for the potential load of case (1). In order to illustrate the effect of exclusion of the layerwise term in w in Equation (10), the present results with $\delta_1 = 0$ are also presented in Figure 8. It is observed that under the potential load, the top and bottom layers of the bimorph actuator undergo, respectively, expansion and contraction of their thickness, and the resulting variation of w across the thickness is accurately predicted by the present model with $\delta_1 = 1$. As expected, the model with $\delta_1 = 0$ is unable to predict this variation. The nonuniform variation of w is more significant for the thick beam with $S = 5$ than the thinner one with $S = 10$. The present results for the variations of $\bar{\sigma}_x$ and $\bar{\phi}$ are indistinguishable from the 2D results. The deflection profile of the centerline and the through-the-thickness distributions of $\bar{\sigma}_x$ and $\bar{\phi}$ for the beam (c) under pressure load case (2) are presented in Figure 9. The results are in excellent agreement with the exact 2D results. The present model is able to accurately predict the quadratic variation of ϕ induced due to the direct piezoelectric
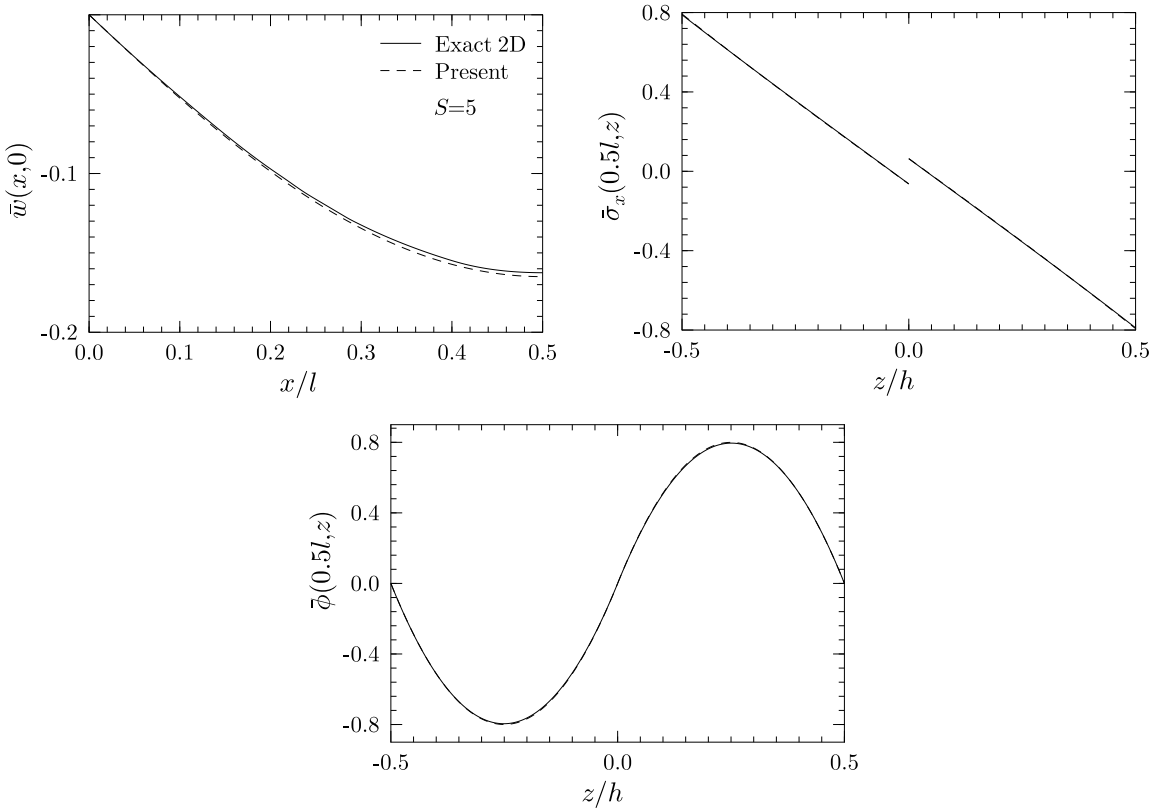
Figure 9. Deflection profile and distributions of $\bar{\sigma}_x$ and $\bar{\phi}$ for bimorph EAM beam (c) under pressure load 2.

effect across the thickness. In earlier publications of Kapuria et al. [2003] it has been observed that, with a sublayerwise linear approximation for the electric potential, a piezoelectric layer needs to be divided into 4 sublayers to capture the quadratic variation of the induced potential accurately, and also to achieve convergence in results. Thus, the number of electric variables with such an approximation would be 189 ($= 9 \times 21$), which is reduced to 45 ($= 2 \times 21 + 3$) in the present model.

6.3. *Shear mode pointer.* A cantilever plane-stress shear mode pointer beam (d), see Figure 5, of PZT-5H with span-to-thickness ratio $S = 10$ is analyzed for an uniform pressure load of case (2), using the

Entity	2D FE	Present model	
		$n_\phi = 3$	$n_\phi = 2$
$\bar{w}(l, 0)$	-1.839	-1.833	-1.884
$\bar{\phi}(0, z)|_{\max}$	11.048	11.927	0.0
$\bar{\sigma}_x(0, 0.5h)$	2.772	2.618	3.049

Table 3. Effect of ϕ-discretization in shear pointer beam (d) under pressure load ($S = 10$).
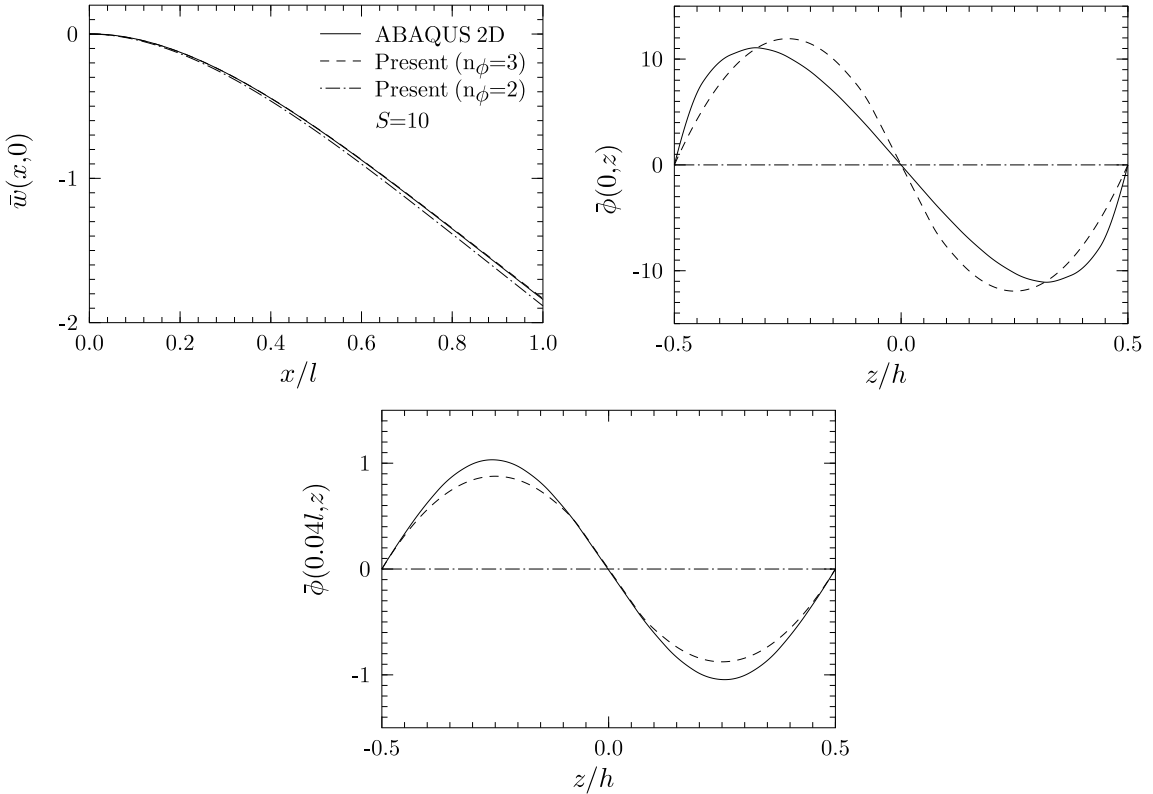
Figure 10. Deflection profile and distribution of $\bar{\phi}$ for shear pointer beam (d) under pressure load 2.

present model and the 2D FE model with eight-node plane stress element, CPS8RE, in ABAQUS. For the present model results are obtained considering 1 ($n_\phi = 2$) and 2 ($n_\phi = 3$) sublayers in the single-layer beam for discretization of ϕ across the thickness. For the 2D FE model the beam is modeled with 1600 [100 (length) $\times$ 16 (thickness)] elements to obtain converged results. The deflection profile of the centerline and the distributions of ϕ across the thickness at two locations at and near the clamped end are plotted in Figure 10. The tip deflection and the maximum values of $\bar{\sigma}_x$ and $\bar{\phi}$ are listed in Table 3. It is revealed from the 2D FE results that the electric potential induced in the shear actuator due to direct piezoelectric effect follows a cubic variation across the thickness, which is quite accurately predicted by the present model with $n_\phi = 3$. It is also revealed that the quadratic component in the third-order variation of ϕ is zero yielding zero potential at the midsurface. This fact justifies the use of two sublayers having quadratic variation of ϕ across each sublayer and an equipotential surface at the midsurface to model the cubic distribution of ϕ. With one sublayer ($n_\phi = 2$), however, the estimated induced potential is zero as expected. Consequently, the deflection profile predicted by the present model with $n_\phi = 3$ matches closely with the 2D FE results, whereas that with one sublayer ($n_\phi = 2$) is not as accurate. It can be seen from Table 3 that $\bar{\sigma}_x$ predicted with $n_\phi = 2$ is also less accurate than that with $n_\phi = 3$. The variation ϕ across the thickness of the beam under the same pressure load, but with the top surface having 5 electrode segments under open circuit condition, is shown in Figure 11 for two locations, $x = 0, l/2$. The
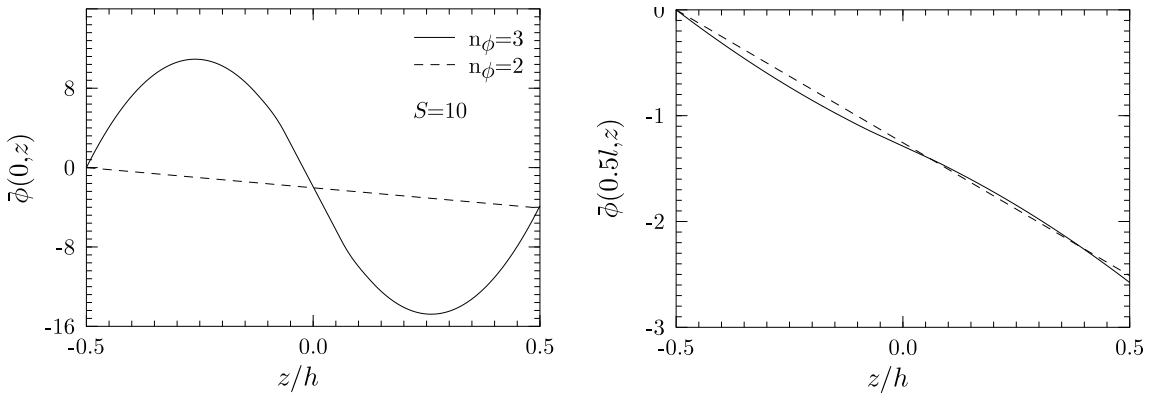
Figure 11. Distribution of $\bar{\phi}$ for shear pointer beam (d) under pressure load with open circuit condition at top.

distribution is again cubic, the cubic component being larger than the linear component at the clamped end. However, at the midspan the cubic component is much smaller than the linear one. It has been observed that the distribution becomes almost linear near the free end. With $n_\phi = 2$, even though the cubic variation is completely missed, the open circuit potential at the top surface is accurately predicted at $x = 0$. However, it is not as accurately predicted at $x = l/2$.

6.4. *Extension and shear mode sensors.* The sensory response of an extension mode bimorph beam (c) and a shear mode beam (d), both under cantilever boundary condition, is obtained for (i) an uniform pressure load (UDL) p_0 on the top and (ii) a concentrated load $P = p_0 l/2$ at the free end (tip load) for thickness ratio $S = 10$. The top surface is in open circuit condition while the bottom surface is grounded. Both beams are modeled with 20 equal-size elements. In order to illustrate the effect of segmentation of the electroded sensor surface, results are obtained with the beam surfaces divided into 1, 2, 5, 10 and 20 electroded patches. This is modeled by assigning an electric node to each electroded patch pair. The variation of the sensory potential induced at the top surface for the two load cases is plotted in Figures 12
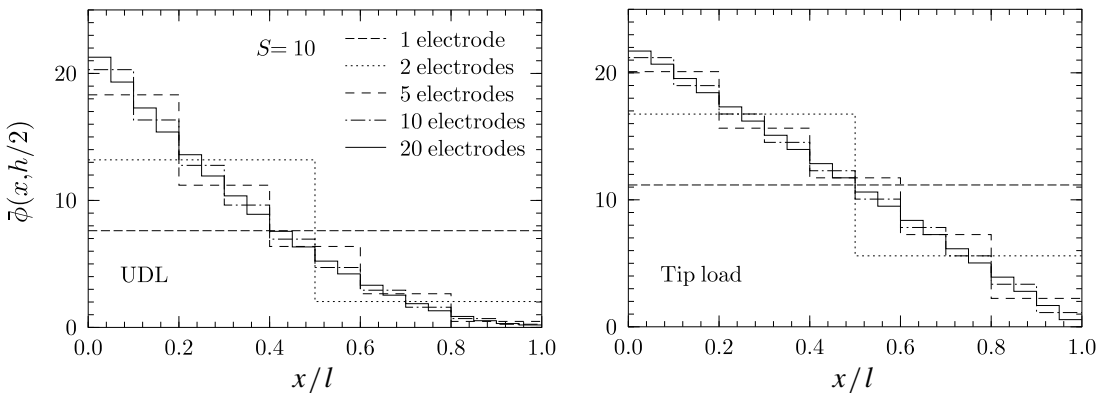
Figure 12. Sensory potential for varying number of electrodes for cantilever EAM beam (c).
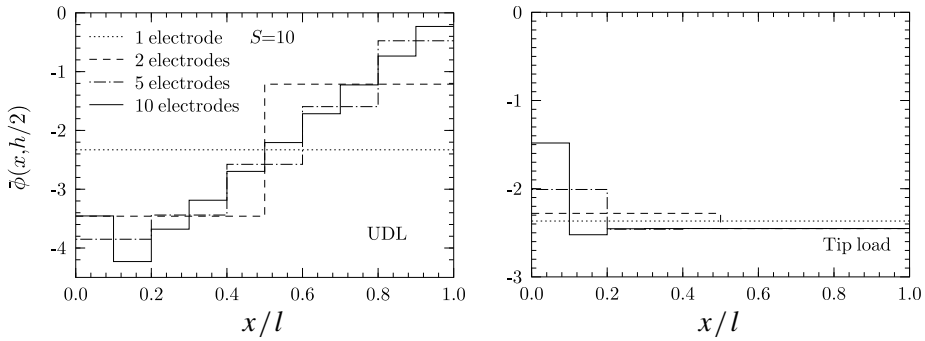
Figure 13. Sensory potential for varying number of electrodes for cantilever SAM beam (d).

and 13, respectively. It is observed that for the extension mode sensor (c), the sensory potential of the electrodes follows a step-wise quadratic variation for the UDL and a step-wise linear variation for the tip load, since it is related to the induced bending moment (axial stress). For the shear mode sensor (d), however, the sensory potential of the electrodes follows a stepwise linear variation for the UDL and an uniform variation for the tip load (except near the clamped end, which is believed to be due to boundary effect). This is because the sensory potential in shear mode is proportional to the induced shear. Thus, the sensory potential is independent of the electrode location, as long as the applied load causes constant transverse shear (as for tip load), but varies with the electrode location if the transverse shear changes (as for the UDL).

It is apparent from Figures 12 and 13 that the potential induced in a larger electrode is approximately equal to the area average of the potentials induced when it is divided into smaller segments. The tip deflection w and the maximum sensory potential ϕ induced for varying number of electrodes are presented in Tables 4 and 5 for beams (c) and (d), respectively. For comparison, the deflection for the closed circuit condition of the top surface (with zero potential) is also listed in these tables. It is revealed that the tip deflections of beam (c) with 1 and 20 electrodes differ by 4% and 3% for the UDL and the tip load, respectively. For the shear mode beam (d), however, the tip deflection is independent of the number of electrodes. It is also observed that, for the extension mode beam, the closed circuit deflection differs from the open circuit deflection with 20 electrodes by about 12.5% for both the load cases. For the shear

| Load case | Entity | Number of electrodes | | | | | Closed circuit |
		1	2	5	10	20	
UDL	$\bar{w}(l,0)$	−1.3422	−1.3021	−1.2910	−1.2894	−1.2890	−1.4516
	$\bar{\phi}(0.5h)\vert_{\max}$	7.6158	13.195	18.315	20.297	21.277	0
Tip load	$\bar{w}(l,0)$	−1.7703	−1.7302	−1.7192	−1.7174	−1.7170	−1.9308
	$\bar{\phi}(0.5h)\vert_{\max}$	11.169	16.750	20.093	21.196	21.714	0

Table 4. Effect of number of electrodes on $\bar{w}$ and $\bar{\phi}$ for cantilever EAM sensory beam (c) ($S = 10$).

Load case	Entity	Number of electrodes					Closed circuit
		1	2	5	10	20	
UDL	$\bar{w}(l, 0)$	−1.8271	−1.8272	−1.8272	−1.8272	−1.8271	−1.8330
	$\bar{\phi}(0.5h)|_{\max}$	−2.3296	−3.4588	−3.8508	−4.2304	−4.5151	0
Tip load	$\bar{w}(l, 0)$	−2.4492	−2.4492	−2.4492	−2.4491	−2.4491	−2.4552
	$\bar{\phi}(0.5h)|_{\max}$	−2.3667	−2.4526	−2.4517	−2.4517	−2.4511	0

Table 5. Effect of number of electrodes on $\bar{w}$ and $\bar{\phi}$ for cantilever SAM sensory beam (d) ($S = 10$).

mode beam, this difference is negligible (0.25–0.3%). The induced sensory potential in the shear mode case is 21 and 11% of the extension mode sensory potential for the UDL and the tip load, respectively.

The undamped natural frequencies of the cantilever sensory EAM beam (c) and SAM beam (d) when the beam surfaces are segmented in to 1, 2, 5, 10 and 20 electroded patches are presented in Table 6 for five modes. All the electrode segments are in open circuit condition. The frequency of the nth mode is nondimensionalized as $\bar{\omega}_n = \omega_n l S (\rho_0/Y_0)^{1/2}$ where $\rho_0 = 7500$ kg/m^3. For comparison, $\bar{\omega}_n$ of the beams with their top surface being under closed circuit condition is also listed in Table 6. It can be seen from Equation (35) that the effective stiffness matrix gets modified by the electromechanical stiffness corresponding to the open circuit potentials Φ_s. Physically, it occurs since a part of the mechanical energy is converted into electric energy through the induced electric potential and results in an increase in the effective stiffness. Thus, the open circuit frequencies are higher than the closed circuit ones, as can be seen from Table 6. Since the degree of constraint of equipotential condition over the electroded surface changes with the number electrode segments, the latter modifies the electromechanical stiffness and consequently the natural frequencies. It is observed that the natural frequencies of the bimorph EAM

Beam	Entity	Open circuit (# of electrodes)					Closed circuit	Combined open-closed
		1	2	5	10	20		
(c)	$\bar{\omega}_1$	5.3281	5.4224	5.4489	5.4529	5.4538	5.1446	5.4367
	$\bar{\omega}_2$	31.209	31.383	32.372	32.527	32.562	30.858	31.761
	$\bar{\omega}_3$	81.605	83.243	84.478	85.103	85.169	81.292	83.093
	$\bar{\omega}_4$	83.781	84.799	85.103	85.158	85.297	83.781	85.169
	$\bar{\omega}_5$	148.09	148.41	150.81	153.59	154.14	147.80	150.63
(d)	$\bar{\omega}_1$	4.5865	4.5871	4.5875	4.5876	4.5877	4.5792	4.5855
	$\bar{\omega}_2$	27.633	27.882	27.913	27.924	27.930	27.593	27.873
	$\bar{\omega}_3$	71.055	71.055	71.055	71.055	71.055	71.055	71.055
	$\bar{\omega}_4$	73.214	73.298	74.697	74.967	75.033	73.137	74.446
	$\bar{\omega}_5$	134.03	134.09	138.51	139.11	139.43	133.88	137.34

Table 6. Effect of number of electrodes on $\bar{\omega}_n$ for cantilever EAM and SAM beams ($S = 10$).

beam with 1 and 20 electrodes differ by 2 and 4% for the first and the fifth modes, respectively. For the SAM beam, the open circuit natural frequencies are little sensitive to the number of electrodes for the first four modes. For the fifth mode, however, the difference between the frequencies of the beam with 1 and 20 electrodes is 4%, similar to the EAM beam. The open circuit frequencies with 20 electrodes differ from the respective closed circuit frequencies by 6 and 4% for the first and fifth modes, for the EAM beam. The corresponding differences for the SAM beam are 0.3 and 4%. For the EAM beam, the lower mode frequencies are generally more sensitive to the electric boundary conditions than the higher mode ones. The reverse is true for the SAM beam. The case of combined open-closed condition with 10 electrodes from the clamped end being under open circuit condition and the remaining 10 under closed circuit condition is also analyzed and the corresponding natural frequencies are presented in the above table. It is observed that the frequencies for this combined case lie in between the corresponding closed circuit and open circuit frequencies (with 20 electrodes).

6.5. *Hybrid SAM-EAM composite beam.* A thin width (plane stress) composite beam (e) with an EAM piezoelectric patch of PZT-5H bonded at the top surface and a SAM patch embedded between two graphite-epoxy composite faces, see Figure 5, is considered next. The beam has a foam core of the same thickness as the SAM patch at the portion where the patch is not present. The material properties of the graphite epoxy and the foam are selected as [Benjeddou et al. 2000; Kapuria and Alam 2006]:

(i) Graphite epoxy:

$$\{Y_1, Y_2, Y_3, G_{12}, G_{23}, G_{31}\} = \{181, 10.3, 10.3, 7.17, 2.87, 7.17\} \, \text{GPa},$$

$$\{\nu_{12}, \nu_{13}, \nu_{23}\} = \{0.28, 0.28, 0.33\}, \quad \rho = 1578 \, \text{kg/m}^3$$

(ii) Foam:

$$\{Y, G\} = \{35.3, 12.76\} \, \text{GPa}, \qquad \rho = 32 \, \text{kg/m}^3.$$

The length of both the PZT patches is taken as $l_p = 0.2l$. The beam is modeled with 50 equal-size elements to obtain converged results. The surfaces of the piezoelectric patches are electroded. Thus all the elements under a patch are connected to one electric node. The beam is analyzed for the following two load cases:

(1) Actuation potential ϕ_0 on the top surface of the EAM or SAM patch with the other piezoelectric surfaces grounded.

(2) Uniform pressure p_0 applied on the top surface over a length of $l/25$ from the free end. For this load case, the top surface of either EAM or SAM patch is under open circuit condition, while the other piezoelectric surfaces are grounded.

The static results for the two load cases and the natural frequencies are nondimensionalized as

(1) $\bar{w} = 10w/S^2 d_0 \phi_0, \qquad \bar{\sigma}_x = \sigma_x h/10 Y_0 d_0 \phi_0,$

(2) $\bar{\phi} = 10^4 \phi Y_0 d_0 / h S^2 p_0, \qquad \bar{\omega}_n = \omega_n l S (\rho_0 / Y_0)^{1/2},$

with $Y_0 = 6.9 \, \text{GPa}$, $d_0 = 274.8 \times 10^{-12} \, \text{CN}^{-1}$ and $\rho_0 = 1000 \, \text{kg/m}^3$.

In order to illustrate the effect of location x_p of the EAM and SAM actuators on their actuation capability, one of the actuators (EAM or SAM) is actuated with electric potential of load case 1 and its

		Potential load					Pressure load	
		EAM			SAM		EAM	SAM
x_p/l	$\bar{w}(l,0)$	$\bar{\sigma}_x^p(x_p,0.5h^+)$	$\bar{\sigma}_x^e(x_p,0.5h^-)$	$\bar{w}(l,0)$	$\bar{\sigma}_x^p(x_p',0.05h^-)$	$\bar{\sigma}_x^e(x_p',-0.5h)$	$\bar{\phi}(0.6h)$	$\bar{\phi}(0.05h)$
0.1	−5.012	−6.881	3.970	−1.358	0.6902	−1.167	−1.899	−0.1381
0.3	−3.982	−6.864	4.053	−1.496	0.2748	−1.303	−1.496	−0.1953
0.5	−2.821	−6.863	4.055	−1.122	0.2748	−1.303	−1.046	−0.1953
0.7	−1.693	−6.863	4.055	−0.7474	0.2748	−1.303	−0.6101	−0.1953
0.9	−0.5598	−6.863	4.057	−0.3718	0.2748	−1.303	−0.1802	−0.1851

Table 7. Effect of actuator/sensor location on the response of hybrid beam (e) ($S = 20$). Here, $x_p' = x_p - 0.5l_p$, x_p denotes x_e for EAM and x_s for SAM.

location is varied from the clamped end ($x_p = 0.1l$) to the free end ($x_p = 0.9l$), while the unactuated patch is kept fixed at the clamped end. x_p refers to x_e for the EAM and x_s for the SAM, see Figure 5. The tip deflection $\bar{w}$, axial stress $\bar{\sigma}_x^e$ in the elastic substrate and $\bar{\sigma}_x^p$ in the actuated piezoelectric patch are presented in Table 7 for the beam with $S = 20$ for both EAM and SAM actuation cases for five different actuator locations. The tip deflection is also plotted against the actuator location in Figure 14. It is observed that the EAM actuator is most effective inducing the maximum deflection, when placed at the clamped end. The SAM actuator develops the maximum tip deflection when it is placed at a clear distance of $0.1l$ from the clamped end ($x_p = 0.2l$).

This observation is in line with the results of Sun and Zhang [1995] obtained for Al/PZT-5H beams, through 2D FE analysis. It, however, does not support the conclusion made by Raja et al. [2004] based on the three-layer sandwich model that the shear actuator for a cantilever beam is most effective if it is placed at the center of the beam. It is revealed from Table 7 that even though the maximum tip deflection developed by shear actuator is 36% of that produced by the extension mode actuator, the maximum stress $\bar{\sigma}_x^p$ induced in the actuator for the SAM is only 10% of that for the EAM. Also, the maximum value of $\bar{\sigma}_x^e$ induced in the elastic substrate for SAM is 29% of that for EAM. Thus, for the same stress level in
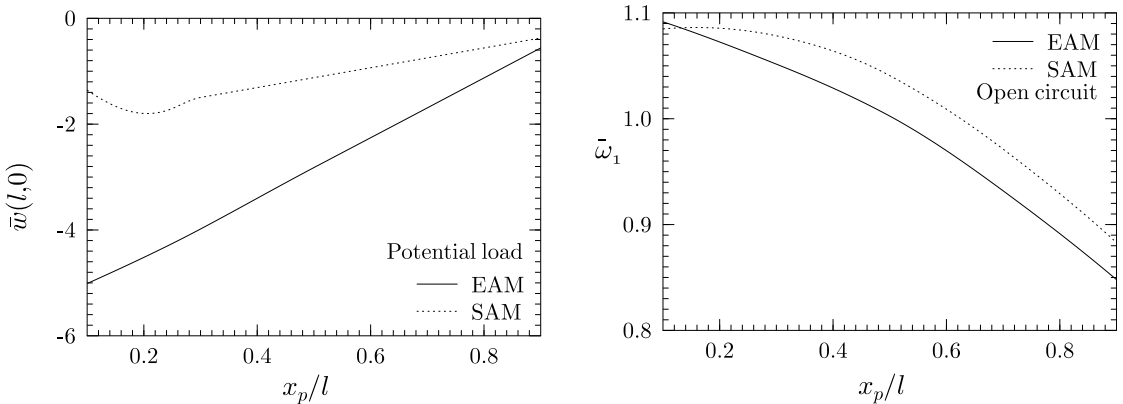
Figure 14. Variation of tip deflection and natural frequency of hybrid beam (e) with actuator/sensor location.
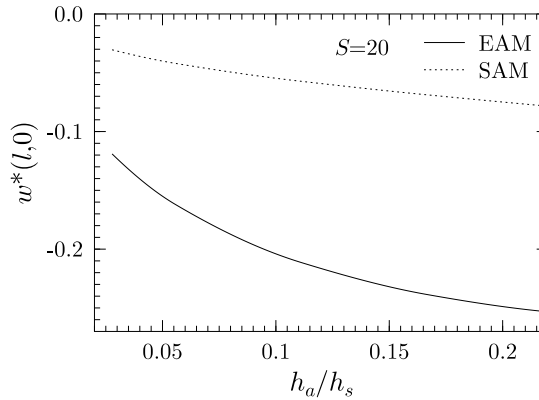
Figure 15. Variation of tip deflection with actuator thickness for actuation with constant energy for hybrid beam (e).

the actuator (which is often the governing criteria), the SAM actuator can develop more tip deflection than the EAM actuator. This is an attractive feature of the SAM actuators, which can be useful in many control applications.

The sensory potential developed when the beam is subjected to mechanical load of case (2) is also presented in Table 7 for different locations of the SAM and EAM sensors. It is revealed that for the extension mode, the sensor is most effective when placed at the clamped end like the actuator. For the shear mode, however, the sensory potential for this tip loading case is independent of the location beyond a small distance from the the clamped end. As explained earlier, this is because the sensory potential is related to the induced shear which is constant in the region $0 \le x \le 0.96l$, for the present loading.

The variation of the fundamental frequency $\bar{\omega}_1$ of the hybrid beam (e) with the location of the EAM and SAM sensors is plotted in Figure 14. As expected, the frequency of the beam reduces as the sensor is moved from the clamped to the free end. This reduction is more for the surface mounted patch than the embedded one.

6.6. *Effect of actuator thickness on actuation capability.* Here the entities are nondimensionalized as $w^* = 1000w/h$, $\phi^* = \phi d_0/h$. The energy required to develop a potential difference ϕ_0^* across an actuator of thickness h_a for the beam (e) with thickness of the composite substrate being h_s is proportional to $E_v = \phi_0^{*2}/(h_a/h_s)$. To illustrate the effect of actuator thickness on its effectiveness, the actuator potential is varied for varying h_a such that E_v is constant $(= 10^{-11})$. The induced deflection w^* is plotted as a function h_a/h_s in Figure 15 for both SAM and EAM actuators. It is observed that in both cases, the actuation authority increases with the increase in h_a/h_s. However, the rate of increase in w^* reduces with the increase in h_a/h_s.

7. Conclusions

The new unified formulation based on the efficient layerwise approximations for the displacement field and sublayerwise quadratic approximation for the electric potential can model actuators, sensors and hybrid adaptive beams with surface-mounted and embedded actuator/sensor patches in extension or shear

mode. The numerical results show that the model accurately predicts the nonuniform variation of w across the thickness in presence of electric field, and also the quadratic and cubic variations of electric potential in the extension and shear modes, respectively, as observed from 2D piezoelasticity solutions. The concept of electric node results in significant reduction in the number of electric DOF.

It is revealed that while for the extension mode sensor, the sensory potential is dependent on the sensor location unless the loading causes a constant bending moment, the sensory potential in shear mode does not change with the location, if the loading causes constant shear. For extension mode sensors, the number of segments in the electroded surface can have appreciable effect on the deflection and natural frequencies. However, for the shear mode sensors, the deflection and lower mode natural frequencies are independent of the segmentation of the electrode. An extension actuator yields maximum tip deflection in a cantilever adaptive beam when it is placed at the clamped end, whereas a shear actuator should be placed at a distance of $l/10$ from the clamped end to develop the maximum tip deflection. The ability of an actuator in inducing deflection for a given energy increases with its thickness for both extension and shear mode actuation.

Appendix

The transformation matrices a, T and R in Equation (2) are given by

$$
R = \begin{bmatrix} 1 & 0 & 0 & 0 & 0 & 0 \\ 0 & 1 & 0 & 0 & 0 & 0 \\ 0 & 0 & 1 & 0 & 0 & 0 \\ 0 & 0 & 0 & 2 & 0 & 0 \\ 0 & 0 & 0 & 0 & 2 & 0 \\ 0 & 0 & 0 & 0 & 0 & 2 \end{bmatrix}, \quad
T = \begin{bmatrix} c^2p^2 & s^2p^2 & q^2 & 2spq & 2cpq & 2csp^2 \\ s^2 & c^2 & 0 & 0 & 0 & -2cs \\ c^2q^2 & s^2q^2 & p^2 & -2spq & -2cpq & 2csq^2 \\ csq & -csq & 0 & cp & -sp & -(c^2-s^2)q \\ -c^2pq & -s^2pq & pq & s(p^2-q^2) & c(p^2-q^2) & -2cspq \\ -csp & csp & 0 & cq & -sq & (c^2-s^2)p \end{bmatrix},
$$

$$
a = \begin{bmatrix} cq & sp & q \\ -s & c & 0 \\ -cp & -sq & p \end{bmatrix},
$$

where $c = \cos\alpha$, $s = \sin\alpha$, $p = \cos\beta$, and $q = \sin\beta$. The expressions of $\bar{s}_{ij}$, $\bar{d}_{ij}$ and $\bar{\epsilon}_{ij}$ in Equation (5) are given, for the case $pq = 0$, by

$$
\bar{s}_{11} = c^4p^4s_{11} + c^2s^2p^2(2s_{12}+s_{66}) + s^4s_{22} + c^2s^2q^2(2s_{23}+s_{44}) + c^4q^4s_{33},
$$

$$
\bar{s}_{55} = s^2p^2s_{44} + c^2(p^4+q^4)s_{55} + s^2q^2s_{66},
$$

$$
\bar{d}_{11} = -cq[s^2(d_{32}+d_{24}) + c^2q^2d_{33}], \qquad \bar{d}_{35} = -cq^3d_{15},
$$

$$
\bar{d}_{31} = p(c^2p^2d_{31} + s^2d_{32}), \qquad \bar{d}_{15} = p(c^2p^2d_{15} + s^2d_{24}),
$$

$$
\bar{\epsilon}_{11} = c^2p^2\epsilon_{11} + s^2\epsilon_{22} + c^2q^2\epsilon_{33}, \qquad \bar{\epsilon}_{33} = q^2\epsilon_{11} + p^2\epsilon_{33}.
$$

The expressions of $\bar{c}_{ij}$, $\bar{e}_{ij}$ and $\bar{\eta}_{ij}$ in Equation (8) are given, for the case $pq = 0$, by

$$\bar{c}_{11} = c^4 p^4 c_{11} + 2c^2 s^2 p^2 (c_{12} + 2c_{66}) + s^4 c_{22} + 2c^2 s^2 q^2 (c_{23} + 2c_{44}) + c^4 q^4 c_{33},$$

$$\bar{c}_{13} = s^2 p^2 c_{23} + c^2 (p^4 + q^4) c_{13} + s^2 q^2 c_{12}, \qquad \bar{c}_{33} = q^4 c_{11} + p^4 c_{33},$$

$$\bar{c}_{55} = s^2 p^2 c_{44} + c^2 (p^4 + q^4) c_{55} + s^2 q^2 c_{66},$$

$$\bar{e}_{11} = -cq[s^2 (e_{32} + 2e_{24}) + c^2 q^2 e_{33}], \qquad \bar{e}_{35} = -cq^3 e_{15},$$

$$\bar{e}_{31} = p(c^2 p^2 e_{31} + s^2 e_{32}), \qquad \bar{e}_{15} = p(c^2 p^2 e_{15} + s^2 e_{24}),$$

$$\bar{\eta}_{11} = c^2 p^2 \eta_{11} + s^2 \eta_{22} + c^2 q^2 \eta_{33}, \qquad \bar{\eta}_{33} = q^2 \eta_{11} + p^2 \eta_{33}.$$

The hatted R-coefficients in Equation (12) are defined as $\{\hat{R}_1^k, \hat{R}_2^k, \hat{R}_3, \hat{R}_4\} = \{R_1^k, R_2^k, R_3, R_4\}/R_2^{k_0}$ with

$$R_1^k = \bar{R}_2^k - \bar{R}_2^{k_0}, \quad R_2^k = a_1^k R_3 + a_2^k R_4, \quad R_3 = \frac{4C_2^L}{\Delta}, \quad R_4 = -\frac{4C_1^L}{3\Delta}, \quad \bar{R}_2^k = \sum_{i=2}^{k} z_{i-1}(R_2^{i-1} - R_2^i),$$

$$a_1^k = 2(C_1^k/\hat{Q}_{55}^k - z_k), \qquad a_2^k = 3(2C_2^k/\hat{Q}_{55}^k - z_k^2), \qquad \Delta = 4z_0^2 C_1^L - 8z_0 C_2^L,$$

$$C_1^k = \sum_{i=1}^{k} \hat{Q}_{55}^i (z_i - z_{i-1}), \qquad C_2^k = \tfrac{1}{2} \sum_{i=1}^{k} \hat{Q}_{55}^i (z_i^2 - z_{i-1}^2).$$

Using Equations (18), (23), (24), (27), (29) and (30), the elements of the submatrices of M^e, C^e and K^e defined in Equation (31) are obtained by exact integration as

$$M_{uu}^e = \begin{bmatrix} I_{11}c_1 & -I_{12}c_2 & I_{13}c_1 \\ & I_{22}c_3 + I_{11}c_4 & -I_{23}c_2^T \\ \text{symm.} & & I_{33}c_1 \end{bmatrix}, \qquad C_{uu}^e = \begin{bmatrix} 0 & 0 & 0 \\ & \hat{c}_1 c_4 & 0 \\ \text{symm.} & & 0 \end{bmatrix},$$

$$K_{uu}^e = \begin{bmatrix} A_{11}c_5 & -A_{12}c_6 & A_{13}c_5 \\ & A_{22}c_7 & -A_{23}c_6^T \\ \text{symm.} & & A_{33}c_5 + \bar{A}_{11}c_1 \end{bmatrix}, \qquad K_{ul}^e = \begin{bmatrix} e_1^{1l'}c_5 + e_{11}^{2l'}c_8 \\ -(e_2^{1l'}c_6^T + e_{12}^{2l'}c_{10}) \\ e_3^{1l'}c_5 + e_{13}^{2l'}c_8 + (e_1^{3l'} - \bar{A}_{12}^{l'})c_8^T + e_{11}^{4l'}c_1 \end{bmatrix},$$

$$K_{uj}^e = \begin{bmatrix} e_{21}^{2j'}c_9 \\ -e_{22}^{2j'}c_{11} \\ e_{23}^{2j'}c_9 + e_{21}^{4j'}c_{12} \end{bmatrix}, \qquad K_{lj}^e = \begin{bmatrix} -(\delta_1 e_{22}^{4lj'} + \eta_2^{2lj'})c_9 - \eta_{12}^{3lj'}c_{12} \end{bmatrix},$$

$$K_{ll}^e = \begin{bmatrix} (\bar{A}_{22}^{ll'} - 2\delta_1 e_2^{3ll'} - \eta_1^{ll'})c_5 - (\delta_1 e_{12}^{4ll'} + \eta_1^{2ll'})(c_8 + c_8^T) - \eta_{11}^{3ll'}c_1 \end{bmatrix},$$

$$K_{jj}^e = \begin{bmatrix} -\eta_{22}^{3jj'}a \end{bmatrix},$$

where c_i are given by

$$c_1 = \int_0^a N^T N \, dx = \frac{a}{3} \begin{bmatrix} 1 & 1/2 \\ 1/2 & 1 \end{bmatrix},$$

$$c_2 = \int_0^a N^T \bar{N}_{,x} \, dx = \frac{1}{2} \begin{bmatrix} -1 & a/6 & 1 & -a/6 \\ -1 & -a/6 & 1 & a/6 \end{bmatrix},$$

$$c_3 = \int_0^a \bar{N}_{,x}^T \bar{N}_{,x} \, dx = \begin{bmatrix} 6/5a & 1/10 & -6/5a & 1/10 \\ 1/10 & 2a/15 & -1/10 & -a/30 \\ -6/5a & -1/10 & 6/5a & -1/10 \\ 1/10 & -a/30 & -1/10 & 2a/15 \end{bmatrix},$$

$$c_4 = \int_0^a \bar{N}^T \bar{N} \, dx = \begin{bmatrix} 13a/35 & 11a^2/210 & 9a/70 & -13a^2/420 \\ 11a^2/210 & a^3/105 & 13a^2/420 & -a^3/140 \\ 9a/70 & 13a^2/420 & 13a/35 & -11a^2/210 \\ -13a^2/420 & -a^3/140 & -11a^2/210 & a^3/105 \end{bmatrix},$$

$$c_5 = \int_0^a N_{,x}^T N_{,x} \, dx = \frac{1}{a} \begin{bmatrix} 1 & -1 \\ -1 & 1 \end{bmatrix},$$

$$c_6 = \int_0^a N_{,x}^T \bar{N}_{,xx} \, dx = \frac{1}{a} \begin{bmatrix} 0 & 1 & 0 & -1 \\ 0 & -1 & 0 & 1 \end{bmatrix},$$

$$c_7 = \int_0^a \bar{N}_{,xx}^T \bar{N}_{,xx} \, dx = \begin{bmatrix} 12/a^3 & 6/a^2 & -12/a^3 & 6/a^2 \\ 6/a^2 & 4/a & -6/a^2 & 2/a \\ -12/a^3 & -6/a^2 & 12/a^3 & -6/a^2 \\ 6/a^2 & 2/a & -6/a^2 & 4/a \end{bmatrix},$$

$$c_8 = \int_0^a N_{,x}^T N \, dx = \frac{1}{2} \begin{bmatrix} -1 & -1 \\ 1 & 1 \end{bmatrix},$$

$$c_9 = \int_0^a N_{,x}^T \, dx = \begin{bmatrix} -1 \\ 1 \end{bmatrix},$$

$$c_{10} = \int_0^a \bar{N}_{,xx}^T N \, dx = \begin{bmatrix} -1/a & 1/a \\ -1 & 0 \\ 1/a & -1/a \\ 0 & 1 \end{bmatrix},$$

$$c_{11} = \int_0^a \bar{N}_{,xx}^{\mathrm{T}} \, dx = \begin{bmatrix} 0 \\ -1 \\ 0 \\ 1 \end{bmatrix},$$

$$c_{12} = \int_0^a N^{\mathrm{T}} \, dx = \frac{a}{2} \begin{bmatrix} 1 \\ 1 \end{bmatrix}.$$

Considering that the loading terms p_z^1, p_z^2, D_{z_0}, D_{z_L} vary linearly over the length of the element with nodal values

$$p_z^{1^e}, \, p_z^{2^e}, \, D_{z_0}^e, \, D_{z_L}^e$$

via the relation $p_z^i = N p_z^{i^e}$, $D_{z_i} = N D_{z_i}^e$, the elements of P_u^e and P_j^e in Equation (31) are obtained as

$$P_u^e = \begin{bmatrix} 0 \\ c_{13} p_z^e \\ 0 \end{bmatrix}, \qquad P_j^e = \begin{bmatrix} b c_{12}^{\mathrm{T}} p_\phi^{j^e} \end{bmatrix},$$

where

$$c_{13} = b \int_0^a \bar{N}^{\mathrm{T}} N \, dx = \frac{b}{10} \begin{bmatrix} 7a/2 & 3a/2 \\ a^2/2 & a^2/3 \\ 3a/2 & 7a/2 \\ -a^2/3 & -a^2/2 \end{bmatrix},$$

$$p_z^e = p_z^{1^e} + p_z^{2^e},$$

$$p_\phi^{j^e} = -\delta_1 \big[p_z^{1^e} \bar{\Psi}_\phi^j(z_0) + p_z^{2^e} \bar{\Psi}_\phi^j(z_L) \big] - D_{z_0}^e \delta_{j1} + D_{z_L}^e \delta_{jn_\phi}.$$

References

[Aldraihem and Khdeir 2003] O. J. Aldraihem and A. A. Khdeir, "Exact deflection solutions of beams with shear piezoelectric actuators", *Int. J. Solids Struct.* **40**:1 (2003), 1–12.

[Auld 1973] B. A. Auld, *Acoustic fields and waves in solids*, vol. 1, Wiley, New York, 1973.

[Benjeddou 2000] A. Benjeddou, "Advances in piezoelectric finite element modeling of adaptive structural elements: a survey", *Comput. Struct.* **76**:1-3 (2000), 347–363.

[Benjeddou et al. 1997] A. Benjeddou, M. A. Trindade, and R. Ohayon, "A unified beam finite element model for extension and shear piezoelectric actuation mechanisms", *J. Intell. Mater. Syst. Struct.* **8**:12 (1997), 1012–1025.

[Benjeddou et al. 1999] A. Benjeddou, M. A. Trindade, and R. Ohayon, "New shear actuated smart structure beam finite element", *AIAA J.* **37**:3 (1999), 378–383.

[Benjeddou et al. 2000] A. Benjeddou, M. A. Trindade, and R. Ohayon, "Piezoelectric actuation mechanisms for intelligent sandwich structures", *Smart Mater. Struct.* **9** (2000), 328–335.

[Bisegna and Caruso 2001] P. Bisegna and G. Caruso, "Evaluation of higher-order theories of piezoelectric plates in bending and in stretching", *Int. J. Solids Struct.* **38**:48-49 (2001), 8805–8830.

[Chandrupatla and Belegundu 2002] T. R. Chandrupatla and A. D. Belegundu, *Introduction to finite elements in engineering*, Pearson Education (Singapore) Pte Ltd., New Delhi, 2002.

[Correia et al. 2000] V. M. F. Correia, M. A. A. Gomes, A. Suleman, C. M. M. Soares, and C. A. M. Soares, "Modelling and design of adaptive composite structures", *Comput. Methods Appl. Mech. Eng.* **185**:2-4 (2000), 325–346.

[Dube et al. 1996] G. P. Dube, S. Kapuria, and P. C. Dumir, "Exact piezothermoelastic solution of simply-supported orthotropic flat panel in cylindrical bending", *Int. J. Mech. Sci.* **38**:11 (1996), 1161–1177.

[Gopinathan et al. 2000] S. V. Gopinathan, V. V. Varadan, and V. K. Varadan, "A review and critique of theories for piezoelectric laminates", *Smart Mater. Struct.* **9**:1 (2000), 24–48.

[Kapuria 2001] S. Kapuria, "An efficient coupled theory for multilayered beams with embedded piezoelectric sensory and active layers", *Int. J. Solids Struct.* **38**:50-51 (2001), 9179–9199.

[Kapuria and Alam 2006] S. Kapuria and N. Alam, "Efficient layerwise finite element model for dynamic analysis of laminated piezoelectric beams", *Comput. Methods Appl. Mech. Eng.* **195**:19-22 (2006), 2742–2760.

[Kapuria et al. 1997] S. Kapuria, G. P. Dube, and P. C. Dumir, "Exact piezothermoelastic solution for simply supported laminated flat panel in cylindrical bending", *Z. Angew. Math. Mech.* **77**:4 (1997), 281–293.

[Kapuria et al. 2003] S. Kapuria, P. C. Dumir, and A. Ahmed, "An efficient coupled layerwise theory for static analysis of piezoelectric sandwich beams", *Arch. Appl. Mech.* **73**:3-4 (2003), 147–159.

[Khdeir and Aldraihem 2001] A. A. Khdeir and O. J. Aldraihem, "Deflection analysis of beams with extension and shear piezoelectric patches using discontinuity functions", *Smart Mater. Struct.* **10**:2 (2001), 212–220.

[Lage et al. 2004] R. G. Lage, C. M. M. Soares, C. A. M. Soares, and J. N. Reddy, "Modelling of piezolaminated plates using layerwise mixed finite elements", *Comput. Struct.* **82**:23-26 (2004), 1849–1863.

[Lee and Saravanos 1996] H. J. Lee and D. A. Saravanos, "Coupled layer-wise analysis of thermopiezoelectric composite beams", *AIAA J.* **34**:6 (1996), 1231–1237.

[Parashar et al. 2004] S. K. Parashar, U. von Wagner, and H. P., "A modified Timoshenko beam theory for nonlinear shear-induced flexural vibrations of piezoceramic continua", *Nonlinear Dyn.* **37**:3 (2004), 181–205.

[Parashar et al. 2005] S. K. Parashar, U. von Wagner, and H. P., "Nonlinear shear-induced flexural vibrations of piezoceramic actuators: experiments and modeling", *J. Sound Vib.* **285**:4-5 (2005), 989–1014.

[Petyt 1990] M. Petyt, *Introduction to finite element vibration analysis*, Cambridge University Press, Cambridge, 1990.

[Plagianakos and Saravanos 2005] T. S. Plagianakos and D. A. Saravanos, "Coupled high-order shear layerwise analysis of adaptive sandwich piezoelectric composite beams", *AIAA J.* **43**:4 (2005), 885–894.

[Raja et al. 2002] S. Raja, G. Prathap, and P. K. Sinha, "Active vibration control of composite sandwich beams with piezoelectric extension-bending and shear actuators", *Smart Mater. Struct.* **11**:1 (2002), 63–71.

[Raja et al. 2004] S. Raja, R. Sreedeep, and G. Prathap, "Bending behavior of hybrid-actuated piezoelectric sandwich beams", *J. Intell. Mater. Syst. Struct.* **15**:8 (2004), 611–619.

[Robbins and Reddy 1991] D. H. Robbins and J. N. Reddy, "Analysis of piezoelectrically actuated beams using a layer-wise displacement theory", *Comput. Struct.* **41**:2 (1991), 265–279.

[Saravanos 1999] D. A. Saravanos, "Damped vibration of composite plates with passive piezoelectric-resistor elements", *J. Sound Vib.* **221**:5 (1999), 867–885.

[Saravanos and Heyliger 1999] D. A. Saravanos and P. R. Heyliger, "Mechanics and computational models for laminated piezoelectric beams plates and shells", *Appl. Mech. Rev.* **52** (1999), 305–320.

[Saravanos et al. 1997] D. A. Saravanos, P. R. Heyliger, and D. A. Hopkins, "Layerwise mechanics and finite element for the dynamic analysis of piezoelectric composite plates", *Int. J. Solids Struct.* **34**:3 (1997), 359–378.

[Shu and Sun 1994] X. Shu and L. Sun, "An improved simple higher order theory for laminated composite plates", *Comput. Struct.* **50**:2 (1994), 231–236.

[Sun and Zhang 1995] C. T. Sun and X. D. Zhang, "Use of thickness-shear mode in adaptive sandwich structures", *Smart Mater. Struct.* **4**:3 (1995), 202–206.

[Sze and Yao 2000] K. Y. Sze and L. Q. Yao, "Modelling smart structures with segmented piezoelectric sensors and actuators", *J. Sound Vib.* **235**:3 (2000), 495–520.

[Sze et al. 2004] K. Y. Sze, X.-M. Yang, and H. Fan, "Electric assumptions for piezoelectric laminate analysis", *Int. J. Solids Struct.* **41**:9-10 (2004), 2363–2382.

[Tiersten 1969] H. F. Tiersten, *Linear piezoelectric plate vibrations*, Plenum Publishing Corporation, New York, 1969.

[Trindade and Benjeddou 2005] M. A. Trindade and A. Benjeddou, "Refined sandwich finite element model for smart beams with shear piezoceramic actuators and sensors", in *Proceedings of II Eccomas Thematic Conference on Smart Structures and Materials*, vol. 1-20, Lisbon, Portugal, 2005.

[Tzou and Tseng 1990] H. Tzou and C. I. Tseng, "Distributed piezoelectric sensor/actuator design for dynamic measurement/control of distributed parameter systems: a piezoelectric finite element approach", *J. Sound Vib.* **138**:1 (1990), 17–34.

[Vasques and Rodrigues 2005] C. M. A. Vasques and J. D. Rodrigues, "Coupled three-layered analysis of smart piezoelectric beams with different electric boundary conditions", *Int. J. Numer. Methods Eng.* **62**:11 (2005), 1488–1518.

[Wang 2004] S. Y. Wang, "A finite element model for the static and dynamic analysis of a piezoelectric bimorph", *Int. J. Solids Struct.* **41**:15 (2004), 4075–4096.

[Zhang and Sun 1996] X. D. Zhang and C. T. Sun, "Formulation of an adaptive sandwich beam", *Smart Mater. Struct.* **5**:6 (1996), 814–823.

SANTOSH KAPURIA: kapuria@am.iitd.ac.in
Dynamics and Vibrations Group, Department of Mechanical Engineering, Technische Universität Darmstadt, Hochschulstrasse 1, 64289 Darmstadt, Germany

PETER HAGEDORN: peter.hagedorn@dyn.tu-darmstadt.de
Dynamics and Vibrations Group, Department of Mechanical Engineering, Technische Universität Darmstadt, Hochschulstrasse 1, 64289 Darmstadt, Germany

A COMPARISON OF OPEN CELL AND CLOSED CELL PROPERTIES FOR LOW-DENSITY MATERIALS

RICHARD M. CHRISTENSEN

The stiffness and strength properties for open cell and closed cell low-density materials are collected and compared. These are the theoretical predictions for the Kelvin cell type and the oct-tet cell type of open cell forms and of the closed cell form from the generalized self-consistent method. The strength properties considered are those for plastic collapse and elastic instability, under both uniaxial stress and dilatational stress conditions.

1. Introduction and conditions of comparison

Low-density materials (LDM) have come into widespread usage. The properties and practice for materials with two-dimensional microstructures such as honeycomb forms, and other forms are well covered and well understood. [Gibson and Ashby 1997] is standard reading on the topic and there have been many review articles, such as that by Christensen [2000]. The situation with low-density materials having three-dimensional microstructures is more complex. They are widely used, but they are less well understood than the two-dimensional cases, partly because of the much more complex microscale geometry. The complications that arise in the three-dimensional case are immediately apparent when one considers whether to focus upon closed cell or open cell forms. This divergence does not even arise in the two-dimensional case. For this reason two-dimensional results are almost useless in projecting what three-dimensional behaviors may involve.

Until rather recently there did not appear to be enough information available to conduct an in-depth comparison of open cell and closed cell forms. Essentially the missing piece was that of the work of Deshpande et al. [2001] on a particular type of open cell form. To describe this further requires an understanding of the two basic types of microstructures for the various open cell forms. These are most easily illustrated by the corresponding two-dimensional cases. If a honeycomb form is deformed in any state except dilatation, its material members resist the deformation by means of a bending mechanism. Alternatively, if a two-dimensional LDM is composed of equilateral triangular cells its material members resist deformation by an axial or direct or stretching mechanism. The same situation exists in three dimensions, different microstructures resist deformation by either a direct or a bending mechanism. However, nearly all of the attention has been focused upon three-dimensional LDM's having only the bending mechanism. The work of Deshpande et al. [2001] convincingly detailed a microstructure which involves only the direct mechanism. In the work to be given here, two fundamental microstructures will be taken

for the open cell case, one involving the bending mechanism and one involving the direct mechanism. These will be compared with each other as well as with a closed cell type microstructure.

Although one could in principle compare experimental data for open cell and closed cell forms, in practice this is difficult to do. Rarely are open cell and closed cell samples available at exactly the same volume fraction of voids and for the exact same constituent materials. Furthermore even when they are at least approximately the same, the experimental scatter and uncertainty renders comparisons difficult. Instead, theoretical predictions of properties will be given here for the three idealized microstructures, thus precise control will be exercised over the morphological forms being compared. It is well understood that imperfections are very important as they can reduce performance levels significantly. Nevertheless the ideal forms considered here will bring out strong differences in a relative sense between the microstructures.

The present considerations will be restricted to the very low-density range. The volume fraction of material will be taken to be much less than 0.1. In effect, this will involve retaining the first term in an expansion in terms of powers of the volume fraction of the material. For larger volume fractions, the differences between open cell and closed cell forms become blurred and they merely become ones of many different possible forms for porous materials wherein rather convoluted surface morphologies become possible.

2. Stiffness and strength properties

The three LDM cellular microstructures to be studied here are now prescribed. The two open cell forms are the Kelvin cell and the oct-tet cell. The closed cell form is that from the generalized self-consistent method (GSCM).

The Kelvin cell is obtained by starting with an octahedron, then cutting off the six corners such that the truncated octahedron is composed of six squares and eight hexagons. The resulting forms can then be perfectly packed into a space filling periodic structure having cubic symmetry. It was Kelvin who first understood the space-filling attribute of this simple cell. The resulting Kelvin cell is shown in Figure 1. For application to LDM's the edges of the cells are taken to be material members.

The oct-tet form was patented by Fuller [1961] and was extensively studied by Deshpande et al. [2001] as an LDM. The cellular form can be thought of as due to the three-dimensional packing of tetrahedrons with the octahedrons existing as the spaces left over from the necessarily imperfect packing of the tetrahedrons. The resulting microstructure is interpreted as an LDM by taking the edges of the tetrahedrons (and octahedrons) as material members. The resulting form has face centered cubic symmetry and is as shown in Figure 2. Material members connect the corners and face centers in the manner shown for the three front faces. Christensen [2004] described this three-dimensional cellular form as being the three-dimensional analog of the classical two-dimensional truss system.

For application to closed cell forms, the GSCM model is as shown in Figure 3. A thin spherical shell of the material is embedded in a continuous medium having the as yet unknown properties of the composite form. This model was developed by Christensen and Lo [1979] for applications to general composite material systems. The specialization of the general model to the case of the inclusion phase as voids and the material in the low volume fraction range gives the LDM model of interest here, for the effective stiffness properties.
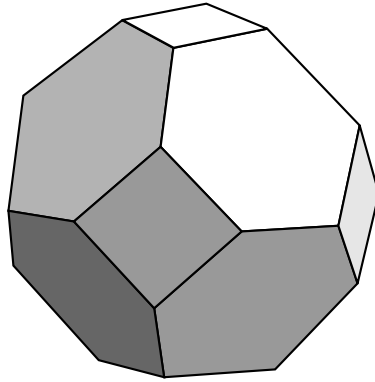
Figure 1. Open cell, Kelvin form, truncated octahedron.

The Kelvin cell has four material members meeting at a node, whereas the oct-tet cell has twelve material members meeting at a node. For the oct-tet cell the resistance to deformation is supplied by the direct mechanism in all possible deformation states. In the Kelvin cell a dilatational deformation is resisted by the direct mechanism of the material members, but all other deformation modes are resisted by the bending mechanism. In these cases of the bending mechanism being operative, the torsion of the material members also must be included. The two open cell forms thus employ fundamentally different mechanisms of material resistance. Also, these two cellular forms are of cubic symmetry and the properties will be stated in cubic symmetry form. The GSCM closed cell form is isotropic. Many
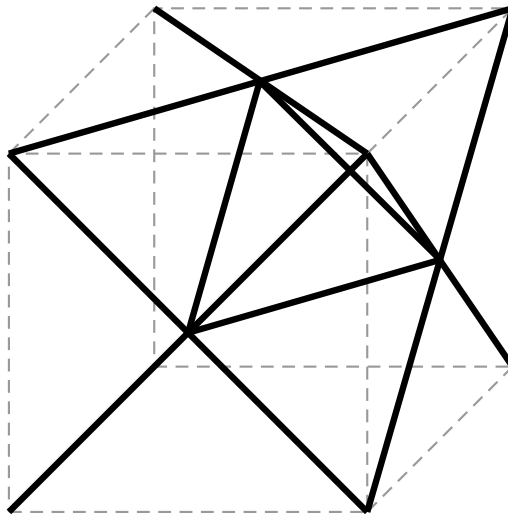
Figure 2. Open cell, oct-tet form.
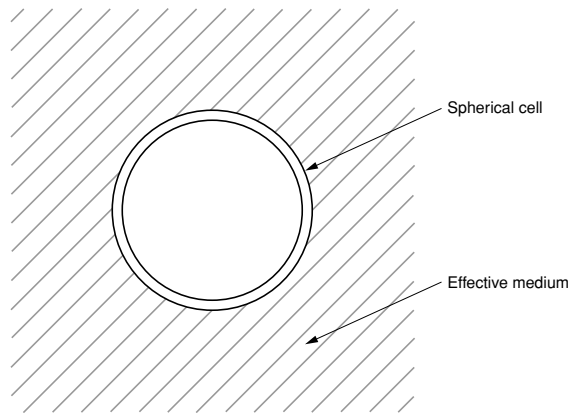
Figure 3. Closed cell, GSCM model.

other cellular forms have been studied (see [Wicks and Hutchinson 2001; Gong et al. 2005; Gong and Kyriakides 2005; Roberts and Garboczi 2001]) but the three forms considered here suffice to cover most of the basic effects needed to compare open cell and closed cell forms.

For the two open cell forms the properties are sometimes stated in terms of (r/ℓ) where r is the radius of a circular material member and ℓ is its length. However, for present purposes of comparing different microstructures it is necessary to use the volume fraction of material, c_m, as the basis of comparison. Various powers of c_m will be found to enter the properties, such as c_m, c_m^2, etc. Since $c_m \ll 0.1$ in the LDM range the different powers of c_m will project very different properties, sometimes different by orders of magnitude. All results to be given here will be for material members having cross sections of solid, circular form in the open cell cases.

A table has been constructed of all the major stiffness and strength properties for all three forms of LDM's. The properties information is in Table 1, and is obtained directly from the references as noted. It should be recognized that many of these results required major expenditures of effort in their original derivations, and as such represent a considerable resource. The first four entries in Table 1 are for the usual stiffness properties and Poisson's ratio of the effective medium. E_m and υ_m are the properties of the composing material. The two plastic collapse entries are for yielding where the material has a uniaxial stress at yield of σ_y. Plastic collapse dilatational refers to the imposition of a hydrostatic stress state which in the open cell cases imposes compressive stress states in the material members. Collapse occurs when this stress reaches the yield value. In the closed cell case, the biaxial stress state reaches its yield value. In Table 1, the term plastic collapse uniaxial stress is similarly defined. In the oct-tet cell and the closed cell cases, these results follow from simple geometry and equilibrium. It is only in the case of the Kelvin cell that the plastic collapse under uniaxial stress is far from obvious and requires a somewhat lengthy derivation. This derivation is given in Appendix A. All of these results will be further described below.

The last two entries in Table 1 are for the elastic stability under compressive dilatational and uniaxial stress. The elastic stability dilatational refers to stress levels in the open cell material members that buckle under the imposition of hydrostatic stress to the cell. In the closed cell case, the result arises

Property	Open cell (bending/Kelvin)	Open cell (direct/oct-tet)	Closed cell GSCM
$\dfrac{E_{11}}{E_m}$	$\dfrac{4\sqrt{2}}{3\pi}c_m^2$	$\dfrac{1}{9}c_m$	$\dfrac{2}{5+3\upsilon_m}c_m$
υ_{12}	$\dfrac{1}{2}$	$\dfrac{1}{3}$	$\dfrac{1+3\upsilon_m}{5+3\upsilon_m}$
μ_{12}/E_m	$\dfrac{2\sqrt{2}}{3\pi}\left(\dfrac{6+5\upsilon_m}{9+8\upsilon_m}\right)c_m^2$	$\dfrac{1}{12}c_m$	$\dfrac{1}{6(1+\upsilon_m)}c_m$
k/E_m	$\dfrac{1}{9}c_m$	$\dfrac{1}{9}c_m$	$\dfrac{2}{9(1-\upsilon_m)}c_m$
Plastic collapse dilatational σ	$\dfrac{\sigma^y}{3}c_m$	$\dfrac{\sigma^y}{3}c_m$	$\dfrac{2}{3}\sigma^y c_m$
Plastic collapse uniaxial σ_{11}	$\dfrac{8(2)^{3/4}}{9\sqrt{3}\pi^{3/2}}\sigma^y c_m^{3/2}$	$\dfrac{\sigma^y}{3}c_m$	$\dfrac{2}{3}\sigma^y c_m$
Elastic stability dilatational σ	$\dfrac{\pi E_m}{4\sqrt{2}}c_m^2$	$\dfrac{\pi E_m}{72\sqrt{2}}c_m^2$	$\left[\dfrac{2}{9}\dfrac{E_m}{\sqrt{3(1-\upsilon_m{}^2)}}\right]c_m^2$
Elastic stability uniaxial σ_{11}	not applicable	$\dfrac{\pi E_m}{72\sqrt{2}}c_m^2$	unknown

Table 1. LDM properties.

directly from the buckling of a thin spherical shell. For the Kelvin cell case, the stiffness properties are from [Warren and Kraynik 1997] and [Zhu et al. 1997]. The strength properties for the Kelvin cell were constructed for this work. For the oct-tet cell the stiffness and strength properties were given by Deshpande et al. [2001]. Some of the properties were put into slightly different forms for the present purposes. The closed-cell stiffness properties were given by Christensen [1998]. The closed cell strength properties were worked out here and are extremely simple to derive.

The method of deducing the strength properties for the oct-tet cell case, given by Deshpande et al. [2001], also forms the basis for deducing the strength properties for the other two cell types. For plastic collapse, plastic hinges form in the Kelvin cell material members, see Appendix A, and plastic yield stress is reached in the closed cell case. The 3/2 power in the Kelvin cell, uniaxial stress plastic collapse term of Table 1 is due to the formation of the plastic hinges in the collapse mechanism. Similarly for elastic stability under compressive stress, the open cell material members reach the limits of elastic stability. These limiting stresses are found under both hydrostatic stress and uniaxial stress states.

In the closed cell case it was necessary to construct the elastic stability under dilatational and uniaxial stress. The dilatational case was taken as that for a free spherical shell under uniform pressure. The effect of the constraining effective medium attached to the spherical shell, Figure 3, was not included. Thus the constraint of the effective medium would increase somewhat the result shown in Table 1. This

Property	Open cell (bending/Kelvin)	Open cell (direct/oct-tet)	Closed cell GSCM
$\dfrac{E_{11}}{E_m}$	$0.600c_m^2$	$\dfrac{1}{9}c_m$	$\dfrac{1}{3}c_m$
υ_{12}	$\dfrac{1}{2}$	$\dfrac{1}{3}$	$\dfrac{1}{3}$
μ_{12}/E_m	$0.197c_m^2$	$\dfrac{1}{12}c_m$	$\dfrac{1}{8}c_m$
k/E_m	$\dfrac{1}{9}c_m$	$\dfrac{1}{9}c_m$	$\dfrac{1}{3}c_m$
Plastic collapse dilatational σ	$\dfrac{1}{3}\sigma^y c_m$	$\dfrac{1}{3}\sigma^y c_m$	$\dfrac{2}{3}\sigma^y c_m$
Plastic collapse uniaxial σ_{11}	$0.155\sigma^y c_m^{3/2}$	$\dfrac{1}{3}\sigma^y c_m$	$\dfrac{2}{3}\sigma^y c_m$
Elastic stability dilatational σ	$0.555E_m c_m^2$	$0.03E_m c_m^2$	$0.136E_m c_m^2$
Elastic stability uniaxial σ_{11}	not applicable	$0.03E_m c_m^2$	unknown

Table 2. Properties for $\upsilon_m = 1/3$.

result in the hydrostatic case follows directly from [Timoshenko 1961]. The case of the elastic stability under uniaxial stress is expected to have a critical value larger than that in the dilational case, but an exact result is unknown.

3. Discussion

The results shown in Table 1 are specialized to the case of Poisson's ratio $\upsilon_m = 1/3$ for ease of interpretation, Table 2. Some particular comparisons between the three cellular forms will be noted here but the main purpose is to collect and codify the significant results shown in Tables 1 and 2. There could be a huge variety of possible applications, most of which cannot even be anticipated here.

In the case of the two open cell forms, the two forms are both cubic and the properties are stated relative to the symmetry axes designated in the references. It is interesting however to note that in the case of the Kelvin cell and for the members of solid circular cross section, the cubic stiffness properties are very nearly isotropic. The properties are within 1.5% of being isotropic at $\upsilon_m = 1/2$ and they are exactly isotropic at $\upsilon_m = 0$. The oct-tet cell form is cubic with the maximum to minimum value of modulus E being in the ratio of 9/5 [Christensen 2004].

It is also interesting to note that the dilatational strength properties are not significantly larger than the uniaxial ones, for two of the three cellular forms. This contrasts somewhat with the behavior of homogeneous materials.

Observe again that properties dependent on c_m^2 are at least an order of magnitude less than those dependent on c_m. Thus the Kelvin cell case has elastic moduli properties as much less than those of the oct-tet cell. On the other hand, it is seen that the oct-tet form has serious shortcomings because of the extremely low value of the elastic stability tolerance due to the relatively large number of material members in the oct-tet cell. However, this result is for solid material members; for applications where hollow members could be used, this deficiency perhaps could be overcome.

In the elastic stability results, the material members in the open cell case could be taken either with pinned or fixed-end conditions. The results shown are for the pinned case. The other case would be a factor of four times larger.

As an overall observation, it can be noted that except for the dilatational elastic stability case, the closed cell properties are always greater, sometimes much greater, than are the open cell properties. The closed cell geometry is simply a more efficient use of the material. However, in particular applications, other requirements could supercede the properties considerations shown here. Finally, it is again cautioned that these results are for the corresponding idealized (perfect) morphologies of microstructure. Imperfections always have a strongly degrading effect.

Appendix A

The uniaxial stress σ_{11} for plastic collapse in the Kelvin cell form is derived here. Referring to Figure 1, take the stress σ_{11} to be in the horizontal direction, normal to the square face on the right hand side of the cell. The material member connecting this face and the top square face in Figure 1 has the horizontal component of force P at its ends given

$$P = \frac{2M}{\ell \sin \phi},$$
(A.1)

where M is the maximum moment in the member, ℓ is the members length, and $\phi = 45°$. Then

$$P = \frac{2\sqrt{2}M}{\ell}.$$
(A.2)

Take the Kelvin cell in Figure 1 as being inside a cube of length a with the square faces in the Kelvin cell being on the faces of the cube. Dimension a is related to ℓ through

$$a = 2\sqrt{2}\ell.$$
(A.3)

The uniaxial stress σ_{11} is related to P through

$$\sigma_{11} = \frac{4P}{a^2}.$$
(A.4)

Combining (A.2), (A.3) and (A.4) gives

$$\sigma_{11} = \sqrt{2}\frac{M}{\ell^3}.$$
(A.5)

For a plastic hinge to form in a fully plastic, circular member the bending moment must attain the value

$$M = \frac{2}{3}\sigma^y r^3, \tag{A.6}$$

where the yield stress is σ^y and r is the radius of the cross section. Combining (A.5) and (A.6) gives

$$\sigma_{11} = \frac{2\sqrt{2}}{3}\sigma^y \left(\frac{r}{\ell}\right)^3. \tag{A.7}$$

The volume fraction c_m of the material members is given by

$$c_m = \frac{3\pi}{2\sqrt{2}}\left(\frac{r}{\ell}\right)^2. \tag{A.8}$$

Combining (A.7) and (A.8) gives the final result

$$\sigma_{11} = \left(\frac{8(2)^{3/4}}{9\sqrt{3}\pi^{3/2}}\right)\sigma^y c_m^{3/2}. \tag{A.9}$$

References

[Christensen 1998] R. M. Christensen, "Two theoretical elasticity micromechanics models", *J. Elasticity* **50**:1 (1998), 15–25.

[Christensen 2000] R. M. Christensen, "Mechanics of cellular and other low-density materials", *Int. J. Solids Struct.* **37**:1-2 (2000), 93–104. MR 2000j:74021

[Christensen 2004] R. M. Christensen, "The three-dimensional analog of the classical two-dimensional truss system", *J. Appl. Mech.*(*Trans. ASME*) **71**:2 (2004), 285–287.

[Christensen and Lo 1979] R. M. Christensen and K. H. Lo, "Solutions for effective shear properties in three phase sphere and cylinder models", *J. Mech. Phys. Solids* **27**:4 (1979), 315–330.

[Deshpande et al. 2001] V. S. Deshpande, N. A. Fleck, and M. F. Ashby, "Effective properties of the octet-truss lattice material", *J. Mech. Phys. Solids* **49**:8 (2001), 1747–1769.

[Fuller 1961] R. B. Fuller, "Octet truss", 1961. U.S. Patent No. 2,986,241.

[Gibson and Ashby 1997] L. J. Gibson and M. F. Ashby, *Cellular solids: structure and properties*, 2nd ed., Cambridge University Press, Cambridge, UK, 1997.

[Gong and Kyriakides 2005] L. Gong and S. Kyriakides, "Compressive response of open cell foams, II: initiation and evolution of crushing", *Int. J. Solids Struct.* **42**:5-6 (2005), 1381–1399.

[Gong et al. 2005] L. Gong, S. Kyriakides, and W. Y. Jang, "Compressive response of open-cell foams, I: morphology and elastic properties", *Int. J. Solids Struct.* **42**:5-6 (2005), 1355–1379.

[Roberts and Garboczi 2001] A. P. Roberts and E. J. Garboczi, "Elastic moduli of model random three-dimensional closed-cell cellular solids", *Acta Mater.* **49**:2 (2001), 189–197.

[Timoshenko 1961] S. P. Timoshenko, *Theory of elastic stability*, 2nd ed., McGraw-Hill, New York, 1961. MR 24 #B80

[Warren and Kraynik 1997] W. E. Warren and A. M. Kraynik, "Linear elastic behavior of a low density kelvin foam with open cells", *J. Appl. Mech.*(*Trans. ASME*) **64** (1997), 787–794.

[Wicks and Hutchinson 2001] N. Wicks and J. W. Hutchinson, "Optimal truss plates", *Int. J. Solids Struct.* **38**:30-31 (2001), 5165–5183.

[Zhu et al. 1997] H. X. Zhu, J. F. Knott, and N. J. Mills, "Analysis of the elastic properties of open-cell foams with tetrakaidecahedral cells", *J. Mech. Phys. Solids* **45**:3 (1997), 319–325.

RICHARD M. CHRISTENSEN: `christensen6@llnl.gov`
Lawrence Livermore National Laboratory, P. O. Box 808, L-356, Livermore, CA 94550, United States
and
Department of Aeronautics and Astronautics, Stanford University, Stanford, CA 94305

PROTECTION PERFORMANCE OF DOUBLE-LAYERED METAL SHIELDS AGAINST PROJECTILE IMPACT

XIAOQING TENG, SUMITA DEY, TORE BØRVIK AND TOMASZ WIERZBICKI

This paper critically evaluates the protection performance of double-layered shields against projectile impact at the subordnance velocity using finite element methods. Four types of projectiles of different weight and nose shape are considered, representing various fragments generated from Improvised Explosive Devices (IEDs). It is found that the double-layer configuration is able to improve the ballistic resistance by 8.0%–25.0% for the flat-nose projectile, compared to the monolithic plate of the same weight. The upgrade is due to the transition of the failure mode from less energy dissipating shear plugging to more energy dissipating tensile tearing. Under impact by the conical-nose projectile, the double-layered target is almost as capable as the monolithic plate. The present research helps resolve the long outstanding issue of the protection effectiveness of the double-layer configuration.

1. Introduction

Optimization design of metal shields for protection against projectile impact has long been of interest in military and civilian applications. As a potential improvement over monolithic plates, a multiple layer configuration that consists of several parallel plates has been proposed. Compared with numerous experimental, numerical, and theoretical investigations on the impact failure response of single-layered shields, only limited studies on the performance of multilayered targets were reported in the open literature.

Marom and Bodner [1979] investigated experimentally and theoretically the perforation behavior of multilayered beams under impact by a spherical-nose bullet projectile. They concluded that the multilayered structures were more effective than the uniform beams of the same weight. Corran et al. [1983b; 1983a] found from a series of impact tests that a double-, triple-layered target would be superior in the ballistic resistance than a monolithic shield if the total thickness exceeded a critical value. An opposite conclusion was obtained by Radin and Goldsmith [1988]. They performed normal impact tests of a blunt-nose and a conical-nose projectile on multilayered plates. The ballistic limits of the single-layered plates were always higher than those of the multiple-layered targets for both types of projectiles. Note that the thickness of the targets tested by Radin and Goldsmith ranges from 1.6 mm to 6.4 mm. Almohandes et al. [1996] confirmed this finding by conducting an extensive experimental study on steel shields of various configurations struck by standard 7.62 mm bullet projectiles. An experimental and numerical study on the protection effectiveness of double-layered steel shields was recently executed by Dey et al. [2007] and Børvik et al. [2006]. It was found that in the case of the blunt-nose projectile the ballistic limits can be improved by more than 30% by adopting the double layer configuration.

Besides experimental and numerical studies, several analytical models were also developed for the estimation of the ballistic resistance of multilayered shields. For example, Ben-Dor et al. [1998; 2006] studied effects of the spacing between plates on the ballistic limits. They concluded that increasing the spacing produced no significant change. Elek et al. [2005] extended the penetration model developed by Liss et al. [1983] to the case with multilayered targets. The theoretical solutions indicate that a monolithic target has greater ballistic resistance than a multilayered shield of the same thickness. Liang et al. [2005] proposed a simple theoretical model for the shear plugging process of multilayered shields.

It appears from the above literature review that the protection effectiveness of multilayered shields remains a subject of controversy. This inconsistency poses an interesting question: Under what kind of projectile impact would a double-layered shield be superior in the ballistic limit than a monolithic plate of the same weight?

Different failure modes may develop in a single target due to changing impact conditions [Børvik et al. 2002a; 2002b; Teng and Wierzbicki 2005a; 2005b]. If we could promote a failure mode with higher energy absorption, the ballistic resistance of a shield can be significantly improved. By replacing a monolithic plate with a double-, multilayered shield, the bending flexibility can be increased allowing a target to undergo considerable deformation before fracture. The objective of the present paper is to evaluate the performance of the double layer configuration against projectile impact.

A variety of projectiles including heavy fragments generated from IEDs and light bullet hard-core projectiles may be encountered in practical applications. An armor shield would behave differently under the impact of different projectiles. To thoroughly investigate the protection effectiveness of a target four types of projectiles of different weight and nose shape are considered in this study.

The introduction of the double layer configuration brings into the analysis three additional important parameters: spacing, material combination, and thickness ratio between two plates. For simplicity, the present paper assumes that the two plates are identical to each other, that is, the two plates are made of the same metal and are of the same thickness. We focus on effects of the spacing between the two plates. The advantage of using two different grades of steels for the two layers is a subject of a separate study.

Even with this simplification, an extensive parametric study has to be conducted to determine the ballistic limit of each projectile-target system. Such an approach would not be affordable by means of tests alone. As an alternative to determine experimentally the V_{50}, leading commercial finite element codes such as ABAQUS/Explicit and LS-DYNA are able to fulfill this task provided that they are equipped with a suitable fracture model. In this study, ABAQUS/Explicit is used to simulate all perforation processes. Numerical modeling provides an insight into failure mechanisms and may help reduce the number of necessary tests. Finally, the paper concludes by pointing out the advantages of the double layer configuration over the monolithic plate.

2. Problem description

2.1. *Computational models.* We consider three types of metal shields including a monolithic plate, a double-layered shield with the plates initially in contact, and a double-layered shield with the plates spaced, as shown in Figure 1. Monolithic plates are commonly used in practice for armor protection, and this case will be taken as a reference in the present study. Two identical plates are defined in the double layer configuration. The plates interact with each other through compression but not tension.

(a) monolithic   (b) double-layered with plates in contact

(c) double-layered with plates separated
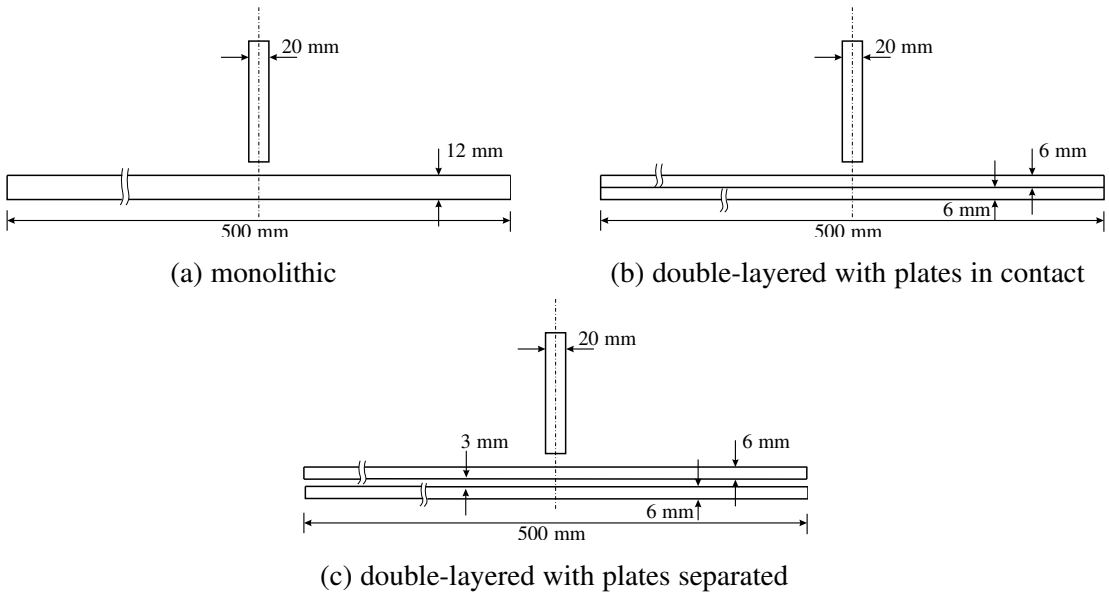
Figure 1. Three types of shields considered in this work.

Limited shear stress due to friction can also be transmitted between the two plates. The shields are of circular shape with the same diameter of 500 mm and the same total thickness of 12 mm. These geometrical dimensions were taken from the impact tests on the monolithic plates conducted by Børvik et al. [2002b]. In the third type of shields the spacing between the two plates is 3 mm, which is 25% of the total thickness still allowing the two plates to interact with each other.

Two major types of armor-piercing projectiles are often encountered in battles: 7.62 mm armor-piercing (AP) bullets from rifles or machine guns and fragments generated from IEDs. The ball rounds have mass usually of the order of 10 g and are of ogival-nose shape. By contrast, fragments may come in a variety of weight and configurations. To design light armor shields for protection against fragments, U.S. military standard MIL-P-46593A prescribes three types of Fragment Simulating Projectiles (FSPs) with mass of 44 g, 207 g, and 830 g, respectively [DoD 1962]. All these FSPs are of cylindrical shape and chisel-nose. In this paper four types of cylindrical projectiles are considered; see Figure 2. We have defined for them two masses of different orders of magnitude: 200 g and 10 g. The heavy projectiles describe typical IED fragments. At the same time, two types of impactor noses were introduced: flat-nose and conical-nose, which denote two limiting cases. The light, conical-nose projectile coarsely represents a 7.62 mm AP round.

With different combinations of the three metal shields and the four projectiles, there are a total of twelve impact cases in this research. For each case, the initial impact velocity of the projectiles varies in a wide range and the ballistic limit is found when the exit (residual) velocity becomes zero. The protection performance of the three metal shields is evaluated by comparing their ballistic limits.

A two-dimensional finite element model was generated for each projectile-target plate system. The target plates were modeled using four-noded axisymmetric elements with reduced integration (CAX4R). The *relax stiffness* option of the integral viscoelastic form was defined to control possible hourglass
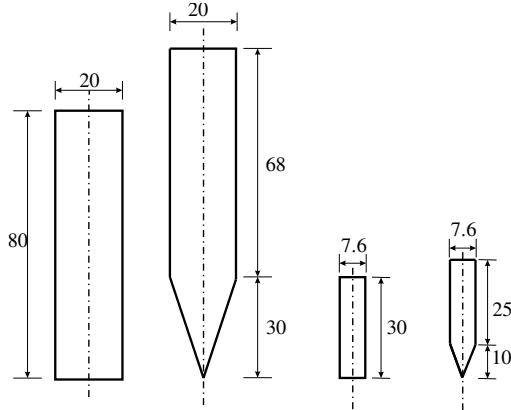
Figure 2. Dimensions of four cylindrical projectiles considered in this work (unit: mm).

deformation for this type of elements. Figure 3 shows a finite element model for the double-layered shield with the plates spaced. The impacted zone below the projectile was discretized with 120 square elements through the thickness, that is, the minimum element size is 0.1×0.1 mm. An early study on mesh size effects indicates that numerical simulations based on such an element size correlate well with experimental results [Teng and Wierzbicki 2005a]. The projectiles were assumed to be undeformable and were simply represented by rigid surfaces in the simulations. The introduction of this assumption may underestimate the ballistic limits of the targets. In reality, projectiles would absorb a certain amount of the kinetic energy and may break into several pieces under shock wave loading [Børvik et al. 2003]. Such complex projectile behaviors are not taken into account in this numerical investigation.

To correctly simulate a whole perforation process, one has to carefully define contact conditions between any two bodies that may interact with each other. For the monolithic shield, the kinematic contact constraint was prescribed between the projectile and the impacted zone of the target. The problem becomes much more complex for the case with the double-layered shield. The projectile may sequentially
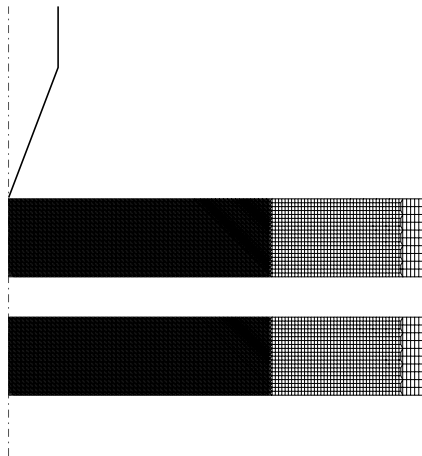
Figure 3. Finite element model of the impacted zone of a double-layered shield with plates spaced, impacted by a conical-nose projectile.

get into contact with the two plates and at the same time the two plates will act on each other. Three contact constraints need to be specified. Two kinematic contact constraints were defined between the projectile and the two target plates, respectively. The penalty contact constraint was prescribed between the two plates. A constant frictional coefficient of 0.1 was defined on all the possible contact interfaces.

2.2. *Plasticity and fracture models for Weldox 460 E steel.*

The target plates were assumed to be made of Weldox 460 E steel. Weldox is the brand name of a class of rolled steels manufactured by SSAB, Sweden. This class of steel is of high strength and at the same time of outstanding ductility. Børvik et al. [2001; 2005] conducted a series of tensile tests on round bars to characterize mechanical properties of Weldox 460 E steel. The material constitutive model proposed by [Johnson and Cook 1983] was selected to describe the plastic behaviors of the steel under dynamic loading. The hardening rule including effects of strain rates and elevated temperature is defined by

$$\bar{\sigma} = \left[A + B\bar{\varepsilon}_{\mathrm{pl}}^n \right] \left[1 + C \ln \left(\frac{\dot{\bar{\varepsilon}}_{\mathrm{pl}}}{\dot{\bar{\varepsilon}}_0} \right) \right] \left[1 - \left(\frac{T - T_0}{T_{\mathrm{m}} - T_0} \right)^m \right],$$

where $\bar{\sigma}$ is the von Mises stress, $\bar{\varepsilon}_{\mathrm{pl}}$ is the effective plastic strain, A, B, n, C, and m are five material constants to be calibrated from tests, $\dot{\bar{\varepsilon}}_{\mathrm{pl}}$ and $\dot{\bar{\varepsilon}}_0$ are the current and reference strain rate, T_{m} and T_0 are the melting and room temperature. Below we list relevant material constants for Weldox 460 E steel:

$E = 200$ GPa,	$\nu = 0.33$,	$\rho = 7850$ kg/m^3,	$\dot{\bar{\varepsilon}}_0 = 5.00 \times 10^{-4}$ s^{-1},	$C = 0.0123$,
$c_{\mathrm{v}} = 452$ J/kg K,	$T_{\mathrm{m}} = 1800$ K,	$T_0 = 293$ K,	$m = 0.94$,	$A = 490$ MPa,
$B = 383$ MPa,	$n = 0.45$,	$D_1 = 0.0705$,	$D_2 = 1.732$,	$D_3 = -0.54$.

A ductile fracture model formulated in the space of the stress triaxiality and the effective plastic strain was adopted to predict the material failure. Such a fracture criterion can be written most generally as

$$D = \int_0^{\bar{\varepsilon}_{\mathrm{pl}}} \frac{1}{\bar{\varepsilon}_{\mathrm{f}}(\eta)} \, \mathrm{d}\bar{\varepsilon}_{\mathrm{pl}},$$

where D is the damage indicator, $\bar{\varepsilon}_{\mathrm{f}}$ is the effective plastic strain to fracture, and η is the stress triaxiality defined by the ratio of the mean stress σ_{m} to the equivalent stress. A material point is said to fail when D reaches or exceeds the unity, that is, $D \geq 1.0$. This type of fracture model was first suggested by Johnson and Cook [1985], and has been incorporated into many leading commercial finite element codes. The effective fracture strain as a function of the stress triaxiality has to be determined from tests. Johnson and Cook [1985] suggested an exponential relationship $\bar{\varepsilon}_{\mathrm{f}} = D_1 + D_2 \exp(D_3 \eta)$, where D_1, D_2, and D_3 are three material coefficients. Based on a series of tensile tests on notched and unnotched round bars, Børvik et al. [2001; 2005] obtained the following data for Weldox 460 E steel: $D_1 = 0.0705$, $D_2 = 1.732$, and $D_3 = -0.54$. In many practical applications Johnson–Cook fracture loci calibrated from tensile tests were often extrapolated to the range of negative stress triaxialities. In such a way, the ductility of materials under compression may be underestimated. Here, the Johnson–Cook fracture locus was modified by incorporating a cut-off value for the negative stress triaxiality at $-1/3$; see Figure 4. The concept of the cut-off value was first introduced by Bao and Wierzbicki [2005] to account for the sharp increase of the ductility of materials under compression. The cut-off value has a critical effect on the reconstruction of various fracture patterns encountered in high velocity impact tests. This has been
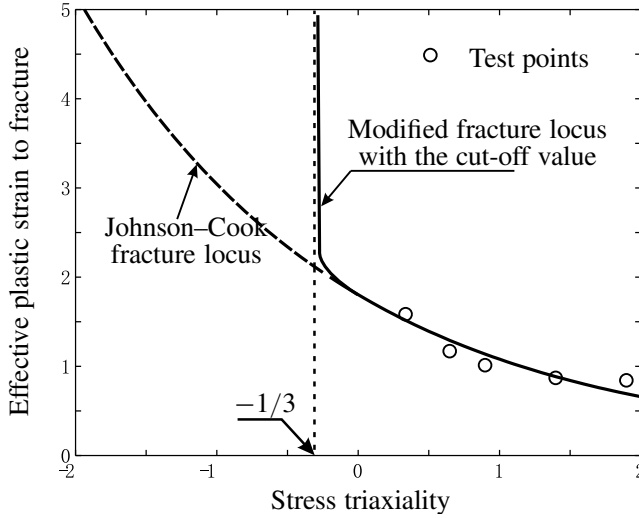
Figure 4. Fracture loci for Weldox 460 E steel.

successfully demonstrated in [Teng and Wierzbicki 2005b; Teng et al. 2005] for a number of impact problems.

Note, that the present fracture criterion is uncoupled with the material plasticity model. An element fails as soon as its damage indicator reaches the critical value. Failed elements completely lose their load-carrying capability and are removed from the rest of the calculation.

3. Perforation response of three types of shields

3.1. *Heavy flat-nose projectile.* The first striker considered is the heavy, flat-nose projectile, which represents a fragment generated from IEDs. Shear plugging is the predominant failure mode for the monolithic target under normal impact by this projectile. Its sharp corner often induces crack formation on the proximal surface. As the crack propagates through the plate thickness, the whole impacted zone beneath the projectile is ejected as a plug. Figure 5 shows a typical fracture process of the monolithic shield captured by the present numerical simulation at $V_0 = 285.4$ m/s. It can be observed that the target

(a) $t = 36 \ \mu$s   (b) $t = 84 \ \mu$s
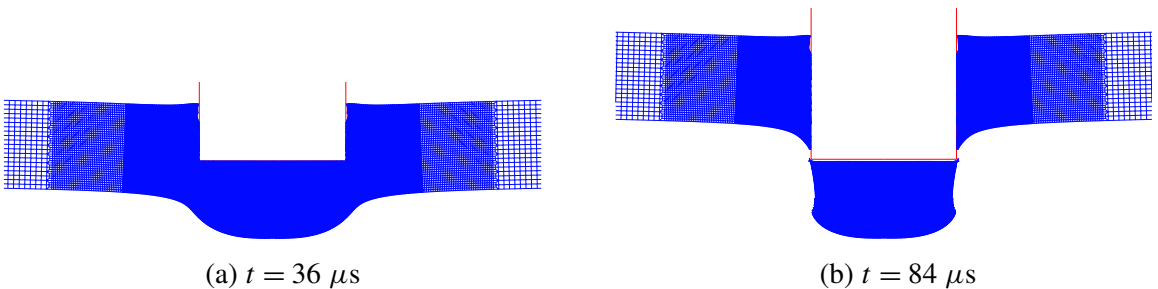
Figure 5. Shear plugging process of monolithic plate impacted by a heavy, flat-nose projectile at $V_0 = 285.4$ m/s.

(a) $t = 20\ \mu s$

(b) $t = 40\ \mu s$

(c) $t = 80\ \mu s$

(d) $t = 90\ \mu s$
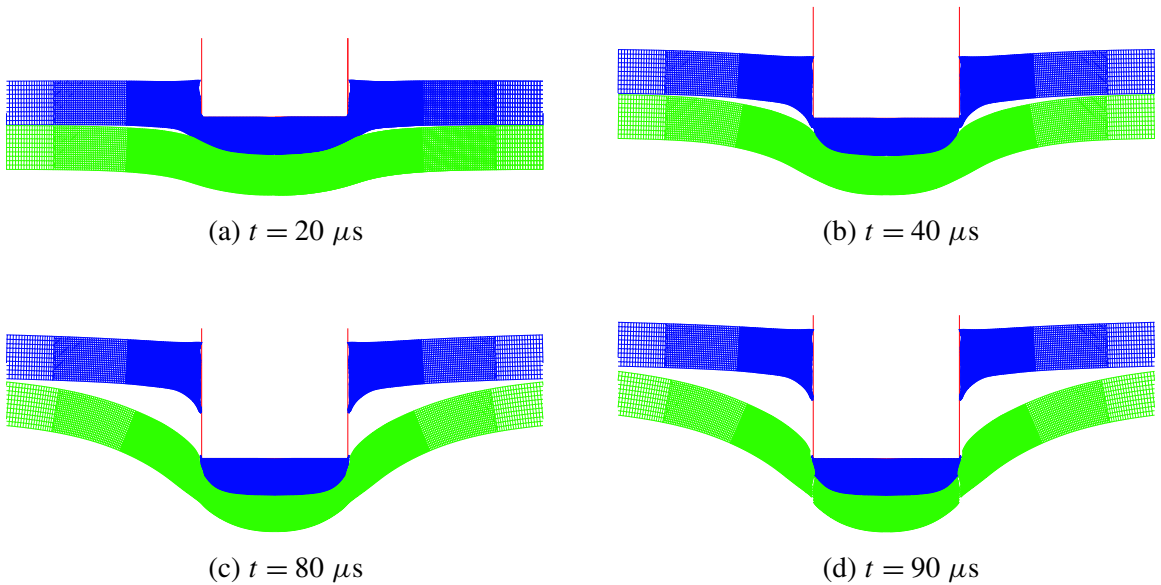
Figure 6. Perforation of double-layered shield with plates in contact impacted by a heavy, flat-nose projectile at $V_0 = 285.4$ m/s.

plate undergoes insignificant global deformation even at the impact velocity near the ballistic limit. Some of the impact velocities in the numerical simulations were selected to be identical to those in the impact tests performed by Børvik et al. [2002b]. In this way, one would be able to directly verify the correctness of the numerical results.

For the double-layered shield with the plates in contact, the upper plate tends to fail by shear plugging and the plastic deformation is localized in the impacted zone. This is similar to the monolithic target. However, the deformation region of the lower plate extends well beyond the impacted zone. Thinning before fracture can be clearly observed in the lower plate; see Figure 6. Unlike the monolithic plate in which one single crack continuously grows through the whole thickness, two separate cracks have to be formed, one for each plate in the double-layered shields. In general, crack initiation requires more energy dissipation than crack propagation.

The failure process of the double-layered shield with the plates spaced is illustrated in Figure 7. It appears that the upper plate suffers considerable bending deformation before contacting with the lower one. At the same time, one can see that the lower plate experiences deep necking and fails mainly by tensile tearing.

The transition of the failure mode from shear plugging in the monolithic plate to tensile tearing in the double-layered shield is accompanied with a large increase in plastic energy dissipation, particularly in the lower plate. Under the same impact condition, tensile tearing usually involves a larger plastically deformed area than shear plugging. Figure 8 shows the time evolution of the plastic energy dissipation of the upper and lower plates among the three types of shields. For comparison, for the monolithic plate, the plastic energy for the upper and lower half was output separately. The plastic energy absorbed by the

(a) $t = 24\ \mu s$

(b) $t = 48\ \mu s$

(c) $t = 120\ \mu s$

(d) $t = 132\ \mu s$
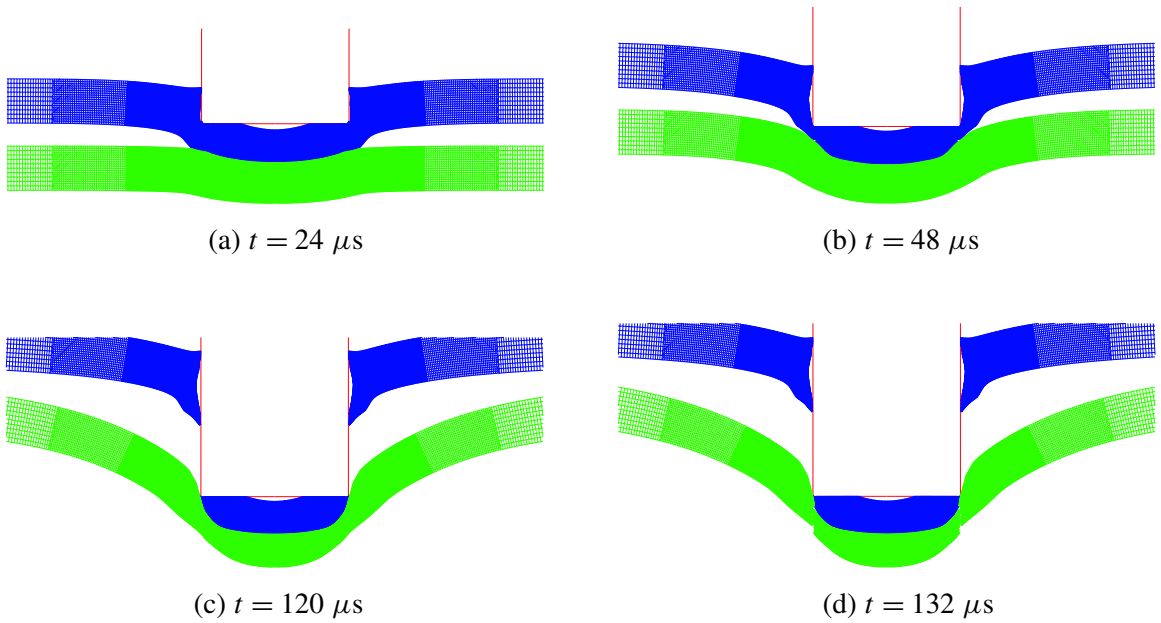
Figure 7. Perforation of double-layered shield with plates spaced impacted by a heavy, flat-nose projectile at $V_0 = 285.4$ m/s.

lower plate of the double-layered shield with the plates spaced is almost twice as large as that absorbed by the lower part of the monolithic target.

Large energy dissipation leads to low residual velocities of the projectile in the case of double-layered shields. Figure 9 shows plots of the residual velocity of the projectile versus the initial impact velocity
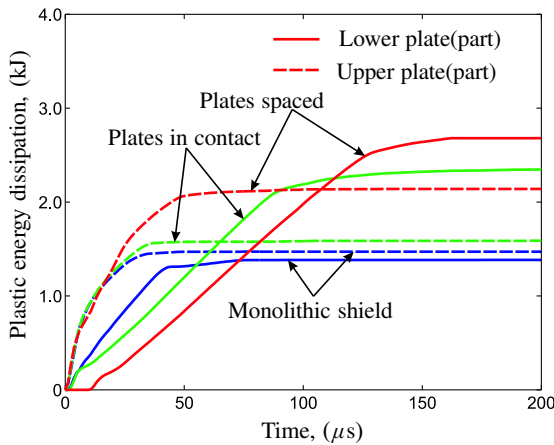
Figure 8. Time history of plastic energy dissipation of three shields at $V_0 = 285.4$ m/s.
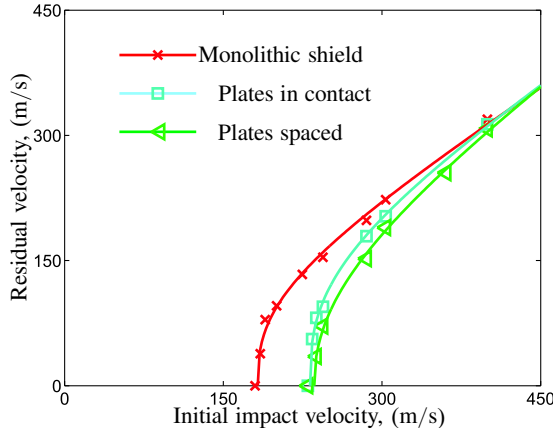
Figure 9. Initial impact velocity vs. residual velocity for three shields impacted by a heavy, flat-nose projectile.

among the three cases. As the impact velocity approaches the ballistic limit, the double-layered shields become superior in resisting perforation to the monolithic plate. Table 1 lists the ballistic limits of the three types of metal shields under impact by the heavy, flat-nose projectile. The ballistic limit of the metal shield is improved by about 25% by replacing the monolithic plate with the double-layered shields of the same total thickness. This finding is confirmed by the impact tests recently conducted by Dey et al. [2007]. They observed that the double layer configuration was able to increase the ballistic resistance by about 30%. The present numerical prediction is also consistent qualitatively with Corran et al.'s experimental results [1983b; 1983a], but contradicts test outcomes of Radin and Goldsmith [1988]. As Corran et al. [1983b; 1983a] pointed out, the double layer configuration would become more effective than the monolithic one as the total thickness exceeded a critical value. Note that the thickness of the targets studied by Radin and Goldsmith ranges from 1.6 mm to 6.4 mm, which is much smaller than in the current study.

It can be seen from Figure 9 that for the double-layered shields an increase in the spacing between the two plates slightly improves the ballistic resistance. This conclusion is contrary to the experimental results obtained by Marom and Bodner [1979], who found that the beams in contact always have higher ballistic limits than the beams spaced. It should be noted, however, that in their study the beams were so widely separated that there was essentially no interaction between them during the whole perforation process. In the present case, the two plates in the double-layered shields strongly interact with one another. This inconsistency indicates that there may exist an optimal spacing for the double-layered shield.

Monolithic plate	Double-layered shield	
	plates in contact	plates spaced
186.1 (1.00)	232.0 (1.25)	236.0 (1.27)

Table 1. Ballistic limits under the impact of a heavy, flat-nose projectile (unit: m/s).

(a) $t = 105.0 \, \mu s$ (b) $t = 175.0 \, \mu s$

(c) $t = 280.0 \, \mu s$
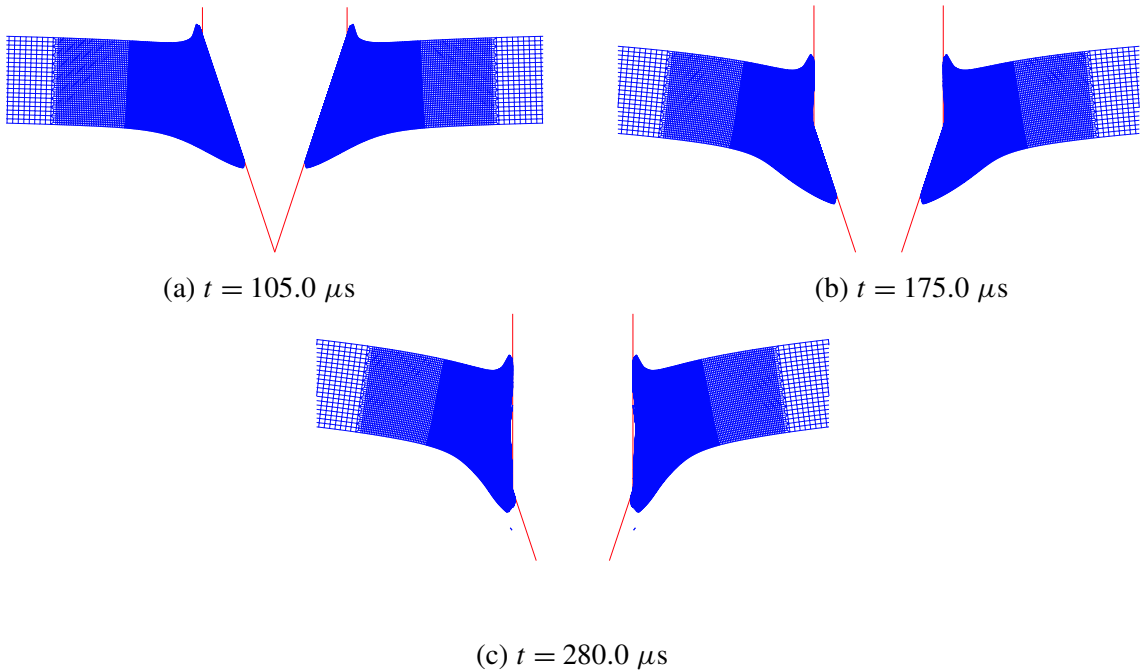
Figure 10. Perforation of monolithic shield impacted by a heavy, conical-nose projectile at $V_0 = 317.9$ m/s.

3.2. *Heavy conical-nose projectile.* In the preceding section the surface contact between the fragment projectile and the target was assumed. It is more likely that the sharp corner of a fragment would first pierce a metal shield in real situations. This type of perforation scenario is considered here by introducing the heavy, conical-nose projectile. Figures 10–12 illustrate the failure processes of the three types of shields under normal impact by the conical-nose projectile. In the second case the lower plate undergoes larger bending deformation than the upper plate. This leads to a clear separation between the two plates, which are initially in close contact. It can also be seen that in the three cases the materials in the impacted zone are pushed aside as the projectile penetrates through the thickness. There is no clear sign of crack formation and propagation. All the target plates fail by ductile hole enlargement, independent of the configuration and the impact velocity. Hence, the introduction of the double-layered configuration does not induce the transition of the failure mode for the conical-nose projectile. This is in contrast to the preceding case with the flat-nose projectile.

Plots of the initial impact velocity versus the residual velocity for the three types of metal shields are shown in Figure 13. The predicted residual velocities for the double-layered shields are always higher than those for the monolithic plate. Since neither large shear nor tensile stresses can be transferred between the two plates, the shear resistance of the double-layered shields is weakened. This leads to an 8% decrease in the ballistic limits compared to the monolithic plate; see Table 2. This conclusion is qualitatively in agreement with the experimental results obtained by Radin and Goldsmith [1988], Almohandes et al. [1996], and Dey et al. [2007].

(a) $t = 105.0\ \mu s$

(b) $t = 157.5\ \mu s$

(c) $t = 245.0\ \mu s$
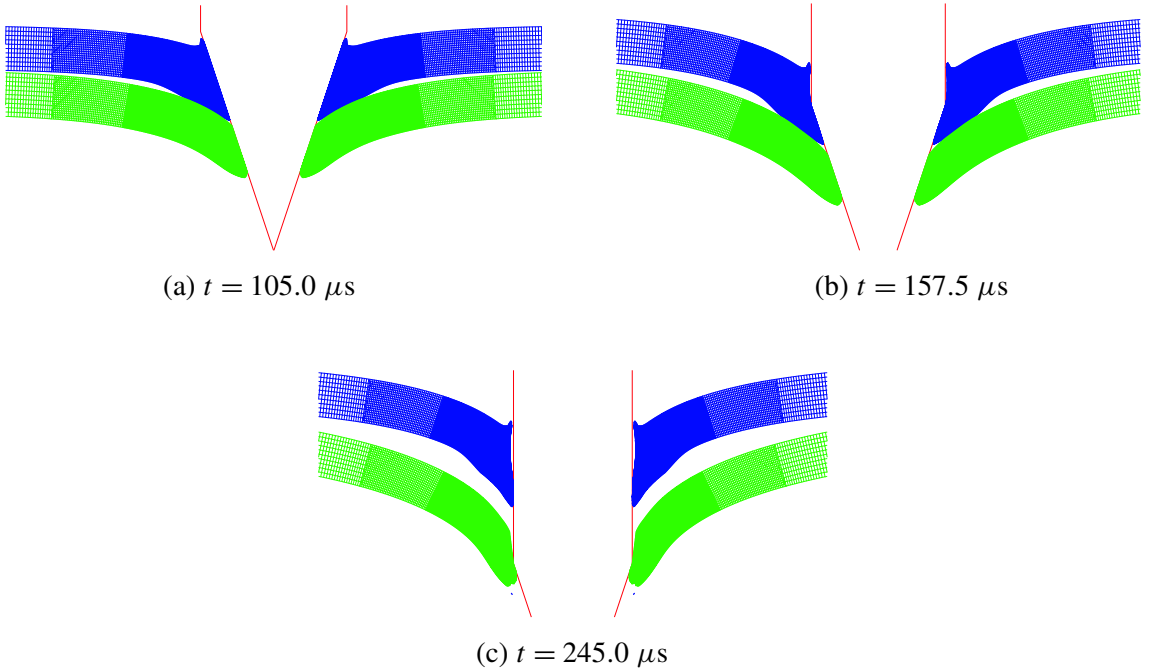
Figure 11. Perforation of double-layered shield with plates in contact impacted by a heavy, conical-nose projectile at $V_0 = 317.9$ m/s.

(a) $t = 40.0\ \mu s$

(b) $t = 140.0\ \mu s$

(c) $t = 240.0\ \mu s$
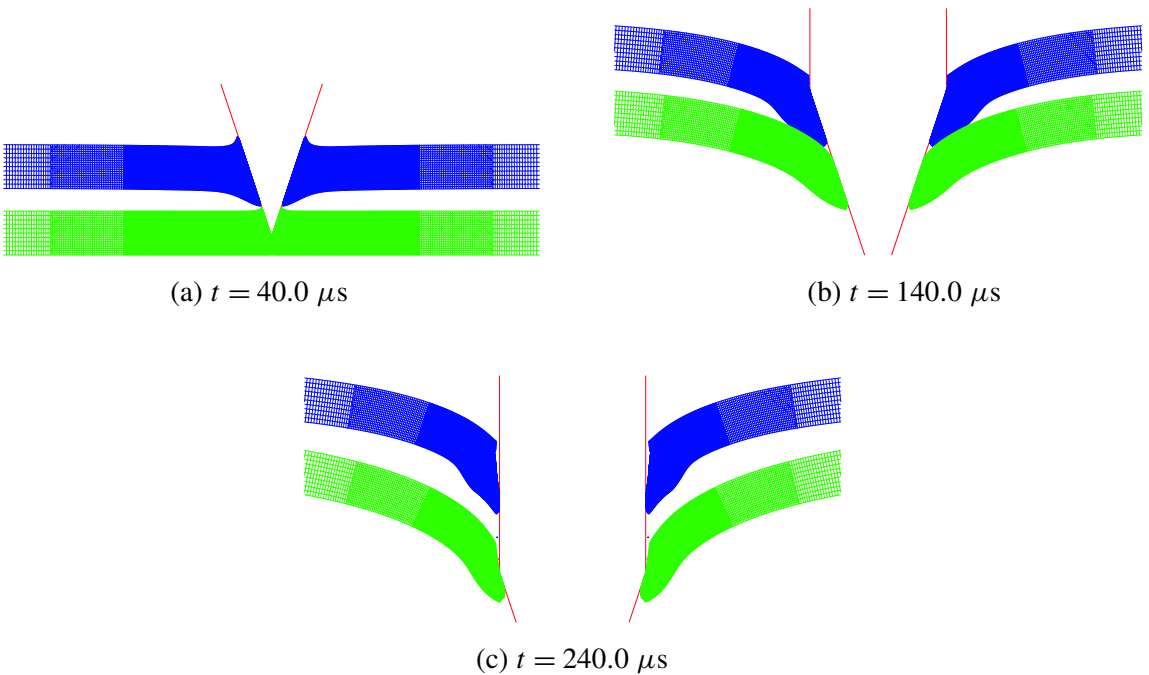
Figure 12. Perforation of double-layered shield with plates spaced impacted by a heavy, conical-nose projectile at $V_0 = 317.9$ m/s.

| Monolithic plate | Double-layered shield | |
	plates in contact	plates spaced
305.9 (1.00)	282.0 (0.922)	280.0 (0.915)

Table 2. Ballistic limits under the impact of a heavy, conical-nose projectile (unit: m/s).

The calculated residual velocities for the double-layered shield with the plates in contact are a little higher than those with the plates spaced. However, the difference is so small as to be indiscernible in Figure 13. The results are again consistent with the experimental observations by Almohandes et al. [1996] and Dey et al. [2007]. It may be concluded, therefore, that an increase in the spacing between the two plates would not considerably improve the protection ability of double-layered shields.

3.3. *Light flat-nose projectile.* IEDs generate fragments of various configuration and masses. Therefore, in addition to the preceding heavy ones, we use a flat-nose projectile of 10 g mass and diameter $d =$ 7.6 mm to represent a light fragment. This striker is close in size to the smallest FSP of $0.30''$ caliber specified in Military Standard MIL-P-46593A [DoD 1962]. Since the projectile is relatively light, a high impact velocity is required to completely perforate the target. This leads to a different failure mode from shear plugging or tensile tearing.

Figure 14 displays the failure process of the monolithic plate at $V_0 = 600$ m/s. It appears that the materials in the impacted zone beneath the projectile are pushed aside as the projectile moves down. The generated cavity is of a larger diameter on the proximal surface than the projectile. By contrast, at a low impact velocity the cavity is of almost the same diameter through the target thickness, as can be seen, for example, in Figure 5. As the projectile approaches the rear surface of the target, shear plugging becomes the dominating failure mode and a plug of reduced thickness is ejected. It should be pointed out that the reduction in the thickness of the plug does not result from artificial element erosion. Although the remainder of the ligament is broken due to the combined action of tension and shear, ductile hole
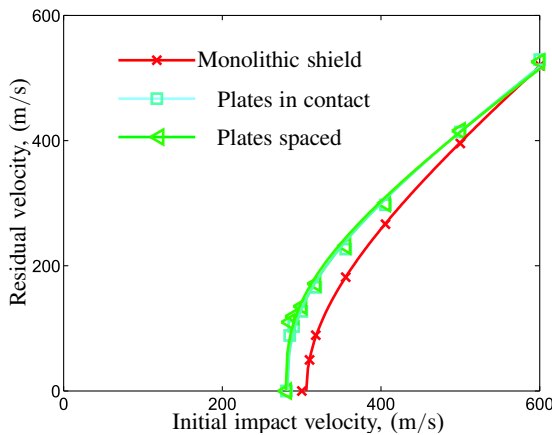
Figure 13. Initial impact velocity vs. residual velocity for three shields impacted by a heavy, conical-nose projectile.

(a) $t = 15.0\ \mu$s

(b) $t = 35.0\ \mu$s

(c) $t = 45.0\ \mu$s
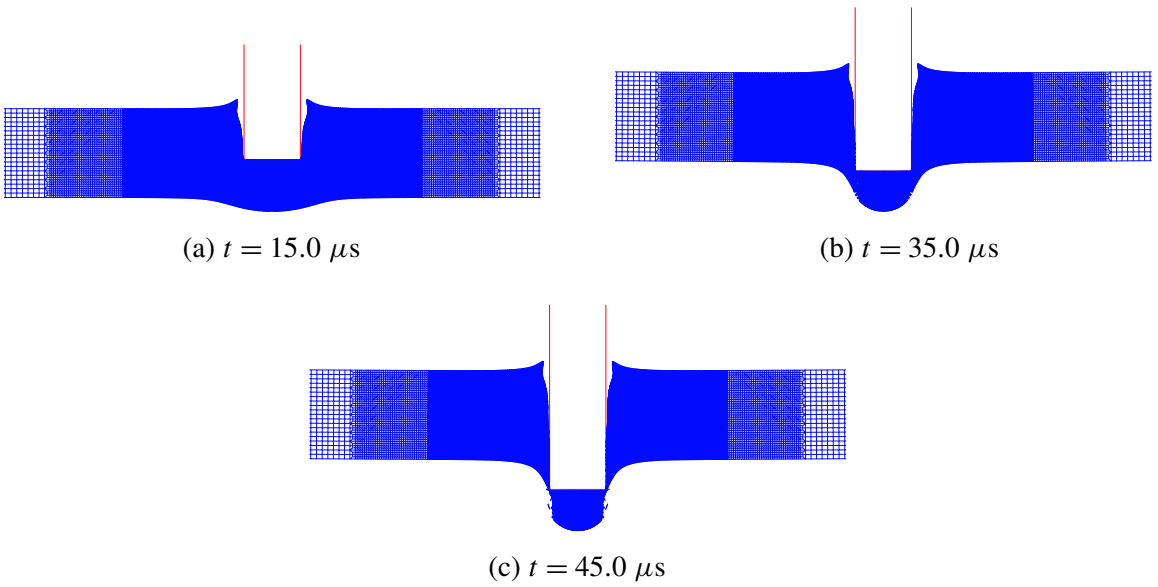
Figure 14. Perforation of monolithic shield impacted by a light, flat-nose projectile at $V_0 = 600.0$ m/s.

(a) $t = 5.0\ \mu$s

(b) $t = 20.0\ \mu$s

(c) $t = 40.0\ \mu$s

(d) $t = 55.0\ \mu$s
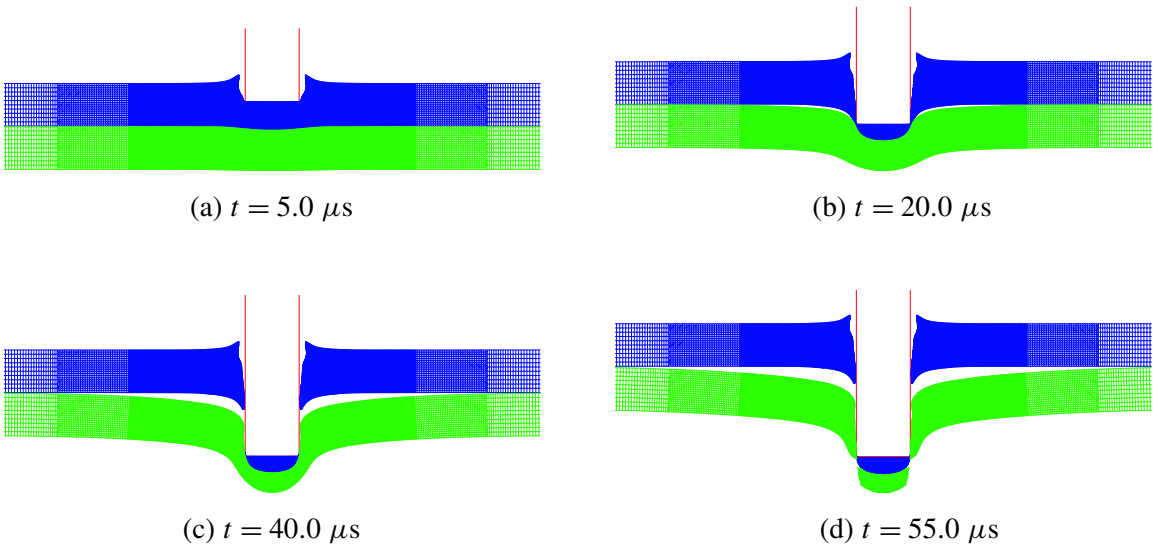
Figure 15. Perforation of double-layered shield with plates in contact impacted by a light, flat-nose projectile at $V_0 = 600.0$ m/s.

(a) $t = 15.0 \, \mu s$ (b) $t = 20.0 \, \mu s$

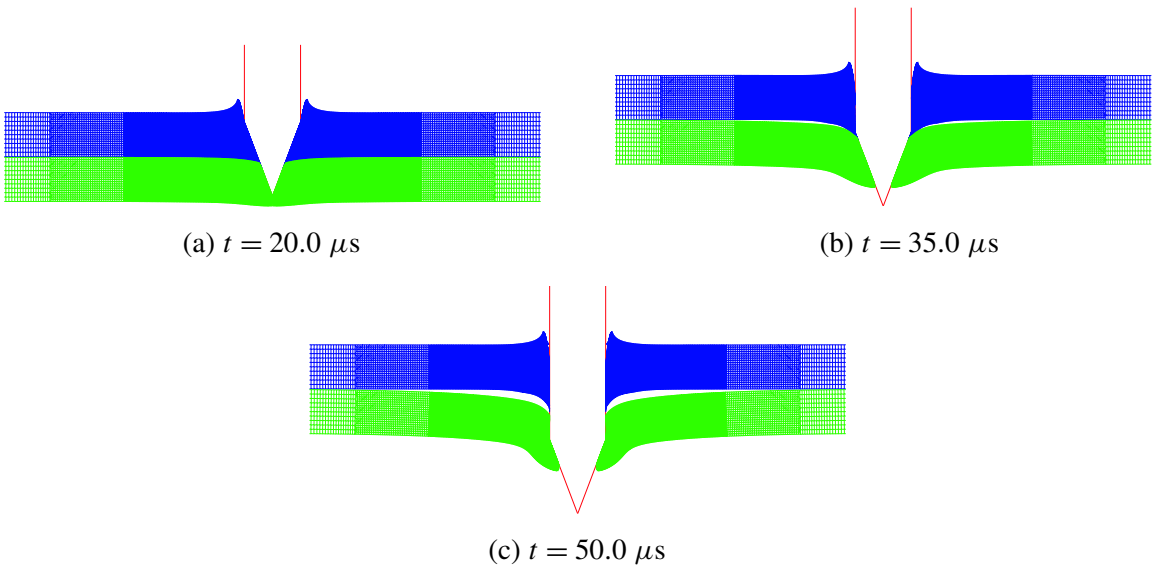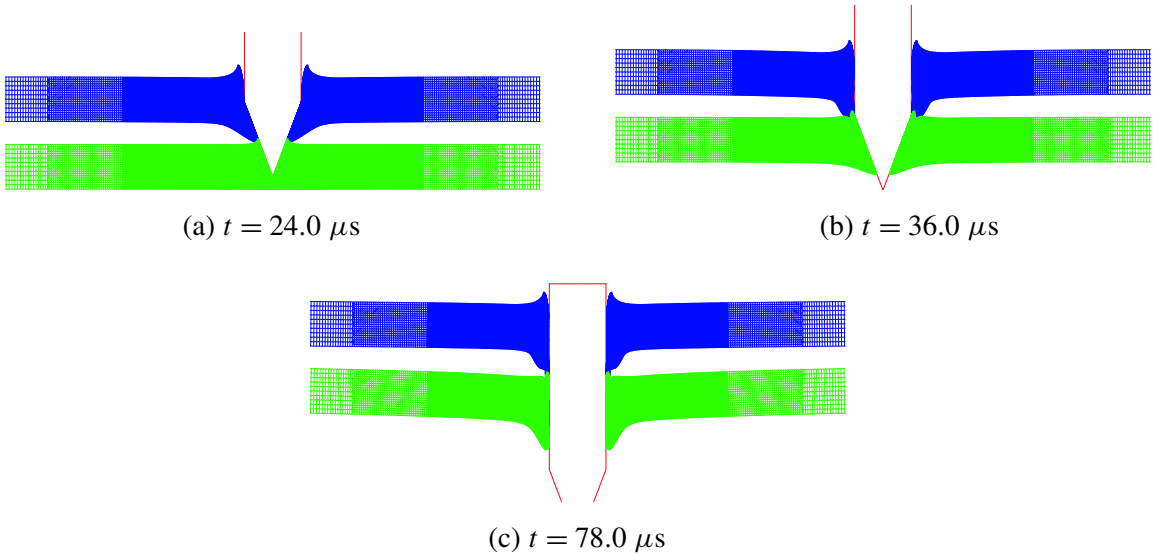(c) $t = 40.0 \, \mu s$ (d) $t = 50.0 \, \mu s$
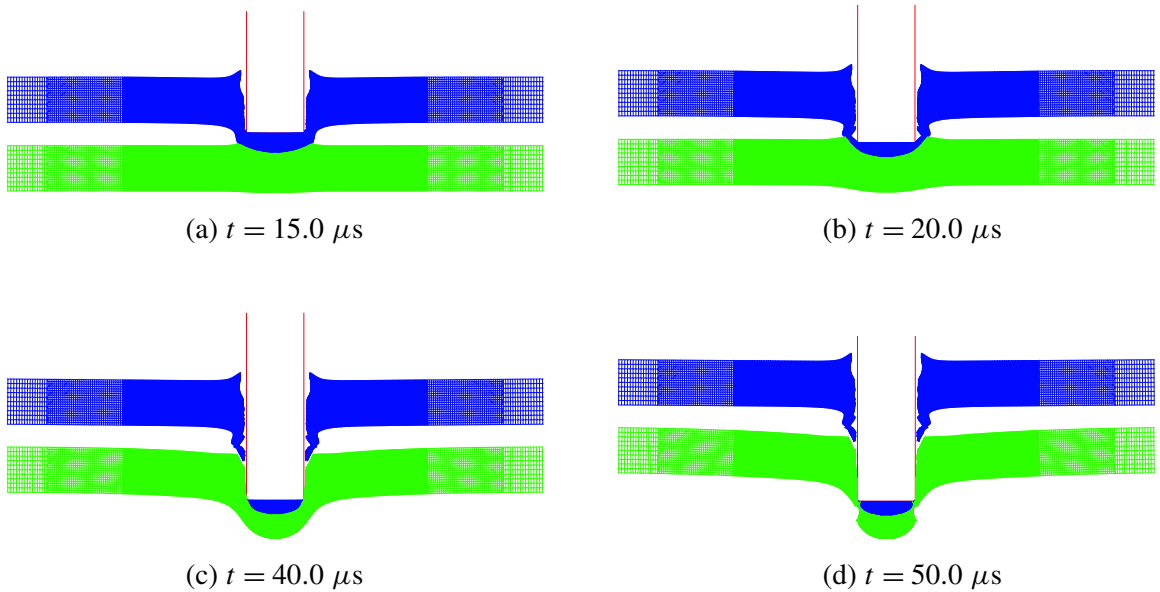
Figure 16. Perforation of double-layered shield with plates spaced impacted by a light, flat-nose projectile at $V_0 = 600.0$ m/s.

enlargement is the predominant failure mechanism. A large part of plastic energy dissipation can be attributed to cavity formation. By contrast, shear plugging is always observed in the monolithic plate under impact by the heavy, flat-nose projectile and the ejected plug is of almost the same thickness as the pretest plate.

A typical fracture process of the double-layered shield with the plates adjacent is given in Figure 15. It can be seen that the upper plate fails mainly by ductile hole enlargement, which is similar to the monolithic shield. The lower plate undergoes a little bending deformation, and necking preceding fracture can be clearly observed. The case with the plates spaced exhibits a similar failure process and pattern; see Figure 16.

Plots of the initial impact velocity versus the residual velocity for the three types of shields are presented in Figure 17. As the impact velocity approaches the ballistic limit, a small advantage of the double-layered shields over the monolithic one becomes clear. The ballistic limit of the double-layered shields is higher by about 7% than that of the monolithic plate; see Table 3 for the detailed information. The increase in the ballistic limit of the double-layer shields can be attributed to the increase in the bending deformation of the lower plate. While the double-layered shield is of the same total thickness as the monolithic one, the elastic bending stiffness of the former is only one quarter of that of the latter.

The predicted ballistic limit of the double-layered shield with the plates spaced is slightly higher than that with the plates in contact. However, the variation in the spacing between the two plates would not be able to considerably improve the protection performance since the failure mode is kept virtually unchanged.

| Monolithic plate | Double-layered shield | |
	plates in contact	plates spaced
487.4 (1.00)	520.0 4(1.07)	523.0 (1.07)

Table 3. Ballistic limits under the impact of a light, flat-nose projectile (unit: m/s).
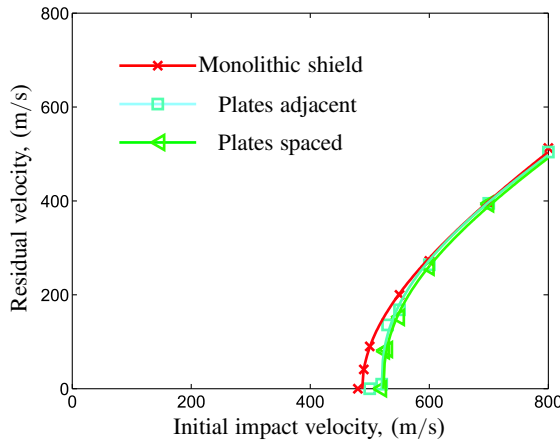
Figure 17. Initial impact velocity vs. residual velocity for three shields impacted by a light, flat-nose projectile.

3.4. *Light conical-nose projectile.* The 10.0 g projectile can be thought of as a simplification of a standard 7.62 mm hard-core bullet. A real bullet projectile consists of a hard core, a actuator, and a jacket and usually has an ogival nose rather than a conical nose. However, Dey et al. [2004] found from a series of tests that a conical-nose projectile has a very similar perforation capability as that of ogival-nose shape.

Figures 18–20 display the typical perforation processes of the three types of shields at $V_0 = 600.0$ m/s. It appears that all the three metal shields simply fail by ductile hole enlargement. The targets are subjected to little structural deformation, while plastic deformation concentrates in the impacted zone beneath the projectile. This fracture pattern is also observed at all the other impact velocities. Note that this failure mechanism is almost identical to the one in the previous case of the heavy projectile. Hence, for the conical-nose projectile, the implementation of the double layer configuration would not introduce a new failure mode.

Plots of the initial impact velocity versus the residual velocity for the three types of shields are displayed in Figure 21. The corresponding ballistic limits are listed in Table 4. It appears that the double

| Monolithic plate | Double-layered shield | |
	plates in contact	plates spaced
525.9 (1.000)	524.5 (0.997)	522.54 (0.994)

Table 4. Ballistic limits under impact of a light, conical-nose projectile (unit: m/s).

(a) $t = 18.0 \ \mu s$ (b) $t = 30.0 \ \mu s$

(c) $t = 60.0 \ \mu s$
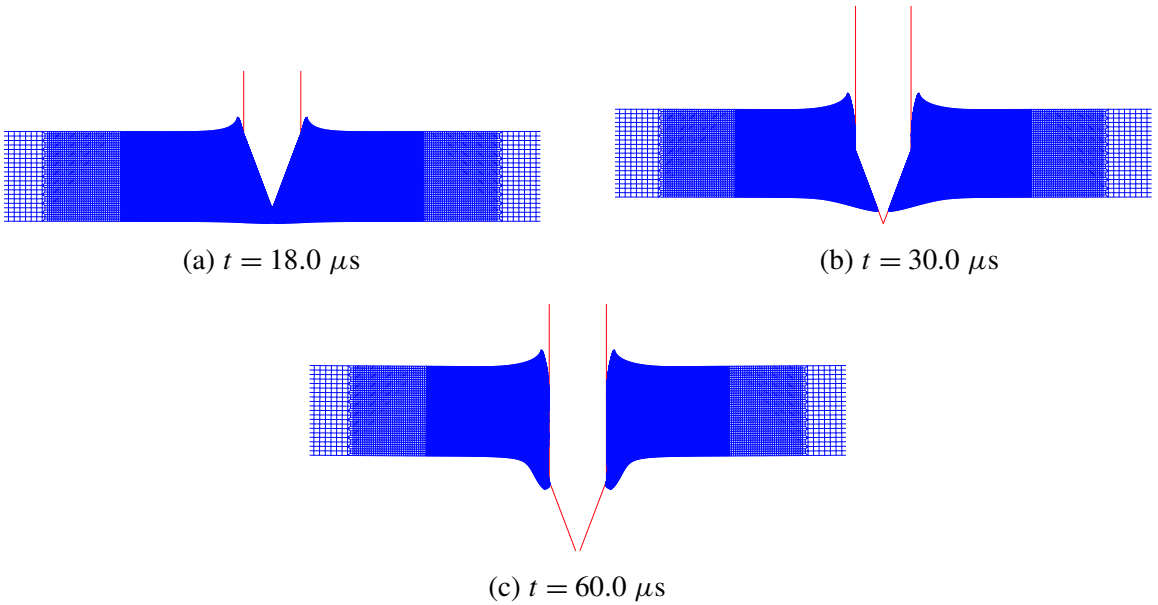
Figure 18. Perforation of monolithic shield impacted by a light, conical-nose projectile at $V_0 = 600.0$ m/s.

(a) $t = 20.0 \ \mu s$ (b) $t = 35.0 \ \mu s$

(c) $t = 50.0 \ \mu s$

Figure 19. Perforation of double-layered shield with plates in contact impacted by a light, conical-nose projectile at $V_0 = 600.0$ m/s.

(a) $t = 24.0\ \mu s$

(b) $t = 36.0\ \mu s$

(c) $t = 78.0\ \mu s$

Figure 20. Perforation of double-layered shield with plates spaced impacted by a light, conical-nose projectile at $V_0 = 600.0$ m/s.

layer configuration slightly weakens the ballistic resistance of the shields. However, the difference between the monolithic plate and the double-layered shields is so small that it can be neglected. At the same time, the numerical results indicate that the increase in the spacing between the two plates does not improve the protection performance of the shield.

A few armor piercing experiments were performed on the double-, multilayered shields under impact by the standard 7.62 mm caliber bullet balls [Almohandes et al. 1996; Gupta and Madhu 1997]. They
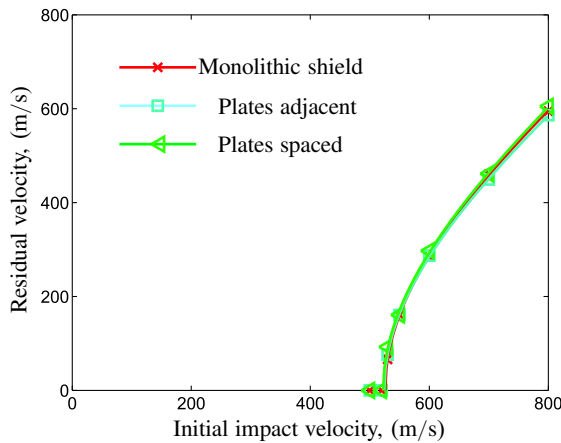
Figure 21. Initial impact velocity vs. residual velocity for three shields impacted by a light, conical-nose projectile.
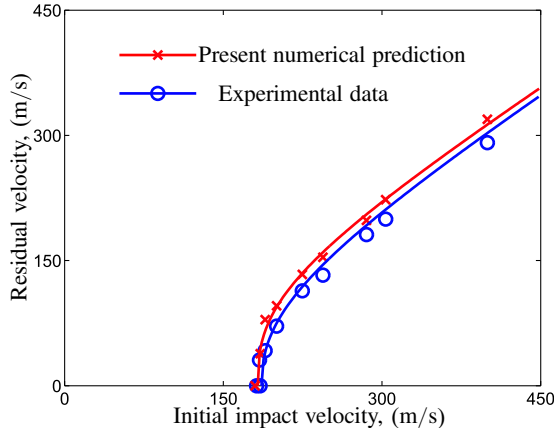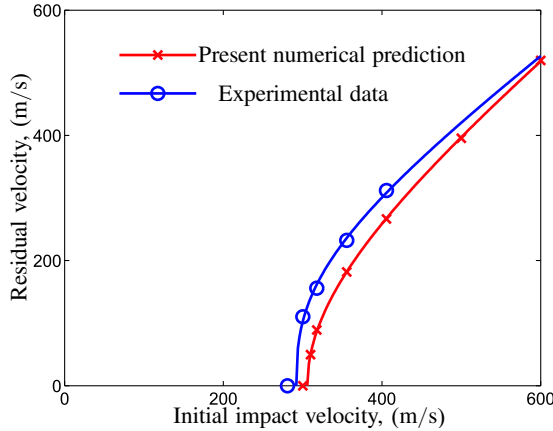
Figure 22. Comparison of residual velocities between numerical prediction and experimental results for monolithic plate impacted by a heavy, flat-nose projectile.

found a slight degradation in the protection behavior of the double-, multilayered shields, compared to the monolithic target of the same total weight. The present numerical prediction qualitatively agrees with those test results.

3.5. *Comparison with experimental results.* Børvik et al. [2002b; 2002a] performed an extensive experimental and numerical study on the ballistic resistance of a Weldox 460 E steel plate impacted by flat-nose, round-nose, and conical-nose projectiles. Strength and fracture properties of Weldox steel were calibrated by conducting a series of tensile tests on round bars under various strain rates and elevated temperature [Børvik et al. 2001]. The complete experimental results published in the literature provide a solid platform to examine numerical procedures.

For this purpose, the geometry configuration of the projectile-target plate system for the monolithic shield was taken to be identical to the one designed by Børvik et al. [2002b]. This allows the present numerical predictions to be verified by direct comparison to the experimental results.

Figures 22 and 23 display plots of the initial impact velocity versus the residual velocity for the case with the monolithic plate under impact by the heavy flat-nose and the conical-nose projectile, respectively. It appears that the numerical results correlate well with the test data. This validates the correctness of the present finite element procedure.

A number of perforation tests on double-layered plates were performed recently by Dey et al. [2007]. Targets made of Weldox 700 E steel were impacted by a flat-nose and a ogival-nose projectile, respectively, using a gas-gun at subordnance velocities. It was found that the ballistic resistance could be increased by about 30% by using the double layer configuration instead of the monolithic plate in the case with the flat-nose projectile as evidenced in Figure 24. The present numerical finding is closely consistent with this experimental conclusion. Since plasticity and fracture properties of Weldox 700 E steel significantly different from those of Weldox 460 E steel, the experimental results cannot be directly compared with the present numerical work. A detailed description of the experimental procedure and results is presented in a separate publication by Dey et al. [2007].

Figure 23. Comparison of residual velocities between numerical prediction and experimental results for monolithic plate impacted by a heavy, conical-nose projectile.

4. Discussion and conclusions

In this work we have examined the effectiveness of the double-layered shield against projectile impact using numerical methods. Four types of projectiles of different mass and nose shape were considered, representing various fragments generated from IEDs. It was found that compared to the monolithic plate, the double layer configuration is able to improve the ballistic limit by 7%–25% for the target under impact by flat-nose projectiles. For conical-nose projectiles the double layer configuration slightly weakens the ballistic resistance. The numerical findings are qualitatively consistent with the experimental results in the open literature. To further verify the findings in the present study, an experimental and numerical program has been carried out at Norwegian University of Science and Technology [Dey et al. 2007].

With the increase in the ballistic limit for the case of a flat-nose projectile, the double layer configuration is able to upgrade the overall protection performance of a target. An armor shield may encounter
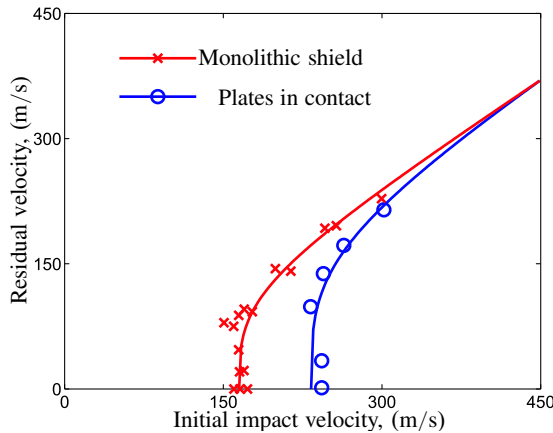
Figure 24. Comparison of experimentally obtained residual velocities between monolithic and double-layered shield [Dey et al. 2007].

the impact of various projectiles. Experimental studies reveal that a projectile of flat-nose is much more detrimental than that of round-nose, conical-nose, or ogival-nose [Børvik et al. 2002b; Dey et al. 2004], that is, a thin or moderately thick target is of the lowest ballistic limit under impact by a flat-nose projectile.

The present numerical investigation indicates that it is not necessary to perfectly bond two layers to enhance the effectiveness of a composite metal shield. The double-layered shield is as effective as, or more effective than, a monolithic plate of the same weight. At the same time, the double layer metal shield would be easily maintained. Partially penetrated/damaged plates can be replaced without changing a whole shield.

This research also indicates that the increase in the spacing between the two plates would not significantly improve the ballistic resistance of the double-layered shields. Actually, the gap decreases the ballistic limit for the case with the conical-nose projectile. Note that by increasing the gap, double-layered shields would occupy more space. However, a systematic parametric study on the effects of the spacing should be further conducted to verify this observation.

In the present study the two plates in the double-layered shield are assumed to be of the same material and thickness. Limited studies indicate that the protection performance of double-layered shields can be further enhanced by placing a thinner plate in front of a thicker plate [Corran et al. 1983b; Corran et al. 1983a]. This conclusion can also be extended to the case with conical-nose projectiles. The experiments conducted by Almohandes et al. [1996] suggest that a double-layered shield consisting of two plates of uneven thickness is of a slightly higher ballistic limit than that of the same thickness. A related question concerns using two different grades of metals with various strengths and ductilities to further increase the ballistic limit of the double-layered shield. This problem is the subject of an ongoing study. The effectiveness of triple-, multilayer configuration also remains to be investigated. For a specific application, these questions can be clarified by conducting an extensive parametric numerical study combined with some experimental validation tests.

References

[Almohandes et al. 1996] A. A. Almohandes, M. S. Abdel-Kader, and A. M. Eleiche, "Experimental investigation of the ballistic resistance of steel-fiberglass reinforced polyester laminated plates", *Compos. B Eng.* **27**:5 (1996), 447–458.

[Bao and Wierzbicki 2005] Y. Bao and T. Wierzbicki, "On the cut-off value of negative triaxiality for fracture", *Eng. Fract. Mech.* **72**:7 (2005), 1049–1069.

[Ben-Dor et al. 1998] G. Ben-Dor, A. Dubinsky, and T. Elperin, "On the ballistic resistance of multi-layered targets with air gaps", *Int. J. Solids Struct.* **35**:23 (1998), 3097–3103.

[Ben-Dor et al. 2006] G. Ben-Dor, A. Dubinsky, and T. Elperin, "Effect of air gaps on the ballistic resistance of ductile shields perforated by nonconical impactors", *J. Mech. Mater. Struct.* **1** (2006), 279–299.

[Børvik et al. 2001] T. Børvik, O. S. Hopperstad, T. Berstad, and M. L. Langseth, "A computational model of viscoplasticity and ductile damage for impact and penetration", *Eur. J. Mech. A: Solids* **20**:5 (2001), 685–712.

[Børvik et al. 2002a] T. Børvik, O. S. Hopperstad, T. Berstad, and M. Langseth, "Perforation of 12 mm thick steel plates by 20 mm diameter projectiles with flat, hemispherical and conical noses, II: Numerical simulations", *Int. J. Impact. Eng.* **27**:1 (2002), 37–64.

[Børvik et al. 2002b] T. Børvik, M. Langseth, O. S. Hopperstad, and K. A. Malo, "Perforation of 12 mm thick steel plates by 20 mm diameter projectiles with flat, hemispherical and conical noses, I: Experimental study.", *Int. J. Impact. Eng.* **27**:1 (2002), 19–35.

[Børvik et al. 2003] T. Børvik, O. S. Hopperstad, M. Langseth, and K. A. Malo, "Effects of target thickness in blunt projectile penetration of Weldox 460 E steel plates", *Int. J. Impact. Eng.* **28**:4 (2003), 413–464.

[Børvik et al. 2005] T. Børvik, O. S. Hopperstad, S. Dey, E. V. Pizzinato, M. Langseth, and C. Albertini, "Strength and ductility of Weldox 460 E steel at high strain rates, elevated temperatures and various stress triaxialities", *Eng. Fract. Mech.* **72**:7 (2005), 1071–1087.

[Børvik et al. 2006] T. Børvik, S. Dey, and A. H. Clausen, "A preliminary study on the perforation resistance of high-strength steel plates", *J. Phys. (France) IV* **134** (2006), 1053–1059.

[Corran et al. 1983a] R. S. J. Corran, C. Ruiz, and P. J. Shadbolt, "On the design of containment shields", *Comput. Struct.* **16**:1–4 (1983), 563–572.

[Corran et al. 1983b] R. S. J. Corran, P. J. Shadbolt, and C. Ruiz, "Impact loading of plates: An experimental investigation", *Int. J. Impact. Eng.* **1**:1 (1983), 3–22.

[Dey et al. 2004] S. Dey, T. Børvik, O. S. Hopperstad, J. R. Leinum, and M. Langseth, "The effect of target strength on the perforation of steel plates using three different projectile nose shapes", *Int. J. Impact. Eng.* **30**:8–9 (2004), 1005–1038.

[Dey et al. 2007] S. Dey, T. Børvik, X. Teng, T. Wierzbicki, and O. S. Hopperstad, "On the ballistic resistance of double-layered steel plates: An experimental and numerical investigation", *Int. J. Solids Struct.* (2007). In press.

[DoD 1962] DoD, "Projectile, calibers 0.22, 0.30, 0.50, and 20 mm fragment-simulating", Military Specification MIL-P-46593A (ORD), Department of Defense, Washington, DC, October 1962.

[Elek et al. 2005] P. Elek, S. Jaramaz, and D. Micković, "Modeling of perforation of plates and multi-layered metallic targets", *Int. J. Solids Struct.* **42**:3–4 (2005), 1209–1224.

[Gupta and Madhu 1997] N. K. Gupta and V. Madhu, "An experimental study of normal and oblique impact of hard-core projectile on single and layered plates", *Int. J. Impact. Eng.* **19**:5–6 (1997), 395–414.

[Johnson and Cook 1983] G. R. Johnson and W. H. Cook, "A constitutive model and data for metals subjected to large strains, high strain rates and high temperatures", pp. 541–547 in *Proceedings of the 7th International Symposium on Ballistics* (Hague), American Defense Preparedness Association, 1983.

[Johnson and Cook 1985] G. R. Johnson and W. H. Cook, "Fracture characteristics of three metals subjected to various strains, strain rates, temperatures and pressures", *Eng. Fract. Mech.* **21**:1 (1985), 31–48.

[Liang et al. 2005] C. C. Liang, M. F. Yang, P. W. Wu, and T. L. Teng, "Resistant performance of perforation of multi-layered targets using an estimation procedure with marine application", *Ocean Eng.* **32**:3–4 (2005), 441–468.

[Liss et al. 1983] J. Liss, W. Goldsmith, and J. M. Kelly, "A phenomenological penetration model of plates", *Int. J. Impact. Eng.* **1**:4 (1983), 321–341.

[Marom and Bodner 1979] I. Marom and S. R. Bodner, "Projectile perforation of multilayered beams", *Int. J. Mech. Sci.* **21**:8 (1979), 489–504.

[Radin and Goldsmith 1988] J. Radin and W. Goldsmith, "Normal projectile penetration and perforation of layered targets", *Int. J. Impact. Eng.* **7**:2 (1988), 229–259.

[Teng and Wierzbicki 2005a] X. Teng and T. Wierzbicki, "Numerical study on crack propagation in high velocity perforation", *Comput. Struct.* **83**:12–13 (2005), 989–1004.

[Teng and Wierzbicki 2005b] X. Teng and T. Wierzbicki, "Transition of failure modes in round-nosed mass-to-beam impact", *Eur. J. Mech. A: Solids* **24**:5 (2005), 857–876.

[Teng et al. 2005] X. Teng, T. Wierzbicki, S. Hiermaier, and I. Rohr, "Numerical prediction of fracture in the Taylor test", *Int. J. Solids Struct.* **42**:9–10 (2005), 2929–2948.

XIAOQING TENG: xteng@alum.mit.edu
Impact and Crashworthiness Lab, Massachusetts Institute of Technology, 77 Massachusetts Avenue, Room 5-218, Cambridge, MA 02139, United States

SUMITA DEY: Sumita.Dey@forsvarsbygg.no
Structural Impact Laboratory, Norwegian University of Science and Technology, Rich. Birkelands vei 1A, NO-7491, Trondheim, Norway

TORE BØRVIK: tore.borvik@ntnu.no
Structural Impact Laboratory, Norwegian University of Science and Technology, Rich. Birkelands vei 1A, NO-7491, Trondheim, Norway

TOMASZ WIERZBICKI: wierz@mit.edu
Impact and Crashworthiness Lab, Massachusetts Institute of Technology, 77 Mass Avenue, Room 5-218, Cambridge, MA 02139, United States

A SURFACE CRACK IN A GRADED COATING BONDED TO A HOMOGENEOUS SUBSTRATE UNDER GENERAL LOADING CONDITIONS

SAMI EL-BORGI, RADHI ABDELMOULA, SERKAN DAG AND NIZAR LAJNEF

The elastostatic problem of a surface crack in a graded coating bonded to a homogeneous substrate under general loading conditions is considered. The coating is graded along the thickness direction and modeled as a nonhomogeneous medium with an isotropic stress-strain law. The problem is solved under the assumption of plane strain or generalized plane stress conditions. The crack surfaces are subjected to arbitrary loadings which give rise to mixed fracture modes which can be uncoupled due to the fact that the crack axis is parallel to the material gradient. Therefore, the opening and sliding mode problems may be formulated separately. For each problem, the solution of the composite medium may be determined by obtaining the solution of the homogeneous substrate and that of the graded layer. The latter solution may be expressed as the sum of two solutions, namely an infinite graded medium with a crack and a graded strip without a crack. The resulting mixed-boundary value problem is reduced to a set of two uncoupled singular integral equations which are solved numerically using Jacobi polynomials. The main objective of the paper is to study the effect of the layer thickness and nonhomogeneity parameter on the crack tip mixed-mode stress intensity factors for the purpose of gaining better understanding on the behavior of graded coatings.

1. Introduction

In high-temperature applications the potential of using homogeneous materials appears to be limited and in recent years the new trends in material design seem to be toward coating the main load-bearing component by a heat-resistive layer, generally a ceramic. Because of the relatively high mismatch in thermal expansion coefficients, the resulting bonded structure is generally subjected to very high residual and thermal stresses. As a result, the composite medium becomes vulnerable to cracking, debonding and spallation [Erdogan 1995].

The materials research community has recently been exploring the possibility of using new concepts in coating design, such as Functionally Graded Materials (FGMs), as an alternative to the conventional homogeneous coatings. These can be at least two-phase inhomogeneous particulate composites synthesized in such a way that the volume fractions of the constituent materials, such as ceramic and metal, vary continuously along a spatial direction to give a predetermined composition profile resulting in a relatively smooth variation of the mechanical properties. FGMs appear to promise attractive applications in a wide variety of wear coating and thermal shielding problems such as gears, cams, cutting tools, high temperature chambers, furnace liners, turbines, microelectronics and space structures [Holt et al. 1992]. FGM structures can also be made through physical vapor deposition techniques such as those described in [Chen et al. 2002c; 2002b], which produce nanolayers having properties varying with depth. In designing

components involving FGMs, an important aspect of the problem is the question of mechanical failure, specifically the fracture failure [Lanutti 1994]. Fatigue and fracture characterization of materials and related analysis require the solution of certain standard crack problems.

Most of the crack problems solved over the past two decades on nonhomogeneous materials [Dhaliwal and Singh 1978; Delale and Erdogan 1983; Erdogan 1985; Ozturk and Erdogan 1993] provide the basis for the fracture mechanics research on FGMs which are essentially nonhomogeneous materials. In [Erdogan 1995] a brief discussion is given on the application of elementary concepts of fracture mechanics in nonhomogeneous materials and a number of typical problem areas are identified which relate to the fracture of FGMs. An important problem is the nature of stress singularities near the tip of a crack embedded in a nonhomogeneous medium. Konda and Erdogan [1994] and Jin and Noda [1994a] showed that such a crack has the standard square-root singularity in addition to others encountered in a homogeneous medium provided the material property model is continuous and piecewise differentiable.

A number of crack problems in FGMs were solved accounting only for mechanical loading or thermal loading or a combination of both. The crack can be either an internal crack parallel to the free surface or perpendicular to it. A particular case of a crack perpendicular to the free surface is the edge crack which is also called the surface crack. Noda and Jin [1993] studied the internal crack problem for an infinite FGM medium subjected to a steady-state heat flux over the crack surfaces by assuming continuously varying thermal properties. The same problem was extended by El-Borgi et al. [2004a] by considering a steady-state heat flux applied away from the crack region, by modeling the crack faces as partially insulated and by accounting for crack-closure effects. The case of an internal fully insulated crack parallel to the boundary of a semi-infinite graded medium subject to a steady-state heat flux applied at the free surface was studied in [Jin and Noda 1993]. This problem was later extended to the case of transient heat flux in [Jin and Noda 1994c]. Lee and Erdogan [1998a] studied the problem of interface cracking in FGM coatings under steady-state heat flow. Chen and Erdogan [1996] studied the problem of a graded coating on homogeneous substrate with an interface crack subjected to mechanically induced crack surface tractions. El-Borgi et al. [2003] extended this problem by considering both thermal and mechanical loads and accounting for crack-closure effects. In [El-Borgi et al. 2004b] we considered the problem of a graded coating bonded to a substrate subjected to a Hertzian contact pressure and with an internal crack embedded in the coating, and in [El-Borgi et al. 2000] the mixed-mode crack parallel to the boundary of an infinite strip, with the elastic modulus varying exponentially in an arbitrary direction. Long and Delale [2005] solved the more general problem of an arbitrarily oriented crack in a graded layer bonded to a homogeneous half-plane.

Jin and Noda [1994b] considered the problem of a surface crack in a semi-infinite nonhomogeneous medium subject to a steady-state heat flux. Erdogan and Wu [1997] considered a graded strip with a surface crack, perpendicular to the boundaries and parallel to the material gradient, subjected to mechanical crack surface tractions. The same problem was also solved in [Erdogan and Wu 1996] by considering thermal loads. Dag et al. [1999] and Kadioglu et al. [1998] studied a similar problem with the graded layer attached to an elastic foundation with a crack subjected, respectively, to thermal and mechanical loads. Yildirim and Erdogan [2004] considered an axisymmetric surface crack problem for thermal barrier coatings under a uniform temperature change. Guo et al. [2004a] investigated the mode I surface crack problem for an orthotropic graded strip. A similar problem was also solved in [Chen et al. 2002a] by considering a transient loading. Guo et al. [2004b] considered the mode I problem of

a graded coating bonded to homogeneous substrate with a crack perpendicular to the coating's surface subjected to a transient load. Dag and Erdogan [2002] solved the problem of a surface crack in a graded semi-infinite medium under general loading conditions in which they proposed a method to uncouple the opening and sliding modes.

The practical use of FGMs is in the form of coating applications. On the other hand, the manufacturing of FGMs may lead to inherent surface flaws which may give rise to surface cracks that can eventually propagate to the component. Therefore, the present work consists of a surface crack located in an isotropic graded coating bonded to homogeneous substrate subjected to general loading conditions. This study is an extension of [Dag and Erdogan 2002] in the sense that problem geometry consists of a graded coating bonded to a substrate rather than a graded half-plane. The main objective of the paper is to study the effect of the coating thickness and material nonhomogeneity on the crack tip stress intensity factors for the purpose of further understanding the behavior and design of graded materials.

2. Problem description and governing equations

As shown in Figure 1, the problem under consideration consists of an infinitely long graded coating of thickness h, bonded to a homogeneous semi-infinite medium. The graded coating contains an edge crack of length d along the x-axis. For the graded coating, the material gradient is oriented along the
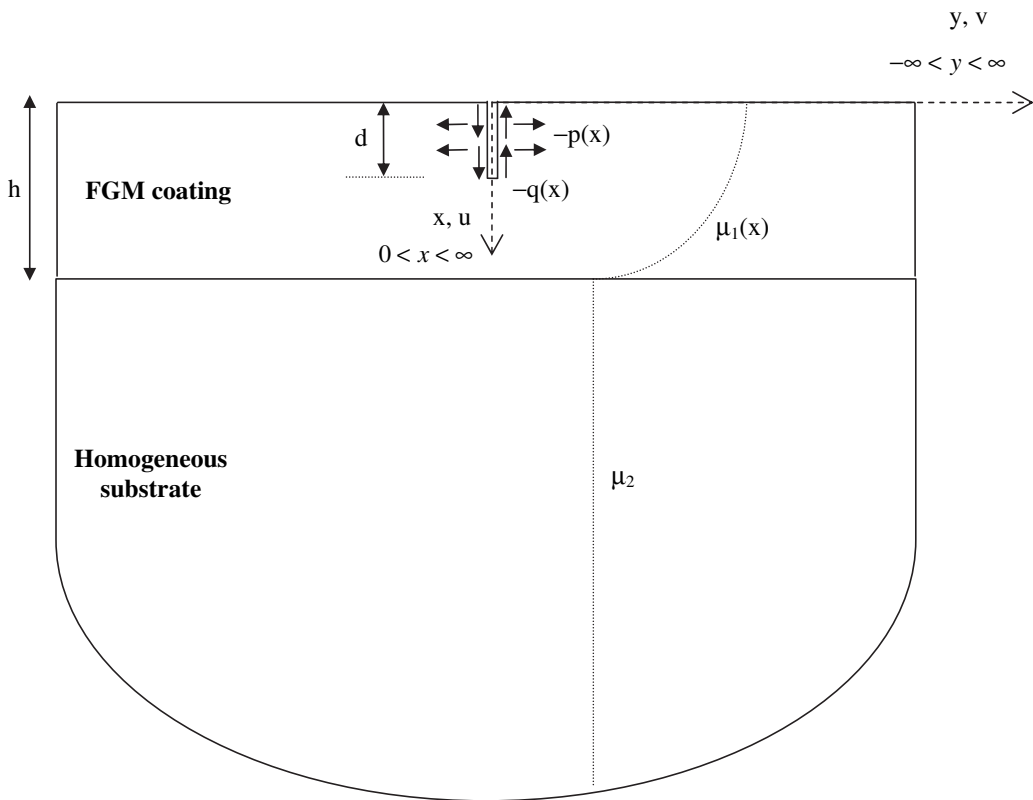
Figure 1. Geometry and loading of the composite medium.

x-direction. The Poisson's ratio ν is assumed to be a constant because the effect of its variation on the crack-tip stress intensity factors was shown in [Erdogan and Wu 1996; 1997] to be negligible and is equal to the same value as that of the homogeneous substrate. On the other hand, the shear modulus in the FGM layer μ_1 depends on the x-coordinate only and is modeled by an exponential function as expressed by

$$\mu_1 = \mu_0 \exp(\beta x), \tag{1a}$$

where μ_0 is the value of the shear modulus in the coating along the free surface $x = 0$ and β is the nonhomogeneity parameter controlling the variation of the shear modulus in the graded coating.

For the homogeneous substrate, the shear modulus μ_2 is a constant and is equal to the value of the FGM coating shear modulus at the interface

$$\mu_2 = \mu_0 \exp(\beta h). \tag{1b}$$

The loading consists of arbitrary crack surface tractions (ie, normal and shear tractions) which can be expressed in terms of the external mechanical loads. The problem under consideration is similar to the graded half-plane surface crack problem studied in [Dag and Erdogan 2002]. In both problems, the material gradient in the graded medium and the crack orientation are both along the x-direction. As a result, a normal loading and a shear loading on the crack faces do not induce, respectively, mode II and mode I stress intensity factors. Therefore, the opening and sliding mode problems turn out to be uncoupled and may be formulated separately, as indicated in the work just cited.

The equations of the plane problem for nonhomogeneous isotropic elastic solids are the equilibrium equations

$$\frac{\partial \sigma_{xx}}{\partial x} + \frac{\partial \sigma_{xy}}{\partial y} = 0, \quad \frac{\partial \sigma_{xy}}{\partial x} + \frac{\partial \sigma_{yy}}{\partial y} = 0, \tag{2}$$

(ignoring body forces), the strain-displacement relationships

$$\varepsilon_{xy} = \frac{1}{2}\left(\frac{\partial u}{\partial y} + \frac{\partial v}{\partial x}\right), \quad \varepsilon_{xx} = \frac{\partial u}{\partial x}, \quad \varepsilon_{yy} = \frac{\partial v}{\partial y}, \tag{3}$$

and the linear elastic stress-strain law

$$\sigma_{xx} = \frac{\mu_j}{\kappa-1}\big((1+\kappa)\varepsilon_{xx} + (3-\kappa)\varepsilon_{yy}\big), \quad \sigma_{xy} = 2\mu_j\varepsilon_{xy}, \quad \sigma_{yy} = \frac{\mu_j}{\kappa-1}\big((3-\kappa)\varepsilon_{xx} + (1+\kappa)\varepsilon_{yy}\big), \tag{4}$$

where $j = 1, 2$ and $\kappa = 3 - 4\nu$ for plane strain, $\kappa = (3-\nu)/(1+\nu)$ for generalized plane stress.

Substituting Equations (3) into (4), inserting the resulting expressions into (2) and using (1a) and (1b), we obtain the equations of plane elasticity

$$(\kappa+1)\frac{\partial^2 u}{\partial x^2} + (\kappa-1)\frac{\partial^2 u}{\partial y^2} + 2\frac{\partial^2 v}{\partial x \partial y} + \beta(\kappa+1)\frac{\partial u}{\partial x} + \beta(3-\kappa)\frac{\partial v}{\partial y} = 0, \quad 0 \le x < h,$$

$$(\kappa-1)\frac{\partial^2 v}{\partial x^2} + (\kappa+1)\frac{\partial^2 v}{\partial y^2} + 2\frac{\partial^2 u}{\partial x \partial y} + \beta(\kappa-1)\frac{\partial v}{\partial x} + \beta(\kappa-1)\frac{\partial u}{\partial y} = 0, \quad 0 \le x < h, \tag{5}$$

together with

$$(\kappa+1)\frac{\partial^2 u}{\partial x^2} + (\kappa-1)\frac{\partial^2 u}{\partial y^2} + 2\frac{\partial^2 v}{\partial x \partial y} = 0 \quad \text{and} \quad (\kappa-1)\frac{\partial^2 v}{\partial x^2} + (\kappa+1)\frac{\partial^2 v}{\partial y^2} + 2\frac{\partial^2 u}{\partial x \partial y} = 0, \quad x \ge h.$$

For both crack mode problems (I and II), these plane elasticity equations are subject to the appropriate boundary conditions, detailed in the next two sections. The main unknowns of interest in these mixed-boundary value problems are the so-called density functions chosen for convenience as the derivatives of the relative crack opening displacements. Because of symmetry, these density functions can be chosen as

$$f_1(x) = \frac{4\mu_0}{\kappa+1} \frac{\partial}{\partial x} v(x, 0^+), \quad f_2(x) = \frac{4\mu_0}{\kappa+1} \frac{\partial}{\partial x} u(x, 0^+). \tag{6}$$

3. Solution of the opening mode problem

For the opening mode problem, the solution of the composite medium may be determined by obtaining the solution in the graded layer and that in the homogeneous substrate. The graded layer solution may be expressed as the sum of two solutions, namely an infinite graded medium with a crack along the x-direction and a graded strip without a crack [Erdogan and Wu 1996; Dag and Erdogan 2002; Bogy 1975]. For the cracked infinite graded medium, the plane elasticity Equations (5) are solved using standard Fourier transforms with respect to the x-coordinate. Furthermore, taking advantage of the problem symmetry and considering that the displacements need to be bounded as y goes to ∞, the solution for the half-plane $y \geq 0$ is given by

$$u_1^{i+}(x, y) = \frac{1}{2\pi} \int_{-\infty}^{+\infty} \sum_{k=3}^{4} C_k(\lambda) e^{m_k y} e^{ix\lambda} d\lambda, \qquad y \geq 0,$$

$$v_1^{i+}(x, y) = \frac{1}{2\pi} \int_{-\infty}^{+\infty} \sum_{k=3}^{4} C_k(\lambda) s_k^i(\lambda) e^{m_k y} e^{ix\lambda} d\lambda, \quad y \geq 0, \tag{7}$$

where the subscript 1 stands for the opening mode problem, the superscript i indicates the cracked infinite medium, the superscript $+$ stands for the half-plane $y \geq 0$, and $C_k(\lambda)$, $k = 3, 4$, are unknown functions. Moreover, $s_k^i(\lambda)$, $k = 3, 4$ are known functions given by

$$s_k^i(\lambda) = -\frac{(\kappa-1)m_k^2 + (\kappa+1)(i\lambda\beta - \lambda^2)}{(2i\lambda + \beta(3-\kappa))m_k} \quad (k = 3, 4), \tag{8}$$

and the m_k are the roots of the characteristic polynomial

$$m^4 - \left(2(\lambda^2 - i\lambda\beta) + \delta^2\right)m^2 + (\lambda^2 - i\lambda\beta)^2 = 0, \tag{9}$$

which are given by

$$m_{1,2} = \tfrac{1}{2}\left(\mp\delta + \sqrt{\delta^2 + 4\lambda^2 - 4i\lambda\beta}\right), \qquad \mathrm{Re}\, m_{1,2} \geq 0, \tag{10a}$$

$$m_{3,4} = \tfrac{1}{2}\left(\mp\delta - \sqrt{\delta^2 + 4\lambda^2 - 4i\lambda\beta}\right), \qquad \mathrm{Re}\, m_{3,4} \leq 0, \tag{10b}$$

where we have set $\delta = \sqrt{(3-\kappa)/(\kappa+1)}\,\beta$.

Substituting (7) into (3) and the result into (4) yields the stress field $\sigma_{xx1}^{i+}(x, y)$, $\sigma_{yy1}^{i+}(x, y)$ and $\sigma_{xy1}^{i+}(x, y)$ in the infinite graded medium:

$$\sigma_{xx1}^{i+}(x, y) = \frac{\mu_1}{2\pi(\kappa-1)} \int_{-\infty}^{+\infty} \sum_{k=3}^{4} p_{xx1,k}^{i}(\lambda)C_k(\lambda)e^{m_k y}e^{ix\lambda}d\lambda, \quad y \geq 0, \tag{11a}$$

$$\sigma_{yy1}^{i+}(x, y) = \frac{\mu_1}{2\pi(\kappa-1)} \int_{-\infty}^{+\infty} \sum_{k=3}^{4} p_{yy1,k}^{i}(\lambda)C_k(\lambda)e^{m_k y}e^{ix\lambda}d\lambda, \quad y \geq 0, \tag{11b}$$

$$\sigma_{xy1}^{i+}(x, y) = \frac{\mu_1}{2\pi} \int_{-\infty}^{+\infty} \sum_{k=3}^{4} p_{xy1,k}^{i}(\lambda)C_k(\lambda)e^{m_k y}e^{ix\lambda}d\lambda, \quad y \geq 0, \tag{11c}$$

where the $C_k(\lambda)$ ($k = 3, 4$) are unknown functions, the roots m_k ($k = 3, 4$) are given by (10b), and

$$p_{xx1,k}^{i}(\lambda) = (i\lambda)(1+\kappa) + (3-\kappa)m_k s_k^{i},$$
$$p_{yy1,k}^{i}(\lambda) = (i\lambda)(3-\kappa) + (1+\kappa)m_k s_k^{i} \quad (k = 3, 4),$$
$$p_{xy1,k}^{i}(\lambda) = m_k + (i\lambda)s_k^{i} \quad (k = 1, \ldots, 4).$$

We now consider the graded strip without a crack. By symmetry, the displacement along the x-axis is an even function, while the displacement along the y-axis is an odd function. Hence, the displacements u and v may be expressed using the cosine and sine transforms with respect to y as follows:

$$u_1^{s}(x, y) = \int_0^{+\infty} \sum_{k=1}^{4} E_k e^{n_k x} \cos(y\alpha) \, d\alpha, \qquad v_1^{s}(x, y) = \int_0^{+\infty} \sum_{k=1}^{4} E_k s_k^{s} e^{n_k x} \sin(y\alpha) \, d\alpha, \tag{12}$$

in which the superscript s indicates the uncracked graded strip, the $E_k(\lambda)$, $k = 1, 2, 3, 4$, are unknown functions, the $s_k^{s}(\lambda)$ are known functions given by

$$s_k^{s}(\lambda) = -\frac{(\kappa+1)n_k^2 + \beta(\kappa+1)n_k - (\kappa-1)\alpha^2}{2\alpha n_k + \beta(3-\kappa)\alpha} \quad k = 1, \ldots, 4 \tag{13}$$

and the n_k are the roots of the characteristic polynomial

$$n^4 + 2\beta n^3 + (\beta^2 - 2\alpha^2)n^2 - 2\beta\alpha^2 n + (\alpha^4 + \alpha^2\delta^2) = 0, \tag{14}$$

which are given by

$$\begin{aligned} n_{1,2} &= \tfrac{1}{2}\left(-\beta - \sqrt{\beta^2 + 4\alpha^2 \pm 4i\alpha\delta}\right), \qquad \operatorname{Re} n_{1,2} \leq 0, \\ n_{3,4} &= \tfrac{1}{2}\left(-\beta + \sqrt{\beta^2 + 4\alpha^2 \pm 4i\alpha\delta}\right), \qquad \operatorname{Re} n_{3,4} \geq 0. \end{aligned} \tag{15}$$

Substituting Equations (12) into (3) and the result into (4) yields the stress field in the uncracked graded strip:

$$\sigma_{xx1}^{s}(x, y) = \frac{\mu_1}{\kappa-1} \int_0^{+\infty} \sum_{k=1}^{4} p_{xx1,k}^{s}(\alpha) E_k e^{n_k x} \cos(y\alpha) \, d\alpha, \tag{16a}$$

$$\sigma_{yy1}^{s}(x, y) = \frac{\mu_1}{\kappa-1} \int_0^{+\infty} \sum_{k=1}^{4} p_{yy1,k}^{s}(\alpha) E_k e^{n_k x} \cos(y\alpha) \, d\alpha, \tag{16b}$$

$$\sigma_{xy1}^s(x, y) = \mu_1 \int_0^{+\infty} \sum_{k=1}^4 p_{xy1,k}^s(\alpha) E_k e^{n_k x} \sin(y\alpha)\, d\alpha, \tag{16c}$$

where $E_k(\lambda)$ $(k = 1, 2, 3, 4)$ are unknown functions, the roots n_k, $k = 1, \ldots, 4$, are given by (15) and

$$p_{xx1,k}^s(\alpha) = (1+\kappa)n_k + (3-\kappa)\alpha s_k^s,$$
$$p_{xy1,k}^s(\alpha) = -\alpha + s_k^s n_k, \quad (k = 1, \ldots, 4),$$
$$p_{yy1,k}^s(\alpha) = (3-\kappa)n_k + (1+\kappa)\alpha s_k^s, \quad (k = 1, \ldots, 4).$$

By superposing the two sets of solutions obtained from the cracked infinite graded medium and the uncracked graded strip, the solution of the cracked graded strip can be established as follows:

$$u_1^+(x, y) = u_1^{i+}(x, y) + u_1^s(x, y), \quad v_1^+(x, y) = v_1^{i+}(x, y) + v_1^s(x, y), \quad y \geq 0,$$
$$\sigma_{kl1}^+(x, y) = \sigma_{kl1}^{i+}(x, y) + \sigma_{kl1}^s(x, y), \quad k, l = x, y, \qquad\qquad y \geq 0, \tag{17}$$

where $u_1^{i+}(x, y)$ and $v_1^{i+}(x, y)$ are given by (7), $u_1^s(x, y)$ and $v_1^s(x, y)$ are given by (12), $\sigma_{kl1}^{i+}(x, y)$ is given by (11) and $\sigma_{kl1}^s(x, y)$ is given by (16).

Considering that the displacements need to be bounded as x goes to ∞, the displacement solution of the homogeneous substrate can be obtained in a similar manner as the uncracked graded strip:

$$u_1^h(x, y) = \int_0^{+\infty} (C_5 + C_7 x)e^{-\alpha x} \cos(y\alpha)\, d\alpha, \tag{18a}$$

$$v_1^h(x, y) = \int_0^{+\infty} \left(\left(C_5 - C_7 \frac{\kappa}{\alpha}\right) + C_7 x\right)e^{-\alpha x} \sin(y\alpha)\, d\alpha, \tag{18b}$$

where C_5 and C_7 are unknown functions.

Substituting (18) into (3) and the result into (4) yields the stress field in the uncracked graded strip:

$$\sigma_{xx1}^h(x, y) = \frac{\mu_2}{\kappa-1} \int_0^{+\infty} \left(p_{xx1,1}^h(\alpha)C_5 + p_{xx1,2}^h(\alpha)C_7 + p_{xx1,1}^h(\alpha)C_7 x\right)e^{-\alpha x} \cos(y\alpha)\, d\alpha, \tag{19a}$$

$$\sigma_{yy1}^h(x, y) = \frac{\mu_2}{\kappa-1} \int_0^{+\infty} \left(p_{yy1,1}^h(\alpha)C_5 + p_{yy1,2}^h(\alpha)C_7 + p_{yy1,1}^h(\alpha)C_7 x\right)e^{-\alpha x} \cos(y\alpha)\, d\alpha, \tag{19b}$$

$$\sigma_{xy1}^h(x, y) = \mu_2 \int_0^{+\infty} \left(p_{xy1,1}^h(\alpha)C_5 + p_{xy1,2}^h(\alpha)C_7 + p_{xy1,1}^h(\alpha)C_7 x\right)e^{-\alpha x} \sin(y\alpha)\, d\alpha, \tag{19c}$$

where C_5 and C_7 are unknown functions and

$$p_{xx1,1}^h(\alpha) = 2(1-\kappa)\alpha, \qquad p_{xx1,2}^h(\alpha) = (\kappa-1)^2,$$
$$p_{yy1,1}^h(\alpha) = -2(1-\kappa)\alpha, \qquad p_{yy1,2}^h(\alpha) = 3 - 2\kappa - \kappa^2,$$
$$p_{xy1,1}^h(\alpha) = -2\alpha, \qquad p_{xy1,2}^h(\alpha) = 1+\kappa.$$

The solution is expressed in terms of the 9 unknown functions C_3, C_4 from (7), C_5, C_7 from (18), $E_1, \ldots, E_4$ from (12), and the density function $f_1(x)$, to be determined from the 9 boundary conditions

$$\sigma_{xy1}(x, 0^+) = 0, \qquad x > 0, \tag{20}$$

$$\left.\begin{aligned} \sigma_{xx1}(x, y) &= 0, \\ \sigma_{xy1}(x, y) &= 0, \end{aligned}\right\} \qquad x = 0, \ y < \infty, \tag{21}$$

$$\left.\begin{aligned} \sigma_{xx1}(h^+, y) &= \sigma_{xx1}(h^-, y), \\ \sigma_{xy1}(h^+, y) &= \sigma_{xy1}(h^-, y), \end{aligned}\right\} \qquad y < \infty, \tag{22}$$

$$\left.\begin{aligned} u_1(h^+, y) &= u_1(h^-, y), \\ v_1(h^+, y) &= v_1(h^-, y), \end{aligned}\right\} \qquad y < \infty, \tag{23}$$

$$v_1(x, 0^+) = 0, \qquad d < x < \infty, \tag{24}$$

$$\sigma_{yy1}(x, 0^+) = -p(x), \qquad 0 < x < d. \tag{25}$$

Equation (20) indicates that the shear stress is zero in the plane of symmetry. Equations (21) show that no tractions are applied at the top surface of the coating. Equations (22) and (23) describe the continuity conditions of the stress and displacement fields along the interface $x = h$. Equation (24) indicates the y-component of the displacement along the plane $y = 0$ is zero outside the crack because of symmetry. Equation (25) describes the applied normal crack surface traction which can be expressed in terms of external general loads. It should be pointed out that the regularity conditions which state that the stresses and displacements need to be bounded at $x \to \infty$ were already incorporated in the solution given by Equations (18) and (19a)–(19c).

Applying the boundary conditions (20) and (24) allows expressing the unknown functions C_3 and C_4 in terms of the density function f_1:

$$C_3 = \frac{\kappa+1}{4\mu_0} \frac{i}{\lambda} \frac{-p^i_{xy1,4}}{s^i_3 p^i_{xy1,4} - s^i_4 p^i_{xy1,3}} \int_0^d f_1(t)e^{-i\lambda t}\, dt, \quad C_4 = \frac{\kappa+1}{4\mu_0} \frac{i}{\lambda} \frac{p^i_{xy1,3}}{s^i_3 p^i_{xy1,4} - s^i_4 p^i_{xy1,3}} \int_0^d f_1(t)e^{-i\lambda t}\, dt.$$

Applying the boundary conditions (21)–(23) yields the linear system of equations

$$\begin{bmatrix} p^s_{xx1,1} & p^s_{xx1,2} & p^s_{xx1,3} & p^s_{xx1,4} & 0 & 0 \\ -p^s_{xy1,1} & -p^s_{xy1,2} & -p^s_{xy1,3} & -p^s_{xy1,4} & 0 & 0 \\ p^s_{xx1,1}e^{n_1 h} & p^s_{xx1,2}e^{n_2 h} & p^s_{xx1,3}e^{n_3 h} & p^s_{xx1,4}e^{n_4 h} & -p^h_{xx1,1}e^{-\alpha h} & -(p^h_{xx1,2}+hp^h_{xx1,1})e^{-\alpha h} \\ -p^s_{xy1,1}e^{n_1 h} & -p^s_{xy1,2}e^{n_2 h} & -p^s_{xy1,3}e^{n_3 h} & -p^s_{xy1,4}e^{n_4 h} & p^h_{xy1,1}e^{-\alpha h} & (p^h_{xy1,2}+hp^h_{xx1,1})e^{-\alpha h} \\ e^{n_1 h} & e^{n_2 h} & e^{n_3 h} & e^{n_4 h} & -e^{-\alpha h} & -he^{-\alpha h} \\ -s^s_1 e^{n_1 h} & -s^s_2 e^{n_2 h} & -s^s_3 e^{n_3 h} & -s^s_4 e^{n_4 h} & e^{-\alpha h} & (h-\frac{\kappa}{\alpha})e^{-\alpha h} \end{bmatrix} \begin{Bmatrix} E_1 \\ E_2 \\ E_3 \\ E_4 \\ C_5 \\ C_7 \end{Bmatrix} = \begin{Bmatrix} F^R_1 \\ F^R_2 \\ F^R_3 \\ F^R_4 \\ F^R_5 \\ F^R_6 \end{Bmatrix},$$

where we have defined

$$F^R_j = \frac{\kappa+1}{4\pi^2\mu_0} \int_0^d f_1(t)R_j(\alpha, t)\, dt \quad (j = 1, \dots, 6),$$

the $R_j(\alpha, t)$ $(j = 1, \ldots, 6)$ being integrals evaluated using the residue theorem [Kreyszig 1999]; their values are

$$R_j(\alpha, t) = L_j \left(H_{1j} \sin \frac{Bt}{2} + H_{2j} \cos \frac{Bt}{2} \right) \quad (j = 1, 2),$$

$$R_j(\alpha, t) = L_j \left(H_{1j} \sin \frac{B(h-t)}{2} + H_{2j} \cos \frac{B(h-t)}{2} \right) \quad (j = 3, \ldots, 6),$$

where L_j, H_{ij}, and B are functions of α, β and κ.

This system of equations can be analytically inverted, leading to the expressions of the unknown functions C_5, C_7, E_1, E_2, E_3, E_4 in terms of the density function f_1:

$$E_1 = Q \int_0^d S_1(\alpha, t) f_1(t) \, dt, \qquad E_3 = Q \int_0^d S_3(\alpha, t) f_1(t) \, dt, \qquad C_5 = Q \int_0^d S_5(\alpha, t) f_1(t) \, dt,$$

$$E_2 = Q \int_0^d S_2(\alpha, t) f_1(t) \, dt, \qquad E_4 = Q \int_0^d S_4(\alpha, t) f_1(t) \, dt, \qquad C_7 = Q \int_0^d S_6(\alpha, t) f_1(t) \, dt,$$

where $Q = (\kappa+1)/(4\pi^2 \mu_0)$ and, for $j = 1, \ldots, 6$,

$$S_j(\alpha, t) = \frac{D_{1j}}{D} R_1(\alpha, t) - \frac{D_{2j}}{D} R_2(\alpha, t) + \frac{D_{3j}}{D} R_3(\alpha, t) - \frac{D_{4j}}{D} R_4(\alpha, t) + \frac{D_{5j}}{D} R_5(\alpha, t) - \frac{D_{6j}}{D} R_6(\alpha, t).$$

4. Solution of the sliding mode problem

Similarly to the opening mode problem, the solution of the composite medium for the sliding mode problem may be determined by obtaining the solution in the graded layer and that in the homogeneous substrate with the exception that $y = 0$ is a plane of antisymmetry. The layer solution may be expressed as the sum of two solutions, namely an infinite graded medium with a crack and a graded strip without a crack [Erdogan and Wu 1996; Dag and Erdogan 2002; Bogy 1975]. By superposing the two sets of solutions, the displacement and stress field solutions of the $y \geq 0$ cracked graded strip can be established as follows:

$$
\begin{aligned}
u_2^+(x, y) &= u_2^{i+}(x, y) + u_2^s(x, y), & v_2^+(x, y) &= v_2^{i+}(x, y) + v_2^s(x, y), & y &\geq 0, \\
\sigma_{kl2}^+(x, y) &= \sigma_{kl2}^{i+}(x, y) + \sigma_{kl2}^s(x, y), & k, l &= x, y, & y &\geq 0,
\end{aligned}
\tag{26}
$$

where the subscript 2 stands for the sliding mode problem, the superscript i and s indicate, respectively, the cracked infinite medium and the strip, the superscript $+$ stands for the half-plane $y \geq 0$, $u_2^{i+}(x, y)$ and $v_2^{i+}(x, y)$ are given by Equations (A-1a), (A-1b) in the Appendix, $u_2^s(x, y)$ and $v_2^s(x, y)$ are given by (A-2a), (A-2b) and $\sigma_{kl2}^{i+}(x, y)$ and $\sigma_{kl2}^s(x, y)(k, l = x, y)$ are, respectively, given by (A-1c)–(A-1e) and (A-2c)–(A-2e).

The solution in the homogeneous half-plane can be obtained by considering the plane $y = 0$ as a plane of antisymmetry and that it needs to be bounded as x goes to ∞. The solution is given by (A-3). As in the opening mode problem, the sliding mode problem contains nine unknowns: D_3, D_4 from (A-1), D_5, D_7 from (A-3), $F_1, \ldots, F_4$ from (A-2), and f_2, which can be determined from the nine boundary conditions

$$\sigma_{yy2}(x, 0^+) = 0, \qquad x > 0, \tag{27}$$

$$\left.\begin{array}{l} \sigma_{xx2}(x, y) = 0, \\ \sigma_{xy2}(x, y) = 0, \end{array}\right\} \quad x = 0, \ y < \infty, \tag{28}$$

$$\left.\begin{array}{l} \sigma_{xx2}(h^+, y) = \sigma_{xx2}(h^-, y), \\ \sigma_{xy2}(h^+, y) = \sigma_{xy2}(h^-, y), \end{array}\right\} \quad y < \infty, \tag{29}$$

$$\left.\begin{array}{l} u_2(h^+, y) = u_2(h^-, y), \\ v_2(h^+, y) = v_2(h^-, y), \end{array}\right\} \quad y < \infty, \tag{30}$$

$$\left.\begin{array}{l} v_1(x, 0^+) = 0, \\ u_2(x, 0^+) = 0, \end{array}\right\} \quad d < x < \infty, \tag{31}$$

$$\sigma_{xy2}(x, 0^+) = -q(x), \quad 0 < x < d. \tag{32}$$

Applying the boundary conditions (27) and (31) allows us to express the unknown functions D_3 and D_4 in terms of the density function f_2, as shown in Equations (A-4a), (A-4b). Applying the boundary conditions (28)–(30) yields the linear system in A.5. This system of equations can be analytically inverted, leading to expressions for the unknown functions D_5, D_7, F_1, F_2, F_3, F_4 in terms of the density function f_2; these are given in A.6.

5. Singular integral equations

Based on the solutions obtained in Sections 3 and 4 for the opening and sliding mode problems, we can apply the boundary conditions (25) and (32), obtaining the dual uncoupled integral equations

$$\int_0^d (K_{11}(x, t) + K_{12}(x, t)) f_1(t) \, dt = -p(x), \quad 0 < x < d, \tag{33a}$$

$$\int_0^d (K_{21}(x, t) + K_{22}(x, t)) f_2(t) \, dt = -q(x), \quad 0 < x < d, \tag{33b}$$

where the kernels $K_{11}(x, t)$ and $K_{12}(x, t)$ representing the infinite graded medium and the graded strip for the opening mode problem are given by

$$K_{11}(x, t) = \frac{\kappa+1}{4\pi(\kappa-1)} e^{\beta x} \lim_{y\to 0^+} \left(\int_0^{+\infty} M_0(\lambda, y) \cos(\lambda(x-t)) \, d\lambda + \int_0^{+\infty} N_0(\lambda, y) \sin(\lambda(x-t)) \, d\lambda \right),$$

$$K_{12}(x, t) = \frac{\kappa+1}{4\pi^2(\kappa-1)} e^{\beta x} \lim_{y\to 0^+} \int_0^{+\infty} \sum_{k=1}^4 p_{yy1,k}^s(\alpha) S_k(\alpha, t) e^{n_k x} \cos(y\alpha) \, d\alpha,$$

where $M_0(\lambda, y) = S_0(\lambda, y) + S_0(-\lambda, y)$ and $N_0(\lambda, y) = i(S_0(\lambda, y) - S_0(-\lambda, y))$ with

$$S_0(\lambda, y) = \frac{i}{2\lambda} \left(\frac{p_{yy1,4}^i p_{xy1,3}^i e^{m_4 y} - p_{yy1,3}^i p_{xy1,4}^i e^{m_3 y}}{s_3^i p_{xy1,4}^i - s_4^i p_{xy1,3}^i} \right),$$

and the corresponding kernels $K_{21}(x, t)$ and $K_{22}(x, t)$ for the sliding mode problem are given by

$$K_{21}(x, t) = \frac{\kappa+1}{4\pi} e^{\beta x} \lim_{y \to 0^+} \left(\int_0^{+\infty} M_0'(\lambda, y) \cos(\lambda(x - t)) \, d\lambda + \int_0^{+\infty} N_0'(\lambda, y) \sin(\lambda(x - t)) \, d\lambda \right)$$

$$K_{22}(x, t) = \frac{\kappa+1}{4\pi^2} e^{\beta x} \left(\lim_{y \to 0^+} \int_0^{+\infty} \sum_{k=1}^{4} q_{xy2,k}^s(\alpha) S_k'(\alpha, t) e^{n_k x} \cos(y\alpha) \, d\alpha \right),$$

where $M_0'(\lambda, y)$ and $N_0'(\lambda, y)$ are given analogously in terms of

$$S_0'(\lambda, y) = \frac{i}{2\lambda} \left(\frac{q_{xy2,4}^i q_{yy2,3}^i e^{m_4 y} - q_{xy2,3}^i q_{yy2,4}^i e^{m_3 y}}{q_{yy2,4}^i - q_{yy2,3}^i} \right).$$

The singular nature of the integral equations above and that of the solutions f_1 and f_2 may be determined by studying the asymptotic behavior of the integrands found in the expressions of $K_{11}(x, t)$, $K_{12}(x, t)$, $K_{21}(x, t)$ and $K_{22}(x, t)$. After a very lengthy analysis, the singular integral equations above become

$$\int_0^d \left(\frac{1}{\pi(t - x)} + h_1^s(x, t) + h_1^f(x, t) \right) f_1(t) \, dt = -e^{-\beta x} p(x), \quad 0 < x < d,$$

$$\int_0^d \left(\frac{1}{\pi(t - x)} + h_2^s(x, t) + h_2^f(x, t) \right) f_2(t) \, dt = -e^{-\beta x} q(x), \quad 0 < x < d,$$

(34)

where $h_1^f(x, t)$ and $h_2^f(x, t)$ are bounded Fredholm kernels and $h_1^s(x, t)$ and $h_2^s(x, t)$ are generalized Cauchy kernels of order $1/t$ that become unbounded as the arguments x and t tend to the end point zero simultaneously. The Cauchy kernels are of the form

$$h_1^s(x, t) = \frac{(\kappa+1)e^{\beta(t-x)/2}}{2(\kappa-1)} \left(\frac{2h_2^*}{(t+x)^3} + \frac{h_1^*}{(t+x)^2} + \frac{h_0}{(t+x)} + \frac{c_1^*}{(2h - t - x)^2} + \frac{c_0}{(2h - t - x)} \right),$$

$$h_2^s(x, t) = \frac{(\kappa+1)e^{\beta(t-x)/2}}{2} \left(\frac{2m_2^*}{(t+x)^3} + \frac{m_1^*}{(t+x)^2} + \frac{m_0}{(t+x)} + \frac{l_1^*}{(2h - t - x)^2} + \frac{l_0}{(2h - t - x)} \right),$$

where each of the coefficients h_0, h_1^*, h_2^*, c_0, c_1^*, m_0, m_1^*, m_2^*, l_0 and l_1^* is a lengthy function of κ, β, x and t.

From these singular integral equations, we conclude there is no singularity at the crack mouth, while the standard square-root or Cauchy singularity, $1/(t-x)$, is retained at the crack tip, in addition to other singularities contained in the generalized Cauchy kernels. The solution of these equations is expressed as follows, where $\tilde{f}_1(t)$ and $\tilde{f}_2(t)$ are unknown bounded functions (see [Erdogan et al. 1973]):

$$f_1(t) = (d - t)^{-1/2} \tilde{f}_1(t), \quad f_2(t) = (d - t)^{-1/2} \tilde{f}_2(t), \quad 0 < t < d,$$

(35)

The limits of the generalized Cauchy kernels are the same as for homogeneous materials [Erdogan and Wu 1997], namely

$$\lim_{\beta \to 0} h_1^s(x, t) = \lim_{\beta \to 0} h_2^s(x, t) = \frac{1}{\pi} \left(\frac{1}{t + x} + \frac{2t}{(t + x)^2} - \frac{4t^2}{(t + x)^3} \right), \quad 0 < (t, x) < d.$$

(36)

6. Solution of the singular integral equations

We have the following normalizations for the singular integral equations (34):

$$t = \tfrac{1}{2}d(r+1), \qquad x = \tfrac{1}{2}d(s+1), \quad 0 < (t, x) < d, \ -1 < (r, s) < 1,$$

$$f_1(t) = \bar{f}_1(r), \qquad f_2(t) = \bar{f}_2(r), \quad 0 < t < d, \ -1 < r < 1,$$

$$h_1^s(x, t) = \bar{h}_1^s(s, r), \qquad h_2^s(x, t) = \bar{h}_2^s(s, r), \quad 0 < (x, t) < d, \ -1 < (s, r) < 1,$$

$$h_1^f(x, t) = \bar{h}_1^f(s, r), \qquad h_2^f(x, t) = \bar{h}_2^f(s, r), \quad 0 < (x, t) < d, \ -1 < (s, r) < 1,$$

$$p(x) = \bar{p}(s), \qquad q(x) = \bar{q}(s), \quad 0 < x < d, \ -1 < s < 1.$$

Hence the equations become

$$\int_{-1}^{1} \left(\frac{1}{\pi(r-s)} + \bar{h}_1^s(s, r) + \bar{h}_1^f(s, r) \right) \bar{f}_1(r)\, dr = -e^{-\beta(d/2)(s+1)} \bar{p}(s), \quad -1 < s < 1,$$

$$\int_{-1}^{1} \left(\frac{1}{\pi(r-s)} + \bar{h}_2^s(s, r) + \bar{h}_2^f(s, r) \right) \bar{f}_2(r)\, dr = -e^{-\beta(d/2)(s+1)} \bar{q}(s), \quad -1 < s < 1.$$

(37)

It was shown in [Erdogan et al. 1973] that the solution of these equations may be expressed as $\bar{f}_i(r) = w(r)\psi_i(r)$, $i = 1, 2$, where $w(r) = 1/\sqrt{1-r}$ is the weight function associated with the Jacobi polynomial $P_n^{(-1/2,0)}(r)$ and $\psi_i(r)$, $(i = 1, 2)$ are continuous and bounded function in the interval $[-1, 1]$ which may be expressed as convergent series of Jacobi polynomials. Hence the solutions of (37) become

$$\bar{f}_1(r) = \frac{1}{\sqrt{1-r}} \sum_{n=0}^{\infty} A_{1n} P_n^{(-1/2,0)}(r), \quad \bar{f}_2(r) = \frac{1}{\sqrt{1-r}} \sum_{n=0}^{\infty} A_{2n} P_n^{(-1/2,0)}(r), \quad -1 < r < 1. \quad (38)$$

Substituting this into (37), truncating the series at N and regularizing the singular terms, the above integral equations reduce to a system of linear algebraic equations in the $2(N+1)$ unknowns A_{1n} and A_{2n}:

$$\sum_{n=0}^{N} \left(-\frac{\Gamma(-1/2)\Gamma(n+1)}{\sqrt{2}\pi\,\Gamma(n+1/2)} F\big(n+1, -n+1/2; 3/2; (1-s)/2\big) + M_1(s) \right) A_{1n}$$
$$= -e^{(-\beta d(1+s)/2)} p(d(1+s)/2), \quad -1 < s < 1, \quad (36a)$$

$$\sum_{n=0}^{N} \left(-\frac{\Gamma(-1/2)\Gamma(n+1)}{\sqrt{2}\pi\,\Gamma(n+1/2)} F\big(n+1, -n+1/2; 3/2; (1-s)/2\big) + M_2(s) \right) A_{2n}$$
$$= -e^{(-\beta d(1+s)/2)} q(d(1+s)/2), \quad -1 < s < 1, \quad (36b)$$

where Γ is the gamma function, F is the hypergeometric function and M_1, M_2 are given by

$$M_k(s) = \int_{-1}^{1} (1-r)^{-1/2} H_k(s, r) P_n^{(-1/2,0)}(r)\, dr \quad (k = 1, 2),$$

with

$$H_k(s, r) = \frac{d}{2} \left(h_k^s\left(\frac{d}{2}s + \frac{d}{2}, \frac{d}{2}r + \frac{d}{2}\right) + h_k^f\left(\frac{d}{2}s + \frac{d}{2}, \frac{d}{2}r + \frac{d}{2}\right) \right).$$

Equations (36) are solved numerically using a suitable collocation technique [Erdogan and Wu 1996]. Once the $2(N+1)$ unknowns coefficients A_{1n} and A_{2n} are obtained, the mixed-mode crack tip stress intensity factors may be estimated as follows:

$$k_1 = \lim_{x \to d+0} \sqrt{2(x-d)}\,\sigma_{yy}(x,0) = -e^{\beta d}\sqrt{d}\sum_{n=0}^{N} A_{1n}P_n^{(-1/2,0)}(1),$$

$$k_2 = \lim_{x \to d+0} \sqrt{2(x-d)}\,\sigma_{xy}(x,0) = -e^{\beta d}\sqrt{d}\sum_{n=0}^{N} A_{2n}P_n^{(-1/2,0)}(1). \tag{40}$$

7. Results and discussion

Table 1 gives the thermomechanical properties of actual functionally graded materials studied in [Zhao et al. 2004; Jin and Paulino 2001; Shodja and Ghahremaninejad 2006; Shao 2005; Ma and Wang 2003; Ching and Yen 2005; Lee and Erdogan 1998b]. The tabulated FGMs are made of two constituents, such as ceramic Al_2O_3 and titanium carbide (TiC), or Rene 41 and zirconia. It is clear from this table that the thermomechanical properties, such as the elastic modulus, the thermal expansion coefficient and the heat conductivity, can be proportional (decreasing or increasing) or nonproportional from one face to the other face of the graded layer. For example, for a Rene 41 and zirconia FGM, the ratio of the elastic moduli,

components	reference	ν	E	E_1/E_2	α	α_1/α_2	k	k_1/k_2
ceramic Al_2O_3	[Zhao et al. 2004]	0.26	380	< 1	8.5	> 1	40.37	> 1
titanium carbide		0.19	450		7.6		24.28	
silicon carbide	[Jin and Paulino 2001]	0.20	400	$= 1$	4.0	< 1	60	> 1
titanium carbide		0.20	400		7.0		20	
titanium nickel	[Shodja and	0.20	600	> 1	8.08	< 1	22	< 1
aluminum alloy	Ghahremaninejad 2006]	0.33	70		23.05		190	
titanium nickel	[Shodja and	0.20	600	> 1	8.08	< 1	22	< 1
carbon steel	Ghahremaninejad 2006]	0.30	207		12.36		40	
mullite	[Shao 2005]	0.27	225	< 1	4.8	≈ 1	5.9	< 1
molybednum		0.30	330		4.9		138	
zirconia	[Ma and Wang 2003]	0.3	151	> 1	9.97	< 1	2.09	< 1
aluminum		0.3	70		22.86		204	
silicon carbide	[Ching and Yen 2005]	0.17	427	> 1	4.3	< 1	65	< 1
aluminum		0.3	70		23.4		233	
Rene 41	[Lee and Erdogan 1998b]	0.3	219.7	> 1	16.7	> 1	25.51	> 1
zirconia		0.3	151		10		2.09	

Table 1. Thermomechanical properties of various types of functionally graded materials. Legend: ν, Poisson's ratio; E, elastic modulus, in GPa; α, thermal expansion coefficient, in $10^{-6}\mathrm{K}^{-1}$, k, thermal conductivity, in $10^3\mathrm{W@(mK)}^{-1}$. Subscript 1 corresponds to the top-row material in each pair and subscript 2 to bottom row.

	$k_1/(\sigma_n d^{1/2})$							
	$p(x) = \sigma_0$		$p(x) = \sigma_1(x/d)$		$p(x) = \sigma_2(x/d)^2$		$p(x) = \sigma_3(x/d)^3$	
βd	lit.	cur.	lit.	cur.	lit.	cur.	lit.	cur.
-3.0	4.4345	4.4481	1.9324	1.9375	1.2148	1.2176	0.8897	0.8916
-2.0	3.1238	3.1254	1.4495	1.4501	0.9525	0.9528	0.7209	0.7211
-1.0	1.9846	1.9853	1.0196	1.0199	0.7152	0.7154	0.5663	0.5664
-0.5	1.4988	1.4991	0.8317	0.8318	0.6099	0.6099	0.4970	0.4970
10^{-4}	1.1215	1.1215	0.6828	0.6828	0.5255	0.5255	0.4410	0.4410
0.5	1.0225	1.0225	0.6439	0.6439	0.5035	0.5035	0.4264	0.4264
1.0	0.9930	0.9931	0.6328	0.6328	0.4947	0.4974	0.4225	0.4225
2.0	0.9807	0.9806	0.6289	0.6289	0.4956	0.4956	0.4215	0.4215
3.0	09884	0.9885	0.6329	0.6329	0.4981	0.4982	0.4233	0.4234

	$k_2/(\tau_n d^{1/2})$							
	$p(x) = \tau_0$		$p(x) = \tau_1(x/d)$		$p(x) = \tau_2(x/d)^2$		$p(x) = \tau_3(x/d)^3$	
βd	lit.	cur.	lit.	cur.	lit.	cur.	lit.	cur.
-3.0	1.6704	1.6708	0.9273	0.9276	0.6738	0.6739	0.5437	0.5438
-2.0	1.4765	1.4767	0.8398	0.8399	0.6202	0.6202	0.5063	0.5063
-1.0	1.2825	1.2824	0.7534	0.7534	0.5678	0.5677	0.4700	0.4700
-0.5	1.1940	1.1939	0.7144	0.7144	0.5443	0.5443	0.4539	0.4539
10^{-4}	1.1215	1.1216	0.6829	0.6829	0.5255	0.5255	0.4410	0.4410
0.5	1.0727	1.0727	0.6620	0.6620	0.5132	0.5132	0.4327	0.4327
1.0	1.0429	1.0428	0.6497	0.6497	0.5062	0.5062	0.4280	0.4280
2.0	1.0164	1.0165	0.6397	0.6397	0.5008	0.5008	0.4245	0.4246
3.0	1.0128	1.0127	0.6394	0.6394	0.5011	0.5011	0.4249	0.4250

Table 2. Normalized mode I (top) and mode II (bottom) stress intensity factors for a graded half-plane: comparison of results from [Dag and Erdogan 2002] (columns labeled "lit.") with those obtained in the current study.

the ratio of the thermal expansion coefficients and the ratio of the heat conductivity are all greater than one. For a titanium nickel (TiNi) and aluminum alloy FGM, the ratio of the elastic moduli is greater than one while the ratio of the thermal expansion coefficients and the ratio of the heat conductivity are both less than one. For a ceramic Al_2O_3 and titanium carbide FGM, the ratio of the elastic moduli is less than one while the ratio of the thermal expansion coefficients and the ratio of the heat conductivity are both greater than one. Since this study is limited only to variations of the elastic modulus, we, therefore, consider two cases of FGM coatings, a stiff graded layer with $\beta d < 0$ and a compliant graded layer with $\beta d > 0$, which correspond, respectively, to a ratio of the elastic moduli greater than and less than 1.

Furthermore, for the problem considered, if the coating thickness tends to infinity ($h \to \infty$), the configuration of the problem tends toward a graded half-plane, with the effect of the homogeneous
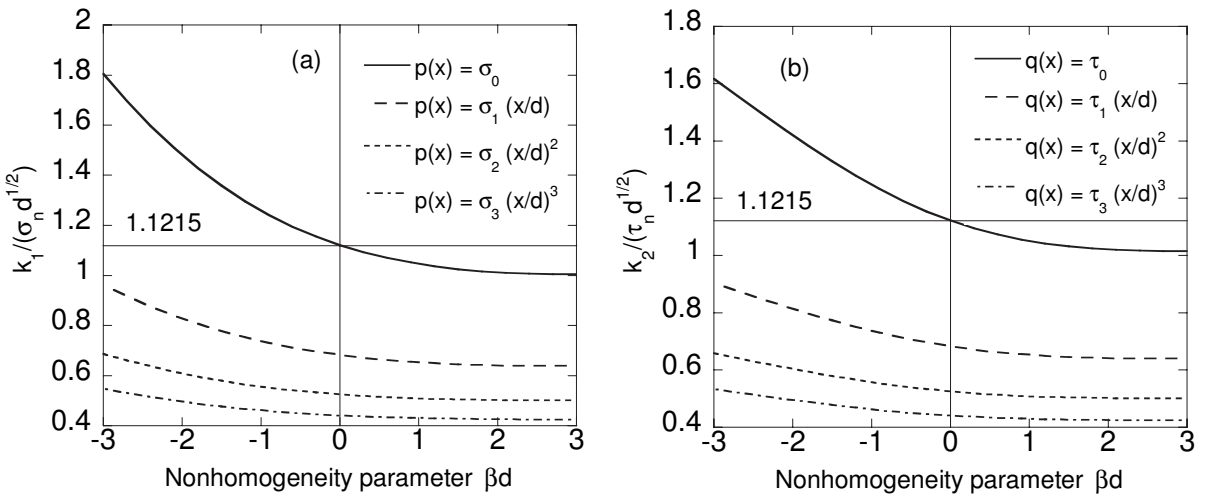
Figure 2. Effect of the nonhomogeneity parameter βd on the normalized mode I (left) and mode (II) stress intensity factors under plane strain and various distributions of crack surface tractions σ_n or τ_n, $n = 0, 1, 2, 3$. In each case, $\nu = 0.25$ and $h/d = 2$.

substrate almost negligible. As mentioned in the introduction, this crack problem was solved in [Dag and Erdogan 2002]. We see in Table 2 that the results obtained here are in agreement with those published in that work; the tables give the normalized mode I and II stress intensity factors for an edge crack in a graded half-plane, assuming different values of the nonhomogeneity parameter βd, various polynomial forms of crack surface tractions, plane strain conditions, a Poisson's ratio $\nu = 0.25$ and a large value of the coating thickness h ($h/d = 50$).

When $|\beta d|$ approaches zero, the composite medium becomes a homogeneous elastic half-plane. The closed-form solution for the stress intensity factor for a surface crack subject to a uniform normal traction $p(x) = \sigma_0$ was obtained in [Koiter 1965] in terms of an infinite integral as

$$\frac{k_1}{\sigma_0\sqrt{d}} = \sqrt{\frac{2(B+1)}{\sqrt{\pi}A}}, \quad \log A = -\frac{1}{\pi}\int_0^\infty \frac{1}{1+\alpha^2}\log\left(\frac{\alpha\sinh(\pi\alpha)}{\sqrt{B^2+\alpha^2}\,(\cosh(\pi\alpha)-2\alpha^2-1)}\right)d\alpha, \quad (41)$$

where B is an arbitrary real constant greater than 1 and the result is independent of the choice of B.

The numerical evaluation of (41), performed in [Kaya and Erdogan 1987], shows that $k_1/(\sigma_0\sqrt{d}) = 1.12152226$, which is the result obtained in Table 2 (top) for $\beta d = 0.0001$.

Figure 2 illustrates the effect of the nonhomogeneity parameter βd [in $\mu_1 = \mu_0\exp(\beta x)$] on the mode I and II crack tip stress intensity factors (SIF) for the case of constant $p(x) = \sigma_0$, linear $p(x) = \sigma_1(x/d)$, quadratic $p(x) = \sigma_2(x/d)^2$ and cubic $p(x) = \sigma_3(x/d)^3$ crack surface normal tractions. The results were calculated for plane strain conditions, a Poisson's ratio $\nu = 0.25$ and a coating thickness $h/d = 2$. Increasing the value of the nonhomogeneity parameter βd from -3 to 3 results in a decrease in both mode I and mode II stress intensity factors. In addition, k_1 and k_2 are much more sensitive to the variations in βd for $\beta d < 0$ (that is, compliant graded coating) than for $\beta d > 0$ (stiff graded coating).
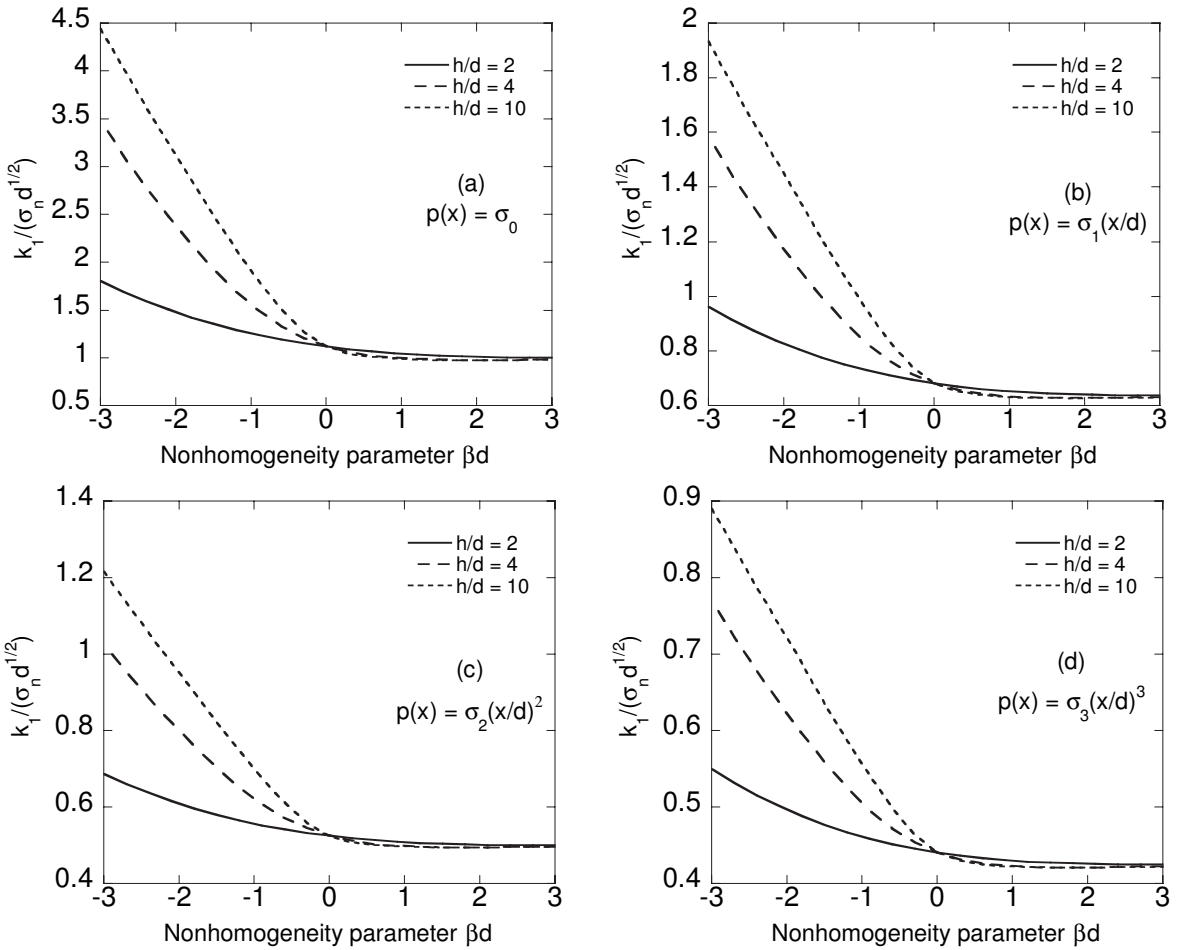
Figure 3. Effect of coating thickness h/d and stiffness parameter βd on the normalized mode I stress intensity factor under various distributions of crack surface normal tractions, $\nu = 0.25$, plane strain, (a) constant normal traction $p(x) = \sigma_0$, (b) linear normal traction $p(x) = \sigma_1(x/d)$, (c) quadratic normal traction $p(x) = \sigma_2(x/d)^2$, (d) cubic normal traction $p(x) = \sigma_3(x/d)^3$; σ_n ($n = 0, 1, 2, 3$), τ_n ($n = 0, 1, 2, 3$).

Figures 3 and 4 illustrate the effect of varying the coating thickness h/d ($= 2, 4, 10$) and the stiffness parameter βd ($= -3, \ldots, 3$) on the normalized mode I and mode II stress intensity factor under various distributions of crack surface normal tractions. The results were calculated for plane strain conditions, a Poisson's ratio $\nu = 0.25$. It can be seen from Figure 3 that k_1 is sensitive to the variations of the coating thickness h/d for $\beta d < 0$ and tends to be insensitive for $\beta d > 0$. Furthermore, for negative values of βd, the value of k_1 tends to increase when the coating thickness is increased. In addition, the rate of change of k_1 with respect to βd for $\beta d < 0$ becomes more important for increasing values of the coating thickness. Moreover, increasing h/d from 2 to 10 indicates that the crack-tip is located more and more in the stiffer side of the coating, and, therefore, the increase of k_1 can be compensated somewhat by a larger fracture toughness which decreases for a compliant graded coating ($\beta d < 0$). On the other hand,
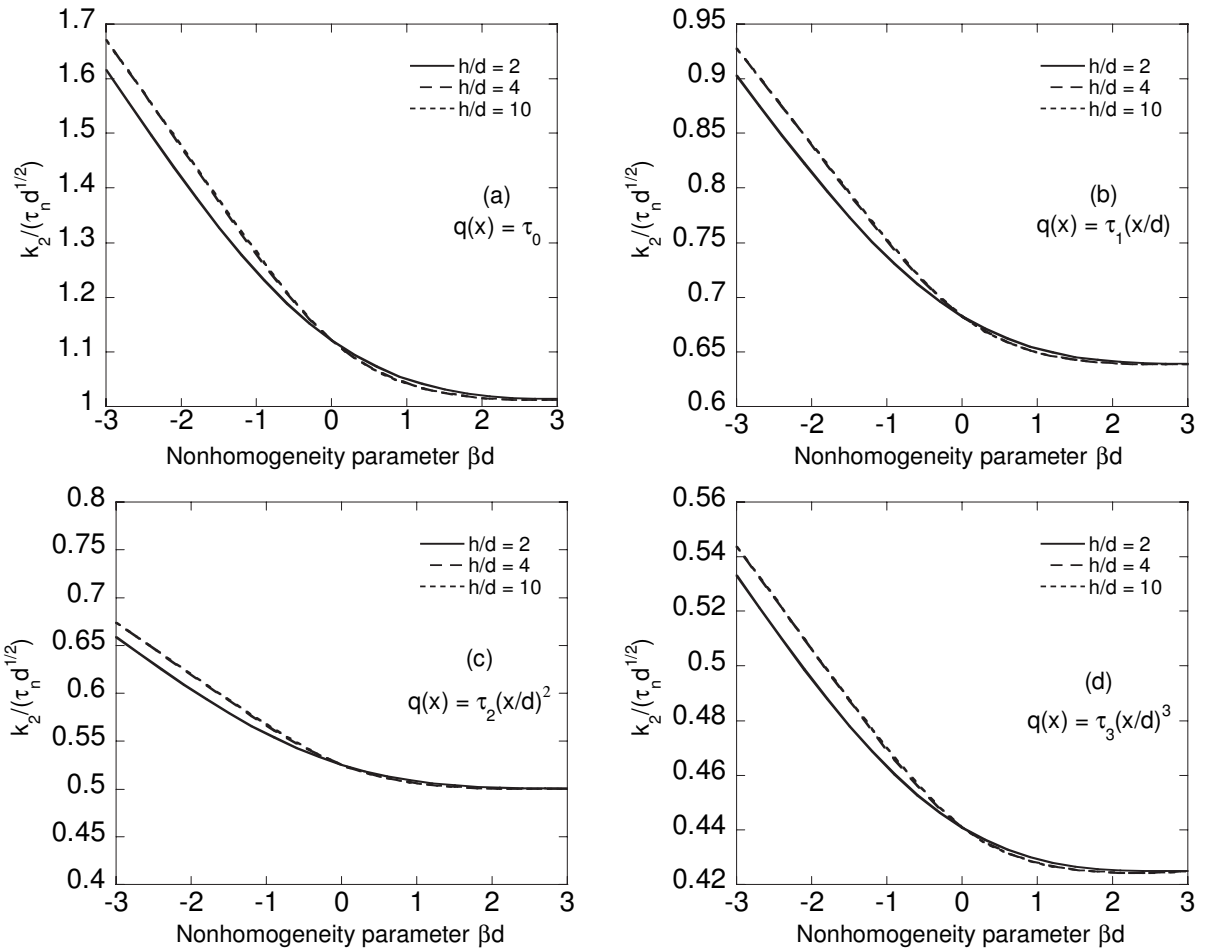
Figure 4. Effect of coating thickness h/d and stiffness parameter βd on the normalized mode II stress intensity factor under various distributions of crack surface shear tractions, $\nu = 0.25$, plane strain, (a) constant shear traction $q(x) = \tau_0$, (b) linear shear traction $q(x) = \tau_1(x/d)$, (c) quadratic shear traction $q(x) = \tau_2(x/d)^2$, (d) cubic shear traction $q(x) = \tau_3(x/d)^3$.

Figure 4 indicates that the mode II stress intensity factor is relatively insensitive to the variations of the coating thickness h/d. In other words, further increase of h/d from 4 to 10 does not seem to affect the values of k_2.

Figure 5 shows some sample results for the normalized normal and tangential crack opening displacements, $v^*(x) = v(x, 0^+) - v(x, 0^-)$ and $u^*(x) = u(x, 0^+) - u(x, 0^-)$, obtained by applying, respectively, constant normal and shear tractions. The results were calculated for plane strain conditions, a Poisson's ratio $\nu = 0.25$ and a coating thickness $h/d = 2$. It may be observed that as βd increases, the crack opening displacements decrease. Furthermore, the influence of βd on the crack opening displacement is more significant for a compliant graded layer ($\beta d < 0$) than for a stiff graded layer ($\beta d > 0$). The crack opening displacements for the homogeneous medium ($\beta d = 0.0001$) is bracketed by the results obtained
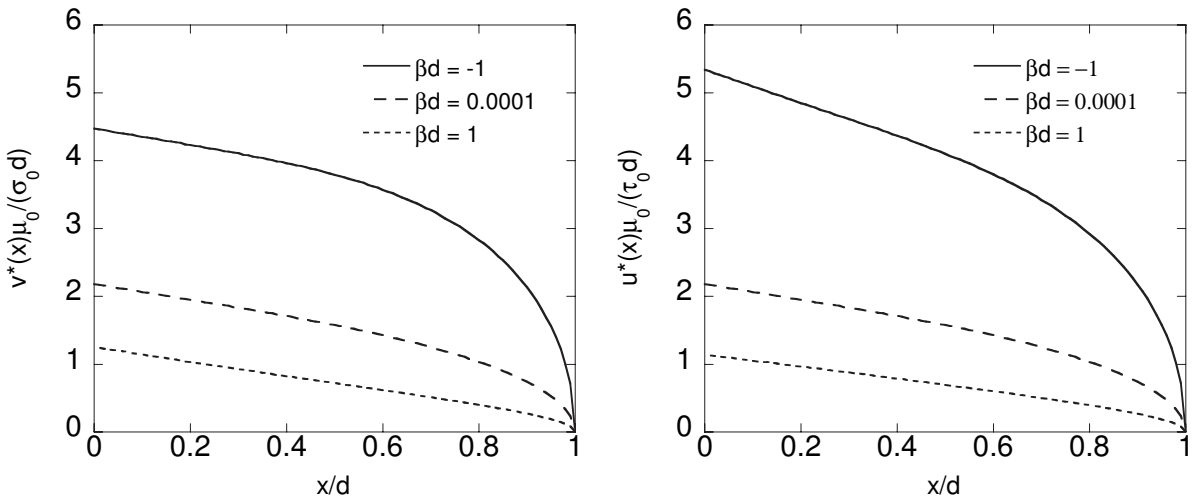
Figure 5. Normal (left) and tangential (right) crack opening displacement under constant normal traction $p(x) = \sigma_0$ (left) or constant shear traction $q(x) = \tau_0$ (right). In both cases, $\nu = 0.25$ and $h/d = 2$.

for $\beta d < 0$ and $\beta d > 0$. In addition, for $\beta d < 0$, crack opening displacements under mode I loading (that is, normal crack surface tractions) is greater than that under mode II loading (shear crack surface tractions).

Acknowledgements

Appendix: Mode II problem expressions

A.1. *Expressions of displacements and stresses in the infinite graded medium (half-plane $y \geq 0$).*

$$u_2^{i+}(x, y) = \frac{1}{2\pi} \int_{-\infty}^{+\infty} \sum_{k=3}^{4} D_k e^{m_k y} e^{ix\lambda} d\lambda, \quad y \geq 0, \tag{A-1a}$$

$$v_2^{i+}(x, y) = \frac{1}{2\pi} \int_{-\infty}^{+\infty} \sum_{k=3}^{4} D_k s_k^i e^{m_k y} e^{ix\lambda} d\lambda, \quad y \geq 0, \tag{A-1b}$$

$$\sigma_{xx2}^{i+}(x, y) = \frac{\mu_1}{2\pi(\kappa-1)} \int_{-\infty}^{+\infty} \sum_{k=3}^{4} p_{xx1,k}^i(\lambda) D_k e^{m_k y} e^{ix\lambda} d\lambda, \quad y \geq 0, \tag{A-1c}$$

$$\sigma_{yy2}^{i+}(x, y) = \frac{\mu_1}{2\pi(\kappa-1)} \int_{-\infty}^{+\infty} \sum_{k=3}^{4} p_{yy1,k}^{i}(\lambda) D_k e^{m_k y} e^{i x \lambda} d\lambda, \quad y \geq 0, \tag{A-1d}$$

$$\sigma_{xy2}^{i+}(x, y) = \frac{\mu_1}{2\pi} \int_{-\infty}^{+\infty} \sum_{k=3}^{4} p_{xy1,k}^{i}(\lambda) D_k e^{m_k y} e^{i x \lambda} d\lambda, \quad y \geq 0, \tag{A-1e}$$

where $D_k(\lambda)$, $(k = 3, 4)$ are unknowns functions, the roots m_k $(k = 3, 4)$ are given by (10b), the known function $s_k^{i}(\lambda)$ is given by (8) and $p_{xx1,k}^{i}(\lambda)$, $p_{yy1,k}^{i}(\lambda)$ and $p_{xy1,k}^{i}(\lambda)$ are known functions given by the equations following (11).

A.2. *Expressions of displacements and stresses in the graded strip.*

$$u_2^{s}(x, y) = \int_{0}^{+\infty} \sum_{k=1}^{4} F_k e^{n_k x} \sin(y\alpha) \, d\alpha, \tag{A-2a}$$

$$v_2^{s}(x, y) = \int_{0}^{+\infty} \sum_{k=1}^{4} F_k r_k^{s} e^{n_k x} \cos(y\alpha) \, d\alpha, \tag{A-2b}$$

$$\sigma_{xx2}^{s}(x, y) = \frac{\mu_1}{\kappa-1} \int_{0}^{+\infty} \sum_{k=1}^{4} q_{xx2,k}^{s}(\alpha) F_k e^{n_k x} \sin(y\alpha) \, d\alpha, \tag{A-2c}$$

$$\sigma_{yy2}^{s}(x, y) = \frac{\mu_1}{\kappa-1} \int_{0}^{+\infty} \sum_{k=1}^{4} q_{yy2,k}^{s}(\alpha) F_k e^{n_k x} \sin(y\alpha) \, d\alpha, \tag{A-2d}$$

$$\sigma_{xy2}^{s}(x, y) = \mu_1 \int_{0}^{+\infty} \sum_{k=1}^{4} q_{xy2,k}^{s}(\alpha) F_k e^{n_k x} \cos(y\alpha) \, d\alpha, \tag{A-2e}$$

where $F_k(\lambda)$ $(k = 1, 2, 3, 4)$, are unknown functions, the roots n_k, $k = 1, \dots, 4$, are given by (15), the known functions $r_k^{s}(\lambda)$, $(k = 1, 2, 3, 4)$, are such that $r_k^{s}(\lambda) = -s_k^{s}(\lambda)$ in which $s_k^{s}(\lambda)$ is given by (13) and $q_{xx2,k}^{s}(\alpha)$, $q_{yy2,k}^{s}(\alpha)$ and $q_{xy2,k}^{s}(\alpha)$ are known functions given by

$$q_{xx2,k}^{s}(\alpha) = (1+\kappa)n_k - (3-\kappa)\alpha r_k^{s},$$
$$q_{xy2,k}^{s}(\alpha) = \alpha + r_k^{s} n_k, \quad (k = 1, \dots, 4),$$
$$q_{yy2,k}^{s}(\alpha) = (3-\kappa)n_k - (1+\kappa)\alpha r_k^{s}, \quad (k = 1, \dots, 4).$$

A.3. *Expressions of displacements and stresses in the homogeneous substrate.*

$$u_2^{h}(x, y) = \int_{0}^{+\infty} (D_5 + D_7 x) e^{-\alpha x} \sin(y\alpha) \, d\alpha, \tag{A-3a}$$

$$v_2^{h}(x, y) = \int_{0}^{+\infty} \left(D_5 + D_7 \frac{\kappa}{\alpha} - D_7 x \right) e^{-\alpha x} \cos(y\alpha) \, d\alpha, \tag{A-3b}$$

$$\sigma_{xx2}^{h}(x, y) = \frac{\mu_2}{\kappa-1} \int_{0}^{+\infty} \left(q_{xx2,1}^{h} D_5 + q_{xx2,2}^{h} D_7 + q_{xx2,1}^{h} D_7 x \right) e^{-\alpha x} \sin(y\alpha) \, d\alpha, \tag{A-3c}$$

$$\sigma_{yy2}^h(x,\,y) = \frac{\mu_2}{\kappa-1} \int_0^{+\infty} \left(q_{yy2,1}^h D_5 + q_{yy2,2}^h D_7 + q_{yy2,1}^h D_7 x\right) e^{-\alpha x} \sin(y\alpha)\, d\alpha, \tag{A-3d}$$

$$\sigma_{xy2}^h(x,\,y) = \mu_2 \int_0^{+\infty} \left(q_{xy2,1}^h D_5 + q_{xy2,2}^h D_7 + q_{xy2,1}^h D_7 x\right) e^{-\alpha x} \cos(y\alpha)\, d\alpha, \tag{A-3e}$$

where D_5 and D_7 are unknown functions and $q_{xx2,1}^h$, $q_{xx2,2}^h$, $q_{yy2,1}^h$, $q_{yy2,2}^h$, $q_{xy2,1}^h$ and $q_{xy2,2}^h$ are known functions given by

$$q_{xx2,1}^h(\lambda) = 2(1-\kappa)\alpha, \qquad q_{xx2,2}^h(\lambda) = (\kappa-1)^2,$$
$$q_{yy2,1}^h(\lambda) = -2(1-\kappa)\alpha, \qquad q_{yy2,2}^h(\lambda) = 3 - 2\kappa - \kappa^2,$$
$$q_{xy2,1}^h(\lambda) = 2\alpha, \qquad q_{xy2,2}^h(\lambda) = -(1+\kappa).$$

A.4. *Expressions of D_3 and D_4 in terms of the density function f_2.*

$$D_3 = \frac{\kappa+1}{4\mu_0} \frac{i}{\lambda} \frac{(-q_{yy2,4}^i)}{q_{yy2,4}^i - q_{yy2,3}^i} \int_0^d f_2(t) e^{-i\lambda t} dt, \tag{A-4a}$$

$$D_4 = \frac{\kappa+1}{4\mu_0} \frac{i}{\lambda} \frac{q_{yy2,3}^i}{q_{yy2,4}^i - q_{yy2,3}^i} \int_0^d f_2(t) e^{-i\lambda t} dt. \tag{A-4b}$$

A.5. *Linear system of equations obtained after applying boundary conditions* (28)–(30).

$$\begin{bmatrix} -q_{xx2,1}^s & -q_{xx2,2}^s & -q_{xx2,3}^s & -q_{xx2,4}^s & 0 & 0 \\ q_{xy2,1}^s & q_{xy2,2}^s & q_{xy2,3}^s & q_{xy2,4}^s & 0 & 0 \\ -q_{xx2,1}^s e^{n_1 h} & -q_{xx2,2}^s e^{n_2 h} & -q_{xx2,3}^s e^{n_3 h} & -q_{xx2,4}^s e^{n_4 h} & q_{xx2,1}^h e^{-\alpha h} & (q_{xx2,2}^h + h q_{xx2,1}^h) e^{-\alpha h} \\ q_{xy2,1}^s e^{n_1 h} & q_{xy2,2}^s e^{n_2 h} & q_{xy2,3}^s e^{n_3 h} & q_{xy2,4}^s e^{n_4 h} & -q_{xy2,1}^h e^{-\alpha h} & -(q_{xy2,2}^h + h q_{xx2,1}^h) e^{-\alpha h} \\ -e^{n_1 h} & -e^{n_2 h} & -e^{n_3 h} & -e^{n_4 h} & e^{-\alpha h} & h e^{-\alpha h} \\ r_1^s e^{n_1 h} & r_2^s e^{n_2 h} & r_3^s e^{n_3 h} & r_4^s e^{n_4 h} & e^{-\alpha h} & (h-\tfrac{\kappa}{\alpha}) e^{-\alpha h} \end{bmatrix} \begin{Bmatrix} F_1 \\ F_2 \\ F_3 \\ F_4 \\ D_5 \\ D_7 \end{Bmatrix} = \begin{Bmatrix} G_1^R \\ G_2^R \\ G_3^R \\ G_4^R \\ G_5^R \\ G_6^R \end{Bmatrix},$$

where we have defined

$$G_j^R = \frac{\kappa+1}{4\pi^2 \mu_0} \int_0^d f_2(t) R_j'(\alpha,\,t)\, dt \quad (j = 1, \ldots, 6),$$

the $R_j'(\alpha,\,t)$ $(j = 1, \ldots, 6)$ being integrals evaluated using the residue theorem in a similar manner as the integrals R_j for the mode I problem.

A.6. *Expressions of D_5, D_7, F_1, F_2, F_3 and F_4 in terms of the density function f_2.*

$$F_1 = Q \int_0^d S_1'(\alpha,\,t) f_2(t)\, dt, \quad F_3 = Q \int_0^d S_3'(\alpha,\,t) f_2(t)\, dt, \quad D_5 = Q \int_0^d S_5'(\alpha,\,t) f_2(t)\, dt,$$

$$F_2 = Q \int_0^d S_2'(\alpha,\,t) f_2(t)\, dt, \quad F_4 = Q \int_0^d S_4'(\alpha,\,t) f_2(t)\, dt, \quad D_7 = Q \int_0^d S_6'(\alpha,\,t) f_2(t)\, dt,$$

in which $Q = (\kappa + 1)/(4\pi^2 \mu_0)$ and, for $j = 1, \ldots, 6$,

$$S'_j(\alpha, t) = \frac{H_{1j}}{H} R'_1(\alpha, t) - \frac{H_{2j}}{H} R'_2(\alpha, t) + \frac{H_{3j}}{H} R'_3(\alpha, t) - \frac{H_{4j}}{H} R'_4(\alpha, t) + \frac{H_{5j}}{H} R'_5(\alpha, t) - \frac{H_{6j}}{H} R'_6(\alpha, t).$$

References

[Bogy 1975] D. B. Bogy, "Solution of the plane end problem for a semi-infinite elastic strip", *Journal of Applied Mathematics and Physics* **26** (1975), 749–769.

[Chen and Erdogan 1996] Y. F. Chen and F. Erdogan, "The interface crack problem for a nonhomogeneous coating bonded to a homogeneous substrate", *Journal of Mechanics and Physics of Solids* **44** (1996), 771–787.

[Chen et al. 2002a] J. Chen, Z. Liu, and Z. Zou, "Transient internal crack problem for a nonhomogeneous orthotropic strip (Mode I)", *International Journal of Engineering Science* **40** (2002), 1761–1774.

[Chen et al. 2002b] Y.-H. Chen, M. Guruz, Y.-W. Chung, and L. M. Keer, "Thermal stability of hard TiN/SiNx coatings with an equiaxed microstructure", *Surface and Coatings Technology* **154** (2002), 162–166.

[Chen et al. 2002c] Y.-H. Chen, I. A. Polonsky, Y.-W. Chung, and L. M. Keer, "Tribological properties and rolling-contact-fatigue lives of TiN/SiNx multilayer coatings", *Surface and Coatings Technology* **154** (2002), 152–161.

[Ching and Yen 2005] H. K. Ching and S. C. Yen, "Meshless local Petrov-Galerkin analysis for 2D functionally graded elastic solids under mechanical and thermal loads", *Composites Part B* **36** (2005), 223–240.

[Dag and Erdogan 2002] S. Dag and F. Erdogan, "A surface crack in a graded medium under general loading condition", *ASME Journal of Applied Mechanics* **69** (2002), 580–588.

[Dag et al. 1999] S. Dag, S. Kadioglu, and O. S. Yahsi, "Circumferential crack problem for an FGM cylinder under thermal stresses", *Journal of Thermal Stresses* **22** (1999), 659–687.

[Delale and Erdogan 1983] F. Delale and F. Erdogan, "The crack problem for a nonhomogeneous plane", *ASME Journal of Applied Mechanics* **50** (1983), 609–614.

[Dhaliwal and Singh 1978] R. S. Dhaliwal and B. M. Singh, "On the theory of elasticity of a non-homogeneous medium", *Journal of Elasticity* **8** (1978), 211–219.

[El-Borgi et al. 2000] S. El-Borgi, L. Hidri, and F. Erdogan, "Stress intensity factors for a crack arbitrarily oriented in a functionally graded layer", *Ceramic Transactions* (2000), 723–730.

[El-Borgi et al. 2003] S. El-Borgi, F. Erdogan, and F. Ben Hatira, "Stress intensity factors for an interface crack between a functionally graded coating and a homogeneous substrate", *International Journal of Fracture* **123** (2003), 139–162.

[El-Borgi et al. 2004a] S. El-Borgi, F. Erdogan, and L. Hidri, "A partially insulated embedded crack in an infinite functionally graded medium under thermo-mechanical loading", *International Journal of Engineering Science* **42** (2004), 371–393.

[El-Borgi et al. 2004b] S. El-Borgi, L. Keer, and W. Ben Said, "An embedded crack in a functionally graded coating bonded to a homogeneous substrate under frictional Hertzian contact", *Wear, An International Journal on the Science and Technology of Friction, Lubrication and Wear* **257** (2004), 760–776.

[Erdogan 1985] F. Erdogan, "The crack problem for bonded nonhomogeneous materials under antiplane shear loading", *ASME Journal of Applied Mechanics* **52** (1985), 823–828.

[Erdogan 1995] F. Erdogan, "Fracture mechanics of functionally graded materials", *Composites Engineering* **5** (1995), 753–770.

[Erdogan and Wu 1996] F. Erdogan and B. H. Wu, "Crack problems in FGM layers under thermal stresses", *Journal of Thermal Stresses* **19** (1996), 237–265.

[Erdogan and Wu 1997] F. Erdogan and B. H. Wu, "The surface crack problem for a plate with functionally graded properties", *ASME Journal of Applied Mechanics* **64** (1997), 449–456.

[Erdogan et al. 1973] F. Erdogan, G. D. Gupta, and T. S. Cook, "Numerical solution of singular integral equations", pp. 368–425 in *Mechanics of Fracture*, edited by G. Sih, Norrdhoff, Leyden, 1973.

[Guo et al. 2004a] L.-C. Guo, Lin-Zhi, L.-Z. Wu, T. Zeng, and L. Ma, "Mode I crack problem for a functionally graded orthotropic strip", *European Journal of Mechanics A/Solids* **23** (2004), 219–234.

[Guo et al. 2004b] L.-C. Guo, L.-Z. Wu, T. Zeng, and L. Ma, "The dynamic fracture behavior of a functionally coating-substrate system", *Composite Structures* **64** (2004), 433–441.

[Holt et al. 1992] J. Holt, M. Koizumi, T. Hirai, and Z. A. Munir (editors), *Functionally gradient materials ceramic transactions*, vol. 34, The American Ceramic Society, Ohio, 1992.

[Jin and Noda 1993] Z.-H. Jin and N. Noda, "An internal crack parallel to the boundary of a nonhomogeneous half plane under thermal loading", *International Journal of Engineering Science* **31** (1993), 793–806.

[Jin and Noda 1994a] Z.-H. Jin and N. Noda, "Crack tip singular fields in nonhomogeneous materials", *ASME Journal of Applied Mechanics* **61** (1994), 738–740.

[Jin and Noda 1994b] Z.-H. Jin and N. Noda, "Edge crack in a nonhomogeneous half plane under thermal loading", *Journal of Thermal Stresses* **17** (1994), 591–599.

[Jin and Noda 1994c] Z.-H. Jin and N. Noda, "Transient thermal stress intensity factors for a crack in a semi-infinite plate of a functionally gradient material", *International Journal of Solids Structures* **31** (1994), 203–218.

[Jin and Paulino 2001] Z.-H. Jin and G. H. Paulino, "Transient thermal stress analysis of an edge crack in a functionally graded material", *International Journal of Fracture* **107** (2001), 73–98.

[Kadioglu et al. 1998] S. Kadioglu, S. Dag, and S. Yahsi, "Crack problem for a functionally graded layer on an elastic foundation", *International Journal of Fracture* **94** (1998), 63–77.

[Kaya and Erdogan 1987] A. C. Kaya and F. Erdogan, "On the solution of integral equations with strong singular kernels", *Quarterly of Applied Mathematics, XLV* (1987), 105–122.

[Koiter 1965] W. T. Koiter, "Discussion of rectangular tensile sheet with symmetrical edge cracks", *Trans. ASME, Journal of Applied Mechanics* **87** (1965), 237–238.

[Konda and Erdogan 1994] N. Konda and F. Erdogan, "Mixed mode crack problem in a non-homogeneous elastic medium", *Engineering Fracture Mechanics* **47** (1994), 533–547.

[Kreyszig 1999] E. Kreyszig, *Advanced engineering mathematics*, 8th ed., Wiley, 1999.

[Lanutti 1994] J. J. Lanutti, "Functionally graded materials: properties, potential and design guidelines", *Composites Engineering* **4** (1994), 81–94.

[Lee and Erdogan 1998a] Y. D. Lee and F. Erdogan, "Interface cracking of FGM coatings under steady state heat flow", *Engineering Fracture Mechanics* **59** (1998), 361–380.

[Lee and Erdogan 1998b] Y.-D. Lee and F. Erdogan, "Interface cracking of FGM coatings under steady-state heat flow", *Engineering Fracture Mechanics* **59**:3 (1998), 361–380.

[Long and Delale 2005] X. Long and F. Delale, "The mixed mode crack problem in an FGM layer bonded to a homogeneous half-plane", *International Journal of Solids and Structures* **42** (2005), 3897–3917.

[Ma and Wang 2003] L. S. Ma and T. J. Wang, "Nonlinear bending and post-buckling of a functionally graded circular plate under mechanical and thermal loadings", *International Journal of Solids and Structures* **40** (2003), 3311–3330.

[Noda and Jin 1993] N. Noda and Z.-H. Jin, "Steady thermal stresses in an infinite nonhomogeneous elastic solid containing a crack", *Journal of Thermal Stresses* **16** (1993), 181–196.

[Ozturk and Erdogan 1993] M. Ozturk and F. Erdogan, "The axisymmetric crack problem in a nonhomogeneous medium", *ASME Journal of Applied Mechanics* **44** (1993), 631–636.

[Shao 2005] Z. S. Shao, "Mechanical and thermal stresses of a functionally graded circular hollow cylinder with finite length", *International Journal of Pressure Vessels and Piping* **82** (2005), 155–163.

[Shodja and Ghahremaninejad 2006] H. M. Shodja and A. Ghahremaninejad, "An FGM coated elastic solid under thermomechanical loading a two dimensional linear elastic approach", *Surface & Coatings Technology* **200** (2006), 4050–4064.

[Yildirim and Erdogan 2004] B. Yildirim and F. Erdogan, "Edge crack problems in homogeneous and functionally graded material thermal barrier coatings under uniform thermal loading", *Journal of Thermal Stresses* **27** (2004), 311–329.

[Zhao et al. 2004] J. Zhao, X. Ai, J. Deng, and J. Wang, "Thermal shock behavior of functionally graded ceramic tool materials", *Journal of the European Ceramic Society* **24** (2004), 847–854.

SAMI EL-BORGI: sami.elborgi@gnet.tn
Applied Mechanics and Systems Research Laboratory, Tunisia Polytechnic School, B.P. 743, La Marsa 2078, Tunisia

RADHI ABDELMOULA: radhi.abdelmoula@lpmtm.univ-paris13.fr
Laboratoire des Propriétés Mechaniques et Thermodynamiques de Matériaux, UPR-CNRS 9001, Institut Galilée, Université Paris 13, 99 avenue Jean-Baptiste Clément, 93430 Villetaneuse, France

SERKAN DAG: sdag@metu.edu.tr
Department of Mechanical Engineering, Middle East Technical University, Ankara 06531, Turkey

NIZAR LAJNEF: lajnef001@yahoo.fr
Applied Mechanics and Systems Research Laboratory, Tunisia Polytechnic School, B.P. 743, La Marsa 2078, Tunisia

BUCKLING AND NONLINEAR RESPONSE OF SANDWICH PANELS WITH A COMPLIANT CORE AND TEMPERATURE-DEPENDENT MECHANICAL PROPERTIES

Yeoshua Frostig and Ole Thybo Thomsen

This paper deals with the buckling response and nonlinear behavior of sandwich panels with *soft* cores that have temperature-dependent mechanical properties and are subjected to thermally induced deformations and mechanical loads simultaneously. This study investigates the effects of the degradation of properties of the core as a result of rising temperature on the response of the sandwich panel. Analyses are carried out for cases of pure thermal loading, with either uniform or gradient temperature fields through the depth of the panel, as well as for thermal loading acting simultaneously with external mechanical loads. The formulation is based on variational principles along with the high-order sandwich panel approach. It takes into account the flexibility of the core in the vertical direction as well as the dependency of the mechanical core properties of the temperature distribution through the core depth. The stress and deformation fields of the core have been solved *analytically*, including the case where the temperature-dependent properties attain a complex pattern. The buckling equations are derived using the perturbation technique, yielding a set of nonlinear algebraic equations for the case of a simply-supported panel and a uniform temperature field. The critical temperatures and modes of wrinkling and global buckling are determined numerically for some foam types of core made by Rohacell and Divinycell. The nonlinear response caused by thermally induced deformations is presented for Divinycell foam core with different temperature distributions through the depth of the core. Finally, the nonlinear response caused by the simultaneous action of external mechanical loading and increased temperatures on the compressive or the tensile side of the panel, with a thermal gradient through the core depth, is presented. The interaction between elevated temperatures and mechanical loads changes the response from a linear into an unstable nonlinear one when the degradation of the mechanical properties due to temperature changes is considered and the panel is unrestrained. Moreover, the unstable nonlinear behavior becomes even more severe when the face, loaded in compression, is subjected to elevated temperatures. This study reveals that a reliable, realistic design of a sandwich panel that is subjected to elevated temperature (within working temperature range) and mechanical loads must take into account the degradation of the properties of the core as a result of the thermal field even at working temperature range, especially when cores made of foam are considered.

1. Introduction

Modern structural sandwich panels are used for a variety of applications in most major industries. They usually consist of two face sheets made of either metal or composite laminated materials that are separated and bonded to a low-strength compliant core material. The use of sandwich structures is on the increase as primary and secondary structural components due to their superior qualities in terms of high strength to weight and stiffness to weight ratios, ease of manufacturing, acoustic and thermal insulation, and flexibility in design. Sandwich structures are often subjected to aggressive service conditions including external mechanical loads and elevated temperatures, which lead to thermally induced deformation loads and degradation of the material properties. Thermally induced deformations with and without external mechanical loads are in general associated with bending, buckling and a nonlinear response of the sandwich panel, with and without degradation of the material properties.

In general, the material properties of the constituents of a sandwich panel depend on the temperature field imposed on the structure. However, this dependency is usually ignored, even for cases where temperature fields are induced and the material properties degrade significantly with increasing temperatures. In many modern sandwich panel applications, the core material is made from polymer foam where significant changes in the properties may occur in the operating range of temperatures for the structure. For example, a Rohacell type of foam looses its heat distortion resistance at about 200° C [Rohacell 2004], while Divinycell foam loses its strength at about 80–100° C [Diab Group 2003; 2005 (private communication)]. Hence, it becomes extremely important to understand how the thermally induced degradation of the core properties lead to deformation loads, and large deformations affect the buckling and the nonlinear response of the sandwich panel with soft cores made of polymer foam. The response of a sandwich panel when subjected to an external mechanical load may involve a stable type of nonlinear response (such as a plate type of buckling response), or an unstable response (like the buckling response of a beam or a shell), and it depends on the sandwich panel layout, the geometrical and mechanical properties of the sandwich constituents, and the boundary conditions.

Moreover, when external mechanical loads act simultaneously with thermal loads (rising temperatures), the degradation of the material properties with rising temperature may shift the response from a linear and stable one into an unstable one. One of the objectives of this investigation is to study this occurrence.

Sandwich panels with vertically rigid cores made of metallic or polymer honeycombs have been considered by many researchers. It is usually assumed that the core is an *antiplane* and is incompressible (see [Plantema 1966; Allen 1969; Zenkert 1995; Vinson 1999]). Usually, the models adopted for predicting the linear and nonlinear load-response of sandwich panels are based on the *equivalent single layer* approach (ESL), where the layered panel (beam, plate or shell type) is replaced by an equivalent single layer with homogenized (equivalent) mechanical properties (see Mindlin first-order theory [Mindlin 1951]), and Reddy's high-order theories [Reddy 1984]. Recently Huang and Kardomateas [2002] and Kardomateas and Huang [2003] have used the ESL approach to analyze a sandwich panel with very large deformations. The classical and ESL computation models usually disregard the changes in the height of the core (the compressibility) when the panel is deformed.

Thermal buckling and nonlinear analyses using the ESL approach and using mechanical properties that are *independent* of temperature have been considered by a few authors: Ko [1994] treated the buckling

problem with various boundary conditions; Kant and S. [2000] used a first-order shear model along with finite element analysis for skew plates; Tessler et al. [2001] used a first-order shear deformable (FOSD) model along with a second–order polynomial for the vertical deflection; and Liew et al. [2004] used a FOSD model to investigate the effects of temperature dependent properties. Several researchers have used high-order models: these researchers include Najafizadeh and Heydari [2004], who adopted a third-order approach for the analysis of functionally graded material (FGM) circular plates; Kapuria and Achary [2004], who used a zig-zag third-order model for simply-supported panels; Shiau and Kuo [2004], who used a 72-DOF triangular finite element; and Matsunaga [2005], who used truncated power series expansions for representing the distribution of the displacements through the thickness of the panel (limited to simply-supported boundary conditions and buckling only).

Some research has been done on the response of panels with temperature-dependent mechanical properties. Chen and Chen [1989; 1991] used an FE solution to deal with buckling and postbuckling of a plate made of composite laminates with temperature-dependent mechanical properties. Gu and Asaro [2005] have analyzed a sandwich panel made of FGM face sheets and an incompressible core. They have used a power fitted function to describe the degradation of the mechanical properties due to rising temperature. Birman [2005] dealt with wrinkling of a simply-supported sandwich panel using the FOSD model, assuming material properties that are linearly dependent on temperature. Using the FOSD theory, Birman et al. [2006] and Liu et al. [2006] have considered the responses of a sandwich panel and a sandwich beam with temperature-dependent properties subjected to elevated temperatures. In general, the classical sandwich, described by ESL/FOSD and high-order computation models, mentioned above, disregards the changes in the height of the core (compressibility) during the deformation of the sandwich panel. Accordingly, they yield inaccurate results when used for sandwich panels with a soft/compliant core such as a polymer foam.

An approach that models the layered sandwich panel—that is, in being made of two face sheets and a core layer that are interconnected through fulfillment of equilibrium and compatibility conditions and in thus being able to incorporate the vertical flexibility of the core—represents a more consistent and rational approach and offers significant advantages when considering sandwich structures with compliant, soft cores. This approach has been implemented through a variational principle into the high-order sandwich panel theory approach (HSAPT), and has been successfully used for the analysis of various linear and nonlinear applications including hygrothermal effects [Frostig 1997]; buckling analysis of unidirectional sandwich panels [Frostig and Baruch 1993]; buckling analysis of sandwich plates [Frostig 1998]; non-linear response to in-plane compressive loads [Sokolinsky and Frostig 2000]; and a general nonlinear response [Frostig et al. 2005]. Recently, Frostig and Thomsen [2007b] used the HSAPT approach to derive governing equations of the thermal buckling and the nonlinear response when taking into account the core thermal expansion in the vertical direction but with thermal independent properties. In a recently published paper, Frostig and Thomsen [2007a], have investigated numerically the thermal buckling and nonlinear response together with localized effects of a sandwich panel which has a compliant, soft core and temperature independent or averaged mechanical properties.

The literature survey reveals that most researchers generally ignore the effects associated with the vertical flexibility of the core. Moreover, they do not consider the nonlinear interaction response when the mechanical and the thermal loads are applied simultaneously, in which case the nonlinear interaction effects are enhanced when the mechanical properties are degrading as a result of their temperature

dependency. In such cases, the mechanical properties generally vary spatially (coordinates dependent), especially when temperature gradients through the depth of the sandwich panel are involved.

The present analysis incorporates the flexibility of the core in the vertical direction, the thermally induced deformations and mechanical loads, and the nonuniform core properties resulting from temperature dependency into the mathematical modeling according to the HSAPT approach. The variational principle of minimum of the total potential energy is used to derive the field equations along with the appropriate boundary conditions.

The formulation is based on the following *classical* assumptions for sandwich structures with compliant cores: the face sheets possess in-plane and bending rigidities; the face sheets and the core material are assumed be linear elastic; the face sheets undergo large displacements and moderate rotations (geometrically nonlinear); the core is considered as a two-dimensional linear elastic continuum with kinematic relations that correspond to small deformations (geometrically linear), where the core height may change during deformation, and section planes do not remain plane after deformation; the core possesses only shear and transverse normal stiffness, whereas the in-plane (longitudinal) normal stiffness is assumed to be nil; thermal fields are applied to the face sheets and the core with temperature dependent mechanical properties; full bond is assumed between the face sheets and the core; and the mechanical loads are applied to the face sheets only.

The paper briefly presents the nonlinear thermomechanical governing equations of the face sheets and the stress and displacement fields of the core. Temperature dependent material properties of the core are implemented into the governing equations through closed-form solutions of the governing core equations. The buckling equations are derived following the perturbation approach. Results of a numerical study investigating the effects of the temperature-dependent mechanical properties on the following are presented: buckling; nonlinear response due to thermal induced deformation only; and interaction response of thermal and mechanical loads. Finally a summary is presented and conclusions are drawn.

2. Nonlinear governing equations

The set of nonlinear governing equations used for the analysis herein have been derived through the minimization of the total potential energy following the procedure presented in [Frostig and Thomsen 2007a; 2007b]. The kinematic relations used for the isotropic face sheets, which are assumed to have temperature independent mechanical properties, correspond to large displacements with moderate rotations.

Thus, the nonlinear thermal field equations for the sandwich panel read:

$$-\left(\frac{d}{dx}N_{xxt}(x)\right) - \tau_{ct}(x)b_w - n_t = 0, \tag{1}$$

$$-N_{xxt}(x)\left(\frac{d^2}{dx^2}w_t(x)\right) - \left(\frac{d}{dx}N_{xxt}(x)\right)\left(\frac{d}{dx}w_t(x)\right) - \frac{1}{2}b_w d_t\left(\frac{d}{dx}\tau_{ct}(x)\right) - \left(\frac{d^2}{dx^2}M_{xxt}(x)\right)$$
$$-\sigma_{zzt}(x)b_w + \left(\frac{d}{dx}m_t(x)\right) - q_t = 0, \tag{2}$$

$$-\left(\frac{d}{dx}N_{xxb}(x)\right) + \tau_{cb}(x)b_w - n_b = 0, \tag{3}$$
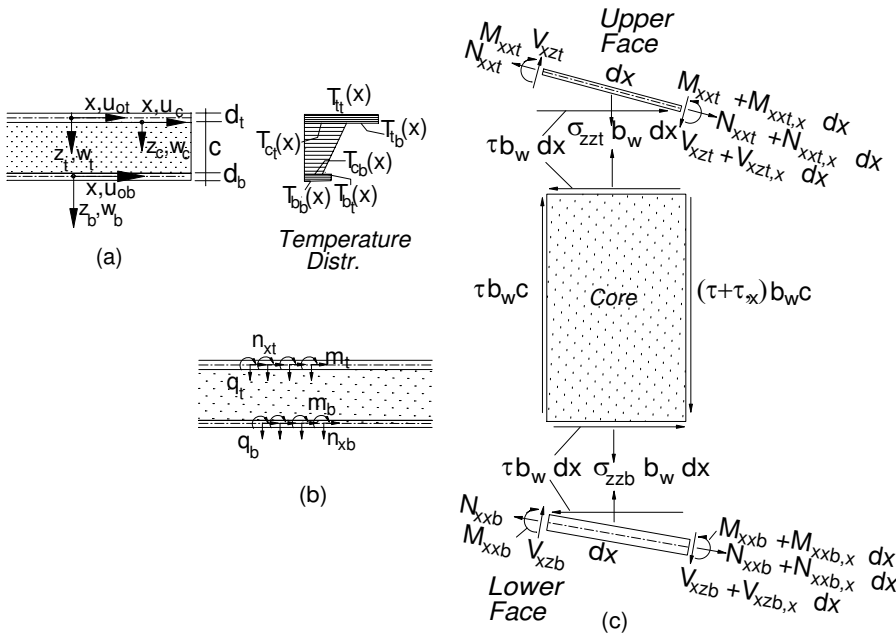
Figure 1. Geometry, loads, temperature distributions and internal stress resultants: (a) geometry, (b) external loads, (c) internal stress resultants and interfacial normal stresses.

$$-N_{xxb}(x)\left(\frac{d^2}{dx^2}w_b(x)\right) - \left(\frac{d}{dx}N_{xxb}(x)\right)\left(\frac{d}{dx}w_b(x)\right) - \frac{1}{2}b_w d_b\left(\frac{d}{dx}\tau_{cb}(x)\right) - \left(\frac{d^2}{dx^2}M_{xxb}(x)\right)$$
$$+\sigma_{zzb}(x)b_w + \left(\frac{d}{dx}m_b(x)\right) - q_b = 0, \quad (4)$$

$$-\left(\frac{\partial}{\partial z_c}\tau_c(x,z_c)\right)b_w = 0, \qquad -\left(\frac{\partial}{\partial x}\tau_c(x,z_c)\right)b_w - \left(\frac{\partial}{\partial z_c}\sigma_{zz}(x,z_c)\right)b_w = 0, \quad (5)$$

where N_{xxj} and M_{xxj} are the in-plane and bending moment stress resultants of each face sheet; $\tau_{cj}(x)$ and $\sigma_{zzj}(x)$ are the shear stresses and the vertical normal stresses at the face-core interfaces; n_j, q_j, and m_j are external distributed loads in the longitudinal and vertical direction and the bending moments exerted at the upper and the lower face sheets respectively; $w_j(x)$ are the vertical displacements of the upper and the lower face sheets; x is the longitudinal coordinate of the panel; b_w, d_j is the width of the panel and the thickness of the face sheets; $j = t, b$ denotes the upper or the lower face sheets; $\tau_c(x, z_c)$ and $\sigma_{zz}(x, z_c)$ are the shear and vertical normal stresses within the core; and z_c is vertical coordinate of the core. For sign conventions of coordinates, stresses, displacements, temperatures distribution, stress resultants, see Figure 1. The notation $(\ )_{,x}$ in Figure 1 refers to a derivative with respect to x.

The isotropic constitutive relations of the face sheets and the core yield the following additional load-displacement equations:

(i) For the face sheets (j=t,b):

$$N_{xxt}(x) - EA_j(x)\left(\left(\frac{d}{dx}u_{oj}(x)\right) + \frac{1}{2}\left(\frac{d}{dx}w_j(x)\right)^2\right) + EA_j(x)\alpha_j\left(\frac{1}{2}T_{j_t}(x) + \frac{1}{2}T_{j_b}(x)\right) = 0, \quad (6)$$

$$M_{xxj}(x) = EI_j\left(-\left(\frac{d^2}{dx^2}w_j(x)\right) - \frac{\alpha_j\left(T_{j_b}(x) - T_{j_t}(x)\right)}{d_j}\right). \quad (7)$$

(ii) For the core:

$$\frac{\sigma_{zz}(x, z_c)}{E_c(T_c(x, z_c))} = \left(\frac{\partial}{\partial z_c}w_c(x, z_c)\right) - \alpha_c T_c(x, z_c), \quad (8)$$

$$\frac{\tau_c(x, z_c)}{G_c(T_c(x, z_c))} = \left(\frac{\partial}{\partial z_c}u_c(x, z_c)\right) + \left(\frac{\partial}{\partial x}w_c(x, z_c)\right), \quad (9)$$

where $T_c(x, z_c)$ is the temperature distribution within the core that equals:

$$T_c(x, z_c) = T_{c_t}(x)\left(1 - \frac{z_c}{c}\right) + \frac{T_{c_b}(x)z_c}{c}, \quad (10)$$

and where the following refers to terms/quantities of the two face sheets: u_{oj} is the mid-plane in-plane displacements of the face sheets; EA_j and EI_j are the in-plane and flexural rigidities, respectively; α_j is the coefficient of thermal expansion of the face sheets; $T_{j_k}(x)$ $(k = t, b)$ are the temperatures at the upper and lower fibers of the faces, respectively. The terms/quantities related to the core include the following: $E_c(T_c x, z_c)$ and $G_c(T_c x, z_c)$ are the vertical modulus of elasticity and the shear modulus, respectively; $w_c(x, z_c)$ and $u_c(x, z_c)$ are the vertical and in-plane displacements, respectively; α_c is the coefficient of thermal expansion; $T_{c_k}(x, z_c)$ $(k = t, b)$ are the temperatures at the upper and lower fiber of the core, respectively; and c is the core height. See Figure 1 for sign conventions and temperature distributions.

The set of field equations, Equations (1) to (4), are given in an inexplicit form, since the face-core interfacial stresses are unknown. In addition, this set of equations does not fulfill the compatibility conditions of a full bond at the upper and the lower face-core interfaces.

The core stress fields using Equation (5) yields:

$$\tau_c(x, z_c) = \tau_{ct}(x) = \tau_{cb}(x) = \tau(x), \qquad \sigma_{zz}(x, z_c) = -\left(\frac{d}{dx}\tau(x)\right)z_c + \sigma_{zzt}(x). \quad (11)$$

Thus, the shear stresses within the core are uniform and the distribution of the vertical normal stresses through the depth of the core is linear. Hence, the vertical stress distribution and the displacements fields of the core are derived through the closed form solution of Equations (8) and (9). The compatibility conditions of the vertical displacement at the upper and the lower core-face interfaces and the compatibility condition of the longitudinal displacement at the upper interface are:

$$\sigma_{zzc}(x, z_c) = -E_{c1}(x, c)w_t(x) + E_{c1}(x, c)w_b(x) + \left(-z_c + \frac{E_{c1}(x, c)}{E_{c2}(x, c)}\right)\left(\frac{d}{dx}\tau(x)\right)$$
$$- \frac{1}{2}E_{c1}(x, c)\alpha_c T_{c_t}(x)c - \frac{1}{2}E_{c1}(x, c)c\alpha_c T_{c_b}(x); \quad (12)$$

$$w_c(x, z_c) = \left(\alpha_c z_c - \frac{1}{2}\frac{E_{c1}(x,c)\alpha_c c}{E_{c1}(x,z_c)} - \frac{1}{2}\frac{\alpha_c z_c{}^2}{c}\right)T_{c_t}(x) + \left(-\frac{1}{2}\frac{E_{c1}(x,c)\alpha_c c}{E_{c1}(x,z_c)} + \frac{1}{2}\frac{\alpha_c z_c{}^2}{c}\right)T_{c_b}(x)$$
$$+ \left(-\frac{E_{c1}(x,c)}{E_{c1}(x,z_c)} + 1\right)w_t(x) + \frac{E_{c1}(x,c)w_b(x)}{E_{c1}(x,z_c)} + \left(-\frac{1}{E_{c2}(x,z_c)} + \frac{E_{c1}(x,c)}{E_{c1}(x,z_c)E_{c2}(x,c)}\right)\left(\frac{d}{dx}\tau(x)\right);$$
$$\tag{13}$$

$$u_c(x, z_c) = \left(\frac{1}{2}\frac{c\alpha_c\left(\frac{\partial}{\partial x}E_{c1}(x,c)\right)}{E_{c1z}(x,z_c)} - \frac{1}{2}\frac{E_{c1}(x,c)c\alpha_c\left(\frac{\partial}{\partial x}E_{c1z}(x,z_c)\right)}{E_{c1z}(x,z_c)^2}\right)T_{c_t}(x)$$

$$+ \left(\frac{1}{2}\frac{c\alpha_c\left(\frac{\partial}{\partial x}E_{c1}(x,c)\right)}{E_{c1z}(x,z_c)} - \frac{1}{2}\frac{E_{c1}(x,c)c\alpha_c\left(\frac{\partial}{\partial x}E_{c1z}(x,z_c)\right)}{E_{c1z}(x,z_c)^2}\right)T_{c_b}(x)$$

$$+ \left(\frac{\frac{\partial}{\partial x}E_{c1}(x,c)}{E_{c1z}(x,z_c)} - \frac{E_{c1}(x,c)\left(\frac{\partial}{\partial x}E_{c1z}(x,z_c)\right)}{E_{c1z}(x,z_c)^2}\right)w_t(x)$$

$$+ \left(-\frac{\frac{\partial}{\partial x}E_{c1}(x,c)}{E_{c1z}(x,z_c)} - \frac{E_{c1}(x,c)\left(\frac{\partial}{\partial x}E_{c1z}(x,z_c)\right)}{E_{c1z}(x,z_c)^2}\right)w_b(x)$$

$$+ \left(\frac{1}{2}\frac{E_{c1}(x,c)c\alpha_c}{E_{c1z}(x,z_c)} - \frac{1}{6}\frac{\alpha_c z_c{}^3}{c}\right)\left(\frac{d}{dx}T_{c_b}(x)\right)$$

$$+ \left(\frac{1}{2}\frac{E_{c1}(x,c)c\alpha_c}{E_{c1z}(x,z_c)} + \frac{1}{6}\frac{\alpha_c z_c{}^3}{c} - \frac{1}{2}\alpha_c z_c{}^2\right)\left(\frac{d}{dx}T_{c_t}(x)\right) + u_{ot}(x)$$

$$+ \left(\frac{E_{c1}(x,c)}{E_{c1z}(x,z_c)} - z_c - \frac{1}{2}d_t\right)\left(\frac{d}{dx}w_t(x)\right) - \frac{E_{c1}(x,c)\left(\frac{d}{dx}w_b(x)\right)}{E_{c1z}(x,z_c)} + \frac{\tau(x)}{G_{c1}(x,z_c)}$$

$$+ \left(-\frac{\frac{\partial}{\partial x}E_{c2z}(x,z_c)}{E_{c2z}(x,z_c)^2} + \frac{E_{c1}(x,c)\left(\frac{\partial}{\partial x}E_{c2}(x,c)\right)}{E_{c2}(x,c)^2 E_{c1z}(x,z_c)}\right.$$

$$\left.+ \frac{E_{c1}(x,c)\left(\frac{\partial}{\partial x}E_{c1z}(x,z_c)\right)}{E_{c2}(x,c)E_{c1z}(x,z_c)^2} - \frac{\frac{\partial}{\partial x}E_{c1}(x,c)}{E_{c2}(x,c)E_{c1z}(x,z_c)}\right)\left(\frac{d}{dx}\tau(x)\right)$$

$$+ \left(-\frac{E_{c1}(x,c)}{E_{c2}(x,c)E_{c1z}(x,z_c)} + \frac{1}{E_{c2z}(x,z_c)}\right)\left(\frac{d^2}{dx^2}\tau(x)\right), \quad \tag{14}$$

where

$$E_{c1}(x,c) = \frac{1}{\int\limits_0^c \frac{1}{E_c(T_c(x,z_c))}dz_c}, \qquad E_{c2}(x,c) = \frac{1}{\int\limits_0^c \frac{z_c}{E_c(T_c(x,z_c))}dz_c},$$

$$E_{c1}(x,z_c) = \frac{1}{\int\limits_0^{z_c} \frac{1}{E_c(T_c(x,z_1))}dz_1}, \qquad E_{c2}(x,z_c) = \frac{1}{\int\limits_0^{z_c} \frac{z_c}{E_c(T_c(x,z_1))}dz_1},$$

$$E_{c1z}(x,z_c) = \frac{1}{\int\limits_0^{z_c}\int\limits_0^{z_2} \frac{1}{E_c(T_c(x,z_1))}dz_1 dz_2}, \qquad E_{c2z}(x,z_c) = \frac{1}{\int\limits_0^{z_c}\int\limits_0^{z_2} \frac{z_1}{E_c(T_c(x,z_1))}dz_1 dz_2},$$

$$G_{c1}(x,z_c) = \frac{1}{\int\limits_0^{z_c} \frac{1}{G_c(T_c(x,z_c))}dz_c}. \tag{15}$$

Hence, the interfacial vertical normal stresses at the upper and lower face-core interfaces (see Equations (2) and (4)) equal:

$$\sigma_{zzt}(x) = -E_{c1}(x,c)w_t(x) + E_{c1}(x,c)w_b(x) + \frac{E_{c1}(x,c)\left(\frac{d}{dx}\tau(x)\right)}{E_{c2}(x,c)} \tag{16}$$

$$-\frac{1}{2}E_{c1}(x,c)\alpha_c T_{c_t}(x)c - \frac{1}{2}E_{c1}(x,c)c\alpha_c T_{c_b}(x)$$

$$\sigma_{zzb}(x) = -E_{c1}(x,c)w_t(x) + E_{c1}(x,c)w_b(x) + \left(-c + \frac{E_{c1}(x,c)}{E_{c2}(x,c)}\right)\left(\frac{d}{dx}\tau(x)\right)$$

$$-\frac{1}{2}E_{c1}(x,c)\alpha_c T_{c_t}(x)c - \frac{1}{2}E_{c1}(x,c)c\alpha_c T_{c_b}(x).$$

The additional governing equation is the one that corresponds to the compatibility requirement in the longitudinal direction at the lower face-core interface, and it reads:

$$\left(-\frac{E_{c1}(x,c)}{E_{c1z}(x,z_c)} - \frac{1}{2}d_b\right)\left(\frac{d}{dx}w_b(x)\right) + \left(\frac{1}{2}\frac{c\alpha_c\left(\frac{\partial}{\partial x}E_{c1}(x,c)\right)}{E_{c1z}(x,z_c)} - \frac{1}{2}\frac{E_{c1}(x,c)c\alpha_c\left(\frac{\partial}{\partial x}E_{c1z}(x,z_c)\right)}{E_{c1z}(x,z_c)^2}\right)T_{c_t}(x)$$

$$+\left(\frac{1}{2}\frac{c\alpha_c\left(\frac{\partial}{\partial x}E_{c1}(x,c)\right)}{E_{c1z}(x,z_c)} - \frac{1}{2}\frac{E_{c1}(x,c)c\alpha_c\left(\frac{\partial}{\partial x}E_{c1z}(x,z_c)\right)}{E_{c1z}(x,z_c)^2}\right)T_{c_b}(x)$$

$$+\left(\frac{\frac{\partial}{\partial x}E_{c1}(x,c)}{E_{c1z}(x,z_c)} - \frac{E_{c1}(x,c)\left(\frac{\partial}{\partial x}E_{c1z}(x,z_c)\right)}{E_{c1z}(x,z_c)^2}\right)w_t(x)$$

$$+\left(-\frac{\frac{\partial}{\partial x}E_{c1}(x,c)}{E_{c1z}(x,z_c)}+\frac{E_{c1}(x,c)\left(\frac{\partial}{\partial x}E_{c1z}(x,z_c)\right)}{E_{c1z}(x,z_c)^2}\right)w_b(x)$$

$$+\left(\frac{1}{2}\frac{E_{c1}(x,c)c\alpha_c}{E_{c1z}(x,z_c)}-\frac{1}{6}\frac{\alpha_c z_c^3}{c}\right)\left(\frac{d}{dx}T_{c_b}(x)\right)+\left(\frac{1}{2}\frac{E_{c1}(x,c)c\alpha_c}{E_{c1z}(x,z_c)}+\frac{1}{6}\frac{\alpha_c z_c^3}{c}-\frac{1}{2}\alpha_c z_c^2\right)\left(\frac{d}{dx}T_{c_t}(x)\right)$$

$$+u_{ot}(x)+\left(\frac{E_{c1}(x,c)}{E_{c1z}(x,z_c)}-z_c-\frac{1}{2}d_t\right)\left(\frac{d}{dx}w_t(x)\right)-u_{ob}(x)+\frac{\tau(x)}{G_{c1}(x,z_c)}$$

$$+\left(-\frac{\frac{\partial}{\partial x}E_{c2z}(x,z_c)}{E_{c2z}(x,z_c)^2}+\frac{E_{c1}(x,c)\left(\frac{\partial}{\partial x}E_{c2}(x,c)\right)}{E_{c2}(x,c)^2 E_{c1z}(x,z_c)}+\frac{E_{c1}(x,c)\left(\frac{\partial}{\partial x}E_{c1z}(x,z_c)\right)}{E_{c2}(x,c)E_{c1z}(x,z_c)^2}\right.$$

$$\left.-\frac{\frac{\partial}{\partial x}E_{c1}(x,c)}{E_{c2}(x,c)E_{c1z}(x,z_c)}\right)\left(\frac{d}{dx}\tau(x)\right)$$

$$+\left(-\frac{E_{c1}(x,c)}{E_{c2}(x,c)E_{c1z}(x,z_c)}+\frac{1}{E_{c2z}(x,z_c)}\right)\left(\frac{d^2}{dx^2}\tau(x)\right)=0,\quad(17)$$

where

$$E_{c1z}(x,z_c)=\frac{1}{\int_0^c\int_0^{z_2}\frac{1}{E_c(T_c(x,z_1))}dz_1 dz_2},\qquad E_{c2z}(x,c)=\frac{1}{\int_0^c\int_0^{z_2}\frac{z_1}{E_c(T_c(x,z_1))}dz_1 dz_2},$$

$$G_{c1}(x,c)=\frac{1}{\int_0^c\frac{1}{G_c(T_c(x,z_c))}dz_c}.\qquad(18)$$

Hence, the thermomechanical nonlinear governing set of equations are derived by substitution of the force-displacements equations, Equations (6) to (9), into the four field equations, Equations (1) to (4), and the fifth equation is the compatibility condition expressed by Equation (17). This set of equations corresponds to five unknowns: the longitudinal and vertical displacement of the upper and the lower face sheets and the shear stress in the core.

The boundary and the continuity conditions are based on fourteen unknown functions and are not presented herein for brevity. For details see [Frostig 1997].

3. Buckling analysis

The buckling analysis is based on the perturbation approach in which the nonlinear governing equations are linearized [Simitses 1976]. The linearized governing equations for the prebuckling and buckling stages appear in [Frostig and Thomsen 2007b] for a sandwich panel with *temperature-independent* mechanical properties and a uniform temperature field through the length and through the height of the panel.

For the case of a sandwich panel with *temperature-dependent* properties subjected to a longitudinally and vertically uniform temperature field, the critical temperatures (the wrinkling and global buckling modes) have been derived assuming the prebuckling case following the perturbation procedure described in [Frostig and Baruch 1993] and [Frostig and Thomsen 2007b]. In this procedure the thermal strain of the core in the vertical direction is ignored, which yields a membrane thermal prebuckling stage where the face sheets are subjected to in-plane stress resultants only due to the in-plane constraints imposed at the edges of the face sheets. The critical temperatures are determined through the closed-form solution of the buckling equations of a simply-supported panel that yields a set of algebraic equations. For this case it, is assumed that the two face sheets are of identical geometry and have temperature-independent mechanical properties that are uniform through the length of the panel. In addition, it is assumed that the core has uniform mechanical properties that depend on the temperature.

For the wrinkling mode where the two face sheets move in opposite directions (symmetric mode with respect to mid-height), the solution reads:

$$-\frac{2b_w E_c(T_{cr,wr})L^4 + EI_t m^4\pi^4 c}{L^2 m^2\pi^2 c} = -EA_t\alpha_t T_{cr,wr}, \tag{19}$$

where the critical half wave number m equals:

$$m = \text{integer}\left(\frac{2^{(1/4)}(b_w E_c(T_{cr,wr})EI_t^3 c^3)^{(1/4)}L}{EI_t\pi c}\right), \tag{20}$$

and where L is the length of the panel and $T_{cr,wr}$ is the critical temperature that yields a wrinkling buckling mode.

For the global buckling mode, where the two face sheets move in the same direction and with the same displacement value (a symmetric mode), the closed-form solution reads:

$$\begin{aligned}
m^2\pi^2\Big(c^3 EA_t EI_t G_c(T_{cr,gl})\pi^4 m^4 + 6b_w EA_t E_c(T_{cr,gl})G_c(T_{cr,gl})L^4 c^2 \\
+12cL^4 b_w EA_t d_t E_c(T_{cr,gl})G_c(T_{cr,gl}) + 12c EA_t EI_t E_c(T_{cr,gl})\pi^2 m^2 L^2 \\
+24b_w EI_t E_c(T_{cr,gl})G_c(T_{cr,gl})L^4 \\
+6L^4 b_w EA_t d_t^2 E_c(T_{cr,gl})G_c(T_{cr,gl})\Big)\Big/\Big(L^2\big(12m^2\pi^2 L^2 c EA_t E_c(T_{cr,gl}) \\
+m^4\pi^4 c^3 EA_t G_c(T_{cr,gl}) + 24b_w L^4 E_c(T_{cr,gl})G_c(T_{cr,gl})\big)\Big) = EA_t\alpha_t T_{cr,gl}, \tag{21}
\end{aligned}$$

where m is the critical half wave number and $T_{cr,gl}$ is the critical temperature, which corresponds to $m = 1$.

It should be noticed that, as a result of the temperature dependency, the critical temperatures can be evaluated only through the solution of the nonlinear algebraic equations, while for the case where the properties are temperature-independent, the critical values can be derived in terms of closed-form expressions [Frostig and Thomsen 2007b].

A numerical study, presented in the forthcoming section, has been conducted in order to determine the effects of the temperature-dependent properties of the core on the critical temperatures for the case of Rohacell WF and Divinycell P- and HP-types of foams. Figure 2 describes the nondimensional elastic
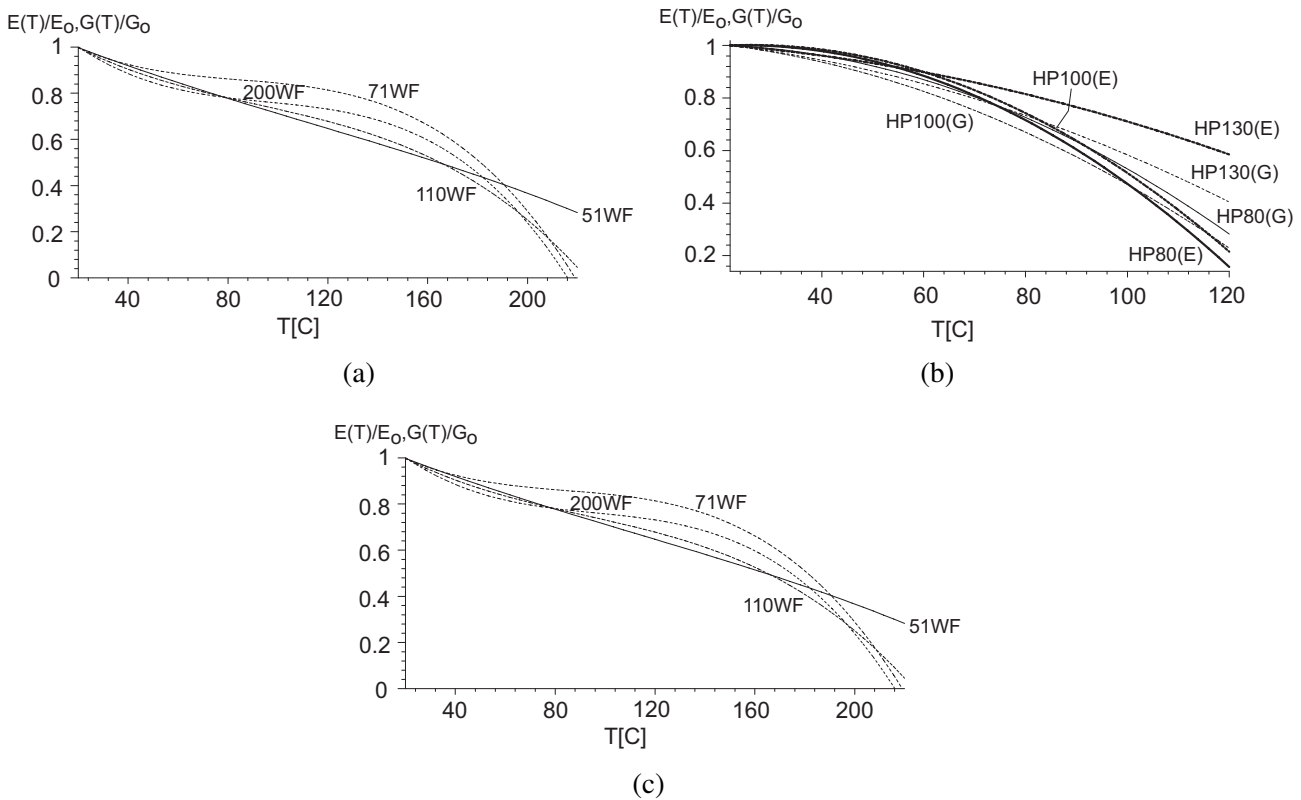
Figure 2. Normalized temperature-dependent elastic and shear moduli of various polymer foam cores: (a) Rohacell WF foam, (b) Divinycell HP foam, (c) Divinycell P foam. Legend: (E) – modulus of elasticity (thick lines), (G) – Shear modulus (dashed thin lines).

and shear moduli of these materials as functions of temperature. The curve fitted data appearing in Figure 2 are based on the data that appear in [Rohacell 2004] and [Diab Group 2005]. For the case of the Rohacell foam it is assumed that the degradation of the elastic and the shear moduli is the same (see Figure 2a). For the two Divinycell foams the degradation is slightly different for the elastic and the shear moduli, and it is denoted by the letters E and G in Figures 2b and Figure 2c.

The critical temperatures have been determined for foams with temperature independent and dependent mechanical properties for comparison (see Tables 1 and 2 for the different core materials). A sandwich beam with length of 1000 mm, width 30 mm, two aluminum face sheets of 0.5 mm thickness, CTE of 1e-5, modulus of elasticity of 69130 MPa, and a core height of 25 mm is investigated. The results in Tables 1 and 2 include the critical temperature for the wrinkling and the global buckling modes, as well as the value of the mechanical properties when the critical temperature values are reached.

The results for the WF foam made by Rohacell (see Table 1), reveal that when the E- and G-moduli at room temperature are considered and denoted as temperature independent properties (TI), the critical temperatures are much above the range of operating temperatures for this material. However, when the

Foam	Buckling-Properties Types	T_{cr}^{o} [C]*	Mode Number (m)	$E_c(T_{cr})$ [MPa]	$G_c(T_{cr})$ [MPa]
51WF	Wr-TI**	384.7	97	70.5	22.1
	Wr-TD	201.7	70	21.1	6.6
	Gl-TI	136.2	1	70.5	22.1
	Gl-TD	122.5	1	44.0	13.8
71WF	Wr-TI	457.5	105	100.3	38.8
	Wr-TD	188.5	68	18.4	7.1
	Gl-TI	145.7	1	100.3	38.8
	Gl-TD	139.2	1	72.3	27.9
110WF	Wr-TI	601.5	121	169.5	63.3
	Wr-TD	194.7	69	19.7	7.3
	Gl-TI	151.2	1	169.5	63.3
	Gl-TD	143.1	1	95.5	35.6
200WF	Wr-TI	719.8	132	237.6	132.7
	Wr-TD	191.7	68	19.05	10.6
	Gl-TI	156.0	1	237.6	132.7
	Gl-TD	152.1	1	139.3	77.8

Table 1. Critical temperatures of Rohacell WF foam. Legend: Wr – wrinkling mode; Gl – global mode; TI – temperature-independent properties; TD – temperature-dependent properties. * With respect to an unheated panel at room temperature (20° C). ** Modulus of elasticity and shear modulus at room temperature.

temperature dependence of the E- and G-moduli of the core is included in the analyses (denoted by TD for *temperature-dependent* in Table 1), the predicted critical temperatures reach the upper range of the operating temperature of the foam, which is associated with very low values of E and G. Notice that for the case of wrinkling buckling mode, the half wave number is significantly reduced compared to the TI case. For most of the cases, the critical buckling mode is associated with global buckling.

Considering the results obtained for the Divinycell foams (see Table 2), similar trends are observed. The differences in the critical temperatures between the TI and the TD cases are significant, especially when the wrinkling buckling mode occurs. The differences between the critical values for the case of global buckling are smaller, and they are almost in the same range. Again, for the case of foams with TD properties, the critical values are predicted to reach the upper range of operating temperature, which is associated with very small values of the core E- and G-moduli. The critical values for the HP foams are higher then those of the P-type foams. For the case of the P foams, the critical temperatures for wrinkling and global buckling are almost identical, and they are in the upper range of the operating temperature for this material. In conclusion, the temperature dependency of polymer foam core materials significantly affects the buckling behavior of sandwich panels with a compliant core. In particular, the

Foam	Buckling-Properties Types	$T_{cr}{}^o$ [C]*	Mode Number (m)	$E_c(T_{cr})$ [MPa]	$G_c(T_{cr})$ [MPa]
HP80	Wr-TI**	356.4	93	63.6	28.4
	Wr-TD	102.2	50	5.4	2.4
	Gl-TI	140.1	1	63.6	28.4
	Gl-TD	95.0	1	13.8	6.2
HP100	Wr-TI	390.8	97	77.0	36.9
	Wr-TD	106.1	51	5.8	2.8
	Gl-TI	144.2	1	77.0	36.9
	Gl-TD	99.8	1	14.6	7.0
HP130	Wr-TI	462.9	106	105.6	44.9
	Wr-TD	155.2	61	12.5	5.3
	Gl-TI	147.1	1	105.6	44.9
	Gl-TD	128.1	1	39.7	16.9
P500	Wr-TI	371.8	95	72.8	38.9
	Wr-TD	71.9	42	2.7	1.4
	Gl-TI	144.4	1	72.8	38.9
	Gl-TD	70.4	1	6.2	3.3
P600	Wr-TI	455.6	105	106.4	49.7
	Wr-TD	68.5	41	2.4	1.1
	Gl-TI	147.9	1	106.4	49.7
	Gl-TD	67.4	1	6.6	3.1
P800	Wr-TI	550.2	116	153.8	68.6
	Wr-TD	69.0	41	2.5	1.1
	Gl-TI	151.2	1	153.8	68.6
	Gl-TD	68.1	1	7.1	3.1

Table 2. Critical temperatures of Divinycell HP and P foams. Legend: Wr – wrinkling mode; Gl – global mode; TI – temperature-independent properties; TD – temperature-dependent properties. *With respect to an unheated panel room temperature (22° C). **Modulus of elasticity and shear modulus at room temperature.

critical temperatures predicted when the temperature dependency is accounted for are always significantly lower than those predicted when the core properties are assumed to be temperature independent, with properties corresponding to room temperature. The reduction is most significant when wrinkling type of buckling occurs, whereas the reduction is less severe for the global buckling mode.

Next, the postbuckling behavior is investigated numerically through the solution of the full nonlinear governing equations under the assumption that a uniform temperature field is applied.

4. Nonlinear governing equations — uniform temperature field

The nonlinear response, for the case of a uniform distribution of the temperature field along the panel length and a linear gradient through its depth (see Figure 1a) is determined. The formulation is based on a set of first-order ordinary differential equations (ODEs) instead of the set of five governing ODEs (see Equations (1) to (4) along with Equations (6) to (9) and Equation (16)). The first-order set consists of fourteen ODEs that are consistent with the fourteen boundary conditions [Frostig 1997]. The transformation of the original ODEs into the first-order has been conducted using well known procedures [Stoer and Bulirsch 1980]. Thus, the nonlinear thermal governing equations read:

(i) For the upper and the lower face sheets ($j = t, b$):

$$\frac{d}{dx} N_{xxj}(x) = (-1)^k \tau(x) b_w - n_j \quad (k = 1 \text{ with } j = t \text{ and } k = 0 \text{ with } j = b),$$

$$\frac{d}{dx} u_{oj}(x) = -\frac{-N_{xxj}(x) - EA_j(x)\alpha_j\left(\frac{1}{2}T_{j_j} + \frac{1}{2}T_{j_b}\right)}{EA_j(x)} - \frac{1}{2} Dw_j(x)^2,$$

$$\frac{d}{dx} V_{xzj}(x) = AA_j b_w - q_j, \quad \text{where } AA_t = -\sigma_{zzt}(x), \ AA_b = \sigma_{zzb}(x),$$

$$\frac{d}{dx} M_{xxj}(x) = V_{xzj}(x) - \frac{1}{2} b_w d_j \tau(x) - N_{xxt}(x)\left(\frac{d}{dx} w_j(x)\right) + m_j(x),$$

$$\frac{d}{dx} w_j(x) = Dw_j(x),$$

$$\frac{d}{dx} Dw_j(x) = -\frac{M_{xxj}(x)}{EI_j} - \frac{\alpha_j(T_{j_b} - T_{j_j})}{d_j}.$$

(ii) For the core:

$$\frac{d}{dx}\tau(x) = D\tau(x)E_{ca} + \frac{-\int_0^c \alpha_c z_c - \frac{1}{2}\frac{E_{c1}(c)\alpha_c c}{E_{c1}(z_c)} - \frac{1}{2}\frac{\alpha_c z_c^2}{c} dz_c T_{c_t} - \int_0^c -\frac{1}{2}\frac{E_{c1}(c)\alpha_c c}{E_{c1}(z_c)} + \frac{1}{2}\frac{\alpha_c z_c^2}{c} dz_c T_{c_b}}{\int_0^c -\frac{1}{E_{c2}(z_c)} + \frac{E_{c1}(c)}{E_{c1}(z_c)E_{c2}(c)} dz_c}, \quad (22)$$

$$\frac{d}{dx} D\tau(x) = \frac{-\frac{\tau(x)}{G_{c1}(c)} + \left(c + \frac{1}{2}d_t - \frac{E_{c1}(c)}{E_{c1z}(c)}\right)Dw_t(x) + \left(\frac{1}{2}d_b + \frac{E_{c1}(c)}{E_{c1z}(c)}\right)Dw_b(x) + u_{ob}(x) - u_{ot}(x)}{\frac{E_{ca}}{E_{c2z}(c)} - \frac{E_{c1}(c)E_{ca}}{E_{c2}(c)E_{c1z}(c)}}, \quad (23)$$

where

$$E_{ca} = \int_0^c \frac{E_c(T_c(x, z_c))}{c} dz_c. \quad (24)$$

The nonlinear response is determined numerically using trapezoid or mid-point methods with Richardson extrapolation or deferred corrections (see [Ascher and Petzold 1998]), as implemented in Maple.
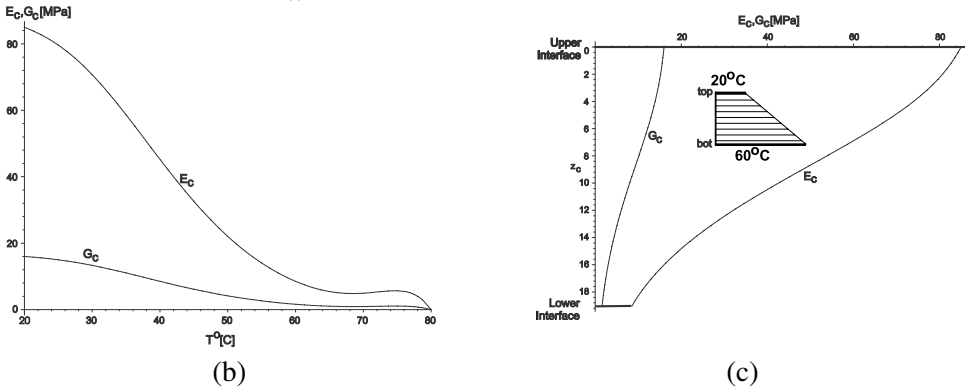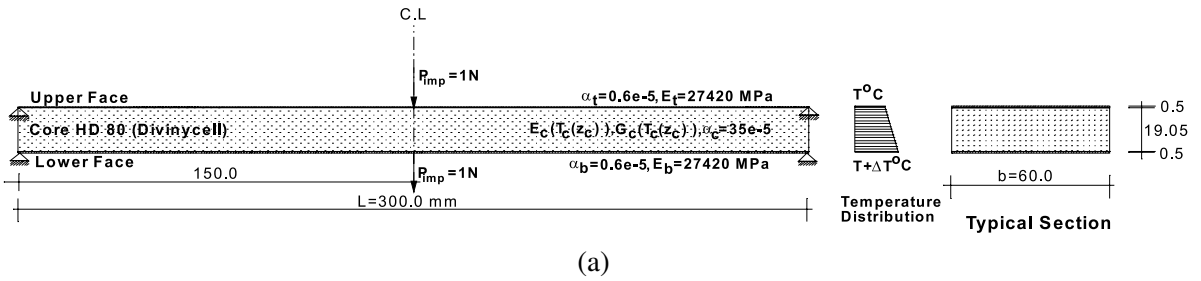
Figure 3. Geometry and temperature-dependent properties of the core and its distribution: (a) geometry and mechanical properties; (b) temperature dependence of elastic and shear moduli of core; (c) distribution of moduli through depth of core for a thermal gradient of 40° C

5. Nonlinear thermomechanical response — numerical study

The numerical study consists of two parts. In the first part the postbuckling response of sandwich panels due to thermally induced deformation associated with a thermal gradient through the core depth is investigated. The second part of the study investigates the nonlinear interaction response when a sandwich panel is loaded simultaneously by an external mechanical load and thermal load with a gradient through the core depth.

5.1. *Postbuckling response.* The postbuckling response plays a major role in the safe design of sandwich panels. It defines whether the buckling loads may be exceeded based on the stability of the sandwich assembly. In general, the postbuckling response can be characterized as belonging to one of the following types: beam, plate or shell form. The plate type response is considered as stable, since any additional deformation is associated by a load increase, while the beam and shell types are unstable since any additional displacement is associated with an unchanged or a reduced load. The postbuckling response of a sandwich panel may fall into all three categories (see [Sokolinsky and Frostig 2000]) depending on the geometry, loading scheme, mechanical properties and boundary conditions.

The study investigates the effects of a thermal gradient through the core depth on the postbuckling response, assuming TD and TI elastic properties. It is assumed that the distribution of the temperatures

through the thickness of each face sheet is uniform, and the difference in temperatures, ΔT, between the lower and upper face sheets is changing from 0° to 40° C (see Figure 3a, where $T_b = T_t + \Delta T$). The temperature at the upper face sheet is increased from 20° C until the lower face sheet reaches a temperature of 79° C.

The nonlinear response examines a typical sandwich panel with face sheets made of Kevlar composite faces and a HD 80 foam core from DIAB. The geometry of the panel and the temperature distribution through the depth of the panel appear in Figure 3a. The panel is pin supported at the edges of the face sheets, which are restrained longitudinally. The temperature distribution is uniform through the length of the panel. The moduli of the core are temperature-dependent, and the $E_c(T)$, $G_c(T)$ versus temperature (T) plots appear in Figure 3b, in the temperature range 20–80° C, based on the data in [Diab Group 2003].

The fitted curve moduli are based on data from [Diab Group 2003] and Figure 3b. The variations of the E- and G-moduli through the depth of the core for a thermal gradient of $\Delta T = 40^o$ C ($T_t = 20^o$ C and $T_b = 40^o$ C) are significant (see Figure 3c).

A global buckling mode has been detected for this case, within the range of the operating temperatures of the foam, and in order to initiate a global buckling mode an imperfection in the form of two very small concentrated loads of 1N have been applied in the same direction to the two face sheets at mid-span, see Figure 3a.

The results corresponding to global buckling of the sandwich panel heated by a uniform temperature field in the longitudinal and the vertical directions appear in Figure 4. The results along the half length of the panel are presented at five different temperature levels. The vertical displacements appear in Figure 4a and reveal that the faces move in opposite directions (upwards and downwards) in the vicinity of the supports as a result of the expansion of the core in the vertical direction. The displacements at mid-span at a temperature of 78° C reach very large values, as compared to those values reached at lower temperatures, due to the loss of the rigidity of the core at this elevated temperature level. The bending moments that are quite small (see Figure 4b) yield localized effects in the vicinity of the support as a result of the inability of the core to expand vertically due to the thermal strains. In addition, bending moments are induced around mid-span due to the small imperfection loads. The in-plane stress results, which are mainly caused by the longitudinal restraints of the supports, appear in Figure 4c. These forces are not constant, due to the existence of shear stresses at the face–core interfaces. Finally, the vertical interfacial stresses appear in Figure 4d, for which it is observed that large localized effects occur in the vicinity of the supports as a result of restraining the expansion of the core in the vertical direction. Small vertical normal stresses occur around mid-span due to the imperfection loads.

The equilibrium curves appear for all temperature gradients in Figure 5, which also includes the cases of TD and TI core properties. The equilibrium curves have been determined using a parametric continuation procedure up to the temperature level when either the solution does not converge, or the upper limit of the range of the operating temperatures (20 to 80° C) has been reached. Hence, there is no case where the E- and G-moduli reaches the value of zero within the core depth. The temperature versus the maximum vertical displacements at the upper and the lower face sheets, assuming a core either with or without temperature dependent properties, appears in Figure 5a. The temperature independent core with room-temperature properties yields a linear curve, almost constant for all gradients, which indicates
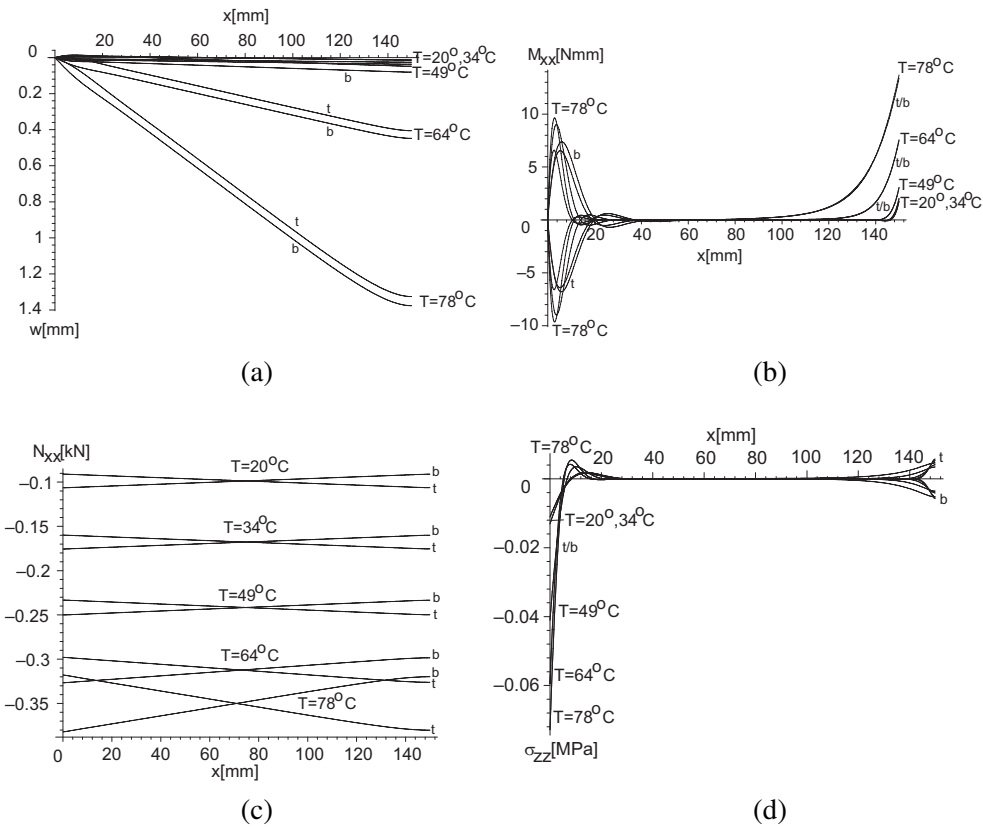
Figure 4. Postbuckling results along the length of a restrained sandwich panel with a zero thermal gradient at various temperatures: (a) vertical displacements, (b) bending moments, (c) in-plane stress resultants, (d) interfacial vertical normal stresses at interfaces. Legend: —— t upper face/ interface; - - - - b lower face/ interface.

that the panel does not buckle within this range of temperatures (denoted by TI). The results reveal also that in the case of *zero* thermal gradient (a uniform distribution in the vertical direction) the behavior is stable up to 77° C, and beyond this temperature the sandwich panel collapses as a result of the very low rigidity of the core. For the case of a thermal gradient of $\Delta T = 10^o$ C, the equilibrium curves exhibit a nonlinear stable response. A nonlinear behavior with smaller deformations occurs for all gradients. The temperature versus the extreme compressive values of the vertical interfacial stresses appear in Figure 5b for cores with and without temperature dependent properties. For the temperature independent case at $\Delta T = 0^o$ C (uniform) and $\Delta T = 40^o$ C, linear responses occur, that is, the peak vertical interfacial stresses (compressive) increase with increasing temperature as a result of the large expansion of the core in the vertical direction (restrained by the fixity of the supports in the vertical direction). The curves obtained for the temperature dependent cores exhibit a nonlinear pattern where the maximum compressive stress occurs around 30° C for all cases. The maximum compressive stresses occur at the support, as a result of the restraint of the expansion of the core in the vertical direction, along with the relatively undegraded core properties (around 30° C) and the minor influence of the global buckling mode.
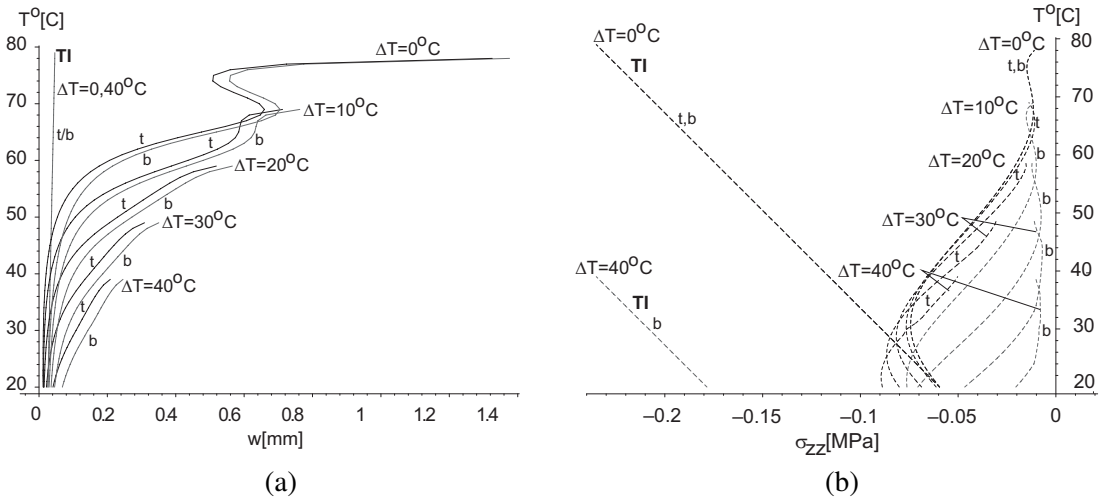
Figure 5. Temperature equilibrium curves of maximum values for a restrained sandwich panel subjected to various thermal gradients: (a) maximum vertical displacements of face sheets, (b) maximum compressive interfacial vertical normal stresses at interfaces. Legend: —— t upper face or interface; - - - - b lower face or interface.

5.2. *Interaction of mechanical loads and thermally induced deformations.* The nonlinear thermomechanical response of restrained and unrestrained sandwich panels loaded by a prescribed mechanical load and a changing thermal gradient is studied. In addition, the study examines the effects on the response of elevated temperature in the imposed thermal gradient when applied either to the tensile (Ten) face sheet or to the compressive (Com) face sheet. Notice that a linear response occurs when the loads are applied separately as well as when the two loads are applied simultaneously, and the core properties are TI.

The investigated sandwich panel consists of two face sheets made of Kevlar composite laminates and a Divinycell core made of HD-80 foam. The layout, dimensions, mechanical properties and loadings appear in Figure 6a. The panel is loaded in a three-points bending scheme, where the load is applied at the upper face sheet and the panel is supported only at its lower face sheet, while the edges of its core and upper face are free of force tractions. The fixity of the panel is achieved by imposing longitudinal restraints on the edges of the face sheets (see dotted supports in Figure 6a). The thermal gradient is imposed only within the core with two different variants (see temperature distribution in Figure 6a). In the first variant the highest temperature is imposed at the lower tensile face sheet (Ten), while in the second variant the highest temperature is imposed at the upper compressed face sheet (Com). The temperature-dependent properties of the core are the same as in the previous case. See Figure 3b and Figure 3c for temperature dependency of the E- and G-moduli and their distribution through the core depth for a gradient of 40° C. The solution procedure uses a parametric continuation approach with the temperature T as the parameter. The procedure halts when the solution does not converge or when it violates the assumption of large displacements and moderate rotations, which in this study occurs when the maximum displacement approaches a value of $L/10$. The results are also limited to a temperature of 79° C, which represents the upper limit of the range of operating temperatures for this particular temperature-dependent DIAB core (HD80).

(a)

(b)
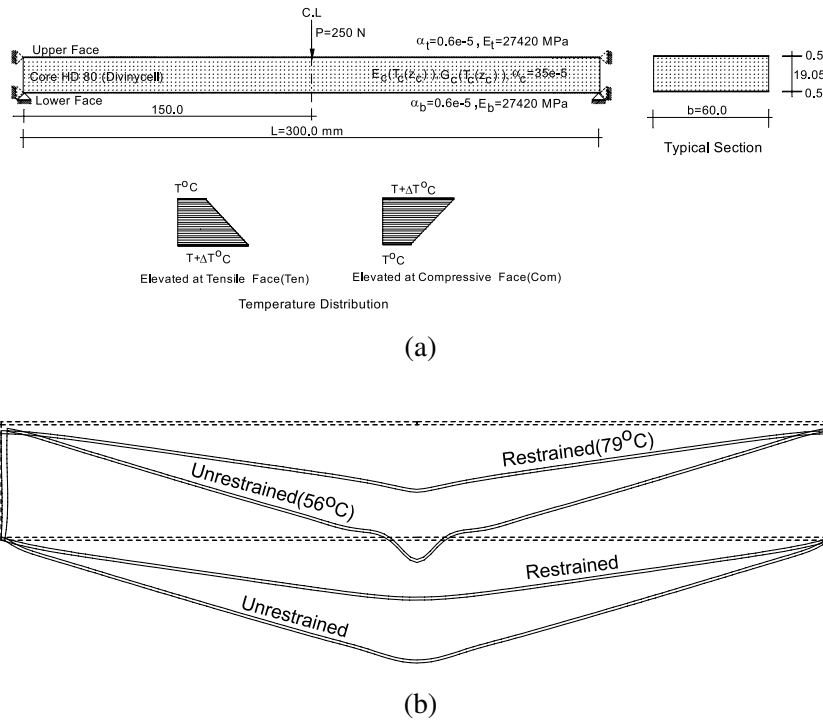
Figure 6. Geometry and deformed shapes of sandwich panel loaded by a mechanical load and thermally induced deformations with a zero thermal gradient: (a) geometry of unrestrained and restrained panels; (b) deformed shape of an unrestrained at $T = 56^o$ C and a restrained panel at $T = 79^o$ C.

The deformed shapes of a sandwich panel which is considered to be either longitudinally restrained or nonrestrained at uniform (zero gradient through the core depth) temperatures of 79° C and 56° C, respectively, appear in Figure 6b. The displacements patterns for the two cases are very different, and it is seen that the displacements for the case of the unrestrained sandwich panel are much larger than for the restrained case. Notice that the indentation zone in the vicinity of the load is significant for the unrestrained deformation pattern, whereas it is almost invisible for the restrained case. If the core material properties are temperature independent and stiffness properties corresponding to room-temperature are used, the predicted deformations are much smaller (see Figure 8a). Moreover, notice that the upper face sheet in the two cases has settled as a result of the unsupported edge.

The results obtained for an unrestrained sandwich panel with a zero gradient through the core depth appear in Figure 7 at five different temperature levels; 20° C, 29° C, 39° C, 49° C and 56° C. The vertical displacements appear in Figure 7a where it is observed that an indentation occurs at mid-span for all temperature levels. Moreover, it is seen that the magnitude of the indentation increases with increasing temperature as a result of the degradation of the mechanical properties of the core. The mid-span displacement at the highest temperature (56° C) is about 2.5 times larger than the mid-span displacement corresponding to the temperature immediately below (49° C) as a result of the loss of stability (see Figure
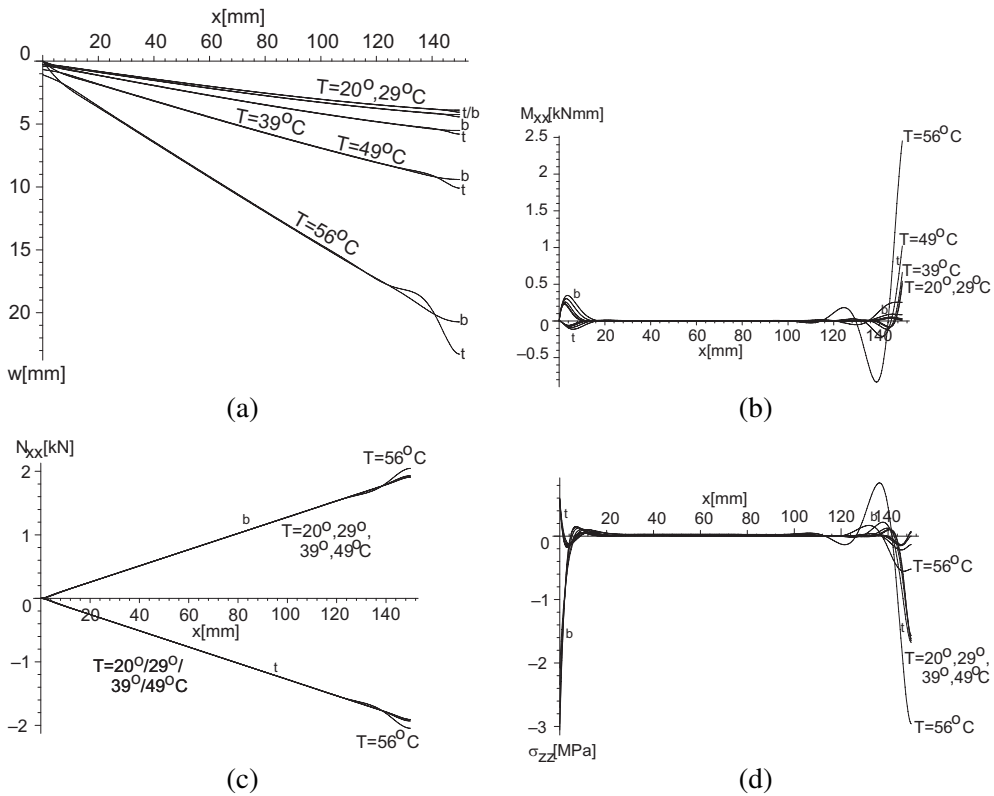
Figure 7. Nonlinear response along sandwich panel loaded simultaneously by a mechanical load and thermally induced deformations with a zero thermal gradient at various temperatures: (a) vertical displacements, (b) bending moments, (c) in-plane stress resultants, (d) interfacial vertical normal stresses at interfaces. Legend: ———— t upper face/ interface; - - - - b lower face/interface.

8a). From the bending moment diagrams (see Figure 7b) it is observed that significant bending moments are present and reach very high values at higher temperatures. The in-plane stress resultants of the face sheets appear in Figure 7c, where it is seen that fluctuations occur around mid-span only at high temperatures as a result of the large vertical displacements in this area. Notice that the in-plane stress resultants are nearly unaffected by the thermal loading, since the structure is statically determined and the overall bending moment corresponds to the three point bending load case. The mid-span fluctuations seen at the highest temperature (56° C) are due to the reduced core height, which is caused by the large vertical displacements in this vicinity (see Figure 7a). Finally, the interfacial vertical normal stresses appear in Figure 7d. From Figure 7d it is seen that very high stresses are induced in the vicinities of the support and the mid-span load at high temperatures as a result of the large displacements and the reduced rigidity of the core.

In Figures 8 and 9, the equilibrium curves are presented for both types of sandwich panels, those with and those without longitudinal restraints, and for all thermal gradients. In addition, three different
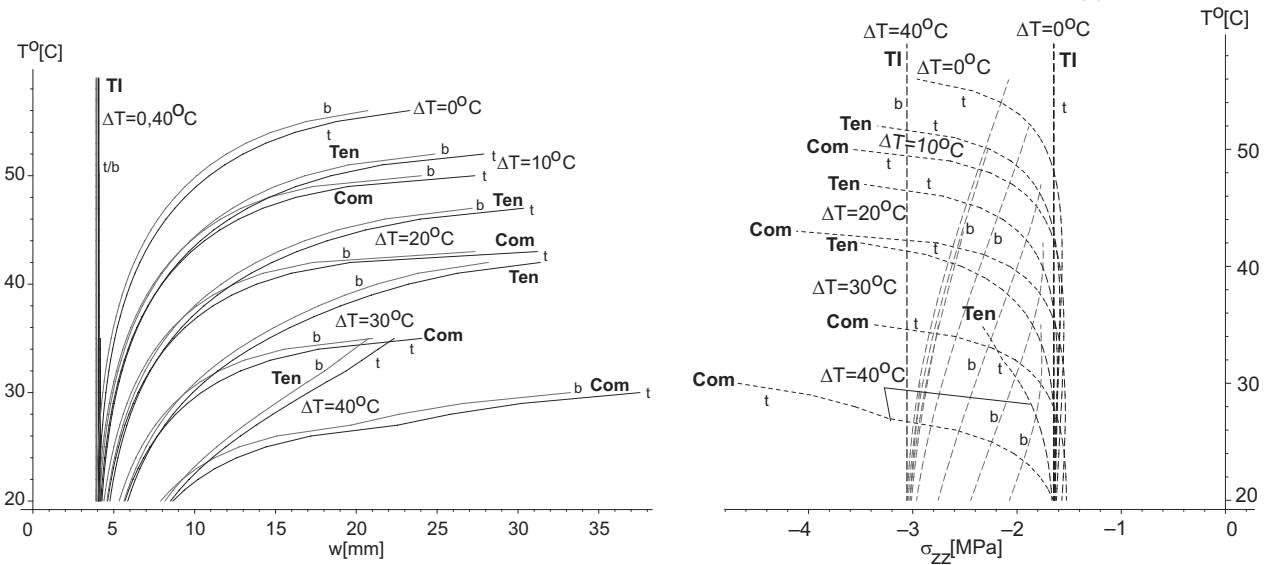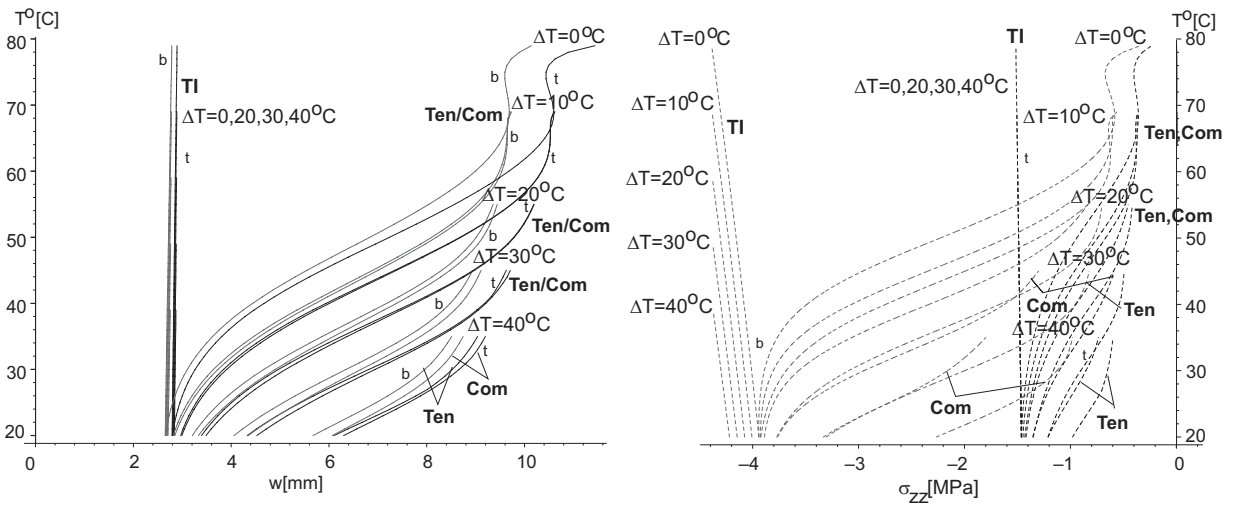
Figure 8. Temperature equilibrium curves of maximum displacements and vertical normal stresses versus temperature for an *unrestrained* sandwich panel loaded with mechanical and thermal loads simultaneously, with temperature-independent and temperature-dependent properties at various thermal gradients, and where the elevated temperatures are imposed either on the tensile (Ten) or the compressed (Com) face sheet: (a) maximum vertical displacements, (b) maximum compressive interfacial vertical normal stresses at interfaces. Legend: ──── t upper face or interface; - - - - - -b lower face or interface.

cases of thermal effects are presented. The first case represents a sandwich panel with TI core properties. The other two cases examine a core with temperature-dependent properties, one case where elevated temperatures are imposed at the tensile face sheets (Ten), and another where elevated temperatures are imposed at the face sheets loaded in compression (Com).

The equilibrium curves for the unrestrained sandwich panel appear in Figure 8. The equilibrium curves of temperature versus maximum vertical displacement appear in Figure 8a. For the TI case it is seen that a thermal gradient exerts a minor effect on the response, which remains linear through the entire range of working temperatures. For the TD cases it is seen that unstable behavior with very large displacements are seen for all thermal gradients at temperatures that lie well below the upper limit of the range of operating temperatures. For the zero thermal gradient case, denoted by $\Delta T = 0^o$ C, the instability starts around 55° C. Beyond 56° C the panel reaches extremely large displacements. The results reveal that when the tensile face sheet is warmer than the bottom face, loss of stability always occurs at a higher temperature than when the compressed face sheet is warmer. This difference is especially significant at a thermal gradient of 40° C. Notice that at this gradient the case with a warmer tensile face sheet exhibits a stable nonlinear behavior, while the case where the compressed face sheet is warmer yields an unstable pattern with the probable existence of a limit point at a very low temperature. The same trends are observed for the maximum compressive interfacial vertical normal stresses (see Figure 8b). In all cases,

Figure 9. Temperature equilibrium curves of maximum displacements and vertical normal stresses versus temperature for a *restrained* sandwich panel loaded with mechanical and thermal loads simultaneously, with temperature-independent and temperature-dependent properties at various thermal gradients and where the elevated temperatures are imposed either on the tensile (Ten) or the compressed (Com) face sheet: (a) maximum vertical displacements of face sheets; (b) maximum compressive interfacial vertical normal stresses at interfaces. Legend: ———— t upper face or interface; - - - - b lower face or interface.

larger compressed stresses are observed when the compressed face sheet is warmer. They always reach very high values, which may exceed the allowable compressive normal stresses (compressive strengths at the relevant temperatures) of the core.

The equilibrium curves for the restrained sandwich panel case appear in Figure 9. The curves of temperature versus maximum values of the vertical face sheet displacements appear in Figure 9a. Again, the TI core yields a linear response, which is associated with larger displacement with increasing thermal gradient, but the peak displacements are still quite small. In contrast to this, the TD cases behave in a stable nonlinear manner, and in all cases the upper limit of the temperature range has been reached. The zero thermal gradient case is the most sensitive one. It consists of a stable curve up to 77° C, and above this temperature the equilibrium curve shows signs of loss of stability similar to the postbuckling case shown in Figure 5a. Generally, in this case it matters little if the compressed face sheet is warmer than the tensile face sheet, and vice versa. The same trends are observed for the maximum compressive interfacial vertical normal stresses (see Figure 9b). Here, notice that in all cases the larger compressive stress occurs at the supports and at the lower temperatures as a result of the fixity of the supports and the high resistance (rigidity) of the core. As the temperatures are raised this resistance reduces due to the degradation of the core material, and much smaller interfacial stresses are induced. This is exactly opposite to the case where the core is assumed to have TI properties. For the TI core case the resistance

of the core is unaffected by increased temperatures, and therefore the higher thermal strains cause higher stresses with a linear behavior.

6. Summary and conclusions

The nonlinear thermal behavior, buckling and postbuckling of a sandwich panel with a compliant core that has temperature-dependent properties is presented. The analysis considers the thermal strains of the core in the vertical direction along with the effects of the vertical flexibility of the core using variational principles and the HSAPT approach. The temperature-dependent properties of the core, along with a thermal gradient, yields stiffness coordinates dependent properties. The stress and displacement fields of the core with such nonuniform properties have been solved analytically.

The buckling analysis follows the perturbation technique. It yields a nonlinear set of algebraic equations which are solved numerically for the wrinkling and the global buckling critical temperatures, assuming a uniform temperature field, simple support conditions and temperature-dependent core properties.

The nonlinear response is determined through a numerical solution of a set of coupled first-order nonlinear ordinary differential equations. The parametric continuation procedure, using the temperature at one of the face sheet as a parameter, has been used to determine the equilibrium curves.

The numerical study includes the responses due to buckling, postbuckling and interactions between mechanical loads and thermal ones. The buckling study examines various foam cores including Rohacell foam from Rohm GmbH & Co. KG and the P and HP Divinycell foams from DIAB. A comparison between the critical wrinkling and global buckling temperatures for a core with TI mechanical properties (room-temperature properties assumed) and a core with TD mechanical properties has been conducted. In all cases the analyses predict a significant reduction of the critical wrinkling temperature of the TD core panels, along with changes in the number of half-waves in the buckling pattern, in comparison with panels with TI cores. The changes in the critical temperatures corresponding to the global buckling mode are much smaller (10 to 30%). In all cases, for a particular sandwich panel configuration, the critical temperatures are predicted to be in the upper part of the feasible range of working temperatures.

The numerical study of the nonlinear response consists of two parts. In the first part a postbuckling response of a panel subjected to a thermal gradient loading with fixed support is examined. The second part examines the effect of rising temperatures imposed simultaneously with a prescribed mechanical load, on either the tensile or the compressed face sheets. The effect on the mechanical response of the sandwich panel with and without restrained supports is measured.

The postbuckling study reveals that for the case of a uniform temperature field the nonlinear response is stable as a result of the fixity of the supports in the longitudinal direction, as long as the temperatures are below the upper limit of the working temperature range. As the temperature approach this value, the panel looses its stability with very large displacements and high stresses due to the very low elastic moduli of the core at elevated temperatures. For all other cases, with a gradient through the depth of the core, the response is stable within the feasible working temperature range.

The interaction between a mechanical load and rising temperature at the tensile and compressive face sheets has been studied for restrained and unrestrained sandwich panels with and without a TI core. The results reveal that the response, for an unrestrained sandwich with a temperature-independent core, remains linear and constant through the entire range of working temperatures. In contrast to this, for the

case of a temperature-dependent core, the response is nonlinear and loss of stability occurs far below the upper limit of the operational temperature range. The case where the elevated temperature is imposed on the compressed face is even more severe, and loss of stability occurs at temperatures below those predicted for the case where the tensile face sheet is warmer. For sandwich panels with fixed boundary conditions (full restraint) the nonlinear response generally is of a stable type.

The interaction between mechanical and a thermally induced deformation loads is highly relevant and likely to occur under practical service conditions. This is especially the case for unrestrained sandwich panels with temperature-dependent core properties (as is always the case for polymer foam core materials), and such interactions may seriously affect structural reliability and safety. Hence, it is important to assess these effects for a reliable design of sandwich panels/structures. This implies that a nonlinear analysis procedure, which accounts for the compliant temperature-dependent core properties and the interaction between the mechanical loads and the loads due to thermally induced deformations, must be adopted.

Acknowledgements

References

[Allen 1969] H. G. Allen, *Analysis and design of structural sandwich panels*, Pergamon Press, Oxford, 1969.

[Ascher and Petzold 1998] U. Ascher and L. Petzold, *Computer methods for ordinary differential equations and differential-algebraic equations*, SIAM, Philadelphia, 1998.

[Birman 2005] V. Birman, "Thermally induced bending and wrinkling in large aspect ratio sandwich panels", *Compos. Part A Appl. S.* **36**:10 (2005), 1412–1420.

[Birman et al. 2006] V. Birman, G. A. Kardomateas, G. J. Simitses, and R. Li, "Response of a sandwich panel subject to fire or elevated temperature on one of the surfaces", *Compos. Part A Appl. S.* **37**:7 (2006), 981–988.

[Chen and Chen 1989] L. W. Chen and L. Y. Chen, "Thermal buckling behavior of laminated composite plates with temperature-dependent properties", *Compos. Struct.* **13**:4 (1989), 275–287.

[Chen and Chen 1991] L. W. Chen and L. Y. Chen, "Thermal postbuckling behaviors of laminated composite plates with temperature-dependent properties", *Compos. Struct.* **19**:3 (1991), 267–283.

[Diab Group 2003] "Data sheet HD grade", Technical report, Diab Group, 2003.

[Diab Group 2005] Diab Group, "P and HP-core — test protocol", 2005. Private communication.

[Frostig 1997] Y. Frostig, "Hygothermal (environmental) effects in high-order bending of sandwich beams with a flexible core and a discontinuous skin", *Compos. Struct.* **37**:2 (1997), 205–221.

[Frostig 1998] Y. Frostig, "Buckling of sandwich panels with a flexible core-high-order theory", *Int. J. Solids Struct.* **35**:3-4 (1998), 183–204.

[Frostig and Baruch 1993] Y. Frostig and M. Baruch, "High-order buckling analysis of sandwich beams with transversely flexible core", *J. Eng. Mech. ASCE* **119**:3 (1993), 476–495.

[Frostig and Thomsen 2007a] Y. Frostig and O. T. Thomsen, "Non-linear thermal response of sandwich panels with a flexible core and temperature dependent mechanical properties", 2007. In press.

[Frostig and Thomsen 2007b] Y. Frostig and O. T. Thomsen, "Thermal buckling and post-buckling of sandwich panels with a transversely flexible core", 2007. Submitted.

[Frostig et al. 2005] Y. Frostig, O. T. Thomsen, and I. Sheinman, "On the non-linear high-order theory of unidirectional sandwich panels with a transversely flexible core", *Int. J. Solids Struct.* **42**:5–6 (2005), 1443–1463.

[Gu and Asaro 2005] P. Gu and R. J. Asaro, "Structural buckling of polymer matrix composites due to reduced stiffness from fire damage", *Compos. Struct.* **69**:1 (2005), 65–75.

[Huang and Kardomateas 2002] H. Y. Huang and G. A. Kardomateas, "Buckling and initial postbuckling behavior of sandwich beams including transverse shear", *AIAA J.* **40**:11 (2002), 2331–2335.

[Kant and S. 2000] T. Kant and B. C. S., "Thermal buckling analysis of skew fibre-reinforced composite and sandwich plates using shear deformable finite element models", *Compos. Struct.* **49**:1 (2000), 77–85.

[Kapuria and Achary 2004] S. Kapuria and G. G. S. Achary, "An efficient higher-order zigzag theory for laminated plates subjected to thermal loading", *Int. J. Solids Struct.* **41**:16-17 (2004), 4661–4684.

[Kardomateas and Huang 2003] G. A. Kardomateas and H. Huang, "The initial post-buckling behavior of face-sheet delaminations in sandwich composites", *J. Appl. Mech.* (*Trans. ASME*) **70**:2 (2003), 191–199.

[Ko 1994] W. L. Ko, "Mechanical and thermal buckling analysis of rectangular sandwich panels under different edge conditions", Technical report TM-4585, National Aeronautics and Space Administration, 1994, Available at http://ntrs.nasa.gov/ search.jsp?R=952948&id=2&qs=Ne%3D20%26N%3D4294826073%2% B53.

[Liew et al. 2004] K. M. Liew, J. Yang, and S. Kitipornchai, "Thermal post-buckling of laminated plates comprising functionally graded materials with temperature-dependent properties", *J. Appl. Mech.* (*Trans. ASME*) **71**:6 (2004), 839–850.

[Liu et al. 2006] L. Liu, G. A. Kardomateas, V. Birman, J. W. Holmes, and G. J. Simitses, "Thermal buckling of a heat-exposed, axially restrained composite column", *Compos. Part A Appl. S.* **37**:7 (2006), 972–980.

[Matsunaga 2005] H. Matsunaga, "Thermal buckling of cross-ply laminated composite and sandwich plates according to a global higher-order deformation theory", *Compos. Struct.* **68**:4 (2005), 439–454.

[Mindlin 1951] R. D. Mindlin, "Influence of transverse shear deformation on the bending of classical plates", *J. Appl. Mech.* (*Trans. ASME*) **8** (1951), 18–31.

[Najafizadeh and Heydari 2004] M. M. Najafizadeh and H. R. Heydari, "Thermal buckling of functionally graded circular plates based on higher-order shear deformation plate theory", *Eur. J. Mech. A Solids* **23**:6 (2004), 1085–1100.

[Plantema 1966] F. J. Plantema, *Sandwich construction: the bending and buckling of sandwich beams, plates, and shells*, Wiley, New York, 1966.

[Reddy 1984] J. N. Reddy, *Energy and variational methods in applied mechanics: with an introduction to the finite element method*, John Wiley, New York, 1984.

[Rohacell 2004] Degussa, WF foam data sheets, 2004. Available from www.rohacell.com through the link Site Map.

[Shiau and Kuo 2004] L. C. Shiau and S. Y. Kuo, "Thermal postbuckling behavior of composite sandwich plates", *J. Eng. Mech. ASCE* **130**:10 (2004), 1160–1167.

[Simitses 1976] G. J. Simitses, *An introduction to the elastic stability of structures*, Prentice-Hall, Englewood Cliffs, NJ, 1976.

[Sokolinsky and Frostig 2000] V. Sokolinsky and Y. Frostig, "Branching behavior in the nonlinear response of sandwich panels with a transversely flexible core", *Int. J. Solids Struct.* **37**:40 (2000), 5745–5772.

[Stoer and Bulirsch 1980] J. Stoer and R. Bulirsch, *Introduction to numerical analysis*, Springer, New York, 1980.

[Tessler et al. 2001] A. Tessler, M. S. Annett, and G. Gendron, "A {1, 2}-order plate theory accounting for three-dimensional thermoelastic deformations in thick composite and sandwich laminates", *Compos. Struct.* **52**:1 (2001), 67–84.

[Vinson 1999] J. R. Vinson, *The behavior of sandwich structures of isotropic and composite materials*, Technomic Publishing, Lancaster, PA, 1999.

[Zenkert 1995] D. Zenkert, *An introduction to sandwich construction*, Engineering Materials Advisory Services, West Midlands, UK, 1995.

YEOSHUA FROSTIG: cvrfros@techunix.technion.ac.il
Faculty of Civil Engineering, Technion — Israel Institute of Technology, Haifa 32000, Israel

OLE THYBO THOMSEN: ott@ime.aau.dk
Department of Mechanical Engineering, Aalborg University, Pontoppidanstraede 101, DK-9220 Aalborg, Denmark

MATERIAL GRADING FOR IMPROVED AEROELASTIC STABILITY IN COMPOSITE WINGS

LIVIU LIBRESCU AND KARAM Y. MAALAWI

A novel analytical formulation has been developed for the aeroelastic design of a class of solid nonuniform composite wings with improved aeroelastic torsional stability. Rectangular, unswept slender configurations made of unidirectional fibrous composites are considered, where the mechanical and physical properties can vary in the spanwise direction. Such a structural configuration yields to grading of the material properties along the wing span. The enhancement of the wing torsional stability can be attained, among others, by increasing the critical flight speed at which flutter or divergence instabilities occur. In this study, the latter problem is addressed, where the wing divergence speed is maximized while maintaining the total structural mass at a value equal to that of a known baseline design. Both continuous and discrete structural models have been examined, using classical elasticity and aerodynamic strip theories. The functional behavior of the divergence speed is comprehensively investigated by varying the volume fraction of the constituent materials in preassigned distributions. Exact solutions were obtained for different categories of unidirectionally reinforced composite wing structures: the linear volume fraction (L-VF), the parabolic volume fraction (PR-VF) and the piecewise volume fraction (PW-VF) wing models.

Our results reveal that in general, the torsional stability of the wing can be substantially improved by using nonuniform, functionally graded composites instead of the traditional ones having uniform volume fractions of the constituent materials. Several solutions are given for determining the optimal in-plane fiber distributions, which maximize the divergence speed of a wing made of carbon/epoxy composites without violating the performance requirements imposed on the total structural weight of the aircraft.

1. Introduction

Aeroelastic instabilities are a crucial factor in the design of modern flight vehicle structure. Friedmann [1999] demonstrated that several important aeroelastic problems are still far from being understood. Furthermore, the emergence of new technologies, such as the use of advanced composites and smart materials have invigorated aeroelasticity, and generated a host of new and challenging research topics that can have a major impact on the design of new generation of aerospace vehicles. The creative use of composite materials is becoming important for controlling aeroelastic instabilities beside the benefits of saving structural weight and increasing the fatigue life as well. For example, in the design of a laminated composite wing, Weisshaar [1987] and Karpouzian and Librescu [1994] showed that aeroelastic tailoring can be achieved commonly by varying the ply thickness, ply material and the stacking sequence. Another new class of composite materials can be produced by varying the volume fractions of their constituents in

a predetermined profile. Such nonuniform composites are called *functionally graded materials* (FGMs), in which the properties are functions of the spatial coordinates. Although the concept of aeroelastic tailoring of flight structures has been considered extensively in the literature [Librescu and Song 1992], functional grading has not yet, been implemented, to the authors' knowledge, in the available works. The main aim of the present paper is to open the door for the subject of aeroelastic tailoring of FGMs flight structures. The application to the optimization aspects in composite rotor blades [Ozbay et al. 2005] would also be a future extension of the current material grading concept.

Basic knowledge on the use of FGMs and their wide applications are given in [Suresh and Mortensen 1998]. FGMs were primarily used in situations where large temperature gradients are encountered and have also found several applications in the semiconductor industry. It was also shown that better performance for both static and dynamic behavior of structures fabricated from such advanced composite materials can be substantially achieved. There are different scenarios in modeling the spatial variation of material properties of a functionally graded structure. For example, Chen and Gibson [1998] performed experimental and theoretical analyses to determine the in-plane fiber distribution in unidirectional reinforced composites. They considered distributions represented by polynomial functions, and applied Galerkin's method to calculate the required polynomial coefficients from the resulting algebraic equations. Finally, they found that the linear variation of the volume fraction is a best fit with that predicted experimentally for selected composite beam specimens. Chi and Chung [2006] studied the mechanical behavior of FGM plates under transverse loading, where a constant Poisson's ratio and variable moduli of elasticity throughout the plate thickness was assumed. The volume fraction of the constituent materials were defined by simple power- laws, and closed form solutions using Fourier series were given for the case of simply- supported plates.

Considering structural stability of functionally graded beams, Elishakoff and Rollot [1999] presented closed-form solutions of the buckling load of a variable stiffness column. The modulus of elasticity was taken as a polynomial of the axial coordinate along the column's length. Cases in which a fourth-order polynomial serves as an exact buckling mode were provided. Another work dealing with the buckling behavior of two dimensional FGM rectangular plates subjected to in-plane edge loads was addressed by Chen and Liew [2004]. They applied a mesh-free approach, which approximates displacements based on a set of scattered nodes instead of the commonly implemented finite elements. Elishakoff and Guede [2004] then derived other closed-form solutions for the natural frequencies of an axially graded beam with variable mass and stiffness properties along its length.

In the field of the optimum design of FGM-structures, Qian and Batra [2005] considered frequency optimization of a cantilevered plate with variable volume fraction according to simple power-laws. They implemented genetic algorithms to find the optimum values of the power exponents, which maximize the natural frequencies, and concluded that the volume fraction needs to be varied in the longitudinal direction of the plate rather than in the thickness direction. More recently, Goupee and Vel [2006] proposed a methodology to optimize the natural frequencies of functionally graded beam with variable volume fraction of the constituent materials in the beam's length and height directions. They used a piecewise bicubic interpolation of volume fraction values specified at a finite number of grid points, and applied a genetic algorithm code to find the needed optimum designs.

As it clearly appears, in spite of its enormous potential benefits in aerospace industry, the use of the in-plane grading was exploited in problems involving only fundamental mechanical problems. The

same conclusions were given in the extensive review paper by Birman and Byrd [2007]. In the present study, analytical solutions are developed and presented for improving the torsional stability of a slender subsonic wing through optimal grading of the material volume fraction in the spanwise direction. Three models have been thoroughly analyzed: continuous linear (L-VF), continuous parabolic (PR-VF) and piecewise (PW-VF) mathematical models. The enhancement of the wing torsional stability is measured by maximization of the divergence speed while maintaining the total structural mass at a value equals to that of a known baseline design. The functional behavior of the divergence speed is comprehensively investigated by varying the volume fraction of the constituent materials in preassigned distributions. Enhanced wing designs made-up from carbon/epoxy composite material have been obtained and discussed. Side constraints are set on the fiber volume fractions to not exceed prescribed lower and upper limiting values.

2. Statement of the problem and basic formulation

When the flight speed of an aircraft exceeds a certain value called the divergence speed, V_{div}, the aerodynamic twist moment applied to the wing exceeds the restoring elastic moment of its structure [Bisplinghoff and Ashley 1962]. This causes static torsional instability of the lifting surface, which may twist to failure. Therefore, high divergence speed can be regarded as a major aspect in designing an efficient lifting surface with enhanced torsional stability. Maximization of the divergence speed can also have other desirable effects on the overall structural design. It helps in avoiding the occurrence of large displacements, distortions and excessive vibrations, and may also reduce fretting among structural parts, which is a major cause of fatigue failure. Consider an unswept, slender wing with rectangular planform and solid cross section, as depicted in Figure 1. The coordinates x_1 and x_2 are associated with the wing middle surface, whereas the x_3-axis points in the airfoil thickness direction. In the present model formulation, the wing is considered to be made of unidirectional fiber-reinforced composites with variable fiber volume fraction in the spanwise direction, x_1. The flow is taken to be steady, and incompressible. The aspect ratio is assumed to be sufficiently large with no major cutouts through the structure so that the classical engineering theory of torsion can be applicable and the state of deformation described in terms of one space coordinate. The elastic axis is assumed to be well defined and, hence, the bending and torsion degrees of freedom can be decoupled. For wings with low aspect ratio, the cross section warping ought to be included to account for three dimensional deformation effects [Librescu and Thangjitham 1991]. This will be considered by the authors in an extension of the present study.

It was shown by in [Lekhnitski 1981, Chapter 6, Sections 55–56] and [Tsai et al. 1990] that the equivalent shear modulus G of a unidirectionally reinforced composite lamina with thin cross section can be determined from the relation

$$G = f_1 G_{12},$$

where f_1 is a function that depends on the geometry and thickness ratio h/C of the cross section (C being the chord length and h the maximum thickness of the cross section) and on the ratio G_{12}/G_{13} between the in-plane and out-of-plane shear moduli G_{12} and G_{13}.

For many types of fibrous composites commonly utilized in aircraft structures, such as carbon/epoxy and graphite epoxy, the two moduli are approximately equal. Some experimental results were given in [Tsai and Daniel 1990] for the determination of the in- and out-of-plane shear moduli. We apply here
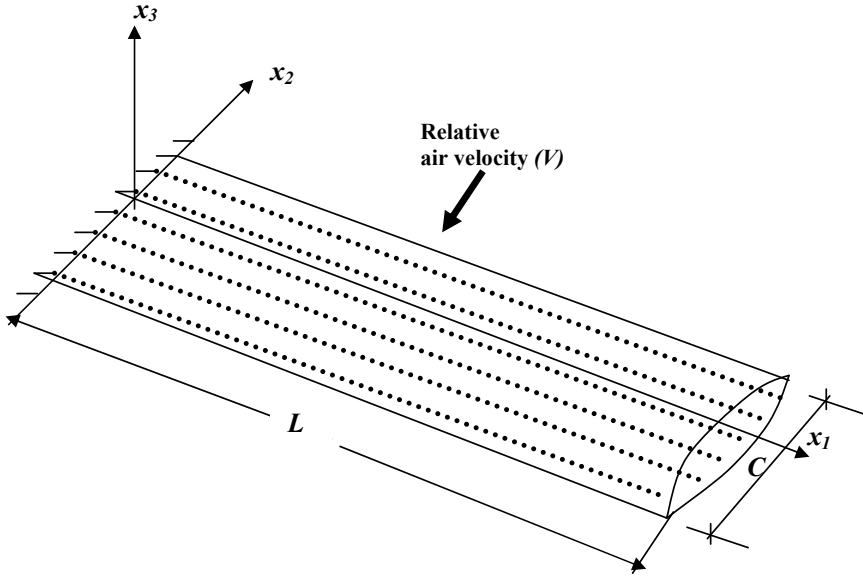
Figure 1. Unidirectional fiber-reinforced composite wing model.

semiempirical formula from [Halpin and Tsai 1967] to determine G_{12}:

$$G_{12} = G_m \frac{1 + \xi \eta V_f}{1 - \eta V_f}, \quad \text{where} \quad \eta = \frac{(Gf/Gm) - 1}{(Gf/Gm) + \xi}, \tag{1}$$

where G_m and G_f ($\equiv G_{f12}$, in the x_1-x_2 plane) are the shear moduli of the matrix and fiber materials, V_f is the fiber volume fraction and the parameter ξ is called the reinforcing efficiency and may be taken as 100% for theoretical analysis [Daniel and Ishai 2006]. The variation of the fiber volume fraction in FGM structures is usually described by power-law or exponential function models:

$$\begin{aligned} V_f(x) &= V_{fr}(1 - \beta x^p), \quad \beta = (1 - \Delta), \\ V_f(x) &= V_{fr} e^{\beta x}, \qquad\quad \beta = \ln \Delta, \end{aligned} \tag{2}$$

where $\Delta = V_{ft}/V_{fr}$ is the ratio between the fiber volume fractions V_{ft} and V_{fr} at the wing tip and at the root, the symbol $x = x_1/L$ denotes the dimensionless spanwise coordinate and p is an integer exponent. Wings with uniform, linear or parabolic distributions of $V_f(x)$ correspond to $p = 0$, 1 and 2. Similar distributions were utilized in [Chi and Chung 2006] to analyze FGM plates under transverse loading. The exponential distribution is not considered in the present investigation.

3. Stability analysis

Using classical elasticity and aerodynamic strip theories, we can write the differential equation governing wing torsional stability (see [Bisplinghoff and Ashley 1962]) as

$$\frac{d}{dx_1}\left(GJ\frac{d\alpha}{dx_1}\right) + \tfrac{1}{2}\rho V^2 C^2 ea\alpha(x_1) = 0, \tag{3}$$

subject to the boundary conditions

$$\alpha(0) = 0 \quad \text{for } x_1 = 0,$$

indicating that the elastic angle of attack α vanishes at the wing root, and

$$\left[GJ \frac{d\alpha}{dx_1} \right]_{x_1=L} = 0 \quad \text{for } x_1 = L,$$

which says that the torsional moment T vanishes at the wing tip. Here J is the torsion constant, which for thin wings with solid cross section, is directly proportional to the cube of the maximum airfoil thickness h, and the chord length C:

$$J = f_2 C h^3,$$

where f_2 is a shape factor that depends upon the geometry of the airfoil section. The other parameters in (3) are defined as follows: ρ is the air density, depending on the flight altitude, V is the flight speed, e is the fractional location of the shear center, positive aft with respect to the aerodynamic center, and a is the airfoil lift-curve slope.

It is convenient to normalize all variables and parameters with respect to a baseline design having uniform mass and stiffness distributions. The baseline is made of a uniform unidirectional fibrous composite with equal volume fraction of the matrix and fiber materials: $V_{f0} = 50\%$. The optimum wing designs presented herein shall have the same material type of construction, wing planform geometry, airfoil section, and same total structural mass as those of the baseline design. Therefore, the preassigned parameters ought to be selected as the type and dimensions of the airfoil section (that is, C, J, e and a are fixed), wing span L, and type of material of construction (that is, G_m, G_f, ρ_m, ρ_f are fixed). The flight altitude is also fixed (that is, ρ is fixed). Therefore, the only remaining variable to be taken into consideration is the distribution of the modulus of rigidity in the spanwise direction. Normalizing with respect to the uniform baseline design defined above, (3) takes the dimensionless form

$$(\hat{G}\alpha')' + \hat{V}^2 \alpha(x) = 0, \quad \alpha(0) = 0, \quad \alpha'(1) = 0, \tag{4}$$

where $\hat{G} = G_{12}/G_{12,0}$ is the dimensionless shear modulus and the prime denotes differentiation with respect to the dimensionless coordinate $x = x_1/L$. The dimensionless flight speed is defined by

$$\hat{V} = VCL\sqrt{\frac{\rho e a}{2GJ_0}},$$

where GJ_0 is the torsional stiffness of the baseline design. The shear modulus $G_{12,0}$ of the baseline design can be calculated from (1) by setting $V_{f0} = 0.5$ and $\xi = 1$. Substituting Equations (1) and (2) into (4), we get

$$(1 - f^2)\alpha'' + 2f'\alpha' + \mu(1 - f)^2 \alpha = 0, \tag{5}$$

where

$$f = \eta V_f(x) \quad \text{and} \quad \mu = \hat{V}^2 \frac{2 + \eta}{2 - \eta}.$$

3.1. *Continuous model: An exact power series solution.* Since f is a polynomial, an exact power series solution to (5) can be obtained by the method of Frobenius [Edwards and Penney 2004], in which the general solution is expressed as

$$\alpha(x) = \sum_{m=1}^{2} C_m \lambda_m(x),$$

where the C_m are constants of integration and the λ_m are two linearly independent solutions having the form

$$\lambda_m(x) = \sum_{n=m}^{\infty} a_{m,n} x^{n-1}, \quad m = 1, 2.$$

The unknown coefficients $a_{m,n}$ can be determined by substitution into the differential equation (5) and equating coefficients of like powers of x. The required recurrence formulas have been evaluated and are given for the linear distribution model by

$$a_{m,n} = \frac{\begin{aligned}2\beta\gamma(n-2)\big(1-\gamma(n-3)\big)a_{m,n-1} + \big((n-3)(n-4)(\beta\gamma)^2 - \mu(1-\gamma)^2\big)a_{m,n-2} \\ - 2\beta\gamma\mu(1-\gamma)a_{m,n-3} - \mu(\beta\gamma)^2 a_{m,n-4}\end{aligned}}{(n-1)(n-2)(1-\gamma^2)}$$

and for the parabolic distribution model by

$$a_{m,n} = \frac{\begin{aligned}\big(2\beta\gamma(n-3)(2-\gamma(n-4)) - \mu(1-\gamma)^2\big)a_{m,n-2} \\ + \big((\beta\gamma)^2(n-5)(n-6) - 2\beta\gamma\mu(1-\gamma)\big)a_{m,n-4} - \mu(\beta\gamma)^2 a_{m,n-6}\end{aligned}}{(n-1)(n-2)(1-\gamma^2)},$$

where $\gamma = \eta V_{fr}$. A coefficient $a_{m,n}$ is set equal to zero whenever n is less than m, and the leading coefficients $a_{m,m}$ in each series are arbitrary and can be set to one. This method was successfully applied by Maalawi and Negm [2002] to determine the exact rotating frequencies of a wind turbine blade in flapping motion.

Application of the associated boundary conditions and consideration of the nontrivial solution lead to the required characteristic equation:

$$\lambda_2'(1) = 0,$$

which is to be solved for the lowest root corresponding to the critical flight speed $\hat{V}_{\text{div}}$ at which divergence of the wing occurs.

3.2. *Piecewise wing model.* A piecewise model concept was used by [Maalawi 2002] to find optimized designs of elastic columns against buckling. The optimization variables included the cross section dimensions as well as the length of each segment composing the column, and several solutions were given for both solid and tubular configurations. It was concluded that the use of piecewise models in structural optimization gives excellent results and can be promising for similar applications. Figure 2 shows a rectangular lifting surface, which is constructed from N uniform piecewise panels, each of which has different fiber volume fractions and length. For the k-th panel (see Figure 3), Equation (4) reduces to

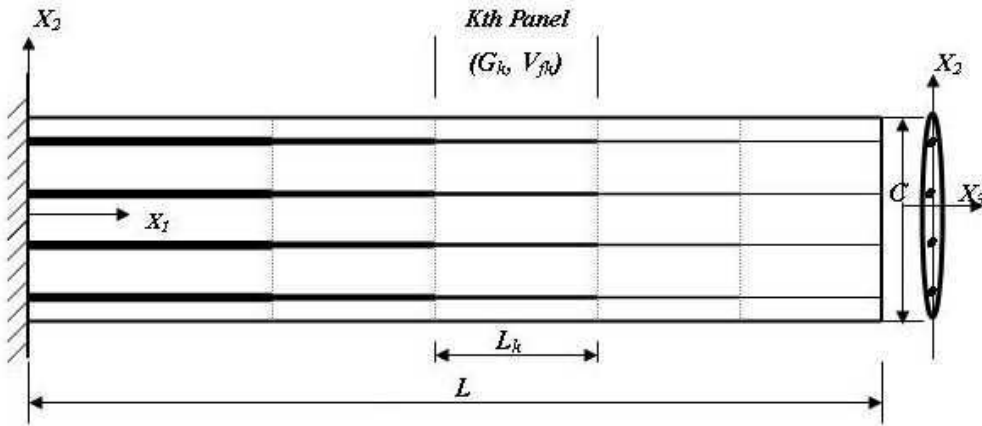$$\alpha''(\hat{x}) + \lambda_k^2 \alpha(\hat{x}) = 0, \qquad \lambda_k = \hat{V}/\sqrt{\hat{G}_k}, \tag{6}$$

Figure 2. Rectangular lifting surface constructed from piecewise panels: wing planform geometry.
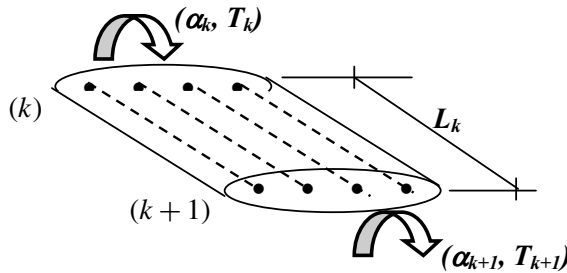

Figure 3. Definition of the state variables for the k-th panel.

where $\hat{x} = x - x_k$ is a local coordinate, ranging from 0 to $\hat{L}_k = L_k/L$, the dimensionless length of the k-th panel, and $\hat{G}_k$ is the dimensionless shear modulus of the kth wing panel.

The exact solution of (6) is of course

$$\alpha(\hat{x}) = A \sin(\lambda_k \hat{x}) + B \cos(\lambda_k \hat{x}),$$

where A and B are the constants of integration. The dimensionless internal torsional moment, $T(\hat{x})$, can be obtained by differentiating this equation and multiplying by the dimensionless torsional rigidity:

$$T(\hat{x}) = \hat{G}_k \alpha' = \lambda_k \hat{G}_k \big(-A \sin(\lambda_k \hat{x}) + B \cos(\lambda_k \hat{x}) \big).$$

Applying the boundary conditions at stations k and $k+1$ (see Figure 3), we obtain at $\hat{x} = 0$ the equations

$$\alpha_k = A, \quad T_k = B \lambda_k \hat{G}_k, \tag{7}$$

and at $\hat{x} = \hat{L}_k$ the equations

$$
\begin{aligned}
\alpha_{k+1} &= A \cos(\lambda_k \hat{L}_k) + B \sin(\lambda_k \hat{L}_k), \\
T_{k+1} &= \lambda_k \hat{G}_k \big(-A \sin(\lambda_k \hat{L}_k) + B \cos(\lambda_k \hat{L}_k) \big).
\end{aligned}
\tag{8}
$$

Substituting from (7) into (8), the relation between the state variables (α, T) at both ends of the k-th panel can be expressed by the matrix equation

$$\begin{Bmatrix} \alpha_{k+1} \\ T_{k+1} \end{Bmatrix} = E^{(k)} \begin{Bmatrix} \alpha_k \\ T_k \end{Bmatrix}, \quad \text{where} \quad E^{(k)} = \begin{bmatrix} \cos \lambda_k \hat{L}_k & \sin \lambda_k \hat{L}_k / (\lambda_k \hat{G}_k) \\ -\lambda_k \hat{G}_k \sin \lambda_k \hat{L}_k & \cos \lambda_k \hat{L}_k \end{bmatrix}.$$

It is now possible to compute the state variables progressively along the wing span by applying continuity requirements of the variables (α, T) among the interconnecting boundaries of the various wing panels. Therefore, the state variables at the extreme boundaries are related by the matrix equation

$$\begin{Bmatrix} \alpha_{N+1} \\ T_{N+1} \end{Bmatrix} = E \begin{Bmatrix} \alpha_1 \\ T_1 \end{Bmatrix}, \tag{9}$$

where

$$E = E^{(N)} E^{(N-1)} \dots E^{(3)} E^{(2)} E^{(1)}.$$

The nontrivial solution of equation (9) can be determined by applying the appropriate boundary conditions at the wing root and tip sections. The resulting transcendental equation, also named the characteristic equation, is given by

$$E_{22} = 0,$$

which can be solved for determining the critical flight speed at which torsional divergence instability occurs.

4. Results and discussion

The mathematical models developed in the previous sections have been applied to obtain wing designs with improved torsional stability, measured in the context of static aeroelasticity, by raising the divergence speed without weight penalties. The selected wing material is carbon-AS4 / epoxy-3501-6 composite, which has favorable characteristics and is highly desirable in both civilian and military aircraft structures. Its properties are given in Table 1. Lower and upper bounds of 25% and 75%, respectively are imposed on the fiber volume fraction. The total structural mass M is kept equal to the mass M_0 of the baseline design, so the dimensionless mass $\hat{M} = M/M_0$ equals 1. Since the fiber volume fraction of the baseline design, V_{f0}, equals 50%, a feasible design must satisfy the constraint equations

$$\int_0^1 V_f(x) \, dx = 0.5$$

for the continuous model or

$$\sum_{k=1}^N V_{fk} \hat{L}_k = 0.5 \tag{10}$$

for the piecewise model, where V_{fk} and $\hat{L}_k$ are the fiber volume fraction and dimensionless length of the k-th panel (Figure 2).

The mass density distribution $\rho_c(x)$ of the composite material is determined by the rule of mixture, assuming no voids are present:

$$\rho_c(x) = \rho_m + (\rho_f - \rho_m) V_f(x).$$

Property	fiber	matrix
Mass density (g/cm^3)	$\rho_f = 1.81$	$\rho_m = 1.27$
Young's moduli (GPa)	$E_{1f} = 235$	$E_m = 4.3$
	$E_{2f} = 15$	
Shear moduli (GPa)	$G_{12f} = 27.0$	$G_m = 1.60$
	$G_{23f} = 7.0$	
Poisson's ratio	$\nu_{12f} = 0.2$	$\nu_m = 0.35$

Table 1. Material properties of carbon-AS4 / epoxy-3501-6 composite. The data are from [Daniel and Ishai 2006]. For a final structural design, however, experimental verifications are necessary.

The developed level curves of the dimensionless critical velocity $\hat{V}_{\mathrm{div}}$ in V_{fr}-V_{ft} design space for the linear grading model (L-VF) are depicted in Figure 4, left. We see that $\hat{V}_{\mathrm{div}}$ is a well behaved function and continuous in the design variables, namely, the fiber volume fractions at the wing root, V_{fr}, and tip, V_{ft}. It increases monotonically with the penalty of increasing the total structural weight, which has a harmful effect on the overall performance characteristics of the aircraft design. Therefore, maintaining the mass constant, one must follow the line $\hat{M} = 1$, as shown in the figure, to attain a feasible design. Results for the parabolic model (PR-VF) are depicted in Figure 4, right.

The variation of $\hat{V}_{\mathrm{div}}$ and the fiber volume fraction at the wing root V_{fr} with the ratio $\Delta = V_{ft}/V_{fr}$ is given in Figure 5. Results for both linear and parabolic grading models are depicted, are based on the preservation of the total structural mass ($\hat{M} = 1.0$). As Δ increases, V_{div} decreases until it reaches its
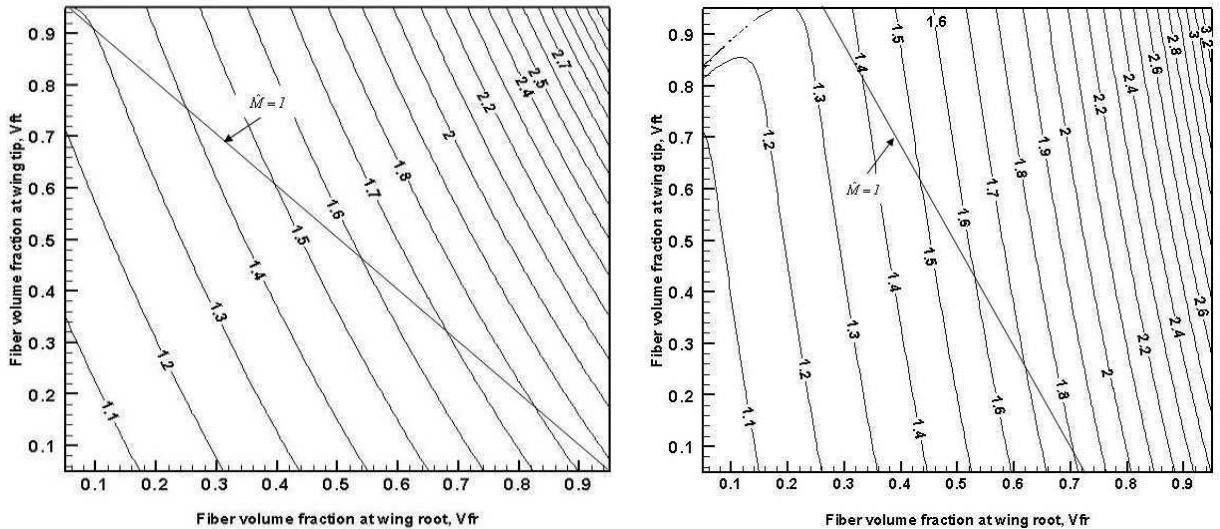
Figure 4. Isomerits of $\hat{V}_{\mathrm{div}}$ in the V_{fr}-V_{ft} design space. Left: L-VF model. Right: PR-VF model.
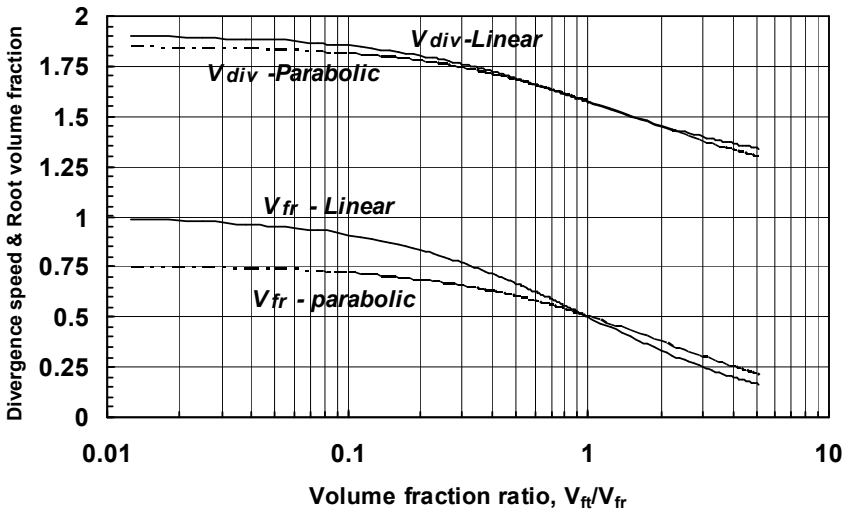
Figure 5. Variation of $\hat{V}_{\text{div}}$ and V_{fr} with volume fraction ratio ($\hat{M} = 1.0$).

principal value $\pi/2$, which corresponds to the uniform baseline design having volume fraction of 50%. When Δ exceeds unity, a noticeable drop in the divergence speed occurs resulting in an undesirable degradation in the overall torsional stability level of the wing. Table 2 gives the final results for both cases with and without the side constraints imposed on $V_f(x)$.

It is observed that the linear grading excels the parabolic one in attaining higher torsional stability levels. However, this may not guarantee satisfactions of other strength requirements. The parabolic distribution seems to be more feasible since the main characteristic length of the fibers' cross section (say, the diameter of a circular fiber) can change linearly along the span.

We next consider the piecewise model (PW-VF). Figure 6, left, shows the developed isomerits for a wing composed from two panels. The design variables are $(V_{f1}, \hat{L}_1)$ and $(V_{f2}, \hat{L}_2)$. However, one of the panel lengths can be eliminated, because of the equality constraint $\hat{L}_1 + \hat{L}_2 = 1.0$. Another variable can also be discarded by applying the mass equality constraint (10), which further reduces the number of variables to only any two of the whole set of variables. The level curves shown in the figure represent the dimensionless critical speed $\hat{V}_{\text{div}}$, augmented with the equality mass constraint, $\hat{M} = 1.0$. It is seen that

	L-VF		PR-VF	
	Case A	Case B	Case A	Case B
V_{fr}	1.0	0.75	0.75	0.625
Δ	0.0	0.33	0.0	0.4
$\hat{V}_{\text{div}}$	1.91	1.75	1.85	1.71
Gain	21%	11%	18%	9%

Table 2. Carbon/epoxy wing designs with improved torsional stability ($\hat{M} = 1.0$). Case A: No side constraints are imposed on $V_f(x)$. Case B: The side constraint $0.25 \leq V_f(x) \leq 0.75$ is imposed. Gain is relative to the baseline value ($\pi/2$) of $\hat{V}_{\text{div}}$.
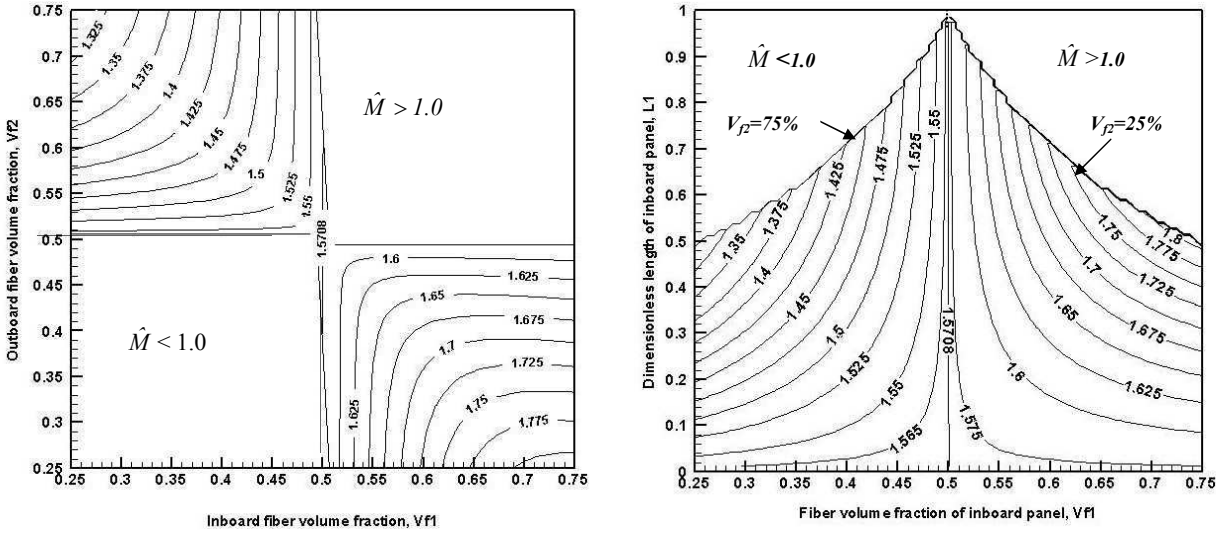
Figure 6. Isomerits of $\hat{V}_{\text{div}}$ in V_{f1}-V_{f2} design space (left) and V_{f1}-$\hat{L}_1$ design space (right) for a two-panel wing.

the function is well behaved and continuous everywhere in the selected design space V_{f1}-V_{f2}, except in the empty regions of the first and third quadrants, where the equality mass constraint is violated. The cross lines $V_{f1} = 0.5$ and $V_{f2} = 0.5$ represent the level curves of the principal value $\pi/2$.

The functional behavior of the divergence speed in the V_{f1}-$\hat{L}_1$ design space is shown in Figure 6, right. The shape of the contour lines resemble the streamlines of a flow originated from a jet at the vertex $(V_{f1}, \hat{L}_1) = (0.5, 1.0)$ and collides with a flat plat located at the horizontal line $\hat{L}_1 = 0$, with the stagnation point $(V_{f1}, \hat{L}_1) = (0.5, 0.0)$. The middle vertical line $V_{f1} = 0.5$ represents the contour of the principal value $\pi/2$ of the uniform baseline wing design. Two empty zones, where the equality mass constraint is violated, are indicated in the figure.

The feasible domain is bounded from above by the two curved lines representing the upper and lower limiting constraints imposed on the volume fraction of the outboard wing panel. The contours inside the feasible domain are not allowed to penetrate these borderlines and obliged to turn sharply to be asymptotes to them, in order not to violate the mass constraint. This is why they appear in the figure as zigzag lines.

The constrained optima were found to be $(V_{f1}, \hat{L}_1) = (0.75, 0.5)$ and $(V_{f2}, \hat{L}_2) = (0.25, 0.5)$, which means that the side constraints are always active [Venkataraman 2002].

The corresponding maximum value of the divergence speed is $\hat{V}_{\text{div}} = 1.81$, representing an optimization gain of 15%. This means that a piecewise grading of the material is slightly better than the parabolic model described by Equation (2). Isomerits of a three-panel wing is depicted in Figure 7, which has a pyramidal shape with its vertex at the design point $(V_{f2}, \hat{L}_2) = (0.5, 1.0)$ having $\hat{V}_{\text{div}} = \pi/2$ and $\hat{M} = 1.0$. The feasible domain is bounded from above by the two lines representing cases of a two-panel wing, with $V_{f1} = 0.75$ for the line to the left and $V_{f3} = 0.25$ for the right line. Both have a zigzag pattern because of the crowded pattern of the interior contours, which are forced to turn and becoming asymptotical to them, in order not to violate the mass equality constraint.
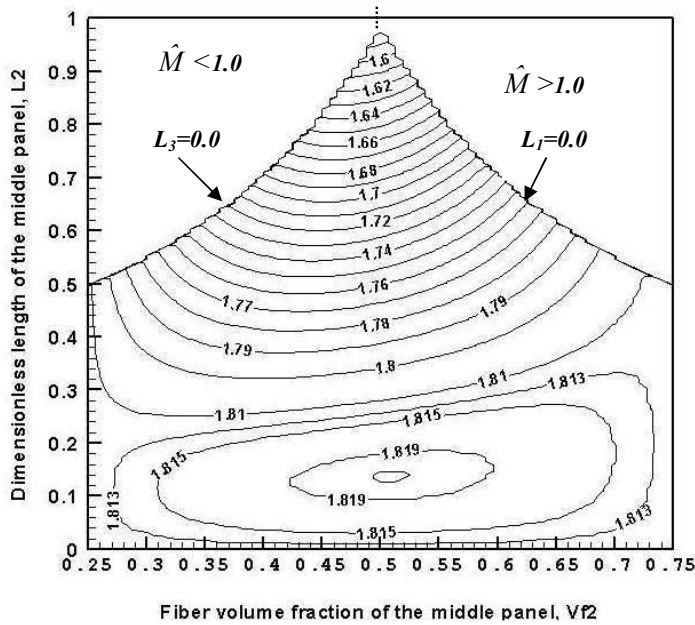
Figure 7. Global optimality solution for a three-panel wing model.

The final global optimal solution, lying in the bottom of the pyramid, can be calculated using the MATLAB optimization toolbox routines [Venkataraman 2002]. We obtain

$$(V_{f1}, \hat{L}_1) = (0.75, 0.43125), \quad (V_{f2}, \hat{L}_2) = (0.50, 0.1375), \quad (V_{f3}, \hat{L}_3) = (0.25, 0.43125), \quad \hat{V}_{\text{div}} = 1.82.$$

This represents an optimization gain of about 16%.

5. Conclusions

We have presented a novel design approach, based on the proper use of functional graded materials for improving the overall torsional stability of a class of unidirectionally reinforced composite wings. The torsional stability is measured by increasing the critical flight speed at which wing divergence occurs while not violating performance requirements imposed on the total structural weight of the aircraft. The mechanical and physical properties of the material are optimized in the spanwise direction, where the spatial distribution of the fiber volume fraction is assumed to be prescribed by either continuous or piecewise mathematical models. Lower and upper bounds are imposed on the design variables in order to avoid having odd-shaped optimized configurations with unrealistic values of the volume fractions. The functional behavior of the divergence speed $\hat{V}_{\text{div}}$ with the selected optimization variables has been thoroughly investigated, and useful design charts are given showing conspicuous design trends for wings with improved aeroelastic performance. The given exact mathematical approaches ensured the attainment of global optimality of the proposed wing model.

To our knowledge, aeroelastic tailoring of a wing with material grading in the spanwise direction had not yet been considered in the available research work. It has been the major aim of this paper to open the door for such a promising direction in the field of aeroelasticity of flight structures. Future work includes

aeroelastic optimization of functionally graded trapezoidal and swept wings. The behavior when grading is performed in both the spanwise and the airfoil thickness directions is now under study.

Acknowledgments

References

[Birman and Byrd 2007] V. Birman and W. L. Byrd, "Modeling and analysis of functionally graded materials and structures", *Applied Mechanics Reviews* (2007). to appear.

[Bisplinghoff and Ashley 1962] R. L. Bisplinghoff and H. Ashley, *Principles of aeroelasticity*, Wiley, New York, 1962.

[Chen and Gibson 1998] W.-H. Chen and R. F. Gibson, "Property distribution determination of non-uniform composite beams from vibration response measurements and Galerkin's method", *J. App. Mech.* **65** (1998), 127–133.

[Chen and Liew 2004] X. L. Chen and K. M. Liew, "Buckling of rectangular functionally graded material plates subject to nonlinearly distributed in-plane edge loads", *J. Smart Materials and Structures* **13** (2004), 1430–1437.

[Chi and Chung 2006] S.-H. Chi and Y.-L. Chung, "Mechanical behavior of functionally graded material plates under transverse load, I: analysis", *International Journal of Solids and Structures* **43** (2006), 3657–3674.

[Daniel and Ishai 2006] I. M. Daniel and O. Ishai, *Engineering mechanics of composite materials*, 2nd ed., Oxford Univ. Press, New York, 2006.

[Edwards and Penney 2004] C. H. Edwards and D. E. Penney, *Differential equations and boundary value problems: computing and modeling*, Prentice Hall, Englewood Cliffs, NJ, 2004.

[Elishakoff and Guede 2004] I. Elishakoff and Z. Guede, "Analytical polynomial solutions for vibrating axially graded beams", *J. Mech. Adv. Mater. Struct.* **11** (2004), 517–533.

[Elishakoff and Rollot 1999] I. Elishakoff and O. Rollot, "New closed-form solutions for buckling of a variable stiffness column by Mathematica", *J. Sound Vib.* **224** (1999), 172–182.

[Friedmann 1999] P. P. Friedmann, "Renaissance in aeroelasticity and its future", *J. Aircraft* **36** (1999), 105–121.

[Goupee and Vel 2006] A. J. Goupee and S. S. Vel, "Optimization of natural frequencies of bidirectional functionally graded beams", *Journal of Structural and Multidisciplinary Optimization* **32**:6 (2006), 73–484.

[Halpin and Tsai 1967] J. C. Halpin and S. W. Tsai, "Effects of environmental factors on composite materials", technical report AFML-TR-67-423, Dayton, OH, 1967.

[Karpouzian and Librescu 1994] G. Karpouzian and L. Librescu, "Comprehensive model of anisotropic aircraft wings suitable for aeroelastic analysis", *J. Aircraft* **31**:3 (1994), 703–712.

[Lekhnitski 1981] S. G. Lekhnitski, *Theory of elasticity of an anisotropic elastic body*, Mir, Moscow, 1981.

[Librescu and Song 1992] L. Librescu and O. Song, "On the static aeroelastic tailoring of composite aircraft swept wings modeled as thin-walled beam structures", *Composite Engineering* **2**:5 (1992), 497–512.

[Librescu and Thangjitham 1991] L. Librescu and S. Thangjitham, "Analytical studies on static aeroelastic behavior of forward-swept composite wing structures", *J. Aircraft* **28**:2 (1991), 151–157.

[Maalawi 2002] K. Y. Maalawi, "Buckling optimization of flexible columns", *Int. J. Solids Struct.* **39** (2002), 5865–5876.

[Maalawi and Negm 2002] K. Y. Maalawi and H. M. Negm, "Optimal frequency design of wind turbine blades", *J. Wind Engineering and Industrial Aerodynamics* **90**:8 (2002), 961–986.

[Ozbay et al. 2005] S. Ozbay, E. Armanios, O. Bauchau, and D. S. Dancila, "Extension-twist coupling optimization in composite rotor blades", in *Proceedings of the 46th AIAA/ASME/ASCE/AHS/ASC Structures, Structural Dynamics and Materials Conference* (Austin, TX, 2005), 2005.

[Qian and Batra 2005] L. F. Qian and R. C. Batra, "Design of bidirectional functionally graded plate for optimal natural frequencies", *J. Sound Vib.* **280** (2005), 415–424.

[Suresh and Mortensen 1998] S. Suresh and A. Mortensen, *Fundamentals of functionally graded materials*, Cambridge Univ. Press, 1998.

[Tsai and Daniel 1990] C. L. Tsai and I. M. Daniel, "Determination of inplane and out-of-plane shear moduli of composite materials", *J. Exper. Mech.* **30** (1990), 295–299.

[Tsai et al. 1990] C. L. Tsai, I. M. Daniel, and G. Yaniv, "Torsional response of rectangular composite laminates", *J. App. Mech.* **57** (1990), 383–387.

[Venkataraman 2002] P. Venkataraman, *Applied Optimization with MATLAB Programming*, Wiley, New York, 2002.

[Weisshaar 1987] T. A. Weisshaar, "Aeroelastic tailoring: Creative uses of unusual materials", technical report 87-0976, 1987.

LIVIU LIBRESCU: Deceased 16 Apr 2007
Department of Engineering Science and Mechanics, Virginia Polytechnic Institute and State University, 318 Norris Hall, Blacksburg, VA 24061, United States

KARAM Y. MAALAWI: maalawi@netscape.net
Department of Mechanical Engineering, National Research Center, 12622 Dokki, Cairo, Egypt

SUBMISSION GUIDELINES

ORIGINALITY

Authors may submit manuscripts in PDF format on-line. Submission of a manuscript acknowledges that the manuscript is *original and has neither previously, nor simultaneously, in whole or in part, been submitted elsewhere.* Information regarding the preparation of manuscripts is provided below. Correspondence by email is requested for convenience and speed. For further information, write to:

Marie-Louise Steele
Division of Mechanics and Computation
Durand Building, Room 262
Stanford University
Stanford CA 94305

LANGUAGE

Manuscripts must be in English. A brief abstract of about 150 words or less must be included. The abstract should be self-contained and not make any reference to the bibliography. Also required are keywords and subject classification for the article, and, for each author, postal address, affiliation (if appropriate), and email address if available. A home-page URL is optional.

FORMAT

Authors are encouraged to use LaTeX and the standard article class, but submissions in other varieties of TeX, and, exceptionally in other formats, are acceptable. Electronic submissions are strongly encouraged in PDF format only; after the refereeing process we will ask you to submit all source material.

REFERENCES

Bibliographical references should be listed alphabetically at the end of the paper and include the title of the article. All references in the bibliography should be cited in the text. The use of BibTeX is preferred but not required. Tags will be converted to the house format (see a current issue for examples), however, in the manuscript, the citation should be by first author's last name and year of publication, e.g. "as shown by Kramer, et al. (1994)". Links will be provided to all literature with known web locations and authors are encouraged to provide their own links on top of the ones provided by the editorial process.

FIGURES

Figures prepared electronically should be submitted in Encapsulated PostScript (EPS) or in a form that can be converted to EPS, such as GnuPlot, Maple, or Mathematica. Many drawing tools such as Adobe Illustrator and Aldus FreeHand can produce EPS output. Figures containing bitmaps should be generated at the highest possible resolution. If there is doubt whether a particular figure is in an acceptable format, the authors should check with production by sending an email to:

production@mathscipub.org

Each figure should be captioned and numbered so that it can float. Small figures occupying no more than three lines of vertical space can be kept in the text ("the curve looks like this:"). It is acceptable to submit a manuscript with all figures at the end, if their placement is specified in the text by means of comments such as "Place Figure 1 here". The same considerations apply to tables.

WHITE SPACE

Forced line breaks or page breaks should not be inserted in the document. There is no point in your trying to optimize line and page breaks in the original manuscript. The manuscript will be reformatted to use the journal's preferred fonts and layout.

PROOFS

Page proofs will be made available to authors (or to the designated corresponding author) at a web site in PDF format. Failure to acknowledge the receipt of proofs or to return corrections within the requested deadline may cause publication to be postponed.

JOURNAL OF
MECHANICS OF MATERIALS AND STRUCTURES